

THE UNIVERSITY OF HULL

**Investigation of a Novel Hybrid Photovoltaic-
Thermoelectric Generator System**

being a Thesis submitted for the Degree of Doctor of Philosophy in the
University of Hull

by

Samson Olaoluwa Shittu

MSc University of Hull, UK

BEng Covenant University, Nigeria

August 2020

CONTENTS

CONTENTS..... I

PUBLICATIONS VII

ACKNOWLEDGEMENT XII

ABSTRACT XIII

LIST OF FIGURES XV

LIST OF TABLES..... XXVII

NOMENCLATURE..... XXVIII

CHAPTER 1 INTRODUCTION1

 1.1 RESEARCH BACKGROUND 1

 1.2 RESEARCH AIM AND OBJECTIVES 8

 1.3 RESEARCH METHODOLOGY..... 9

 1.4 RESEARCH NOVELTY 11

 1.5 THESIS STRUCTURE 13

CHAPTER 2 LITERATURE REVIEW17

 2.1 CHAPTER INTRODUCTION 17

 2.2 PHOTOVOLTAIC SYSTEMS 18

 2.2.1 Modelling of the Photovoltaic Cells 19

 2.2.2 Influence of Temperature on Photovoltaic Cells 20

 2.3 THERMOELECTRIC DEVICES 21

 2.3.1 Thermoelectric Effects 22

 2.3.2 Thermoelectric Materials 25

 2.3.3 Modelling of Thermoelectric Generator 26

 2.3.4 Applications of Thermoelectric Generator 27

CONTENTS

2.4 HEAT PIPES	27
2.4.1 Basic Operational Principle	27
2.4.2 Types of Heat Pipes	28
2.4.3 Working Fluid.....	29
2.4.4 Heat Transfer Limits.....	29
2.5 HYBRID PHOTOVOLTAIC-THERMOELECTRIC SYSTEMS	30
2.5.1 Hybrid System Integration Methods.....	30
2.5.2 PV-TEG Study Type	46
2.5.3 Current Research Focus Areas	50
2.6 THERMOELECTRIC GEOMETRY AND STRUCTURE OPTIMIZATION.....	63
2.6.1 Thermoelectric Geometry	63
2.6.2 Thermoelectric Structure.....	71
2.6.3 Three-Dimensional Finite Optimization Method	75
2.6.4 Thermal Stress Optimization	77
2.6.5 Finite Element Method	79
2.6.6 Computational Procedure	81
2.7 DISCUSSION AND RECOMMENDATIONS	83
2.7.1 Summary of Research Achievement.....	83
2.7.2 Research Gaps and Challenges	85
2.7.3 Potential Opportunities in the Development of Hybrid PV-TE Systems.....	87
2.7.4 Added Value of Present Research Relative to the Current State-of-Art.....	89
2.8 CHAPTER SUMMARY.....	90
CHAPTER 3 CONCEPTUAL DESIGN, MATHEMATICAL ANALYSIS AND SIMULATION MODEL	
DEVELOPMENT.....	92
3.1 CHAPTER INTRODUCTION	92
3.2 SYSTEM DESIGN	92
3.2.1 Research Questions	95
3.2.2 Potential Solutions.....	96

CONTENTS

3.3 OPERATING PRINCIPLE	96
3.4 COMPONENTS AND DIMENSIONS	97
3.4.1 Photovoltaic Module	97
3.4.2 Flat Plate Microchannel Heat Pipe	98
3.4.3 Thermoelectric Generator	99
3.4.4 Cooling Block and Water Tank	100
3.5 COMPUTER SIMULATION MODELS	101
3.5.1 Modelling Equations	102
3.5.2 Other Optimization Models	111
3.6 MODELLING RESULTS AND DISCUSSION.....	116
3.6.1 Boundary Conditions	116
3.6.2 Effect of Wind Speed	118
3.6.3 Effect of Ambient Temperature.....	121
3.6.4 Transient Response.....	124
3.6.5 Temperature and Voltage Distributions	127
3.7 CHAPTER SUMMARY.....	131
CHAPTER 4 EXPERIMENTAL TESTING AND MODEL VALIDATION.....	133
4.1 CHAPTER INTRODUCTION	133
4.2 SYSTEM AND MEASURING COMPONENTS	133
4.2.1 PV-TE-MCHP Prototype and Major Components	133
4.2.2 Test Rig and Major Components	137
4.2.3 Other Measurement Instruments and Elements.....	142
4.3 EXPERIMENTAL SETUP AND PROCEDURE.....	146
4.3.1 Experimental Procedure	150
4.3.2 Laboratory Health and Safety.....	151
4.4 RESULTS AND DISCUSSION.....	153
4.4.1 Effect of Thermoelectric Load Resistance	153
4.4.2 Effect of Solar Radiation	155

CONTENTS

4.4.3 Effect of Insulation and Comparison with Photovoltaic Only	159
4.5 MODEL VALIDATION/REFINEMENT	162
4.5.1 Validation with Experimental Results.....	163
4.5.2 Validation with Published Data.....	167
4.6 CHAPTER SUMMARY.....	170
CHAPTER 5 HYBRID PHOTOVOLTAIC-THERMOELECTRIC OPTIMIZATION RESULTS.....	172
5.1 CHAPTER INTRODUCTION	172
5.2 STEADY STATE PHOTOVOLTAIC-THERMOELECTRIC	172
5.2.1 Boundary Conditions	177
5.2.2 Geometry Area Ratios.....	177
5.2.3 Geometric Parameters.....	179
5.2.4 Section Conclusion.....	183
5.3 TRANSIENT STATE PHOTOVOLTAIC-THERMOELECTRIC	184
5.3.1 Boundary Conditions	187
5.3.2 Effect of Thermoelectric Leg Height and Area.....	187
5.3.3 Effect of Ceramic Height	192
5.3.4 Effect of Thermoelectric Geometry Optimization	194
5.3.5 Three-Dimensional Temperature and Voltage Distributions.....	195
5.3.6 Section Conclusion.....	198
5.4 PHOTOVOLTAIC-THERMOELECTRIC CONTACT RESISTANCE.....	199
5.4.1 Boundary Conditions	201
5.4.2 Contact Resistance Study	202
5.4.3 Comparison of Contact Resistance Effects	209
5.4.4 Section Conclusion.....	214
5.5 PHOTOVOLTAIC-THERMOELECTRIC-HEAT PIPE.....	214
5.5.1 Boundary Conditions	216
5.5.2 Influence of Solar Concentration Ratio.....	217
5.5.3 Influence of Ambient Temperature	220

CONTENTS

5.5.4 Influence of Wind Speed.....	222
5.5.5 Influence of Thermoelectric Generator Cold Side Temperature	224
5.5.6 Temperature and Voltage Distributions	226
5.5.7 Section Conclusion.....	228
5.6 CHAPTER SUMMARY.....	229
CHAPTER 6 THERMOELECTRIC GENERATOR OPTIMIZATION AND RESULTS DISCUSSION	231
6.1 CHAPTER INTRODUCTION	231
6.2 SEGMENTED ANNULAR THERMOELECTRIC GENERATOR	231
6.2.1 Boundary Conditions	234
6.2.2 Effect of Heat Source Temperature	234
6.2.3 Effect of Thermoelectric Leg Length	237
6.2.4 Effect of Thermoelectric Leg Angle.....	241
6.2.5 SATEG von Mises Stress Nephogram	243
6.2.6 Section Conclusion.....	245
6.3 SEGMENTED ASYMMETRICAL THERMOELECTRIC GENERATOR	246
6.3.1 Boundary Conditions	249
6.3.2 Thermal and Electrical Responses to Pulsed Heat Flux	250
6.3.3 Optimization of SASTEG.....	253
6.3.4 Thermal Stress Distribution in SASTEG and TEG	257
6.3.5 Section Conclusion.....	258
6.4 SEGMENTED SOLAR THERMOELECTRIC GENERATOR.....	259
6.4.1 Boundary Conditions	262
6.4.2 Effect of Solar Radiation	262
6.4.3 Thermal Stress Analysis	267
6.4.4 Three-Dimensional Distributions.....	270
6.4.5 Section Conclusion.....	272
6.5 SOLAR THERMOELECTRIC GENERATOR WITH PHASE CHANGE MATERIAL.....	273
6.5.1 Boundary Conditions	277

CONTENTS

6.5.2 Effect of PCM Fin Number	277
6.5.3 Effect of PCM Height.....	279
6.5.4 Effect of PCM and Thick Copper Plate	282
6.5.5 Temperature Distribution and Liquid Fraction	285
6.5.6 Section Conclusion.....	288
6.6 CHAPTER SUMMARY.....	289
CHAPTER 7 CONCLUSION AND FUTURE WORK.....	291
7.1 CONCLUSION	291
7.1.1 PV-TE-MCHP Design.....	291
7.1.2 Computer Simulation Models.....	292
7.1.3 Experimental Testing Under Laboratory Conditions	293
7.1.4 Thermoelectric Geometry Optimization.....	294
7.2 LIMITATIONS AND RECOMMENDATIONS FOR FUTURE WORK	295
7.2.1 Limitations	295
7.2.2 Recommendations for Future Work	296
REFERENCES	298
APPENDIX	324

PUBLICATIONS

Book Chapter

1. Li G, Ma X, **Shittu S**, Zhao X. Solar Thermoelectric Technologies for Power Generation. In: Zhao X, Ma X, editors. Adv. Energy Effic. Technol. Sol. Heating, Cool. Power Gener., Cham: Springer International Publishing; 2019, p. 341–71. doi:10.1007/978-3-030-17283-1_10.

Journal Publications

1. **Shittu S**, Li G, Zhao X, Ma X. Review of thermoelectric geometry and structure optimization for performance enhancement. Appl Energy 2020;268:115075. doi:10.1016/j.apenergy.2020.115075.
2. **Shittu S**, Li G, Tang X, Zhao X, Ma X, Badiei A. Analysis of thermoelectric geometry in a concentrated photovoltaic-thermoelectric under varying weather conditions. Energy 2020;202:117742. doi:10.1016/j.energy.2020.117742.
3. **Shittu S**, Li G, Xuan Q, Zhao X, Ma X, Cui Y. Electrical and mechanical analysis of a segmented solar thermoelectric generator under non-uniform heat flux. Energy 2020;199:117433. doi:10.1016/j.energy.2020.117433.
4. **Shittu S**, Li G, Xuan Q, Xiao X, Zhao X, Ma X. Transient and non-uniform heat flux effect on solar thermoelectric generator with phase change material. Appl Therm Eng 2020;173:115206. doi:10.1016/j.applthermaleng.2020.115206.
5. **Shittu S**, Li G, Zhao X, Zhou J, Ma X. Experimental study and exergy analysis of photovoltaic-thermoelectric with flat plate micro-channel heat pipe. Energy Convers Manag 2020;207:112515. doi:10.1016/j.enconman.2020.112515.
6. **Shittu S**, Li G, Zhao X, Ma X, Akhlaghi YG, Fan Y. Comprehensive study and optimization of concentrated photovoltaic-thermoelectric considering all

- contact resistances. *Energy Convers Manag* 2020;205:112422. doi:10.1016/j.enconman.2019.112422.
7. **Shittu S**, Li G, Zhao X, Ma X, Akhlaghi YG, Ayodele E. Optimized high performance thermoelectric generator with combined segmented and asymmetrical legs under pulsed heat input power. *J Power Sources* 2019;428:53–66. doi:10.1016/j.jpowsour.2019.04.099.
 8. **Shittu S**, Li G, Zhao X, Akhlaghi YG, Ma X, Yu M. Comparative study of a concentrated photovoltaic-thermoelectric system with and without flat plate heat pipe. *Energy Convers Manag* 2019;193:1–14. doi:10.1016/j.enconman.2019.04.055.
 9. **Shittu S**, Li G, Akhlaghi YG, Ma X, Zhao X, Ayodele E. Advancements in thermoelectric generators for enhanced hybrid photovoltaic system performance. *Renew Sustain Energy Rev* 2019;109:24–54. doi:10.1016/j.rser.2019.04.023.
 10. **Shittu S**, Li G, Zhao X, Ma X, Akhlaghi YG, Ayodele E. High performance and thermal stress analysis of a segmented annular thermoelectric generator. *Energy Convers Manag* 2019;184:180–93. doi:10.1016/j.enconman.2019.01.064.
 11. **Shittu S**, Li G, Zhao X, Ma X. Series of detail comparison and optimization of thermoelectric element geometry considering the PV effect. *Renew Energy* 2019;130:930–42. doi:10.1016/j.renene.2018.07.002.
 12. Rejeb O, **Shittu S**, Ghenai C, Li G, Zhao X, Bettayeb M. Optimization and performance analysis of a solar concentrated photovoltaic-thermoelectric (CPV-TE) hybrid system. *Renew Energy* 2020;152:1342–53. doi:10.1016/j.renene.2020.02.007.

13. Li G, **Shittu S**, Zhou K, Zhao X, Ma X. Preliminary experiment on a novel photovoltaic-thermoelectric system in summer. *Energy* 2019;188:116041. doi:10.1016/j.energy.2019.116041.
14. Li G, **Shittu S**, Ma X, Zhao X. Comparative analysis of thermoelectric elements optimum geometry between Photovoltaic-thermoelectric and solar thermoelectric. *Energy* 2019;171:599–610. doi:10.1016/j.energy.2019.01.057.
15. Li G, **Shittu S**, Diallo TMO, Yu M, Zhao X, Ji J. A review of solar photovoltaic-thermoelectric hybrid system for electricity generation. *Energy* 2018;158:41–58. doi:https://doi.org/10.1016/j.energy.2018.06.021.
16. Li G, Lu Y, **Shittu S**, Zhao X. Scale effect on electrical characteristics of CPC-PV. *Energy* 2020;192:116726. doi:10.1016/j.energy.2019.116726.
17. Akhlaghi YG, Zhao X, **Shittu S**, Badiei A, Cattaneo MEGV, Ma X. Statistical investigation of a dehumidification system performance using Gaussian process regression. *Energy Build* 2019;202:109406. doi:10.1016/j.enbuild.2019.109406.
18. Badiei A, Akhlaghi YG, Zhao X, **Shittu S**, Xiao X, Li J, et al. A chronological review of advances in solar assisted heat pump technology in 21st century. *Renew Sustain Energy Rev* 2020;132. doi:10.1016/j.rser.2020.110132.
19. Akhlaghi YG, Ma X, Zhao X, **Shittu S**, Li J. A statistical model for dew point air cooler based on the multiple polynomial regression approach. *Energy* 2019;181:868–81. doi:10.1016/j.energy.2019.05.213.
20. Li G, Diallo TMO, Akhlaghi YG, **Shittu S**, Zhao X, Ma X, et al. Simulation and experiment on thermal performance of a micro-channel heat pipe under different evaporator temperatures and tilt angles. *Energy* 2019;179:549–57. doi:10.1016/j.energy.2019.05.040.

21. Diallo TMO, Yu M, Zhou J, Zhao X, **Shittu S**, Li G, et al. Energy performance analysis of a novel solar PVT loop heat pipe employing a microchannel heat pipe evaporator and a PCM triple heat exchanger. *Energy* 2019;167:866–88. doi:<https://doi.org/10.1016/j.energy.2018.10.192>.
22. Akhlaghi YG, Badiei A, Zhao X, Aslansefat K, Xiao X, **Shittu S**, et al. A constraint multi-objective evolutionary optimization of a state-of-the-art dew point cooler using digital twins. *Energy Convers Manag* 2020;211:112772. doi:10.1016/j.enconman.2020.112772.
23. Fan Y, Zhao X, Li J, Li G, Myers S, Cheng Y, Badiei A, Yu M, Akhlaghi YG, **Shittu S**, Ma X. Economic and environmental analysis of a novel rural house heating and cooling system using a solar-assisted vapour injection heat pump. *Appl Energy* 2020;275:115323. doi:10.1016/j.apenergy.2020.115323.
24. Li G, Xuan Q, Akram MW, Golizadeh Akhlaghi Y, Liu H, **Shittu S**. Building integrated solar concentrating systems: A review. *Appl Energy* 2020;260:114288. doi:10.1016/j.apenergy.2019.114288.
25. Li G, Zhao X, Jin Y, Chen X, Ji J, **Shittu S**. Performance Analysis and Discussion on the Thermoelectric Element Footprint for PV–TE Maximum Power Generation. *J Electron Mater* 2018;47:5344–51. doi:10.1007/s11664-018-6421-4.
26. Ma X, Zhao H, Zhao X, Li G, **Shittu S**. Building Integrated Thermoelectric Air Conditioners — A Potentially Fully Environmentally Friendly Solution in Building Services. *Futur Cities Environ* 2019;5:1–13.

Conference Proceedings and Presentations

1. **Shittu S**, Li G, Zhao X, Ma X. Numerical Analysis of a Segmented Annular Thermoelectric Generator. 16th UK Heat Transfer Conference, Nottingham, UK: 2019.
2. **Shittu S**, Li G, Zhao X, Ma X. Geometry Effect on Photovoltaic-Thermoelectric Transient Performance. 11th Int. Conf. on Applied Energy, Västerås, Sweden: 2019, p. 1-6.
3. **Shittu S**, Li G, Zhao X, Ma X. Thermoelectric Generator Performance Enhancement by the Application of Pulsed Heat Power. 6th Int. Conf. Fluid Flow, Heat Mass Transf., Ottawa, Canada: 2019, p. 1–9. doi:10.11159/ffhmt19.146.
4. **Shittu S**, Li G, Zhao X, Ma X. Thermoelectric Element Geometry Optimization for Maximum Hybrid Photovoltaic-Thermoelectric System Efficiency. 17th Int. Conf. Sustain. Energy Technol., Wuhan, China: 2018, p. 1–9.
5. **Shittu S**, Li G, Zhao X, Ma X. Detailed Comparison and Optimization of Thermoelectric Element Geometry for Photovoltaic-Thermoelectric. EU-China Symposiums on Renewable/Sustainable Energy and Energy Storage Technologies, Hull, UK: 2018.

Posters

1. **Shittu S**, Li G, Zhao X, Ma X. Numerical Study of a Segmented Solar Thermoelectric Generator. Poster for EEI Summer Conference at the University of Hull, 3rd August 2020.
2. **Shittu S**, Li G, Zhao X. A Novel Hybrid Photovoltaic-Thermoelectric Power Generation System Employing a Flat-plate Micro-channel Heat Pipe. Poster for Postgraduate Research Posters at the University of Hull, 25th January 2018.

ACKNOWLEDGEMENT

Firstly, I would like to thank God almighty for giving me the strength and grace to finish this program. Thank you, Jesus, for always favouring me.

I would like to express my sincere gratitude to my main supervisor, Professor Xudong Zhao, who I have had the pleasure of working with for 4 years now. Since the days of supervising my masters project to the conclusion of my PhD, he has provided me with continuous support and guidance needed to successfully complete my PhD. I am forever grateful to him for believing in me and adding me to his world-class research centre.

I would also like to extend my gratitude to my other supervisors, Dr Guiqiang Li and Dr Xiaoli Ma. It has been a pleasure working and learning closely from Dr Li throughout this PhD period and I am grateful for all his help especially regarding paper publications and the experiment setup.

Furthermore, I would like to thank the University of Hull for the financial support of international tuition fee bursary for the duration of my PhD. Thank you to all my research centre colleagues especially, Yousef Golizadeh Akhlaghi, Yi Fan and Min Yu who I have had the pleasure of going through this PhD journey with. Thank you for all the wonderful memories. In addition, thank you to Dr Jinzhi Zhou for his help with the experiment setup. I would also like to thank my friends especially, Oluwatobi Ojewola, Tolulope Ojewola and Emmanuel Ayodele, for their support.

I would like to express my sincere appreciation to my mother for her constant love, support, prayer and encouragement. Thank you, mum, for the motivation to finish this PhD and for everything you have done for me. Also, my appreciation goes to my wonderful sister, brother and lovely nieces. Finally, this thesis is dedicated to my late dad, I finished what you started.

ABSTRACT

Effective thermal management of photovoltaic is essential for improving its conversion efficiency and increasing its life span. Photovoltaics can convert the ultraviolet and visible regions of the solar spectrum into electrical energy directly while thermoelectric generators utilize the infrared region to generate electrical energy. Consequently, the combination of photovoltaic (PV) and thermoelectric generators would enable the utilization of a wider solar spectrum. Therefore, this research aims to present an innovative thermal management technique for photovoltaic by the incorporation of thermoelectric generator (TEG) and heat pipe to form a hybrid photovoltaic system with improved overall efficiency, increased electricity generation and greater energy harvesting from the solar spectrum.

The strength and innovation of the hybrid system studied in this thesis are as follows: (1) a low cost and high efficiency microchannel heat pipe (MCHP) is used to reduce thermal resistance of heat flow across interfaces and increase heat transfer capacity; (2) the flat plate structure of the MCHP eliminates geometry mismatch and reduces thermal losses; (3) water cooling is used for the TEG cold side thus, the hybrid system feasibility for co-generation of electricity and hot water is demonstrated; and (4) the use of flat plate MCHP results in significant reduction in TEG quantity needed thereby reducing the system cost. These structural innovations are intended to overcome some of the drawbacks and provide experimental data for the development of hybrid photovoltaic-thermoelectric (PV-TE) systems.

A basic methodology of combined theoretical and experimental analysis is followed in this thesis and it involves, detailed literature review, conceptual design, mathematical analysis, computer simulation model development, experimental testing, model validation, and optimization case studies. Computer simulation models

are developed to predict and optimize the performance of the systems using three-dimensional finite element models and COMSOL Multiphysics software.

Experimental results show that the electrical conversion efficiencies of the PV-TE-MCHP with and without insulation and that of the photovoltaic only after 1 h are 11.98%, 12.19% and 11.94% respectively. Therefore, the hybrid system provides an enhanced performance. In addition, the highest and lowest thermal efficiencies obtained are 69.53% and 56.57% respectively under certain conditions. Steady state computer simulation results show that that at a high ambient temperature of 50 °C, the PV-TE-MCHP overall efficiency is greater than that of the PV only and PV-TE systems by 9.76% and 14.46% respectively. Therefore, the hybrid PV-TE-MCHP is recommended for sunny regions with high ambient temperature. Results also show that the asymmetrical leg geometry provides enhanced TEG only performance compared to the symmetrical leg geometry although the reverse is the case for the hybrid concentrated PV-TE system.

This research shows that the hybrid PV-TE-MCHP design is feasible and provides enhanced performance compared to the PV only and PV-TE systems. In addition, the effectiveness of thermoelectric geometry optimization for performance enhancement is demonstrated in this research. Therefore, the experimental and simulation results from this research provide fundamental data for developing highly efficient hybrid photovoltaic-thermoelectric systems and thermoelectric generators.

LIST OF FIGURES

Figure 1.1: Final energy consumption in buildings by fuel (BP, 2019).....	2
Figure 1.2: Global power generation (McKinsey & Company, 2019)	4
Figure 1.3: Energy supplies from solar energy technologies (top) and global solar PV annual additions by segment, 2013-24 (bottom) (International Energy Agency, 2019d)	5
Figure 1.4: Annual PV installations from 2010 to 2019 estimates (Jäger-Waldau, 2019)	5
Figure 1.5: Thermoelectric generator market by region (Markets and Markets, 2019a)	6
Figure 1.6: Thesis structure.....	13
Figure 2.1: Photovoltaic cell (a) p-n junction structure (Huen and Daoud, 2017) and (b) simplified equivalent circuit (El Chaar et al., 2011)	18
Figure 2.2: Effect of cell temperature on efficiency, open circuit voltage and short circuit current of a monocrystalline silicon cell (Singh et al., 2008).....	21
Figure 2.3: Influence of temperature on the I-V characteristics of a photovoltaic cell (Fisac et al., 2014).....	21
Figure 2.4: Schematic of a thermoelectric (a) generator and (b) cooler (J. F. Li et al., 2010)	22
Figure 2.5: Schematic of the Seebeck effect in an open circuit (Enescu, 2019).....	23
Figure 2.6: Schematic of Peltier effect (Chen, 2009).....	24
Figure 2.7: Schematic of Thomson effect (Chen, 2009).....	24
Figure 2.8: Schematic of a conventional heat pipe (Faghri, 2014)	28
Figure 2.9: Schematic of spectrum splitting PV-TEG integration (Tritt et al., 2008)	32
Figure 2.10: Schematic of direct coupling PV-TEG integration (Fisac et al., 2014).	37

LIST OF FIGURES

Figure 2.11: Schematic diagram of PV-TEG with PV operating at (A) low and (B) high temperatures (Vorobiev et al., 2006)	50
Figure 2.12: Hybrid PV-TEG (a) cross-sectional view, (b) bottom view, (c) global view and (d) physical diagram (Zhu et al., 2016)	52
Figure 2.13: Schematic diagram of experimental PV-TEG setup (Mahmoudinezhad et al., 2018a).....	52
Figure 2.14: Schematic of PV-TEG system for (a) direct and (b) indirect coupling (Hajji et al., 2017)	55
Figure 2.15: Schematic of PV-TEG system with heat storage unit (Li et al., 2014) .	56
Figure 2.16: Schematic diagram and energy flow of the hybrid PV-PCM-TE system	56
Figure 2.17: Different types of thermoelectric generator cooling systems (Yin et al., 2017)	58
Figure 2.18: Hybrid system overall efficiency variation with concentration ratio for (a) crystalline silicon cell, (b) polycrystalline silicon cell, (c) amorphous silicon cell and (d) polymer cell (Yin et al., 2017).....	58
Figure 2.19: (a) Electroencephalography diadem: (1) right-side hybrid module, and (2) electronic module and 2.4 GHz wireless link. (b) Schematic cross-section of hybrid module: (1) thermophile, (2) radiator, (3) PV cells, and (4) thermal shunts (Leonov et al., 2010).....	61
Figure 2.20: Conceptual design of a hybrid PV-TEG for automated greenhouse system (Ariffin et al., 2017)	62
Figure 2.21: Effect of leg length on (a) output power and (b) efficiency for three different thermoelectric generators (Tian et al., 2015)	64

LIST OF FIGURES

Figure 2.22: Conversion efficiency variation with leg cross-sectional areas (Fan et al., 2016)	66
Figure 2.23: Relationship between number of legs and (a) output power and (b) conversion efficiency (Liang et al., 2014)	68
Figure 2.24: Fabrication steps for thermoelectric legs (Fabián-Mijangos et al., 2017)	70
Figure 2.25: Fabricated module (a) with symmetrical legs (b) with asymmetrical legs (c) temperature difference (d) open circuit voltage (Fabián-Mijangos et al., 2017)..	70
Figure 2.26: Schematic of (a) thermoelectric generator (b) thermoelectric uni-couple and (c) energy flow diagram (He et al., 2019b)	72
Figure 2.27: Schematic diagram of ATEG: (1) heat source (2) heat sink (3) p-type leg (4) n-type leg (5) ceramic (6) copper electrode (Zhang et al., 2018a).....	72
Figure 2.28: Compatibility factor (s) for (a) p-type and (b) n-type thermoelectric materials (Snyder, 2004)	74
Figure 2.29: Schematic of STEG with active cooling heat exchanger (Hadjistassou et al., 2013).....	74
Figure 2.30: TEG (a) voltage and (b) temperature distributions (Liao et al., 2018)..	76
Figure 2.31: (a) 3D temperature distribution and (b) thermal stress distribution (Al-Merbaty et al., 2013)	78
Figure 2.32: Mesh discretization used in finite element method (Rapp, 2017)	80
Figure 2.33: Finite element analysis process (Bathe, 2014)	81
Figure 2.34: Simulation process in COMSOL.....	83
Figure 3.1: Schematic diagram of PV-TE-MCHP system in (a) 2-dimension and (b) 3-dimension.....	93

LIST OF FIGURES

Figure 3.2: (a) PV-MCHP layout with back surface insulation and (b) TEG-cooling block layout.....	94
Figure 3.3: Layout of waste heat recovery system attached to MCHP condenser section	95
Figure 3.4: Photovoltaic module (a) layers and (b) dimensions	98
Figure 3.5: Flat plate microchannel heat pipe (a) outer structure and (b) inner structure	99
Figure 3.6: Thermoelectric generator in (a) 3-dimension and (b) 2-dimension.....	100
Figure 3.7: Schematic of cooling block and water tank.....	101
Figure 3.8: Schematic diagram of (a) PV-TE-MCHP and (b) PV-TE.....	118
Figure 3.9: Variation of wind speed with (a) overall efficiency and (b) TE efficiency	120
Figure 3.10: Variation of wind speed with (a) PV temperature and (b) TE temperature difference.....	121
Figure 3.11: Variation of ambient temperature with (a) overall efficiency and (b) TE efficiency.....	122
Figure 3.12: Variation of ambient temperature with (a) PV temperature and (b) TE temperature difference	123
Figure 3.13: Time variation with (a) overall efficiency and (b) TE efficiency.....	125
Figure 3.14: Time variation with (a) PV temperature and (b) TE temperature difference.....	126
Figure 3.15: Three-dimensional PV temperature distribution in (a) PV only (b) PV-TE and (c) PV-TE-MCHP.....	128
Figure 3.16: PV-TE-MCHP temperature distribution (a) side view and (b) back view	129

LIST OF FIGURES

Figure 3.17: PV-TE temperature distribution (a) side view and (b) back view	129
Figure 3.18: Voltage distribution in (a) PV-TE-MCHP and (b) PV-TE.....	130
Figure 4.1: Photovoltaic module used in experiment.....	135
Figure 4.2: Flat plate microchannel heat pipe used in experiment	136
Figure 4.3: Thermoelectric generator module used in experiment	136
Figure 4.4: Solar simulator used in experiment	137
Figure 4.5: Water tank (a) without insulation and (b) with insulation.....	138
Figure 4.6: Cooling block used in experiment.....	139
Figure 4.7: Pump used in experiment	139
Figure 4.8: DC power supply used in experiment	140
Figure 4.9: Resistor box used in experiment.....	140
Figure 4.10: Insulation material with (a) rubber and (b) foam	141
Figure 4.11: Thermal (a) grease and (b) adhesive.....	141
Figure 4.12: Pyranometer used in experiment	142
Figure 4.13: K-type thermocouples used in experiment	143
Figure 4.14: Data logger used in experiment.....	143
Figure 4.15: Solar module analyser used in experiment.....	144
Figure 4.16: Voltmeter and ammeter used in experiment.....	145
Figure 4.17: Flowmeter used in experiment	145
Figure 4.18: Computers used in experiment	146
Figure 4.19: PV-TE-MCHP arrangement	146
Figure 4.20: PV-TE-MCHP experimental setup.....	147
Figure 4.21: PV-TE-MCHP (a) with back surface insulation and (b) without insulation	147
Figure 4.22: Photovoltaic experimental setup.....	148

LIST OF FIGURES

Figure 4.23: Complete experimental setup for testing	149
Figure 4.24: Laboratory condition during system operation.....	152
Figure 4.25: Variation of load resistance with (a) current (b) voltage and (c) power output of TE	154
Figure 4.26: Solar radiation variation with (a) voltage, current (b) power output and (c) efficiency	156
Figure 4.27: Variation of solar radiation with (a) PV, TE temperature (b) water tank, ambient temperature, (c) thermal efficiency and (d) exergy efficiency.....	158
Figure 4.28: Time variation with (a) efficiency and (b) power output	160
Figure 4.29: Time variation with (a) PV temperature (b) TE temperature difference and (c) water tank temperature.....	162
Figure 4.30: Variation of experimental and simulation (a) efficiency and (b) temperature of a conventional photovoltaic module.....	163
Figure 4.31: Variation of experimental and simulation (a) efficiency and (b) temperature of PV in PV-TE-MCHP	164
Figure 4.32: Variation of experimental and simulation (a) efficiency and (b) temperature difference of TE in PV-TE-MCHP	166
Figure 4.33: Variation of experimental and simulation temperature difference of MCHP in PV-TE-MCHP	167
Figure 4.34: Validation of thermoelectric generator model with manufacturer datasheet (European Thermodynamics Limited, 2014a)	168
Figure 4.35: Validation of PCM model with previous study (Manikandan et al., 2019)	168
Figure 4.36: Validation of contact resistance model with previous study (He et al., 2019a).....	169

LIST OF FIGURES

Figure 4.37: Validation of thermal stress model with previous study (Yilbas et al., 2016)	169
Figure 5.1: Schematic diagrams of a PV-TE with different leg geometries for RA = 0.5 and a) RS = 0.5 b) RS = 1 c) RS = 2	174
Figure 5.2: Schematic diagrams of a PV-TE with different leg geometries for RA = 1 and a) RS = 0.5 b) RS = 1 c) RS = 2.....	174
Figure 5.3: Schematic diagrams of a PV-TE with different leg geometries for RA = 2 and a) RS = 0.5 b) RS = 1 c) RS = 2.....	175
Figure 5.4: PV-TE 3-dimensional a) Temperature and b) Voltage distributions for RA = 0.5	175
Figure 5.5: PV-TE 3-dimensional a) Temperature and b) Voltage distributions for RA = 1	176
Figure 5.6: PV-TE 3-dimensional a) Temperature and b) Voltage distributions for RA = 2	176
Figure 5.7: Overall PV-TE efficiency vs geometry area ratios for Cell A	178
Figure 5.8: Overall PV-TE efficiency vs geometry area ratios for Cell B.....	179
Figure 5.9: Hybrid system efficiency vs thermoelectric element height for RA = 0.5 and a) Cell A b) Cell B.....	181
Figure 5.10: Hybrid system efficiency vs thermoelectric element height for RA = 1 and a) Cell A b) Cell B.....	182
Figure 5.11: Hybrid system efficiency vs thermoelectric element height for RA = 2 and a) Cell A b) Cell B.....	183
Figure 5.12: Schematic of hybrid system with different geometries (a) Case 1 (b) Case 2 (c) Case 3 and (d) Case 4	185

LIST OF FIGURES

Figure 5.13: Hourly weather data (a) solar radiation (Met Office, 2019a) and (b) ambient temperature and wind speed (Met Office, 2019b).....	186
Figure 5.14: Variation of leg height with (a) CPV cell temperature, CPV-TE power output density and (b) CPV-TE efficiency, temperature difference	189
Figure 5.15: Leg area variation with (a) CPV cell temperature, CPV-TE power output density and (b) CPV-TE efficiency, temperature difference	191
Figure 5.16: Variation of ceramic height with (a) CPV cell temperature, CPV-TE power output density (b) CPV-TE efficiency, temperature difference and (c) TEG power output density	193
Figure 5.17: Variation of time with CPV-TE (a) power output density (b) efficiency and (c) CPV cell temperature	195
Figure 5.18: Surface temperature plots for leg height of (a, c) 1 mm and (b, d) 6 mm	196
Figure 5.19: Electric potential plots for leg area of (a, c) 1 mm ² and (c, d) 4 mm ²	197
Figure 5.20: CPV-TE temperature distribution plots for (a, b) original geometry and (c, d) optimized geometry	197
Figure 5.21: Schematic diagram of (a) PV-TE three-dimensional view (b) PV-TE front view and (c) TE uni-couple.....	200
Figure 5.22: Relationship between TE thermal contact resistance and (a) efficiency, power output and (b) temperature	203
Figure 5.23: Effect of TE electrical contact resistance on (a) efficiency, power output and (b) temperature	204
Figure 5.24: Relationship between PV-TE interface thermal contact resistance and (a) efficiency and (b) temperature	206

LIST OF FIGURES

Figure 5.25: Variation of TEG-heat sink thermal contact resistance with (a) efficiency and (b) temperature	207
Figure 5.26: Comparison of PV-TE interface and TEG-heat sink thermal contact resistance effect.....	207
Figure 5.27: (a) Temperature and (b) voltage distribution for base values.....	208
Figure 5.28: (a, b) Temperature distribution for TE thermal contact resistance interface and (c, d) voltage distribution for TE electrical contact resistance interface.....	209
Figure 5.29: Effect of different contact resistance case with (a) PV-TE efficiency (b) PV efficiency (c) TE efficiency and (d) temperature.....	211
Figure 5.30: Overestimation calculation for (a) PV-TE (b) PV and (c) TE.....	213
Figure 5.31: Schematic diagram of (a) PV front view (b) three dimensional PV-TE (c) three dimensional PV-TE-Heat pipe (d) PV-TE-Heat pipe side view	215
Figure 5.32: Variation of concentration ratio with (a) overall (b) PV (c) TE efficiency and power output.....	219
Figure 5.33: Ambient temperature variation with (a) overall (b) PV (c) TE efficiency and power output.....	221
Figure 5.34: Variation of wind speed with (a) overall (b) PV (c) TE efficiency and power output	223
Figure 5.35: TEG cold side temperature variation with (a) overall (b) PV (c) TE efficiency and power output.....	225
Figure 5.36: PV-TE temperature distribution in (a) three-dimension (b) side view (c) voltage distribution	226
Figure 5.37: PV-TE-Heat pipe temperature distribution in (a) three-dimension (b) side view (c) voltage distribution	227

LIST OF FIGURES

Figure 6.1: SATEG geometry; (a) schematic diagram and (b) three-dimensional view232

Figure 6.2: ATEG geometry; (a) three-dimensional view and (b) front view233

Figure 6.3: Variation of SATEG and ATEG (a) efficiency and (b) output power with temperature difference when $L = 2$, $\theta_1 = 6$, $\theta_2 = 2$ and $RL = 0.01 \Omega$235

Figure 6.4: Variation of maximum von Mises stress in legs of SATEG and ATEG with temperature difference when $L = 2$, $\theta_1 = 6$ and $\theta_2 = 2$ 236

Figure 6.5: Variation of Bismuth telluride ATEG leg length with (a) Efficiency and (b) Output power when $\theta_1 = 3$, $\theta_2 = 3$, and $RL = 0.001 \Omega$237

Figure 6.6: Variation of Skutterudite ATEG leg length with (a) Efficiency and (b) Output power when $\theta_1 = 3$, $\theta_2 = 3$, and $RL = 0.001 \Omega$ 238

Figure 6.7: Variation of SATEG leg length with (a) Efficiency and (b) Output power when $\theta_1 = 3$, $\theta_2 = 3$, and $RL = 0.001 \Omega$ 240

Figure 6.8: Effect of Bismuth telluride thermoelectric leg length in SATEG and ATEG when $\theta_1 = 6$ and $\theta_2 = 2$240

Figure 6.9: Effect of Skutterudite thermoelectric leg length in SATEG and ATEG when $\theta_1 = 6$ and $\theta_2 = 2$241

Figure 6.10: Variation of leg angle with SATEG (a) efficiency and (b) output power when $\theta = 8$, $T_h = 623K$ and $RL = 0.001$ 242

Figure 6.11: Variation of leg angle with maximum von Mises stress in (a) Bismuth telluride and (b) Skutterudite materials of the SATEG when $\theta = 8$ and $T_h = 623 K$ 243

Figure 6.12: Nephogram of the von Mises stress in Bismuth telluride material of the SATEG when $L = 2$, $T_h = 623 K$, $\theta_2 = 3$, (a) $\theta_1 = 3$, (b) $\theta_1 = 5$, (c) $\theta_1 = 7$ and (d) $\theta_1 = 9$ 244

Figure 6.13: Nephogram of the von Mises stress in Skutterudite material of the SATEG when $L = 2$, $T_h = 623$ K, $\theta_2 = 3$, (a) $\theta_1 = 3$, (b) $\theta_1 = 5$, (c) $\theta_1 = 7$ and (d) $\theta_1 = 9$ 245

Figure 6.14: Schematic diagram of (a) thermoelectric generator (b) segmented asymmetrical thermoelectric generator and (c) optimized SASTEG geometry (d) rectangular heat flux pulse248

Figure 6.15: Transient and steady state responses of the SASTEG and TEG (a) temperature (b) open circuit voltage (c) load current (d) power output and (e) von Mises stress251

Figure 6.16: (a) Variation of von Mises stress with SASTEG p-type height ratio (H_p) and (b) first optimized SASTEG p-type leg.....254

Figure 6.17: (a) Variation of von Mises stress with SASTEG n-type height ratio (H_n) and (b) second stage optimized SASTEG.....255

Figure 6.18: Second stage optimized SASTEG (a) power output response comparison with TEG (b) three-dimensional temperature distribution and (c) voltage distribution256

Figure 6.19: Thermal stress distribution in (a) thermoelectric generator (b) segmented asymmetrical thermoelectric generator and (c) optimized SASTEG geometry.....258

Figure 6.20: Schematic of (a) segmented thermoelectric generator (b) thermoelectric generator and (c) CPC flux distribution260

Figure 6.21: Effect of solar radiation on (a) power output (b) efficiency (c) temperature difference.....263

Figure 6.22: Comparison of non-uniform and uniform heat flux power output for (a) Case 1 (b) Case 2 (c) Case 3 (d) Case 4 and (e) Case 5266

LIST OF FIGURES

Figure 6.23: Effect of solar radiation on maximum von Mises stress in (a) different cases (b) bismuth telluride TEG and (b) Skutterudite segment	268
Figure 6.24: Three-dimensional temperature distribution for (a) non-uniform and (b) uniform heat flux at solar radiation of 5000 W/m^2	271
Figure 6.25: Thermal stress nephogram for (a) case 1 (b) case 2 (c) case 3 (d) case 4 and (e) case 5 at solar radiation of 5000 W/m^2	272
Figure 6.26: Solar thermoelectric generator (a) with PCM and (b) without PCM ..	275
Figure 6.27: Variation of solar radiation with time (Mahmoudinezhad et al., 2018b)	276
Figure 6.28: DSC curve of RT25HC PCM (Mankel et al., 2019)	276
Figure 6.29: Number of PCM fins variation with (a) power output (b) temperature difference (c) efficiency and (d) average power output and average temperature difference.....	278
Figure 6.30: Height of PCM variation with (a) power output (b) temperature difference (c) efficiency and (d) average power output and average temperature difference...	280
Figure 6.31: Variation of time with (a) power output and (b) temperature difference for solar TEG with and without PCM.....	284
Figure 6.32: Temperature distribution of solar TEG at (a) 5 min (b) 15 min and front view of thermoelectric legs at (c) 5 min (d) 15 min.....	285
Figure 6.33: Temperature distribution of solar TEG with PCM at (a) 5 min (b) 15 min and front view of thermoelectric legs at (c) 5 min (d) 15 min	286
Figure 6.34: Liquid fraction of PCM with (a) 5 mm height, 5 min (b) 5 mm height, 15 min and (c) 10 mm height, 5 min (d) 10 mm height, 15 min.....	287

LIST OF TABLES

Table 2.1: Summary of some selected spectrum splitting PV-TEG systems reviewed33

Table 2.2: Summary of some selected direct coupling PV-TEG systems reviewed..38

Table 2.3: Power output and efficiency enhancement of hybrid system using different cooling systems (Soltani et al., 2017)60

Table 4.1: Experimental test rig component specification..... 134

Table 4.2: Thermoelectric generator module manufacturer data 136

Table 4.3: Position of thermocouples in experimental setup 149

Table 4.4: Experimental relative mean error of variables..... 153

Table 5.1: Contact resistance case description.....209

Table 6.1: Material proportions in different design cases.....261

NOMENCLATURE

A	Area, m^2	σ	Electrical conductivity, S/m
A_c	Area of PV collector, m^2	ε	Emissivity
A_s	Area of SSA, m^2	$\varphi_{\text{srad,max}}$	Maximum efficiency ratio
C	Concentration ratio	α	Seebeck coefficient, V/K
C_p	Specific heat capacity, $J/kg \cdot K$	α_s	SSA absorptivity
G	Solar irradiance, W/m^2	β	Temperature coefficient, 1/K
H	Convective heat transfer coefficient, $W/m^2 \cdot K$	κ	Thermal conductivity, $W/m \cdot K$
H	Leg height, mm	Abbreviations	
H_{pcm}	PCM height, mm	ATEG	Annular thermoelectric generator
h_{sink}	Heat sink heat transfer coefficient, $W/m^2 \cdot K$	Bi_2Te_3	Bismuth telluride
I	Current, A	CIGS	Copper indium gallium selenide
I_{sc}	Short circuit current, A	CoSb_3	Copper antimony
m	Mass, kg	CPC	Compound parabolic concentrator
M_n	Molar mass, g/mol	CPV	Concentrated photovoltaic
P	Power output, W	CPV-TE	Concentrated photovoltaic-thermoelectric
p_c	Capillary pressure, Pa	CZTS	Copper zinc tin sulfide

NOMENCLATURE

p_g	Gravitational pressure, Pa	DSSC	Dye-sensitized solar cell
P_{gen}	PV power generation, W	EVA	Ethylene vinyl acetate
P_{hybrid}	Hybrid system power output, W	FEM	Finite element method
p_l	Liquid pressure, Pa	FVM	Finite volume method
p_{sat}	Saturation pressure, Pa	GaAs	Gallium arsenide
P_{teg}	TEG power output, W	GeTe	Germanium telluride
p_v	Vapor pressure, Pa	MCHP	Microchannel heat pipe
Q_h	TEG input power, W	PbTe	Lead telluride
q_{sol}	Volumetric solar energy absorption, W/m^3	PCM	Phase change material
\dot{Q}_{th}	Water heating capacity, J	PV	Photovoltaic
r	Radius, mm	PV-TE	Photovoltaic-thermoelectric
R	Resistance, Ω	PV-TEG	Photovoltaic-thermoelectric generator
R_A	Cross-sectional area ratio of TE hot and cold junctions	PV-TE-MCHP	Photovoltaic-thermoelectric-flat plate microchannel heat pipe
R_c	Thermoelectric thermal contact resistance, $m^2 \cdot K/W$	SASTEg	Segmented asymmetrical thermoelectric generator
R_{cont}	Thermoelectric electrical contact resistance, $\Omega \cdot m^2$	SATEg	Segmented annular thermoelectric generator
R_{in}	Internal resistance, Ω	SnTe	Tin telluride

NOMENCLATURE

R_L	Load resistance, Ω	SSA	Solar selective absorber
R_{pv_te}	PV-TE interface thermal contact resistance, $mm^2 \cdot K/W$	STEG	Segmented thermoelectric generator
R_S	Area ratio of n- and p-type TE modules	TE	Thermoelectric
R_{teg_hsink}	TEG-heat sink interface thermal contact resistance, $mm^2 \cdot K/W$	TEG	Thermoelectric generator
T	Temperature, $^{\circ}C$	TPT	Tedlar polyester tedlar
\bar{T}	Average temperature, $^{\circ}C$	Subscripts	
v	Wind speed, m/s	a	Ambient
V	Voltage, V	c	Cold side
V_L	Load voltage, V	h	Hot side
V_{OC}	Open circuit voltage, V	n	n-type
ZT	Figure of merit	p	p-type
Greek symbols		pv	Photovoltaic
ρ	Density, kg/m^3	sky	Sky
η	Efficiency, %	w_tank	Water tank

CHAPTER 1 INTRODUCTION

1.1 Research Background

The seventh sustainable development goal outlined by the United Nations is to ensure access to affordable, reliable, sustainable and modern energy for all. Universal access to affordable, reliable and modern energy services is targeted by 2030 including a substantial increase in the renewable energy share in the global energy mix (United Nations, 2015a). Furthermore, improvements in the quality of life of people is intrinsically linked with access to cheap and abundant energy. In addition, availability of electricity provides a means to boost economic productivity and improve human condition. However, in 2018, 860 million people were estimated to lack access to electricity, and this was a record in recent years (International Energy Agency, 2019a). The global energy demand is expected to rise by 20% from 2017 to 2040, while global electricity demand will rise by 60%. Population growth and industrialization contribute to the unprecedented increase in energy demand. It is estimated that by 2040, the global population will attain 9.2 billion people with India soon surpassing China as the most populous nation (ExxonMobil, 2019).

The world energy consumption is estimated to rise by about 50% between 2018 and 2050 in the reference case. Organisation for Economic Co-operation and Development (OECD) countries will experience a 15% increase in energy consumption between 2018 and 2050 while energy consumption in non-OECD countries will increase by about 70% (U.S. Energy Information Administration, 2019). Furthermore, over a third of the global energy growth is accounted for by buildings due to the increase in power demand in the developing world while electricity provides most of the increasing energy used in buildings as shown in Figure 1.1 (BP, 2019).

Direct emissions from buildings increased to over 3 GtCO₂ in 2018 and when indirect emissions from upstream power generation are considered, buildings accounted for 28% of global energy-related CO₂ emissions in 2018 (International Energy Agency, 2019b). Carbon emissions can be reduced by the increase of energy efficiency and reduction of energy consumption is an effective solution to increase energy savings.

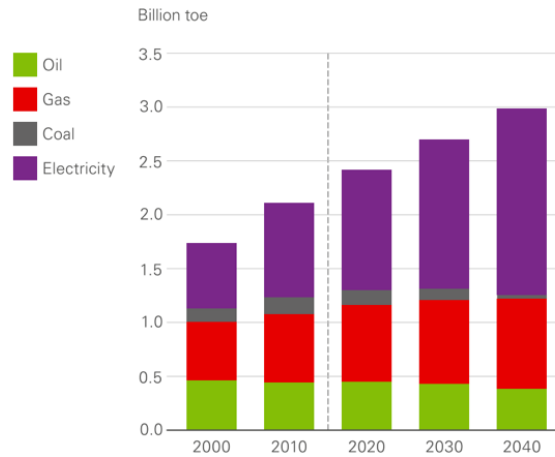


Figure 1.1: Final energy consumption in buildings by fuel (BP, 2019)

Extensive use of fossil fuels has led to an increase in environmental issues such as global warming and air pollution. Consequently, more attention is being paid by governments to abate the negative environmental impact of fossil fuel use. In addition, the recent Amazon rainforest fire has attracted global interest from grassroot to the highest levels of government thereby making issues such as climate change and carbon reduction of utmost importance. The Paris Agreement provides a global framework for limiting global warming to well below 2 °C; and to pursue efforts to limit the increase to 1.5 °C (United Nations, 2015b). Furthermore, the European Union (EU) aims to achieve net-zero greenhouse gas emissions by 2050. The EU is responsible for 10% of the global greenhouse gas emissions therefore the new climate and energy policies, aim to deliver on the EU’s contribution under the Paris Agreement to reduce emissions by at least 40% by 2030 compared to 1990 (European Commission, 2018).

The United Kingdom has a specific goal to reduce greenhouse gas (GHG) emissions by at least 80% by 2050 from the 1990 levels. In addition, the UK government plans to reduce the energy use of new buildings by at least half by 2030 and policies have been set out to ensure the achievement of this goal and improve the building energy efficiency (International Energy Agency, 2019c).

Renewable energy sources offer unique advantages such as inexhaustibility, zero carbon emissions and no air pollution. Consequently, a paradigm shift towards renewable energy sources from fossil fuel has been observed globally. In fact, it is estimated that renewable energy sources will increase their global generation share from about 25% today to about 50% by 2035 and close to 75% by mid-century as shown in Figure 1.2 (McKinsey & Company, 2019). Solar energy is the most abundant and free renewable energy source which is available globally. Energy is emitted from the sun at a rate of $3.8 \times 10^{23} \text{ kW}$ and approximately $1.8 \times 10^{14} \text{ kW}$ of this energy is intercepted by the earth. Furthermore, the earth's surface receives about 60% of this energy while the remaining is reflected back to space and absorbed by the atmosphere. Converting only 0.1% of this energy at an efficiency of 10% will provide four times the total global generating capacity. In addition, the total annular solar radiation incident on the earth is 7500 times greater than the global total annular primary energy consumption (Thirugnanasambandam et al., 2010). Therefore, it is obvious that the global energy demand can be met by the use of solar energy as a result of its vast energy capacity.

Solar energy can be converted into two main forms including electrical and thermal energy. Solar energy can be harvested using three main technologies including photovoltaic (PV), solar thermal and concentrating solar power (CSP). Photovoltaic cells convert solar radiation directly into electricity, solar thermal collectors convert

solar energy into thermal energy while concentrating solar power converts concentrated solar radiation into heat to drive a heat engine which is connected to a generator. PV and CSP are the two main technologies for generating electricity from the sun.

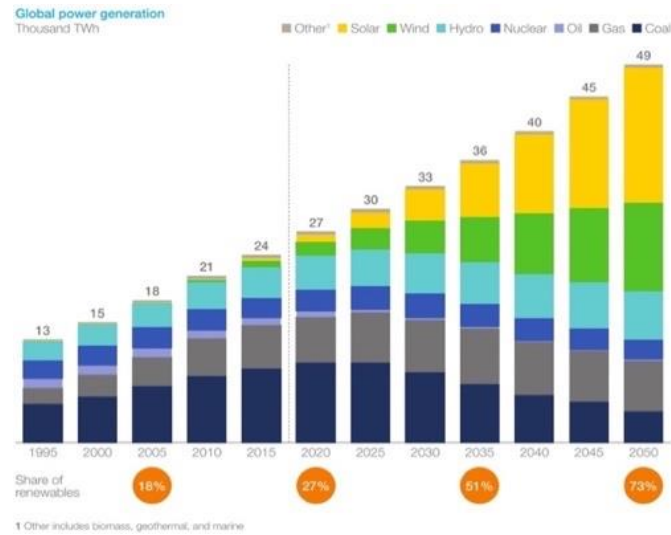


Figure 1.2: Global power generation (McKinsey & Company, 2019)

Photovoltaic cells and modules utilize both direct and diffuse solar radiation for electricity generation and the PV technology can be used for on-grid and off-grid applications. Furthermore, although the PV was an expensive technology for generating electricity about ten years ago, it is gradually becoming one of the most affordable. In fact, in terms of energy supplies, the PV has now overtaken the solar heating and cooling (SHC) energy supply by 2018 as shown in Figure 1.3. In addition, it is estimated that the PV annual capacity additions will grow from 115 GW to about 130 GW in the next five years. By 2023 latest, the total cumulative capacity of the PV is estimated to reach 1 TW and 1195 to 1375 GW by the end of 2024 depending on the case (International Energy Agency, 2019d). Furthermore, the installation of photovoltaic globally has been growing yearly as shown in Figure 1.4. The annual installed PV power in 2018 was about 5% higher than in 2017 and this led to an

increase in the global PV power to about 520 GW at the end of 2018 (Jäger-Waldau, 2019). Although photovoltaic systems have been commercially available for several years, some of the barriers to their widespread application are: elevated temperature in the PV, limited conversion efficiency and dust accumulation (Makki et al., 2015). Depending on the cell material used, the PV efficiency decreases by a range of 0.25% to 0.5% per degree Celsius (Grubisić-Čabo et al., 2016). This means that even the slight decrease in PV temperature can significantly increase its efficiency therefore, cooling techniques are very essential to PV systems.

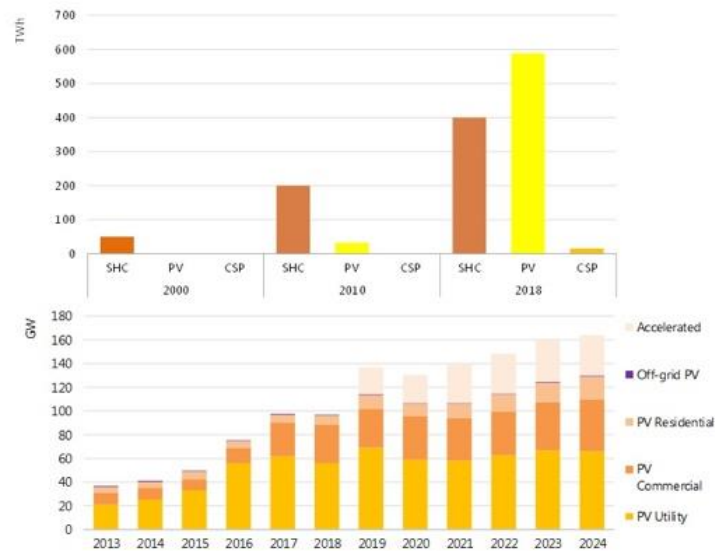


Figure 1.3: Energy supplies from solar energy technologies (top) and global solar PV annual additions by segment, 2013-24 (bottom) (International Energy Agency, 2019d)

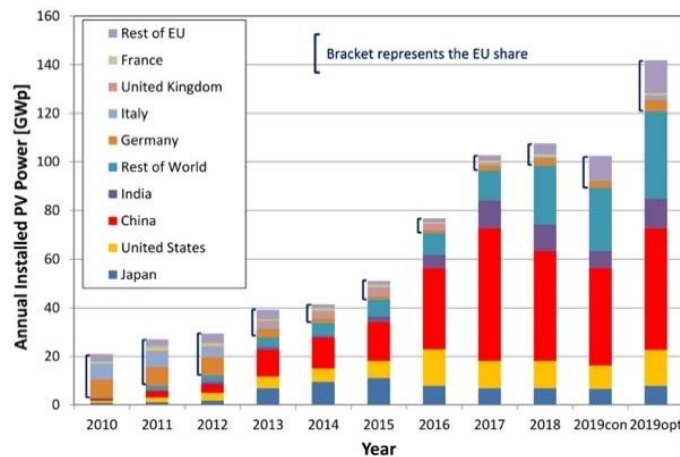


Figure 1.4: Annual PV installations from 2010 to 2019 estimates (Jäger-Waldau, 2019)

Asides the photovoltaic which generates electricity directly from sunlight, the thermoelectric generator (TEG) can also generate electricity directly from thermal energy. The thermoelectric generator market size is expected to grow from US\$ 460 million in 2019 to US\$ 741 million by 2025, at a compound annual growth rate (CAGR) of 8.3% with thermoelectric generator market in Europe expected to grow at the highest CAGR during the forecast period (Research and Markets, 2019). The market growth of thermoelectric generators is driven by the increasing demand for clean energy converters which could be used for waste heat recovery in automobiles and wearable applications. The thermoelectric generator market by region is shown in Figure 1.5 and it can be seen that North America accounts for the largest share of the thermoelectric generator market in 2019 while the thermoelectric generator market is expected to continue growing in the future (Markets and Markets, 2019a).



Figure 1.5: Thermoelectric generator market by region (Markets and Markets, 2019a)

Furthermore, the thermoelectric modules market size is expected to grow from US\$ 668 million in 2019 to US\$ 1,023 million by 2024 at a CAGR of 8.9% (Markets and Markets, 2019b). A thermoelectric (TE) module is a bi-directional energy converter which can be used for generating electricity or for heating/cooling. When it is used for electricity generation, it is referred to as a thermoelectric generator (TEG)

while it is called a thermoelectric cooler (TEC) when used for cooling/heating. The advantages of thermoelectric energy converters are; solid-state operation, gas-free emission, maintenance free operation, vast scalability, zero pollution and long-time operational reliability (He et al., 2015b).

Although the photovoltaic has numerous advantages, its conversion efficiency is still low for wider electricity generation globally and similarly, the conversion efficiency of the thermoelectric generator is also too low to justify its cost. Consequently, researchers have focussed on a complementary technology called photovoltaic-thermoelectric generator (PV-TEG) which could make use of the advantages of both individual technologies. Furthermore, photovoltaic cells utilize the visible and ultraviolet regions of the solar spectrum while the thermoelectric utilizes the infrared region of the solar spectrum. Therefore, combining both technologies would allow a wider utilization of the solar spectrum for energy harvesting. In addition, the synergetic integration of the photovoltaic and thermoelectric generator could result in an improved photovoltaic efficiency, and an increase in electricity generation per unit area compared to the conventional PV only. Furthermore, depending on the integration method used for the PV-TEG, the thermoelectric generator could be used for thermal management of the photovoltaic which will in turn lead to an increase in the PV efficiency and additional energy generation from the thermoelectric generator. Consequently, the market potential of the PV-TEG technology for electricity generation would be high although the technology is still in the development phase.

1.2 Research Aim and Objectives

Despite the advancements made in the photovoltaic technology which has made it commercially available at a reduced cost for years, the widespread application of the photovoltaic technology is still hindered by its low conversion efficiency resulting from increase in its temperature. Therefore, this research aims to present an innovative thermal management technique for photovoltaic by the incorporation of thermoelectric generator (TEG) and heat pipe to form a hybrid photovoltaic system with improved overall efficiency, increased electricity generation and greater energy harvesting from the solar spectrum. In addition, this research aims to investigate an innovative technique for enhancing the electrical and mechanical performance of thermoelectric generators by geometry optimization. To achieve this goal, the research has set out the following objectives:

- 1) To carry out an extensive literature review of photovoltaic thermal management with thermoelectric generator and heat pipe, and to study the various thermoelectric geometry and structure optimization techniques while also providing recommendations for future research.
- 2) To design a conceptual hybrid photovoltaic system with thermoelectric generator and flat plate microchannel heat pipe with enhanced overall efficiency.
- 3) To present mathematical analysis and develop computer simulation models to predict and optimise the performance of the proposed system through the use of three-dimensional finite element models.
- 4) To setup and test a prototype system in laboratory-controlled conditions and validate the simulation models using the experimental results and published data.

- 5) To perform optimization of photovoltaic-thermoelectric system, photovoltaic-thermoelectric-heat pipe system and thermoelectric generator for performance enhancement using the validated simulation models.

1.3 Research Methodology

The proposed research is a typical applied research to develop a new hybrid photovoltaic-thermoelectric system and perform thermoelectric geometry optimization. It follows the process of research assumption, questions identification, mathematical analysis, computer numerical simulation, experimental testing, model validation, and optimization case studies. The objectives of this research are achieved through combined research actions and interaction. The research assumption and questions identification form the basis for the concept formation while a combination of theoretical and experimental analysis is used to achieve the research objectives. The methods used to achieve the objectives of this research are described briefly below.

Approach to objective 1: Review of literature on hybrid photovoltaic-thermoelectric systems and thermoelectric geometry optimization.

This approach would involve (1) definition and identification of the basic operating principles of each individual technology including photovoltaic, thermoelectric generator and heat pipe; (2) review of design, research and development works on hybrid photovoltaic-thermoelectric systems; (3) identification of the current research focus areas and technical barriers regarding existing hybrid PV-TE systems including niche applications; (4) review of works on thermoelectric geometry and structure optimization; (5) identification of main optimization method and thermal stress studies; (6) description of the numerical solution using finite element method (FEM) and explanation of the computational procedure; and (7)

discussion and recommendation for future research direction of hybrid PV-TE systems and thermoelectric geometry optimization. This approach would enable the understanding of the current state-of-art of hybrid photovoltaic-thermoelectric systems and thermoelectric geometry optimization and provide a solid foundation for the achievement of the remaining objectives.

Approach to objective 2: Conceptual design of the proposed system.

This approach would involve (1) complete drawings of the proposed system components and integrated hybrid photovoltaic-thermoelectric-heat pipe system; (2) description of the basic operating principle of the system; and (3) identification of system components and dimensions.

Approach to objective 3: Mathematical analysis and computer simulation model development to predict system performance.

This approach would enable the achievement of the technical objective of this research using numerical simulation. It will involve (1) description of modelling equations for individual components in the hybrid system; and (2) simulation of system performance under steady state and transient conditions.

Approach to objective 4: Experimental testing and computer model validation.

This approach would involve (1) experimental test rig setup; (2) investigation of the system performance under laboratory conditions; and (3) simulation model validation with experimental results and published data. This approach would provide valuable experimental results to characterise the performance of the proposed system and validate the developed simulation model.

Approach to objective 5: Optimization of hybrid photovoltaic-thermoelectric systems and thermoelectric generator using the validated simulation models.

The validated simulation models will be used to optimize the performance of the systems. This approach would involve (1) optimization of photovoltaic-thermoelectric system; (2) optimization of photovoltaic-thermoelectric-heat pipe system; and (3) optimization of thermoelectric generator for electrical and mechanical performance enhancement. The general optimization methodology for most of the numerical studies is thermoelectric geometry optimization. The main objective is to enhance the performance of the hybrid and TEG only systems by optimizing the thermoelectric generator geometry which is an effective method to achieve improved performance.

1.4 Research Novelty

Considering the current state of the hybrid photovoltaic-thermoelectric and thermoelectric generator technologies, this research has the following novelties which address the gaps identified in the literature review.

- 1) Structural innovation:** Introduction of the low cost and high efficiency microchannel heat pipe into the hybrid system can reduce the thermal resistance of the heat flow across the PV-MCHP and MCHP-TE interfaces and increase the heat transfer capacity of the MCHP from its evaporator to condenser, thus leading to an effective PV-to-TE energy transfer. In addition, the use of flat plate MCHP rather than cylindrical heat pipes can enhance better heat extraction from the photovoltaic due to absence of geometry mismatch and reduction of thermal losses. Furthermore, water cooling is a more effective

cooling method compared to air cooling. Therefore, the thermoelectric generator cold side is cooled using water instead of free air or forced air cooling and this enhances the performance of the hybrid system. In addition, the use of water cooling allows for the demonstration of the hybrid system feasibility for co-generation of electricity and hot water.

2) Theoretical innovation: Simulation models for thermoelectric generator, photovoltaic-thermoelectric and photovoltaic-thermoelectric-heat pipe are developed and validated. The developed models can be used to predict the performance of the systems under steady state and transient conditions. In addition, the models can be used to optimize the design parameters and improve the performance of the system. While there is an abundance of research on one-dimensional and two-dimensional simulation of photovoltaic-thermoelectric systems, there are very few research works carried out using three-dimensional simulation. Therefore, for the first time, a three-dimensional numerical simulation of a hybrid PV-TE system with and without flat plate heat pipe is presented in this research. Furthermore, the use of three-dimensional modelling in this research provides a better understanding of the heat transfer process in the systems and temperature distribution thereby enabling a more accurate prediction of the system performance. COMSOL Multiphysics is used to perform the numerical simulations using finite element method (FEM).

3) Conceptual innovation: The placement of the photovoltaic and thermoelectric generator module separately onto the microchannel heat pipe

(MCHP) evaporator and condenser respectively can significantly reduce the quantity of thermoelectric modules used. Although thermoelectric generator modules are commercially available, they are expensive. Therefore, the use of a heat pipe will minimise the quantity of TEG modules attached to the system and hence reduce the overall cost of the hybrid system. Furthermore, additional electricity can be obtained from the thermoelectric generator thereby increasing the overall system electrical output.

1.5 Thesis Structure

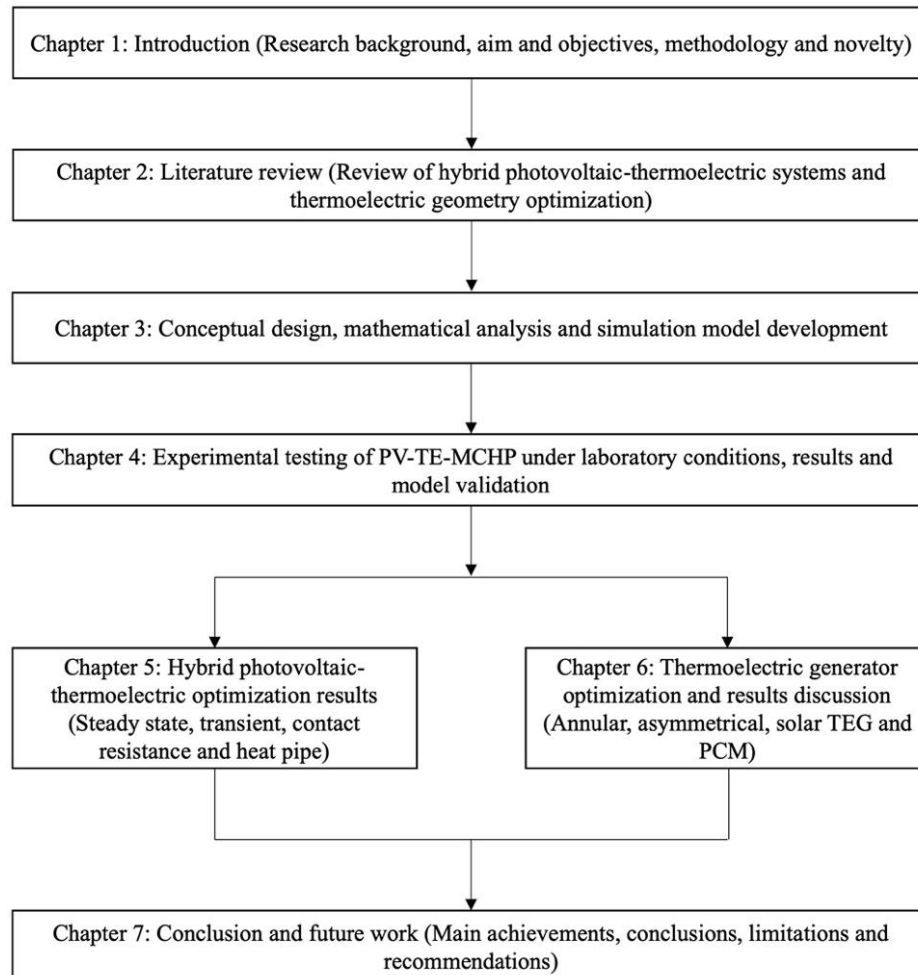


Figure 1.6: Thesis structure

The structure of the thesis including the details and interdependence of the different chapters is shown in Figure 1.6 and described as follows:

Chapter 1 – Introduction: This chapter briefly describes the research background, aim, objectives, methodology and novelty. The research background describes the global energy demand and consumption, carbon emission targets globally, in the EU and the UK. In addition, the advantages of renewable energy sources especially solar energy which is the main energy source considered in this research are provided. Furthermore, the current market profiles of photovoltaic, thermoelectric generator and photovoltaic-thermoelectric are provided.

Chapter 2 – Literature review: This chapter presents a detailed review of literature on photovoltaic thermal management with thermoelectric generator and heat pipe. It presents an explanation of the basic operating principles of photovoltaic, thermoelectric and heat pipe which are the main technologies considered in this research. Furthermore, two main integration methods and study types for hybrid photovoltaic-thermoelectric systems are presented. Current research focus areas in hybrid PV-TE are explained in detail. In addition, research works on thermoelectric geometry and structure optimization are explored in detail including different geometries for performance enhancement. Furthermore, the thermoelectric geometry optimization method is presented in addition to thermal stress optimization. Finite element method which is used for the numerical solution is explained and the computational procedure in COMSOL Multiphysics software is presented. Lastly, discussion and recommendations for future research direction in hybrid PV-TE and thermoelectric geometry optimization are provided for guidance.

Chapter 3 – Conceptual design of proposed system, mathematical analysis and

computer modelling: This chapter presents the conceptual design of the proposed system including system components drawings. Furthermore, the operating principle of the system is explained and the dimensions for each component are provided. In addition, computer simulation models for the photovoltaic, thermoelectric generator and heat pipe are developed in this chapter. Furthermore, modelling equations are presented. In addition, the modelling results are presented and discussed in detail.

Chapter 4 – Experimental testing and model validation:

The experimental study carried out is presented in this chapter. The experimental test rig setup is presented including the experimental procedure. Furthermore, the experimental results obtained for different case studies considered under laboratory conditions are presented. In addition, the simulation model validation with experimental results and published data is presented.

Chapter 5 – Hybrid photovoltaic-thermoelectric optimization results:

This chapter presents the results from optimization studies on hybrid photovoltaic-thermoelectric system and hybrid photovoltaic-thermoelectric-heat pipe system using the validated simulation models.

Chapter 6 – Thermoelectric generator optimization results:

This chapter presents the results from thermoelectric generator optimization studies using the validated simulation models. Innovative thermoelectric geometries are optimized numerically for electrical and mechanical performance enhancement.

Chapter 7 – Conclusion and future work: This chapter provides a conclusion for the research including a summary of the works carried out to achieve the aim and objectives of the research. Furthermore, the main findings of the research are provided, and limitations encountered in the research are presented. Lastly, recommendations for future work are presented for guidance.

All the above chapters are arranged and linked systematically to provide the detailed process of achieving the set research aim and objectives. In addition, the thesis structure aids easy understanding of the research carried out and provides a concise overview of the work done in this research.

CHAPTER 2 LITERATURE REVIEW

2.1 Chapter Introduction

This chapter explores the concept of photovoltaic thermal management with the use of thermoelectric generators and heat pipes for performance enhancement. Furthermore, this chapter presents a detailed review of thermoelectric geometry and structure optimization research. The following tasks are addressed in this chapter:

- 1) Providing an explanation of the basic operating principles of photovoltaic, thermoelectric and heat pipe.
- 2) Describing the concept of hybrid photovoltaic-thermoelectric including integration methods and study types.
- 3) Presenting a detailed overview of the current research focus areas in PV-TE and outcomes.
- 4) Providing a detailed review of the different thermoelectric geometry and structure optimization available in literature and optimization method.
- 5) Presenting a review of thermal stress optimization for mechanical performance enhancement.
- 6) Explaining the finite element method and the computational procedure.
- 7) Discussing the opportunities for further development of PV-TE technology and thermoelectric geometry optimization.

This part of the work provides a solid foundation for the research and presents all the essential elements and research areas in hybrid photovoltaic-thermoelectric and thermoelectric geometry optimization. It is envisaged that this chapter will enable the fundamental understanding of photovoltaic thermal management with thermoelectric generators and heat pipes, and thermoelectric geometry optimization.

2.2 Photovoltaic Systems

The photovoltaic effect was first discovered by French physicist, Edmond Becquerel in 1839. However, the first silicon solar cell with a p-n junction was developed in 1954 by a group of researchers led by Chapin D.M at the Bell telephone laboratories (Chapin et al., 1954). A photovoltaic cell is made up of p-type and n-type semiconductors that absorb incoming photons and convert them into electron-hole pairs. Basically, electrons are promoted from the valence band to conduction band when the absorbed energy is equal to or greater than the band gap energy. This process generates electron-hole pairs which diffuse and separate at the p-n junction of the semiconductors due to the generated electric field. Subsequently, electrons are attracted to the negative side while the holes move to the positive side. Finally, the electrons flow in the external circuit and current is generated as shown in Figure 2.1a (Huen and Daoud, 2017). Monocrystalline silicon cell still has the best conversion efficiency however, PV material optimization research is still on-going and better efficiency values could be achieved in the future (Green et al., 2018).

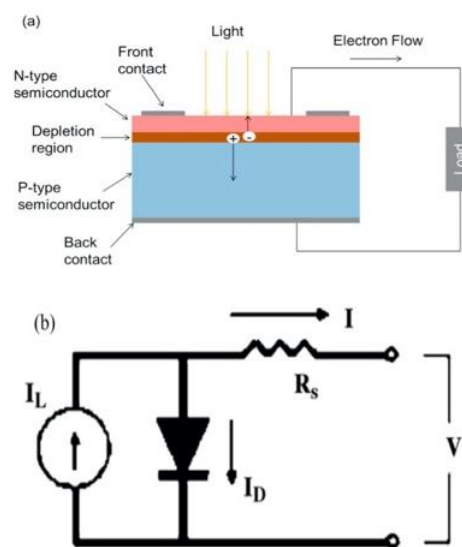


Figure 2.1: Photovoltaic cell (a) p-n junction structure (Huen and Daoud, 2017) and (b) simplified equivalent circuit (El Chaar et al., 2011)

2.2.1 Modelling of the Photovoltaic Cells

A photovoltaic cell can be modelled as a current source with a parallel diode as shown in Figure 2.1b. The diode current can be obtained from the Shockley equation as (El Chaar et al., 2011):

$$I_D = I_0 \left[\exp\left(\frac{q(V+IR_S)}{\gamma k T_c}\right) - 1 \right] \quad (2.1)$$

Reverse saturation current is obtained as,

$$I_0 = DT_{ab}^3 \exp\left(\frac{q\varepsilon_G}{AkT_{ab}}\right) \quad (2.2)$$

where D is the diode diffusion factor, T_{ab} is absolute temperature, q is electron charge, ε_G is material band gap energy, k is Boltzmann constant and A is cross sectional area.

Depending on the required voltage and current levels, solar cells are connected in series and parallel respectively. The solar cell generator voltage and current can be obtained as,

$$V_g = I_g R_s \frac{N_s}{N_p} \ln\left(1 + \frac{N_p I_{ph} - I_g}{N_p I_0}\right) \quad (2.3)$$

where R_s is the series resistance, N_s is number of cells in series, N_p is number of cells in parallel and I_{ph} is the cell photocurrent proportional to solar irradiance.

$$I_g = I_{ph} - I_0 \exp\left(\frac{qV_g}{kT} - 1\right) \quad (2.4)$$

where T is the cell temperature

The PV cell short circuit current (I_{sc}) can be obtained by setting $V_g = 0$ and $I_{sc} = I_{ph}$. This value varies with cell irradiance and the PV cell open circuit voltage (V_{oc}) can be obtained by setting $I_g = 0$ thus,

$$V_{oc} = \frac{kT}{q} \ln\left[\frac{I_{ph}}{I_0}\right] \quad (2.5)$$

The maximum output power of the PV is expressed as,

$$\frac{d(V_g \times I_g)}{dt} = 0 \quad (2.6)$$

$$V_{mp} = V_{oc} - \frac{kT}{q} \ln \left[\frac{V_{mp}}{kT/q} + 1 \right] \quad (2.7)$$

The fill factor (FF) can be expressed as,

$$FF = \frac{V_{mp} \times I_{mp}}{V_{oc} \times I_{sc}} \quad (2.8)$$

The efficiency of the PV can be expressed as,

$$\eta_{pv} = \frac{FF \times V_{oc} \times I_{sc}}{P_{in}} \quad (2.9)$$

where P_{in} is the incident power on the PV cell.

2.2.2 Influence of Temperature on Photovoltaic Cells

Majority of the research on PV system has been on efficiency enhancement by application of effective thermal management techniques. The conversion efficiency of the PV is largely dependent on the solar cell temperature therefore, cooling of the PV is of utmost importance. It is obvious from Figure 2.2 that the solar cell temperature affects the cell efficiency, open circuit voltage and short circuit current (Singh et al., 2008). In addition, Figure 2.3 shows the influence of cell temperature on the current-voltage (I-V) characteristics of the PV cell (Fisac et al., 2014). Generally, the PV performs better at lower cell temperature values. The temperature dependence of PV's efficiency is often characterized by a property known as Temperature coefficient. It is used in quantifying the temperature sensitivities of the PV cell performance. To compare different PV cells, the temperature coefficient are usually given at a normalized value of 25 °C or 298.15 K (Dupré et al., 2017).

The PV electrical efficiency can be increased by removing the accumulated heat from the concealed PV surface and using this heat appropriately (Zhang et al., 2012). Different technologies such as Photovoltaic/Thermal (PV/T) and Photovoltaic-Thermoelectric Generator (PV-TEG) have been developed for this purpose. However, the PV-TEG can only fulfil this purpose if the TEG is in physical contact with the PV

(i.e. direct coupling method). Nevertheless, the TEG will have to operate at a temperature higher than the ambient temperature to produce some electrical power and it most likely will heat up the solar cell if not properly cooled. If the TEG is not in physical contact with the PV (i.e. spectrum splitting method), it cannot cool down the PV cell.

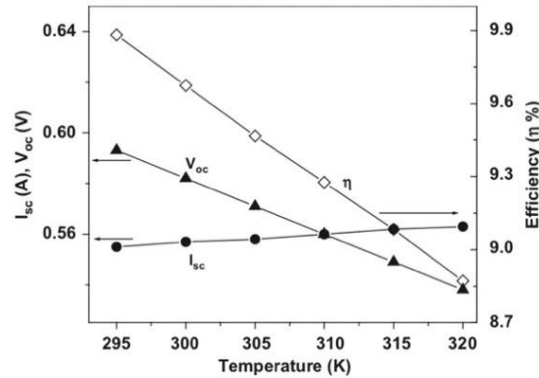


Figure 2.2: Effect of cell temperature on efficiency, open circuit voltage and short circuit current of a monocrystalline silicon cell (Singh et al., 2008)

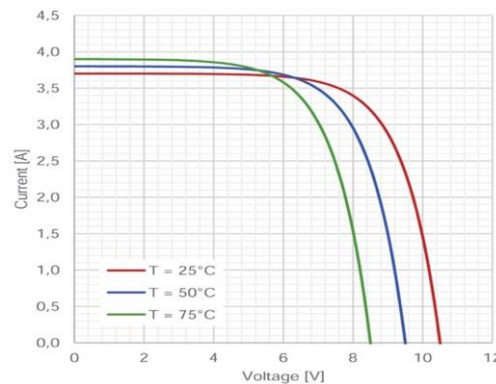


Figure 2.3: Influence of temperature on the I-V characteristics of a photovoltaic cell (Fisac et al., 2014)

2.3 Thermoelectric Devices

Thermoelectric devices can operate either as a generator as shown in Figure 2.4a or as a cooler as shown in Figure 2.4b (J. F. Li et al., 2010). Direct conversion of energy is dependent on the physical transport properties of thermoelectric materials including thermal conductivity, Seebeck coefficient and electrical conductivity, and

their energy conversion efficiency which is expressed in terms of thermoelectric figure of merit.

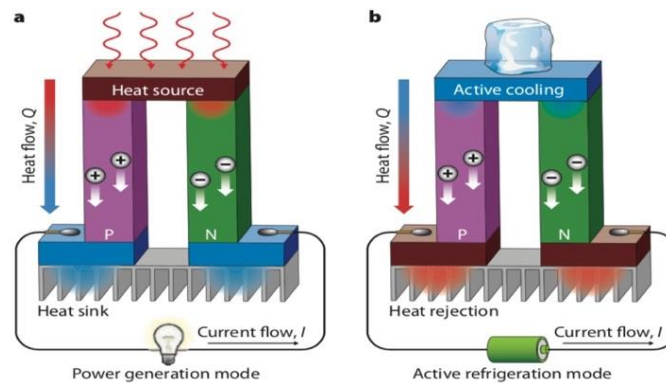


Figure 2.4: Schematic of a thermoelectric (a) generator and (b) cooler (J. F. Li et al., 2010)

2.3.1 Thermoelectric Effects

Direct conversion of thermal energy to electrical energy and vice versa can be achieved by a thermoelectric device based on the thermoelectric effect which consists mainly of three separate effects including Seebeck effect, Peltier effect, and Thomson effect. The thermoelectric effects are described below:

2.3.1.1 Seebeck Effect

The Seebeck effect which was discovered in 1821 by Thomas Seebeck describes the generation of voltage at the junction of two different conductors when a temperature difference is present across the junctions. The thermoelectric generator operates based on the Seebeck effect for direct conversion of thermal energy to electrical energy. A schematic of the Seebeck effect is shown in Figure 2.5 where two different conductors A and B are joined together to form an electrical circuit. The conductors are connected thermally in parallel and electrically in series with one junction acting as the hot junction with temperature T_h while the other junction is the cold junction with temperature T_c . Voltage generation occurs only when the hot junction temperature is larger than the cold junction temperature thereby creating a

temperature difference across the junctions. Furthermore, the Seebeck effect occurs as a result of thermal diffusion which causes the transfer of charge carriers (electrons or holes) across (or against) temperature difference in the conductors (Enescu, 2019). In addition, the Seebeck effect is used in thermocouples for temperature measurement. The Seebeck coefficient is given as:

$$\alpha_{AB} = \frac{V}{\Delta T} \quad (2.10)$$

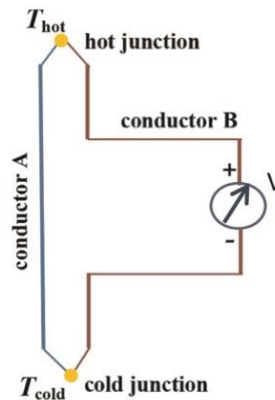


Figure 2.5: Schematic of the Seebeck effect in an open circuit (Enescu, 2019).

2.3.1.2 Peltier Effect

Peltier effect which was discovered in 1834 by Jean-Charles Peltier describes the direct conversion of electrical energy into thermal energy which can be used for heating or cooling. Based on the Peltier effect, an electric current creates a heating or cooling effect at the junction of two different conductors depending on the direction of current flow as shown in Figure 2.6 (Chen, 2009). Furthermore, the thermoelectric cooler (TEC) operates based on the Peltier effect and the Peltier coefficient is given as:

$$\pi_{AB} = \frac{q}{I} \quad (2.11)$$

where q is the rate of heat absorption or release and I is the current in the circuit.

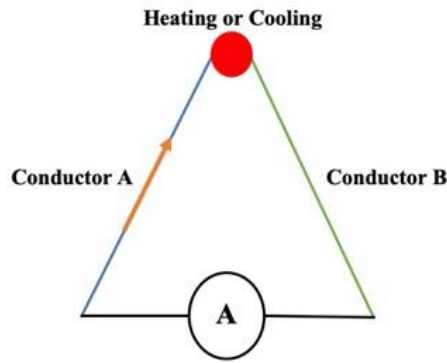


Figure 2.6: Schematic of Peltier effect (Chen, 2009).

2.3.1.3 Thomson Effect

The Thomson effect which was discovered in 1852 by William Thomson describes the process of heat absorption or release due to the flow of current through a portion of a single conductor in the presence of a temperature difference as shown in Figure 2.7. The Thomson coefficient is given as:

$$\beta = \frac{q}{I\Delta T} \quad (2.12)$$

where ΔT is temperature difference, q is the rate of heat absorption or release and I is the current in the circuit.

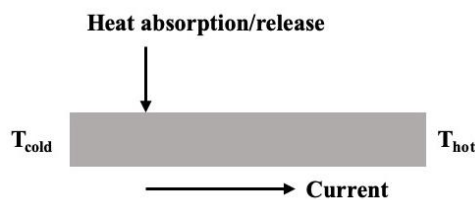


Figure 2.7: Schematic of Thomson effect (Chen, 2009).

2.3.1.4 Kelvin Relationships

The three thermoelectric coefficients described above are related by the Kelvin relationships. Furthermore, the relationships between the thermoelectric coefficients (Seebeck, Peltier and Thomson) can be obtained by the principles of irreversible

thermodynamics. These relationships are known as Kelvin's laws and are given as (Goldsmid, 2017):

$$\pi_{AB} = \alpha_{AB}T \quad (2.13)$$

$$\beta_A - \beta_B = T \frac{d\alpha_{AB}}{dT} \quad (2.14)$$

The relationship between the Seebeck coefficient and Peltier coefficient is described by Eq. (2.13) which shows that the same thermoelectric material can be used for the thermoelectric generator and the thermoelectric cooler. Furthermore, the Peltier coefficient is difficult to determine, while the Seebeck coefficient is very easy to measure therefore, the theory of thermoelectric energy conversion is usually developed in terms of the Seebeck coefficient and Eq. (2.13) is used to obtain the Peltier coefficient if needed (Goldsmid, 2017). The relationship between the Seebeck coefficient and the Thomson coefficient is described by Eq. (2.14).

2.3.2 Thermoelectric Materials

The quality of thermoelectric materials used for generating electric power via the Seebeck effect or cooling (refrigeration) via the Peltier effect is mainly determined by three intrinsic material properties including, electrical conductivity, Seebeck coefficient and thermal conductivity. Materials with high electrical conductivity are favourable because electrical current is passed in both the power generation and cooling mode. In addition, a large Seebeck coefficient is essential because a large generated voltage per unit temperature gradient is desired. Lastly, a low thermal conductivity is essential for TE materials because temperature difference must be maintained across the material (Minnich et al., 2009). A dimensionless parameter known as thermoelectric figure of merit (ZT) is usually used to obtain the thermoelectric efficiency and it is expressed as (Elsheikh et al., 2014),

$$ZT = \frac{\alpha^2 \sigma}{\kappa} T \quad (2.15)$$

where α is the Seebeck coefficient, σ is the electrical conductivity, κ is the thermal conductivity and T is the absolute temperature.

Classifying thermoelectric materials based on operating temperature range, Bismuth telluride (Bi_2Te_3) is used for low temperature (< 500 K) power generation. Materials based on group-IV tellurides such as PbTe, GeTe and SnTe are used for mid-temperature (500-900 K) power generation. Lastly, silicon-germanium alloys are used for high temperature (> 900 K) power generation (Twaha et al., 2016). For thermoelectric devices to gain wider application, materials with high ZT and low price must be developed, and this is an achievable future goal due to the extensive research being carried out in this area.

2.3.3 Modelling of Thermoelectric Generator

The efficiency of a thermoelectric generator is expressed as (Rowe, 2006),

$$\eta = \frac{\text{Energy supplied to the load}}{\text{Heat energy absorbed at the hot junction}} \quad (2.16)$$

Assuming constant thermoelectric material properties and negligible contact resistances, the efficiency can be expressed as,

$$\eta_{teg} = \frac{I^2 R}{\alpha I T_h = \kappa(T_h - T_c) - \frac{1}{2} I^2 R} \quad (2.17)$$

where I is current, R is series resistance, T_h is hot side temperature and T_c is cold side temperature.

The maximum conversion efficiency is given as,

$$\eta_{max} = \eta_c \frac{\sqrt{1+ZT}-1}{\sqrt{1+ZT} + \frac{T_c}{T_h}} \quad (2.18)$$

where η_c is the Carnot efficiency and it is expressed as,

$$\eta_c = \frac{T_h - T_c}{T_h} \quad (2.19)$$

2.3.4 Applications of Thermoelectric Generator

Thermoelectric generators have a wide range of applications such as in waste heat recovery for automobiles (Hsiao et al., 2010; Saqr et al., 2008; Shu et al., 2018; Yang, 2005), wearable sensors (Francioso et al., 2010; Kim et al., 2014; Qing et al., 2018; Suarez et al., 2017), micropower generation (Amatya and Ram, 2010), wireless sensor network (Madan et al., 2015), space power (Pichanusakorn and Bandaru, 2010) and buildings (He et al., 2015b). Detailed explanation of the application of the thermoelectric generator in the aforementioned sectors can be found in the referenced literatures. For the sake of this review, more focus is placed on the application of hybrid PV-TEG in the later sections.

2.4 Heat Pipes

Heat pipes are passive devices which are highly effective for transferring heat at high rates over considerable distances with extremely small temperature drops, simple construction, exceptional flexibility and easy control with no need for external pumping power (Faghri, 1995). Heat pipes are efficient thermal management solutions which have been used for numerous applications such as electronic equipment cooling, solar thermal systems, solar photovoltaic cooling, aerospace equipment cooling, heat exchangers and heat pumps, automobile applications, medicine and human body temperature control and permafrost stabilization (Faghri, 2014).

2.4.1 Basic Operational Principle

A conventional heat pipe as shown in Figure 2.8 comprises of a sealed container (pipe wall and end caps), wick structure and a small amount of working fluid that is in a state of equilibrium with its own vapor. The heat pipe consists of three main parts including evaporator section, adiabatic (transport) section and condenser section.

The heat pipe operates in such a way that when heat is externally applied to its evaporator section, the heat is conducted through the pipe wall and wick structure, where vaporization of the working fluid occurs. Furthermore, the resulting vapor pressure drives the vapor through the adiabatic section to the condenser section where condensation of the vapor occurs thereby releasing its latent heat of vaporization to the attached heat sink. A capillary pressure is created by the menisci in the wick which causes the condensed fluid to be pumped back to the evaporator section. Consequently, a continuous transportation of the latent heat of vaporization from the evaporator to the condenser section of the heat pipe is possible and it will continue forasmuch as the capillary pressure is sufficient enough to drive the process (Faghri, 2014).

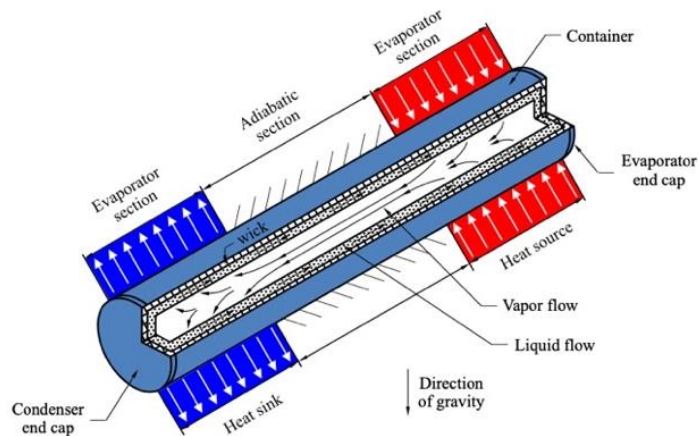


Figure 2.8: Schematic of a conventional heat pipe (Faghri, 2014)

2.4.2 Types of Heat Pipes

Different heat pipe configurations are available for different applications however, to simplify the design and manufacturing process, heat pipe containers are generally circular cylinders while others are rectangular (flat heat pipes), conical (rotating heat pipes), corrugated flexible heat pipes, and nose cap (Faghri, 2012). Furthermore, there are various types of heat pipes commercially viable for various applications which require moderate to high temperature fluctuations (Chaudhry et al.,

2012). In this research, a flat plate microchannel heat pipe (MCHP) is used because it is currently one of the most preferred heat pipes because it provides greater heat transfer characteristics and a better performance over small temperature gradients due to its microchannel structure (Li et al., 2019a).

2.4.3 Working Fluid

The working fluid is one of the three basic components of a heat pipe in addition to wick or capillary structure and the container. The operating vapour temperature range is an important parameter which must be considered before the selection of a suitable working fluid. In addition, thermodynamic considerations influence the working fluid selection in terms of various heat transfer limitations in the heat pipe.

2.4.4 Heat Transfer Limits

In a heat pipe, the maximum heat transfer capacity is hindered by five limits including viscous limit, sonic limit, capillary limit, entrainment limit and boiling limit (Reay et al., 2014). The heat pipe thermal performance is limited by one of the five limits depending on the operating temperature range and heat pipe geometry. A brief description of each limit is given as (Byon, 2016):

- 1) Viscous limit: The viscous forces prevent the flow of vapor within the heat pipe.
- 2) Sonic limit: The flow of vapor reaches sonic velocity when leaving the evaporator thereby choking the flow.
- 3) Capillary limit: The capillary limit occurs when the working fluid circulation rate increases till the flow path drop in pressure attains the developed capillary pressure.

- 4) Entrainment limit: This is friction occurring between the working fluid and the vapor which both travel in opposite directions.
- 5) Boiling limit: This occurs in the wick which prevents the return of the working fluid.

2.5 Hybrid Photovoltaic-Thermoelectric Systems

Integrating thermoelectric devices into photovoltaic systems can enable the efficient thermal management of PV thus, enhancing its overall performance. When thermoelectric generators are combined with PV, depending on the integration method of the PV-TEG, the TEG can utilize the waste heat from the PV to generate some electrical energy if it is properly cooled and there is sufficient temperature difference across it. In addition, the overall hybrid system performance could potentially be enhanced by the integration of thermoelectric generators into PV if the system is properly designed although there is a possibility of reduced performance due to the complex relationship between PV and TEG.

2.5.1 Hybrid System Integration Methods

The combination of photovoltaic and thermoelectric allows for the wider use of the solar spectrum. This is because PV converts the ultraviolet and visible regions (200 – 800nm) of the solar spectrum into electricity while TEG converts the infrared region (800-3000nm) into electricity (Tritt et al., 2008). The two main PV-TEG integration methods are the spectrum splitting and direct coupling integration. The difference is the presence or absence of a reflective component (e.g. spectrum-splitter or prism). Determining the best integration method for the hybrid system by comparing the two integration methods (spectrum splitting and direct coupling) is not straightforward. This is because, when conversion efficiency is used as the only

comparison parameter, the direct coupling hybrid system can perform better than the spectrum splitting hybrid system (Contento et al., 2017). However, the spectrum splitting hybrid system has an advantage over the direct coupling hybrid system because it requires a smaller quantity of active thermoelectric material per unit area due to the smaller hybrid system fill factors at maximum efficiency.

In addition, the spectrum splitting system requires a smaller area which must be covered by cooling devices thus, the costs of the spectrum splitting system should be lower than that of the direct coupling system (Lorenzi et al., 2017). Nevertheless, the larger size of the system along with the additional cost of the splitting device might result in a balance between the pros and cons of the spectrum splitting and direct coupling integration methods (Contento et al., 2017). Consequently, the final decision on the best integration method for the hybrid system can only be reached upon completion of a detailed comparison between the pros and cons (including a cost evaluation) of the two integration methods (Lorenzi et al., 2017). Integrating thermoelectric generators into solar panels could provide an additional energy of 2-10% depending on the thermoelectric material, connection and configuration (Babu and Ponnambalam, 2017). Therefore, research on PV-TEG is increasing expeditiously due to its huge potential to provide enhanced performance compared to stand alone PV or TEG systems.

2.5.1.1 Spectrum Splitting Method

Basically, in the spectrum splitting system, the solar radiation is reflected by a splitter at a specific wavelength (cut-off wavelength) and this separates the radiation used by the PV and TEG for energy conversion as shown in Figure 2.9. The PV and TEG are usually placed perpendicularly when the spectrum splitting integration method is used and the radiation that is longer than the cut-off wavelength is reflected

by the TEG while those shorter than the cut-off wavelength transmit through the spectrum splitter and are absorbed by the PV (Huen and Daoud, 2017). It is important to note that when this integration method is used, the PV and TEG work independently on converting solar energy into electricity thus, the TEG doesn't cool down the PV or use the PV's waste heat for energy conversion.

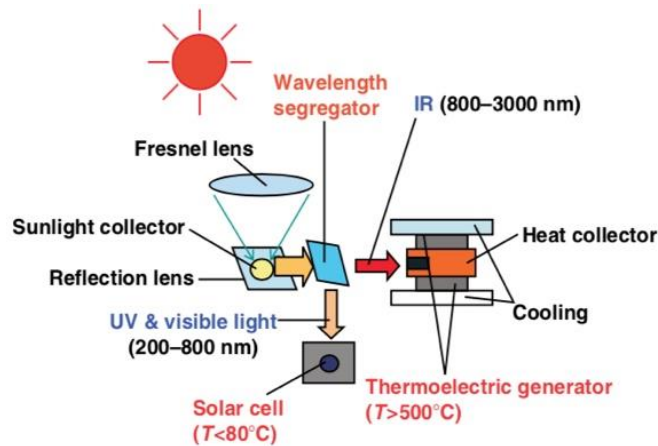


Figure 2.9: Schematic of spectrum splitting PV-TEG integration (Tritt et al., 2008)

Kraemer et al. (2008) presented a general optimization methodology for a hybrid PV-TEG system using the spectrum splitting method. Three different PV types were studied experimentally, and it was found that the amorphous silicon cell provided the best hybrid system efficiency of 13.26% when a TEG with efficiency of 8% was used. A comprehensive study of a spectrum splitting concentrated PV-TEG system was performed by Ju et al. (2012). The influence of cut-off wavelength, concentration ratio and heat transfer coefficient on the performance of the hybrid system were studied and optimization of the hybrid system was performed. They found that the TEG contributed about 10% of the total hybrid system power and the optimized hybrid system efficiency was about 27.49%. A comparison of the hybrid system with the conventional PV system was made and it was found that the hybrid system is better suited for high concentration conditions due to its enhanced performance.

Furthermore, the optimum design for a concentrated spectrum splitting PV-TEG was proposed by Yin et al. (2018a) to optimize the distribution of solar energy in a spectrum splitting CPV-TEG without compromising the optimum design state of the individual systems. The authors argued that the thermoelectric structure factor influences the optimum temperature distribution in the TEG. It was also found that the spectral splitter optimum cut-off wavelength and thermoelectric figure of merit have an inverse relationship.

Yang et al. (2018) studied the performance of a spectrum splitting PV-TEG system using numerical simulation. It was found that the efficiency of the hybrid system increased by 2.67% and 2.19% compared to that of the PV only system at concentration factors of 30 and 100 respectively. Bjørk et al. (2018) studied the maximum theoretical performance of a PV-TEG system without concentration. The authors used an analytical model to study the performance of the system and found that the hybrid system using spectrum splitting could achieve a maximum efficiency increase of 1.8 percentage point compared to the PV only system. Furthermore, Liang et al. (2018) performed an experimental and numerical investigation on the performance of a spectrum splitting concentrated hybrid PV-TEG system. Results showed that the direct normal irradiation (DNI), optical concentration ratio and height ratio of the two TEG stages could significantly affect the performance of the hybrid PV-TEG system. The performance data for some of the spectrum splitting PV-TEG systems reviewed can be found in Table 2.1.

Table 2.1: Summary of some selected spectrum splitting PV-TEG systems reviewed

Material	Efficiency	Remarks
----------	------------	---------

CHAPTER 2 LITERATURE REVIEW

Reference	PV	TE	Study type	PV-TEG	PV	
Kraemer et al. (2008)	Monocrystalline silicon	N/A	Simulation	11.45 %	9.09 %	TEG efficiency of 8% corresponding to figure of merit (ZT = 1.7) was used.
	Amorphous silicon	N/A	Simulation	13.26 %	9.40 %	
	Polymer thin film	N/A	Simulation	8.32%	3.41 %	
Ju et al. (2012)	GaAs	Skutterudite CoSb ₃	Simulation	27.49 %	N/A	Figure of merit (ZT = 1.4) at 800K, heat transfer coefficient of 4500 W/m ² /K were used, and the optimized results were given.
Mizoshiri et al. (2012)	Amorphous silicon	Thin-film Bismuth	Experiment	N/A	N/A	Open circuit voltage of hybrid system increased by 1.3% compared to PV only system.
Li et al. (2014)	N/A	N/A	Simulation	31-34%	N/A	Figure of merit (ZT = 1) was used and 30% power

CHAPTER 2 LITERATURE REVIEW

						output
						enhancement was obtained.
Elsarrag et al. (2015)	Monocrystalline silicon	Bismuth telluride	Experiment and simulation	N/A	N/A	Hybrid system performed better than PV only system.
Skjølstrup et al. (2016)	Amorphous silicon	N/A	Simulation	19.1%	15.8%	Beam splitter layer was 114 and TE efficiency was 8%.
	Microcrystalline silicon	N/A	Simulation	19.8%	17.5%	Beam splitter layer was 128 and TE efficiency was 8%.
Sibin et al. (2017)	N/A	N/A	Experiment	N/A	N/A	ITO/Ag/ITO spectral beam splitter coating was developed, and it had a high visible transmittance of 88%.
Yin et al. (2018a)	GaAs	N/A	Simulation	30%	N/A	Figure of merit was 1 and cut-off wavelength was

							equal to maximum wavelength of PV.
Yang et al. (2018)	Silicon	N/A	Simulation	40.2%	39.32%	Concentration factor was 100.	
Bjørk et al. (2018)	N/A	N/A	Simulation	1.8 percent	N/A	Maximum hybrid system efficiency without concentration was studied.	
Mustofa et al. (2018)	N/A	Bismuth telluride	Experiment	N/A	N/A	Long wavelengths of around 800nm were emitted by the halogen lamps for the TEG.	
Shou et al. (2012)	Crystalline silicon	N/A	Simulation	3.24%	N/A	Hybrid system had a filter at 150 suns.	

2.5.1.2 Direct Coupling Method

In the direct coupling system, no splitter is used thus, the PV and TEG are directly coupled and placed in a parallel arrangement. The PV is placed directly above the TEG and a heat sink is attached to the bottom of the TEG just as in the case of the spectrum splitting as shown in Figure 2.10. The reason for placing the PV above the TEG is because the PV absorbs the shorter wavelengths while the TEG absorbs the

longer wavelength (Huen and Daoud, 2017). In addition, when the direct coupling method is used, the unabsorbed solar radiation from the PV transmits through the PV to the TEG below and this serves as the input heat flux for the TEG to generate some electrical power. Van Sark (2011) proposed an effective thermal management technique for photovoltaic cells by integrating thermoelectric modules into the PV using the direct coupling method to form a hybrid PV-TEG system with enhanced electrical performance. Two case studies were presented for Malaga, Spain and Utrecht, Netherlands. Using a typical figure of merit value of 0.004/K at 300 K, the authors observed an efficiency increase of 23% for the roof integrated PV-TEG. The results obtained also showed that by using the annual irradiance and temperature profiles of Malaga and Utrecht, the annual energy of these cities could increase by about 14.7% and 11% respectively.

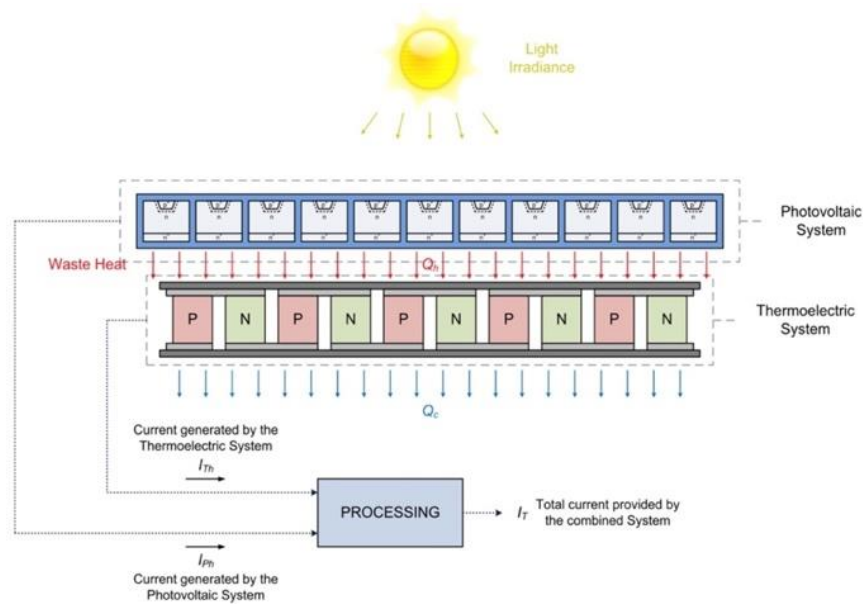


Figure 2.10: Schematic of direct coupling PV-TEG integration (Fisac et al., 2014)

Yin et al. (2018b, 2018c) performed a couple of detailed investigations on the optimum design of hybrid PV-TEG system using direct coupling method. The actual performance of a PV-TEG system throughout a single day was studied to see the

influence of solar radiation variation with time on the hybrid system performance (Yin et al., 2018b). The results obtained showed that the hybrid system performed better than the PV only system within a one-day period and a high efficiency of 16.7% was achieved by the hybrid system (Yin et al., 2018b). Furthermore, an optimum design method and selection principle for a concentrated direct coupling PV-TEG system was presented in (Yin et al., 2018c). It was found that the minimum TEG figure of merit value can be used to perform a feasibility study for the CPV-TEG and select the coupling devices. The authors also found that the optimum temperature and thermoelectric thermal resistance both have an inverse relationship with the PV temperature coefficient. The performance data for some of the direct coupling PV-TEG systems reviewed can be found in Table 2.2.

Table 2.2: Summary of some selected direct coupling PV-TEG systems reviewed

Referenc e	Material		Study type	Efficiency		Remarks	
	PV	TE		PV- TEG	PV		
Guo et al. (2010)	Dye- sensitized solar cell (DSSC)	N/A	Experimen t	10% incre ase	N/A	Hybrid	efficiency was compared with a single DSSC.
Wang et al. (2011)	Dye- sensitized solar cell	N/A	Experimen t	13.8 %	9.26 %	Solar	selective absorber was used.

CHAPTER 2 LITERATURE REVIEW

Van Sark (2011)	Polycrystalline silicon	Bismuth telluride (Bi ₂ Te ₃)	Simulation	13.98 %	10.7 8%	Typical figure of merit value of 1.2 and coefficient $c = 0.058$ were used.
Daud et al. (2012)	Polycrystalline silicon	Bismuth telluride	Experiment	9.064 %	5.97 0%	Solar radiation of 868 W/m ² and liquid cooling was used.
Park et al. (2013)	Crystalline silicon	Bismuth telluride	Experiment and simulation	16.30 %	12.5 %	30% optimized efficiency increase at 15°C TE temperature difference.
Zhang et al. (2013)	Polymer	Bismuth telluride	Experiment	N/A	N/A	Hybrid system power output increase of 46.6% compared to PV only system was observed.
Li et al. (2018b)	Crystalline silicon	N/A	Simulation	11.07 %	9.5 %	TE load resistance was 0.75Ω and figure of merit was 0.0085/K.
	GaAs	N/A	Simulation	22.94 %	21.9 1%	TE load resistance was 1.60Ω and figure of merit was 0.0022/K

CHAPTER 2 LITERATURE REVIEW

Zhang et al. (2014)	Crystalline silicon	Nanostructured bismuth - silicon	Simulation	18.6 %	18.4 %	Concentration ratio was 16.
	Thin-film silicon	bismuth -	Simulation	14%	11%	Concentration ratio was 12.
	Polymer	antimony-	Simulation	12%	4%	Concentration ratio was 5.
Cui et al. (2016)	CIGS	telluride	Simulation	23.5 %	21.5 %	Concentration ratio was 30.
	Crystalline silicon	Bismuth telluride	Simulation	20.1 %	N/A	Operating temperature was 300K, optical concentration was 100 and PCM was used.
	CIGS	Bismuth telluride	Simulation	20.5 %	N/A	Operating temperature was 300K and optical concentration was 0.
	Single-junction GaAs	Bismuth telluride	Simulation	28.09 %	N/A	Operating temperature was 425K, figure of merit was 1.5, and optical concentration was 500.

CHAPTER 2 LITERATURE REVIEW

	GaInP/In GaAs/Ge (III-V)	Bismuth telluride	Simulation	38.90 %	N/A	Operating temperature was 300K and optical concentration was 500.
Liao et al. (2014)	Polycryst alline	Bismuth telluride	Simulation	15%	N/A	CG (Concentration ratio x Solar irradiance) was 875W/m ² .
Chen et al. (2014)	DSSC	N/A	Simulation	24.60 %	N/A	Maximum power output of 1.389mW was obtained.
Lin et al. (2015)	Crystallin e silicon	Bismuth telluride	Simulation	13%	10.2 4%	Power and efficiency enhancement of about 27% was observed.
Beeri et al. (2015)	Multijunc tion	Bismuth telluride	Experimen t and simulation	32.09 %	32.0 8%	Concentration factor was 20 and hybrid power output was 0.190W.
Da et al. (2016)	GaAs	N/A	Simulation	18.51 %	N/A	Figure of merit was 2.5 and Air Mass was 1.5.
Dou et al. (2016)	DSSC	Bi ₂ Te ₃ / ZnO	Simulation	4.27 %	N/A	Hybrid efficiency was 44.3% higher

							than efficiency of ZnO photoanode.
Attivissimo et al. (2015)	Polycrystalline	Bismuth telluride	Simulation	N/A	N/A	TEG	contributes about 12.2% to the hybrid system energy in Pachino.
Luo et al. (2016)	Heterojunction	Bismuth telluride	Experiment	23.30%	N/A	Efficiency increase	was achieved after 1 min illumination.
Pang et al. (2017)	Monocrystalline silicon	Bismuth telluride	Simulation	5.9%	5.7%	Efficiency increase	of 3.9% was observed.
Cotfas et al. (2016)	Monocrystalline silicon	Bismuth telluride	Simulation	N/A	18.9%	Solar irradiance	was 920W/m ² .
	Polycrystalline silicon	Bismuth telluride	Simulation	N/A	16.7%	Solar irradiance	was 1020W/m ² .
	Amorphous silicon	Bismuth telluride	Simulation	N/A	2.88%	Solar irradiance	was 720W/m ² .
Lamba et al. (2016)	Monocrystalline silicon	Bismuth telluride	Simulation	5.8%	5.2%	Number of TEG	was 127 and concentration ratio was 3.

CHAPTER 2 LITERATURE REVIEW

Zhu et al. (2016)	Monocrystalline silicon	N/A	Experiment and simulation	23%	19%	TEG	contributed extra electrical energy of 648J during zero solar radiation period.
Hashim et al. (2016)	Amorphous silicon	Bismuth telluride	Simulation	10.2%	N/A	Hybrid	system power output increased to 163mW.
Kossyvak is et al. (2016)	Polycrystalline silicon	Bismuth telluride	Experiment and simulation	22.5%	N/A	Hybrid	system efficiency was obtained theoretically.
	DSSC	Bismuth telluride	Experiment and simulation	30.2%	N/A	Hybrid	system efficiency was obtained theoretically.
Zhang et al. (2016)	Perovskite	Bismuth telluride	Simulation	18.6%	17.8%	Solar absorber	selective absorber was used.
Cui et al. (2017)	Single-junction GaAs	Bismuth telluride	Experiment	13.45%	13.4%	Phase change material (PCM)	change material (PCM) was used.
Zhou et al. (2016)	DSSC	p-type Bi _{0.4} Sb _{1.6} Te ₃ , n-type	Experiment	9.08%	7.21%	Hybrid	efficiency was greater than TEG efficiency by 725.5%.

		$\text{Bi}_{2.85}\text{Se}_0$					
		$.15\text{Te}_3$					
Lamba et al. (2018)	Monocrystalline silicon	Bismuth telluride	Simulation	7.44 %	7.06 %	Maximum power output of the hybrid system was 595.5mW.	
Dallan al. (2015)	Monocrystalline silicon	Bismuth telluride	Experiment	13.2 %	8.05 %	PV and TE power output were $60.5\text{W}/\text{m}^2$ and $0.01\text{W}/\text{m}^2$ respectively.	
Kil et al. (2017)	Single junction GaAs	Bismuth telluride	Experiment	23.2 %	22.5 %	Solar concentration was 50 suns.	
Soltani et al. (2017)	Crystalline silicon	Bismuth telluride	Experiment	3.355 %	N/A	$\text{SiO}_2/\text{water}$ nanofluid cooling was used and power output was increased by 8.26% compared to natural cooling.	
Li et al. (2017)	CIGS	Bismuth telluride	Simulation	21.6 %	20.7 %	Concentration ratio was 200.	
	Thin film silicon	Bismuth telluride	Simulation	13.1 %	12.8 %	Concentration ratio was 200.	

CHAPTER 2 LITERATURE REVIEW

	Polymer	Bismuth telluride	Simulation	8%	7.47	Concentration ratio was 180.
Contento et al. (2017)	Amorphous silicon	Nanostructured Bi_2Te_3	Simulation	$\approx 57\%$ increase	N/A	$\approx 57\%$ increase and $\approx 42\%$ for directly and indirectly coupled systems respectively.
	Heterojunction CZTS	Nanostructured Bi_2Te_3	Simulation	$\approx 35\%$ increase	N/A	$\approx 35\%$ increase and $\approx 24\%$ for directly and indirectly coupled systems respectively.
Liu et al. (2017)	Perovskite	Bismuth telluride	Experiment	22.2%	9.88%	Ice bath was used for TE cooling and Air mass was 1.5.
Zhang et al. (2017)	Silicon	N/A	Experiment	N/A	N/A	Hybrid system achieved high absorption for wavelengths of 0.3-1.1 μm .
Machrafi et al. (2017)	Monocrystalline silicon	p- Sb_2Te_3 n- Bi_2Se_3	Simulation	25%	N/A	Thermoelectric nanoparticles were used, and optimum cooling velocity was 10m/s.

Jeyashree et al. (2017)	Polycrystalline silicon	Bismuth telluride	Experiment	N/A	N/A	Ice block was used for TEG cooling and hybrid system power output was 10.772W.
Nishijima et al. (2017)	Black silicon	N/A	Simulation	N/A	N/A	Ge-Sn layer was added to the solar cell and voltage increase of 7% was observed.
Babu et al. (2018)	Polycrystalline	Bismuth telluride	Simulation	6% increase	N/A	TEG contributed energy of 1-3% of PV rating.
Li et al. (2018)	InGaP/InGaAs/Ge triple-junction	Bismuth telluride	Experiment	33.53%	32.86	PCM and water cooling were used. Average efficiency was considered.

2.5.2 PV-TEG Study Type

Recently, there has been an increasing number of research works published relating to PV-TEG due to the high level of interest in such hybrid systems and its huge potential for enhanced performance compared to PV only systems. Some of the most recently published works on PV-TEG as at the time of writing this review are discussed in this section based on the type of study conducted. Generally, hybrid PV-TEG is usually studied experimentally or theoretically. The theoretical study also involves computational/numerical study.

2.5.2.1 Experimental Study

Mahmoudinezhad et al. (2019) presented an experimental study of the transient behaviour of a hybrid concentrating triple junction solar cell-thermoelectric generator system. Results obtained showed that the use of a thermoelectric generator in a hybrid system is an effective way to stabilize the overall power output of the hybrid system. In addition, the authors argued that geometry and material optimization are two effective ways to enhance the contribution of the thermoelectric generator to the overall hybrid system power output. Yin et al. (2019) performed an experimental investigation on the feasibility of a concentrated photovoltaic-thermoelectric (CPV-TE) system with phase change material (PCM) and the thermal resistance analysis of such hybrid system. Results obtained showed that the phase change material efficiently maintained the temperature of the PV cell in the hybrid CPV-PCM-TE to about 50 °C while the PV temperature in the hybrid CPV-TE system attained a high value of 80 °C. In addition, the results showed that the average power output of the hybrid CPV-PCM-TE system increased by 23.52% compared to that of the hybrid CPV-TE system.

The feasibility and optimization of a hybrid PV-TEG system was studied experimentally by Lekbir et al. (2019). Results from the experiment carried out showed that the maximum power output of the hybrid system was 0.12W and this was greater than that of the PV cell and TEG therefore, the hybrid system performed better under the same environmental conditions. Marandi et al. (2018) performed an experimental investigation of a hybrid PV-TEG system with a solar cavity receiver. A novel method to reduce re-radiation from PV panels by using cavity receiver was presented and the developed cavity hybrid PV-TEG system achieved a peak efficiency of 21.9%. Zhang et al. (2019) presented a unique structural arrangement for enhanced

performance of hybrid PV-TEG system. In the design, ceramic plates on the TE module were eliminated to enhance heat transfer by reducing thermal resistance and a V-type groove was used to enhance absorption of solar energy by keeping each PV cell in a perpendicular position to its adjacent PV cells. The authors performed an experimental investigation and found that the new TE structure enhanced the performance of the hybrid system. Some of the other experimental papers on hybrid PV-TEG system can be seen under the column ‘study type’ in Table 2.1 and Table 2.2 with their corresponding performance data.

2.5.2.2 Theoretical/Computational Study

Rodrigo et al. (2019) presented a theoretical study on the performance and economic limits of passively cooled hybrid PV-TEG systems. Results obtained showed that the optimization of the thermoelectric generator area is essential for keeping the cell operating temperature within acceptable limits. A detailed parametric study on the performance of a hybrid PV-TEG system using numerical simulation was performed by Lakeh et al. (2019). Results obtained showed that the electrical performance of the hybrid system in terms of maximum power output was highly dependent on the geometrical characteristics of the device.

Lekbir et al. (2018) performed a numerical investigation of a nanofluid based concentrated photovoltaic/thermal-thermoelectric generator (CPV/T-TEG) hybrid system with a cooling channel. Compared to the nanofluid based CPV/T, CPV and CPV-TEG with heat sink, the proposed hybrid system electric energy was higher by 10%, 47.7% and 49.5% respectively. Lorenzi et al. (2018) presented a model for determining the theoretical efficiency of a hybrid PV-TEG system for terrestrial application. The authors argued that there is an optimum operating temperature for obtaining maximum hybrid system efficiency and this temperature is not influenced

by the TEG geometrical dimensions and number of legs. Efficiency increase of 4-5% compared to PV only system was observed for the hybrid system.

Babu et al. (2018) also performed a theoretical investigation of an unconcentrated hybrid PV-TEG system using the MATLAB/Simulink environment. It was found that the hybrid system had an overall efficiency increase of 6% and additional energy projection of 5%. Motiei et al. (2018) performed a numerical simulation of a hybrid PV-TEG system using an unsteady, two dimensional numerical model. It was found that in the hybrid system, the PV conversion efficiency and electrical power output increased by 0.59% and 5.06% respectively compared to the PV only system. Similarly, Mahmoudinezhad et al. (2018b) studied the transient response of a hybrid CPV-TEG system. A numerical investigation was carried out using finite volume algorithm. The results showed that increase in thermal contact resistance leads to a decrease in efficiency of the TEG and CPV.

A rare three-dimensional numerical simulation of a PV-TEG was performed by Fallan Kohan et al. (2018). Electric power output in the hybrid system was modelled as an internal energy sink and finite volume method was used for the numerical simulation. It was found that under certain environmental conditions, the hybrid PV-TEG system generated more power than the PV only system. Zhou et al. (2018) developed a Multiphysics coupling mathematical model for studying the performance of a hybrid PV-TEG system. It was found that the power output density of the PV-TEG increased by 9.1% due to the optimization of the hybrid system heat transfer structure. Under the column ‘study type’ in Table 2.1 and Table 2.2, some of the other theoretical papers on hybrid PV-TEG system can be seen with their corresponding performance data.

2.5.3 Current Research Focus Areas

A plethora of studies on hybrid PV-TEG have been performed recently with each study addressing a particular area in the hybrid system research. This section presents some of the main research focus areas being explored by researchers on hybrid photovoltaic-thermoelectric generator and some niche applications of hybrid PV-TEG.

2.5.3.1 Concentrated Hybrid System

Vorobiev et al. (2006) presented a theoretical study of two different approaches for the thermal management of PV (Figure 2.11). In the first approach, the unabsorbed solar radiation from the semiconductor material of the PV was concentrated on a thermoelectric generator for further conversion into electrical energy thus, the PV operated at a low temperature. The second approach sees the PV cell operating at elevated temperatures while the thermoelectric generator is used to convert the excess heat. The only difference between both approaches is the position of the concentrator and PV.

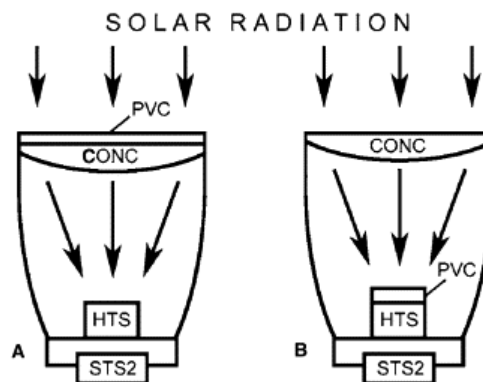


Figure 2.11: Schematic diagram of PV-TEG with PV operating at (A) low and (B) high temperatures (Vorobiev et al., 2006)

The basic elements of the systems shown in Figure 2.11 are; Concentrator (CONC), PV cell (PVC), Thermoelectric Generator/High Temperature Stage (HTS) and the 2-axis Solar Tracking System (STS2). The authors found that using the first

approach, the hybrid system obtained enhanced efficiency of 5-10% while the second approach didn't significantly improve the overall hybrid system efficiency. A drawback from this research is that an assumed high ZT value was used which is not currently practical.

Zhu et al. (2016) performed a detailed experimental and numerical investigation of the performance of a thermal concentrated hybrid PV-TEG system (Figure 2.12). A copper plate operating as the thermal concentrator and conductor was sandwiched between the PV and TEG and it increased the temperature difference across the TEG. Finite element simulation software, ANSYS was used to study the temperature distribution and water cooling was applied to the hybrid system. Results obtained showed that the use of the copper plate enhanced temperature uniformity and the efficiency of the hybrid system was about 23%. Lamba et al. (2018, 2016) performed a couple of investigations on concentrated PV-TEG systems. Results obtained showed that the power output of the hybrid PV-TEG system decreases due to Thomson heating when the Thomson effect is considered in the TEG analysis. It was found that Thomson effect significantly reduces the hybrid system power output especially for highly concentrated systems (Lamba and Kaushik, 2016). It was also observed that the TEG contributes more to the total hybrid system power output when higher concentration ratios are used. In addition, the hybrid system obtained a maximum efficiency of 7.44% which was 5% higher than that of the PV only system (Lamba and Kaushik, 2018).

An additional study on hybrid concentrated PV-TEG system was carried out by Rezanian and Rosendahl (2017). It was observed that the concentrated photovoltaic-thermoelectric (CPV-TEG) system using the current available thermoelectric materials ($ZT \approx 1$) had a better conversion efficiency compared to the CPV only system.

Recently, Mahmoudinezhad et al. (2018a) performed a feasibility study of a hybrid CPV-TEG system for low solar concentrations (Figure 2.13). An experimental and numerical investigation was carried out to study the performance of the hybrid system. It was found via the experiment that the maximum and minimum efficiency of the CPV were 35.33% and 23.02% respectively.

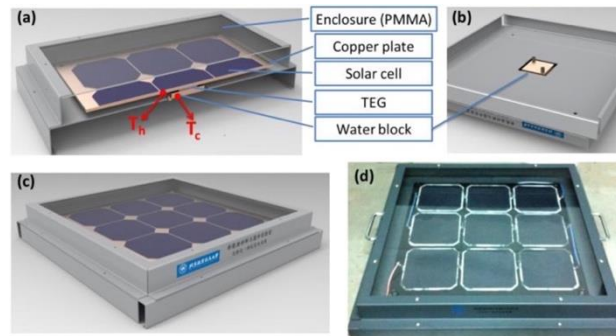


Figure 2.12: Hybrid PV-TEG (a) cross-sectional view, (b) bottom view, (c) global view and (d) physical diagram (Zhu et al., 2016)

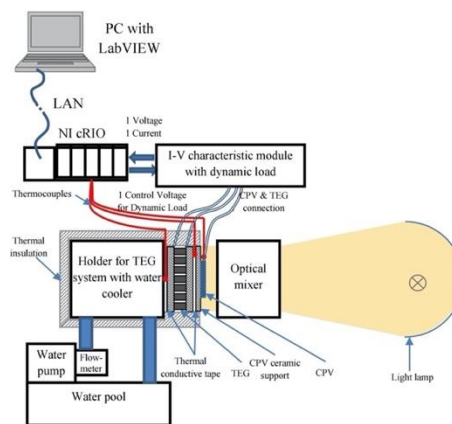


Figure 2.13: Schematic diagram of experimental PV-TEG setup (Mahmoudinezhad et al., 2018a)

2.5.3.2 Hybrid System Coupling

Effective coupling of the photovoltaic and thermoelectric systems can enhance the performance of the hybrid system and reduce losses. In fact, it is essential to perform a lossless matching of the two different systems (PV and TE) to obtain optimized efficiency results. In addition, a TEG possesses an internal resistance which

must be adequately matched with that of the PV so as to ensure the hybrid system performance is not worse than that of the individual systems. Park et al. (2013) performed the optimization of a hybrid PV-TEG system via lossless coupling and observed an efficiency enhancement of about 30% in the hybrid system compared to the conventional PV system. In addition, Lorenzi et al. (2018) analysed the effect of several parameters on the power output of an electrically coupled PV-TEG system. Results obtained showed that for solar cells with a small series resistance, the voltage needed for electrical lossless coupling was smaller.

Load resistance matching is another optimization technique to enhance the performance of the hybrid system. Successfully matching the internal resistance of the hybrid system with the external load resistance would ensure maximum power output is obtained. Li et al. (2018b) studied the inconsistent phenomenon of the thermoelectric load resistance in PV-TEG systems. Results obtained showed that the thermoelectric load resistance for maximum power output from the TEG alone, TEG in PV-TEG and PV-TEG are entirely different. Therefore, the authors concluded that using the optimum TE load resistance in a TEG only system for the analysis of a PV-TEG system would cause errors and prevent the attainment of hybrid system maximum power output. Lin et al. (2015) performed a similar research to (G. Li et al., 2018b) on hybrid PV-TEG load resistance matching. Results obtained showed that the maximum power output and maximum efficiency of the hybrid system could be obtained at the same operating current. In addition, hybrid system efficiency and power output of about 27% compared to the PV only system were observed.

The potential negative effect of PV-TEG coupling was presented by Lin et al. (2014). The authors placed emphasis on the coupling between discretized nodal temperatures and the hybrid system electrical power output. Results obtained showed

that for the specific parametric values chosen, the efficiency of the hybrid system was lower than that of the PV only system. It is therefore imperative to properly couple the PV-TEG for the achievement of enhanced overall efficiency rather than reduced efficiency when compared to the PV only system. Similar to (Lin et al., 2014), Bjørk et al. (2015) observed a negative effect of hybrid system coupling due to the reduced performance of the hybrid system compared to the PV only system. The authors found that only the hybrid system with amorphous silicon had an enhanced efficiency and power output compared to the PV only system. Contrarily, the hybrid system with the other types of PV considered had a worse performance than the PV only system. The explanation for this trend was that the PV performance degradation with increased temperature was much greater than the TEG power production due to the low efficiency of the TEG.

Hajji et al. (2017) deviated from the norm by presenting an indirect coupling of a hybrid PV-TEG system (Figure 2.14). Basically, in the directly coupled system, all the components were physically connected while for the indirect coupling, the optical concentrator had no direct physical contact with the PV and TEG. The developed system was properly insulated to reduce heat loss and it was observed that the indirect coupling method significantly improved the hybrid system overall efficiency. Adopting a similar approach as (Hajji et al., 2017), Contento et al. (2017) investigated the performance of an optically coupled (indirect) PV-TEG system using a vacuum-sealed compound parabolic concentrator and a thermally coupled (direct) PV-TEG system. Results obtained showed that direct coupling of hybrid PV-TEG system enables the achievement of large conversion efficiency while indirect coupling reduces the temperature of the PV thus, improving its reliability and lifespan.

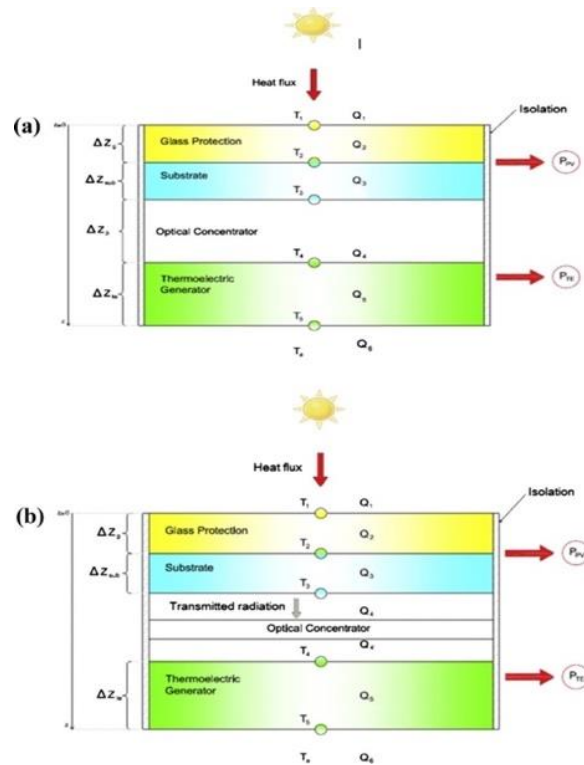


Figure 2.14: Schematic of PV-TEG system for (a) direct and (b) indirect coupling (Hajji et al., 2017)

2.5.3.3 Energy Storage

Due to the intermittent nature of solar radiation, it is sometimes necessary to add an energy storage unit to the hybrid PV-TEG system. The storage unit can help store thermal energy for use during periods of low solar radiation. Li et al. (2014) investigated the performance of a hybrid PV-TEG system with an energy storage unit (Figure 2.15). The thermal energy which was stored in the energy storage unit was used as the heat source for the TEG hot side. The authors argued that it is essential to store thermal energy for both heating and cooling reservoirs using phase change materials (PCMs) so as to maintain stable PV and TE operating temperatures. The results obtained showed an overall hybrid system efficiency enhancement of about 31-34% using thermoelectric materials with $ZT = 1$.

Figure 2.16. The main novelty of this study is the introduction of phase change material (PCM) into the hybrid PV-TEG system to maintain the system operating temperature. It was observed that the novel hybrid system had a higher efficiency compared to the PV only system due to the use of phase change material.

2.5.3.4 Thermoelectric Generator Cooling

Adopting a similar approach used by (Vorobiev et al., 2006), Willars-Rodríguez et al. (2017) performed an experimental investigation of a hybrid PV-TEG. The PV cells were operated in a cold area (≤ 310 K) while the cooling unit and the TEG were operated in a high temperature area (≤ 500 K). The reason for this arrangement is because the PV performs better at lower temperatures while the TEG requires high temperature for high performance thus, their separation into two areas (cold and hot) would enhance the performance. In addition, the TEG was cooled using the thermosiphon effect of running water while the hybrid system generated thermal energy was stored in the water tank. Results obtained showed that the hybrid system generated an electric power of 7 W and thermal power of 30 W.

Yin et al. (2017) investigated the performance of a hybrid PV-TEG system using three different cooling methods (Figure 2.17). Natural cooling, forced air cooling and water cooling were compared and the influence of optical concentration ratio, water velocity and thermal contact resistance were studied. Results obtained showed that a reduction in the cooling system thermal resistance could lead to enhanced heat flux to the TEG thus, improving its total power output. The effect of the cooling system on the performance of the hybrid system with different PV cells is shown in Figure 2.18. It is obvious that natural cooling (free cooling) is not suitable for concentrated hybrid systems due to its inferior performance compared to the other cooling methods. In addition, Figure 2.18 shows that water cooling is more effective

for hybrid systems than natural cooling and forced air cooling. Therefore, the authors concluded that water cooling is the most suitable cooling method for hybrid PV-TEG systems, especially highly concentrated systems.

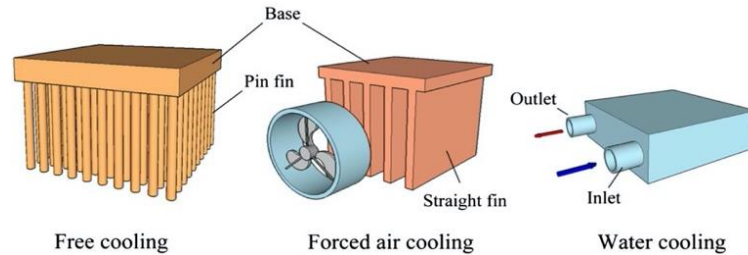


Figure 2.17: Different types of thermoelectric generator cooling systems (Yin et al., 2017)

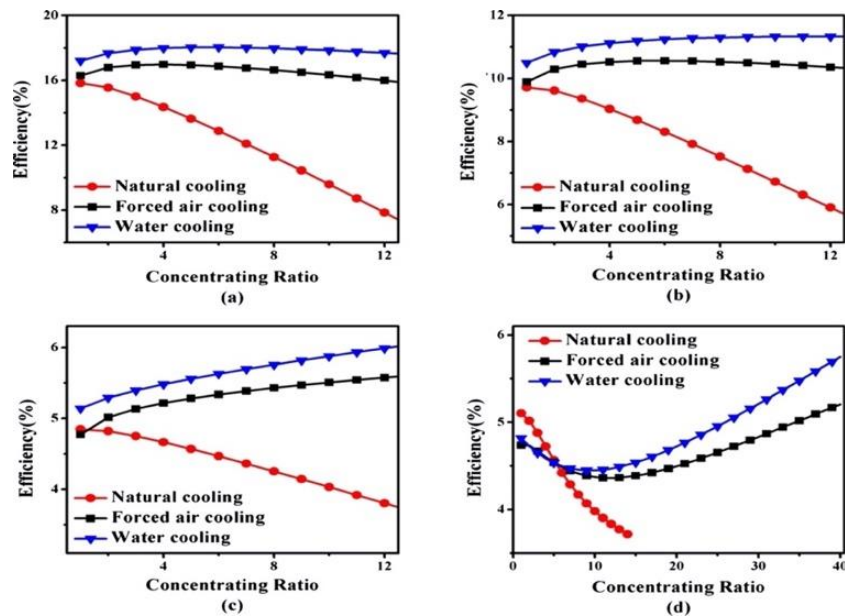


Figure 2.18: Hybrid system overall efficiency variation with concentration ratio for (a) crystalline silicon cell, (b) polycrystalline silicon cell, (c) amorphous silicon cell and (d) polymer cell (Yin et al., 2017)

Adopting a similar research objective as (Yin et al., 2017), Zhang et al. (2016) carried out a thermal resistance analysis of a concentrated PV-TEG system. In addition, the influence of the cooling system, thermal resistance and concentration were studied. Water and air cooling were applied to the hybrid system and the performance of the system was observed. It was observed that the insertion of a copper

plate between the PV and TE can decrease the thermal resistance between the systems as the copper plate improves the temperature uniformity and this is in agreement with (Zhu et al., 2016). Furthermore, the authors argued that the natural convection and radiation do not affect the performance of highly concentrated PV-TEG systems. Finally, water cooling was observed to be more suitable for highly concentrated PV-TEG systems compared to air cooling. This finding is in agreement with (Yin et al., 2017).

Pang et al. (2015) investigated experimentally, the significance of heat sinks in a hybrid PV-TEG system. Results obtained showed that the heat sink with natural convection cooled the PV-TE system by 8.29 °C which was 1.8 °C greater than that of the PV only system. However, the authors argued that the integration of thermoelectric into PV, amplified the fluctuation of the cooling performance of the hybrid system with heat sink. Compared to the conventional cooling methods like water and air, nanofluid was proposed as a more efficient cooling method for hybrid PV-TEG by Wu et al. (2015). The authors used a theoretical approach to investigate the performance of glazed and unglazed PV-TEG systems. It was found that the efficiency of unglazed PV-TEG is higher than that of the glazed PV-TEG when figure of merit $Z = 0.0021/\text{K}$. Finally, the results obtained showed that nanofluid cooling enhances the performance of PV-TEG systems compared to water cooling especially for the glazed system.

Soltani et al. (2017) investigated a new nanofluid-based cooling system for enhancing the performance of hybrid PV-TEG systems and an experimental comparison with conventional cooling systems was presented. The results obtained in terms of efficiency and power output enhancement are shown in Table 2.3. It was found that the performance of the TEG was mainly affected by the cooling system

while the PV cell's temperature was also influenced by the cooling system. The authors argued that nanofluid cooling performed better especially SiO₂/water nanofluid cooling which enhanced the efficiency and power output of the hybrid system by 3.35% and 8.26% respectively compared to the natural cooling.

Table 2.3: Power output and efficiency enhancement of hybrid system using different cooling systems (Soltani et al., 2017)

	Natural cooling	Forced cooling	Water cooling	SiO₂/water nanofluid cooling	Fe₃O₄/water nanofluid cooling
Total power	Base	4.885	5.776	8.26	6.284
increase (%)					
Total efficiency	Base	1.865	3.051	3.355	3.131
increase (%)					

2.5.3.5 Niche Applications

Yu et al. (2008) investigated a PV-TEG for powering wireless sensor networks. Compared to a single PV, the PV in the hybrid system had an efficiency increase of 5.2% due to a solar cell temperature reduction of 13 °C. Energy storage devices were incorporated into the hybrid system to store energy for use during periods of low solar irradiance. A lithium ion battery with storage capacity of 1400 mAh and an ultra-capacitor with storage capacity of 30 F were used to store energy from the PV

and TEG respectively. The developed hybrid system had the capacity to renew energy by itself thus it could provide reliable and long-time power to the sensor node.

Leonov et al. (2010) investigated the use of a PV-TEG to power an autonomous medical device: electroencephalography (EEG) in a shirt. The device was battery free and the PV was positioned about the radiators used to heat up the TEG (Figure 2.19). The authors developed an ultralow power biopotential readout integrated circuit which had a power consumption of $60 \mu W$ per channel. The signal quality provided by the readout was the same with that of modern ambulatory systems and the developed system had an extra advantage of being wireless compared to wired commercial systems thus, the biopotential signals could be transmitted to a doctor in real time.

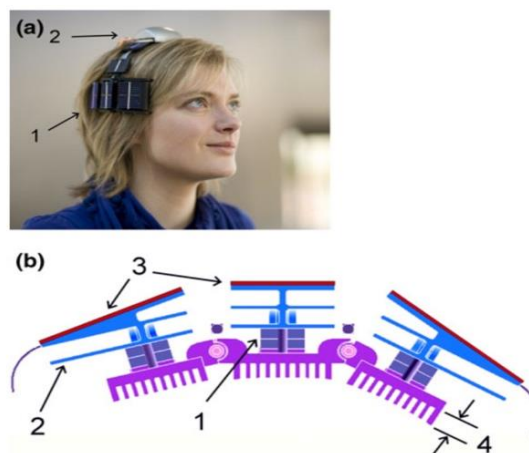


Figure 2.19: (a) Electroencephalography diadem: (1) right-side hybrid module, and (2) electronic module and 2.4 GHz wireless link. (b) Schematic cross-section of hybrid module: (1) thermophile, (2) radiator, (3) PV cells, and (4) thermal shunts (Leonov et al., 2010)

The feasibility of PV-TEG for terrestrial and space applications was investigated by Da et al. (2016). A similar approach used by (Xu et al., 2015) was employed in this study which is the use of photon and thermal management to enhance the performance of the hybrid PV-TEG system. Results obtained showed that for hybrid PV-TEG systems, low concentration ratio is better especially when used in

terrestrial and space applications. It was also found that for terrestrial application (corresponding to Air Mass 1.5), the overall hybrid system efficiency increased from 13.79 to 18.51% due to the use of the moth-eye structured surface. While for space application (Air Mass 0), the use of the moth-eye structured surface in the hybrid system increased the efficiency to 16.84%.

Kwan et al. (2016) studied the performance of a hybrid PV-TEG system for outer space application. Results obtained from this study showed that for space applications, the power generation contribution of the thermoelectric generator in a hybrid PV-TEG system is negligible. Furthermore, it was observed that single stage TEG is for hybrid PV-TEG systems compared to two stage TEG. Finally, the authors also argued that the optimized PV-TEG system had a lower efficiency compared to the PV only system. This finding is in agreement with other similar findings like (Lin et al., 2014) and (Bjørk and Nielsen, 2015). Ariffin et al. (2017) presented a conceptual design of a hybrid PV-TEG system for application in an automated greenhouse system project (Figure 2.20). The developed system was compared to conventional PV only system. They recommended the use of automated semi-transparent thin film solar panel to efficiently absorb solar radiation.

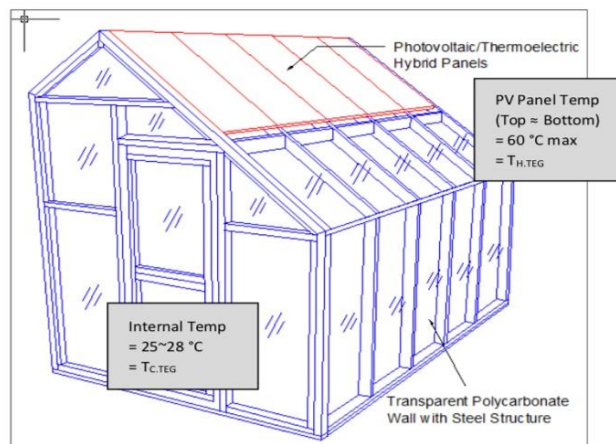


Figure 2.20: Conceptual design of a hybrid PV-TEG for automated greenhouse system (Ariffin et al., 2017)

2.6 Thermoelectric Geometry and Structure Optimization

Depending on the heat source and heat sink shape, thermoelectric devices could have different structures such as the conventional flat plate structure and annular structure. In addition, segmented structure can be adopted for high temperature applications. Furthermore, different geometries for the thermoelectric leg have been studied including conventional rectangular and asymmetrical geometries.

2.6.1 Thermoelectric Geometry

The four main parameters which are paid attention to during optimization of thermoelectric geometry are leg length/height, cross-sectional area, number of legs and leg shape.

2.6.1.1 Leg Length or Height

The thermoelectric leg length or height is an important parameter which can be optimized for performance enhancement of the thermoelectric generator. Optimization of thermoelectric leg length has been performed in flat plate, annular and segmented thermoelectric devices. In addition, the thermoelectric leg length has been optimized in a hybrid photovoltaic-thermoelectric system and enhanced performance was obtained. Min et al. (1992) found that a decrease in thermoelectric leg length by 55% caused a 48% increase in power output and a 10% decrease in conversion efficiency. Furthermore, Tian et al. (2015) presented a detailed parametric optimization of a segmented thermoelectric generator (STEG) for diesel engine exhaust waste heat recovery and the authors recommended the use of STEG rather than traditional TEG especially for applications with high heat source temperature. In addition, results revealed that the highest TEG efficiency and power output had,

respectively a linear and inverse relationship, with the thermoelectric leg length as shown in Figure 2.21.

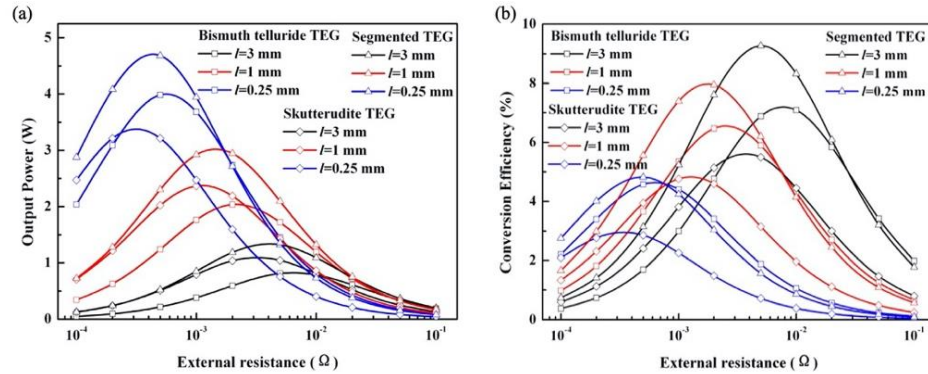


Figure 2.21: Effect of leg length on (a) output power and (b) efficiency for three different thermoelectric generators (Tian et al., 2015)

Zhang et al. (2015) optimized the leg length ratio of a STEG for power and efficiency enhancement and found the optimum leg length ratios for maximum efficiency and output power to be different. Ma et al. (2019) presented a detailed investigation on the optimization of STEG leg length ratio for engine exhaust heat recovery. It was found that the optimal proportion of medium temperature material (CoSb₃) increased with longer thermoelectric legs and increased coefficient of heat transfer however, the leg area showed hardly any influence on it. In addition, results revealed that the application of optimal segmented ratio design in the TEG provided an enhanced performance and increased the power output by 6.8%. Besides the optimization of thermoelectric leg length in flat plate and segmented thermoelectric devices, the idea of leg length optimization has also been utilized in annular thermoelectric devices. Shen et al. (2017) studied the performance (power output and efficiency) of an annular thermoelectric generator (ATEG) using a theoretical model and constant heat flux. They observed an increase in power output as thermoelectric leg length increased however, a reverse trend was observed under constant temperature condition. Zhang et al. (2018b) used a theoretical model to study the

interface layers' effect on ATEG performance and found that the interface layers negatively influenced the ATEG performance. Furthermore, they found that for ATEG with very short legs, the annular shape parameter significantly influences the ATEG performance.

Shen et al. (2018) investigated a segmented annular thermoelectric generator (SATEG) theoretically and a comparison with ATEG was presented. They found that the SATEG efficiency initially increased as the height ratios increased until it reached a maximum after which it decreased. The mechanical reliability and thermoelectric performance of SATEG was investigated by Fan et al. (2019). Results revealed that the SATEG output power increased initially before decreasing as the structural parameter increased. In addition, they found that the power output of the SATEG increased by 18.3% compared to that of the single-Skutterudite TEG. In a hybrid system like photovoltaic-thermoelectric (PV-TE), thermoelectric geometry optimization can enhance the hybrid system performance. Hashim et al. (2016) optimized the geometry of TE devices in a photovoltaic-thermoelectric system for output power enhancement. It was also found that operating the PV-TE in a vacuum greatly increased its output power and they recommended the use of thermoelectric modules which had a smaller area than the area of photovoltaic.

Li et al. (2019b) also optimized the geometry of TE in a PV-TE. They found that the efficiency of the hybrid PV-TE decreased as the leg height increased. Mahmoudinezhad et al. (2019) recommended TE geometry optimization in a PV-TE for output power enhancement. In addition, the authors performed a transient experimental and numerical study and found that the hybrid system thermal resistance increased with leg length. Recently, Cui et al. (2020) optimized the leg height ratio in a segmented photovoltaic-thermoelectric system and found that the optimized height

of the TE model which corresponds to the highest performance decreases with the height ratio of the upper to lower TE leg.

2.6.1.2 Leg Cross-Sectional Area

Another important parameter which could be optimized for enhancing the performance of the thermoelectric generator is the leg cross-sectional area. Lavric (2010) studied the sensitivity of TEG to geometry variation using a one-dimensional model and found that a higher power output can be obtained by using thermoelectric legs with larger cross-sectional area. Fan et al. (2016) found the optimal thermoelectric leg area for enhanced TEG power output. The authors argued that under specific thermal boundary conditions, the maximum power output can be obtained at an optimal leg cross-sectional area. In addition, they found that the thermoelectric conversion efficiency was almost constant at constant surface temperature boundary condition (case 4), while the efficiency was inversely proportional to the leg cross-sectional area at constant heat transfer coefficient boundary condition (case 5 and 6) as shown in Figure 2.22.

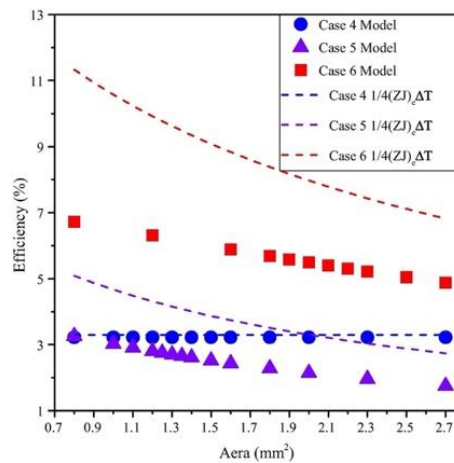


Figure 2.22: Conversion efficiency variation with leg cross-sectional areas (Fan et al., 2016)

He et al. (2019b) presented a comprehensive one-dimensional model for thermoelectric generator module geometric optimization based on the Hill-climbing

algorithm for power output enhancement. It was found that for any given leg length, the maximum power output always increases as the leg area increases. Furthermore, using a theoretical model, Zhang et al. (2018a) investigated the effect of the geometry of ATEG legs on system performance. Results revealed that the performance of the ATEG and flat plate TEG were similar when the TE leg cross-sectional area configuration was kept constant. In addition, results showed that the maximum power output per unit mass could be obtained only when the leg cross-sectional area is constant for the ideal ATEG. Cui et al. (2019) studied the potential of porous ATEG for utilization of waste heat and observed a superior performance from the porous ATEG compared to the bulk TEG. They found that the TEG output power had a linear relationship with temperature difference and an inverse relationship with cross-sectional area.

2.6.1.3 Number of Thermoelectric Legs

Dongxu et al. (2019) performed an experimental and numerical study on thermoelectric module geometry optimization for power output enhancement at a low cost. Results obtained revealed that the power output monotonically increases as the leg number increases due to the decrease in thermal and electrical contact resistances. In addition, they found that the efficiency first increases and then decreases as the leg number is increased. Furthermore, Hodes (2010) presented a method to optimize the thermoelectric leg number for obtaining maximum power output and conversion efficiency for a specified performance. Results showed that in refrigeration mode, the number of thermoelectric legs affects neither the performance or efficiency however, in generation mode, both the number of thermoelectric legs and height of thermoelectric legs must be optimized simultaneously when both power output and load resistance are specified. Liang et al. (2014) optimized a two-stage TEG and

compared it with a single TEG. They found that the absorbed heat and output power increased as the total number of thermoelectric legs increased however, the conversion efficiency decreased. The relationship between the total number of thermoelectric legs (M), number of thermoelectric legs in bottom stage (n), output power and efficiency of the two-stage TEG is shown in Figure 2.23. It was found that the increase of M caused an increase in the maximum optimum output power and a decrease in the conversion efficiency.

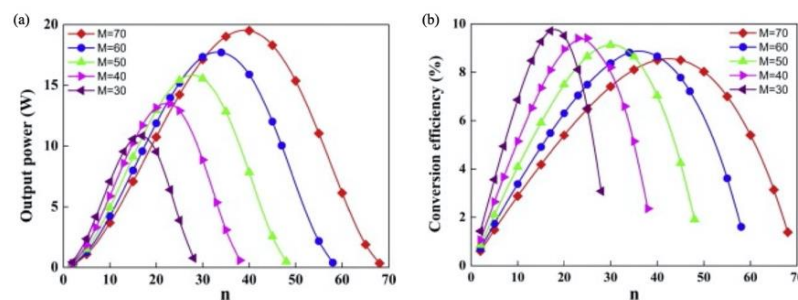


Figure 2.23: Relationship between number of legs and (a) output power and (b) conversion efficiency (Liang et al., 2014)

Yin et al. (2018d) studied the effect of leg number on the performance of a solar thermoelectric generator under non-uniform solar radiation. The authors argued that reducing the thermoelectric leg number is an effective method to increase the performance of a thermoelectric generator under non-uniform solar illumination. They found that under the same non-uniform solar radiation, the maximum power output increased by 73.5% when the leg number decreased from 32 to 18 and it increased by 244.9% when the leg number decreased from 32 to 8. Recently, Luo et al. (2020) recommended the use of more thermoelectric legs to achieve a greater power output from the TEG. In addition, they found that the maximum power output and maximum efficiency of the thermoelectric module with increased thermoelectric leg number increased by 1% and 1.2% respectively. Miao et al. (2020) analysed and optimized the mechanical stability of thermoelectric modules. They found that optimization of the

thermoelectric leg number can reduce the internal stress generated in the module and improve the working stability of the module. Furthermore, the effect of TE leg number on the PV-TE performance was investigated by Lakeh et al. (2019). A parametric study was performed, and they found that the PV-TE efficiency for any given length of arms would have an optimum range versus different number of TE legs.

2.6.1.4 Thermoelectric Leg Shape

The conventional thermoelectric legs are rectangular/symmetrical however, asymmetrical thermoelectric legs are being researched as a method to improve the transfer of heat in the legs and enhance the TE performance. In fact, the TE legs temperature gradient can be increased due to the reduction of the TEG overall thermal conductance which is achieved by using asymmetrical legs. Furthermore, asymmetrical thermoelectric legs usually have variable cross-sectional area resulting in a trapezoid shape. Sahin et al. (2013) studied theoretically, the effect of thermoelectric geometry on the performance of a TEG. A TEG which had variable cross-section legs was studied and they found that the trapezoid shape leg geometry significantly improved the TEG efficiency.

The influence of TE geometry configuration on the TEG performance was studied by Lamba et al. (2017). They found that the exergy and energy efficiency of the trapezoidal shaped TEG increased by 2.31% and 2.32% respectively. In addition, they found that the point at which highest output power was obtained was different from that at which the highest exergy and energy efficiency was obtained. Fabián-Mijangos (2017) investigated numerically and experimentally, thermoelectric generators with asymmetrical legs. Figure 2.24 shows the thermoelectric legs fabrication process while Figure 2.25 demonstrates the superiority of the asymmetrical legs in comparison to the symmetrical legs. This study provided the first experimental

proof of concept which showed the feasibility of asymmetrical thermoelectric legs for performance enhancement.

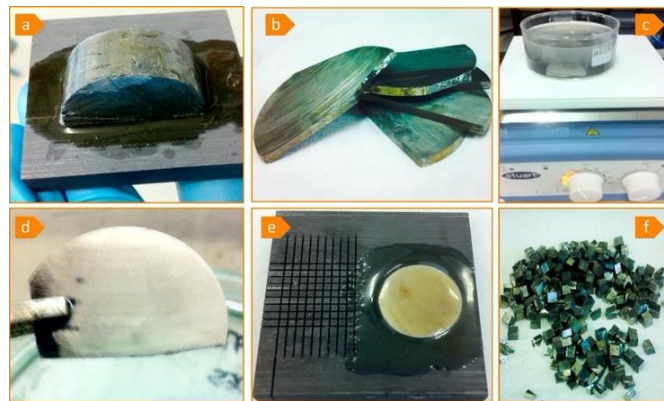


Figure 2.24: Fabrication steps for thermoelectric legs (Fabián-Mijangos et al., 2017)

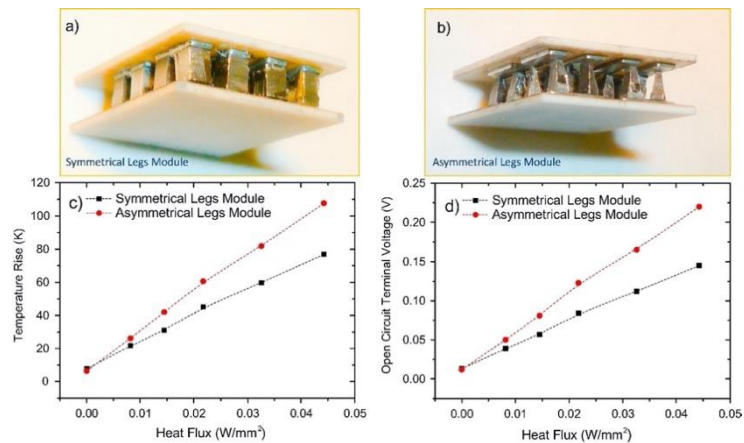


Figure 2.25: Fabricated module (a) with symmetrical legs (b) with asymmetrical legs (c) temperature difference (d) open circuit voltage (Fabián-Mijangos et al., 2017)

Liu et al. (2018) presented a novel solar thermoelectric generator design which had thermoelectric materials that were segmented and thermoelectric legs with asymmetrical geometry. They found that the use of asymmetrical legs with the segmented design enabled a 4.21% additional power output enhancement in comparison to the optimized segmented legs without asymmetrical geometry. Furthermore, a segmented asymmetrical TEG was studied by Karana et al. (2019) and they investigated geometric parameter effect on the system performance. The authors argued that due to advancement in the technology required to manufacture the TE legs,

the new unconventional shape of the TE leg could be made more cost effective. The power generation capability of the newly designed TEG was observed to be higher than that of the traditional TEG.

2.6.2 Thermoelectric Structure

This section presents a brief overview of the different thermoelectric structure currently being researched and some of the results obtained using these structures.

2.6.2.1 Flat Plate Thermoelectric Generator

The most common and conventional structure of a thermoelectric module is the flat plate as shown in Figure 2.26 (He et al., 2019b). As shown, a thermoelectric module consists mainly of ceramic substrate, copper electrode, solder layer and semiconductor thermoelectric legs which are usually connected in parallel thermally and in series electrically. Thermal and electrical contacts are usually present in a thermoelectric module with thermal contact existing between the copper surface and the ceramic surface while electrical contact occurs between the thermoelectric leg surface and the copper surface. The ceramic substrate provides thermal conductivity and electric insulation while the copper electrode provides the electrical connectivity. The solder layer connects the copper layer and thermoelectric legs while also helping to decrease thermal stress effect.

Luo et al. (2019) presented a novel thermoelectric module structure. A numerical and experimental study was carried out and results showed the new TE module structure had a superior performance than the traditional TE module using the same material quantity. He et al. (2015a) optimized the design of a TEG for use as an engine waste heat recovery system and argued that improved TEG performance can be achieved by optimizing the module area.

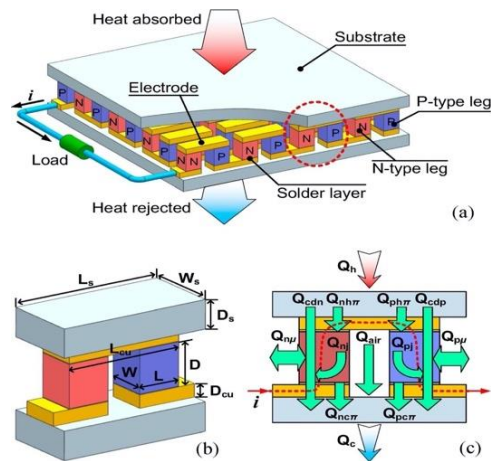


Figure 2.26: Schematic of (a) thermoelectric generator (b) thermoelectric uni-couple and (c) energy flow diagram (He et al., 2019b)

2.6.2.2 Annular Thermoelectric Generator

When circular heat sinks or heat sources are to be used, annular thermoelectric modules are beneficial as shown in Figure 2.27 (Zhang et al., 2018a). This is because they can eliminate any contact resistance resulting from mismatch of geometry. Applications with a radial heat flow or cylindrical heat source would require a different type of thermoelectric configuration besides the conventional flat plate thermoelectric configuration which would be unsuitable in such applications (Min and Rowe, 2007).

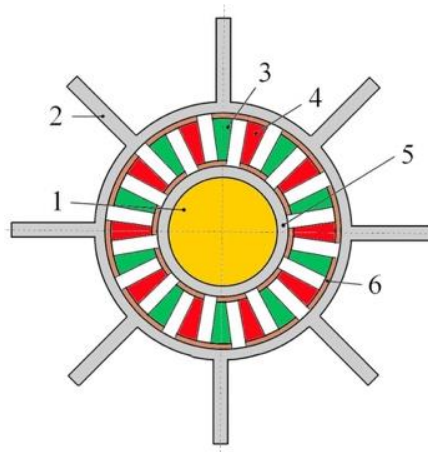


Figure 2.27: Schematic diagram of ATEG: (1) heat source (2) heat sink (3) p-type leg (4) n-type leg (5) ceramic (6) copper electrode (Zhang et al., 2018a)

Bauknecht et al. (2013) analysed the performance of annular thermoelectric couples under non-uniform temperature distribution. Results showed that uniform temperature distribution provides a better performance. Manikandan et al. (2016) analysed the performance of ATEG with solar heat pipe. They found that in addition to the solar ATEG providing better performance compared to the flat plate TEG, it also provides improved heat transfer characteristics. Furthermore, the authors argued that the new solar ATEG could be installed and maintained easily in comparison to the flat plate TEG due to its structure which is cylindrical in nature. Shen et al. (2015) presented a one-dimensional steady state model to analyse an ATEG performance. They found that the ATEG and flat plate TEG operate using similar fundamental formulas with the only difference being the total electrical resistance and thermal conductance expressions. In addition, when the annular shaped parameter is 1, the ATEG turns into a flat plate TEG.

2.6.2.3 Segmented Thermoelectric Generator

Since thermoelectric materials are only efficient in specific temperature ranges, the idea of segmented thermoelectric generator has attracted more interest recently. The reason for this is that materials that are highly efficient at specific temperature ranges can be combined due to segmentation. For example, highly efficient medium temperature range thermoelectric material (CoSb_3) can be combined with a low temperature range TE material with high efficiency (Bi_2Te_3). Consequently, the two materials will function in the temperature range in which they are most efficient thereby leading to an enhanced overall performance. However, not all thermoelectric materials are compatible (Ursell and Snyder, 2002) therefore, the compatibility factor must be considered because for a segmented thermoelectric, it is

the most important parameter as thermoelectric material properties are subject to change from one segment to another (Snyder, 2004).

Figure 2.28 shows the compatibility factor (s) for thermoelectric materials. When the relative current density ($u = J/\kappa\nabla T$) is equal to the compatibility factor ($s = (\sqrt{1 + zT} - 1)/\alpha T$), maximum conversion efficiency can be achieved (Snyder and Ursell, 2003). Consequently, segmentation will become inefficient if the compatibility factor differs by a factor of 2 or more (Snyder, 2004). Generally, spark plasma sintering (SPS) method is used to fabricate most non-segmented and segmented thermoelectric materials because it is less time consuming and it provides improved thermoelectric material performance (Sallehin et al., 2018).

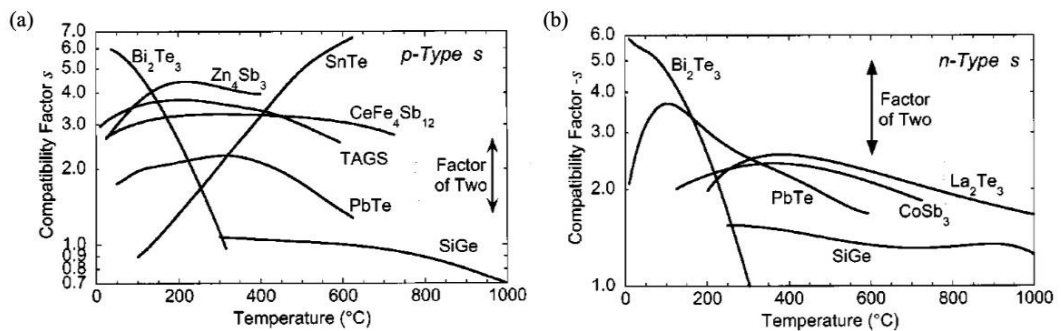


Figure 2.28: Compatibility factor (s) for (a) p-type and (b) n-type thermoelectric materials (Snyder, 2004)

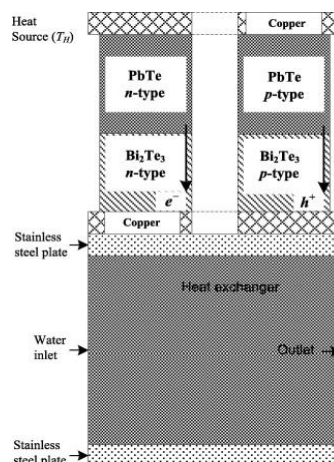


Figure 2.29: Schematic of STEG with active cooling heat exchanger (Hadjistassou et al., 2013)

Hadjistassou et al. (2013) presented a methodology formulated on computation and analytical modelling for designing highly efficient segmented thermoelectric generator (STEG) shown in Figure 2.29 and found that the STEG achieved a 5.29% maximum efficiency at a 324.6 K temperature gradient. Shu et al. (2018) analysed the STEG and TEG performance for diesel engine waste heat recovery. The results revealed a 13.4% increase in the solar thermoelectric generator maximum output power compared to that of the TEG. The authors recommended the use of STEG for waste heat recovery as it was more effective. The design of a STEG with high performance and with cost considered was presented by Ouyang et al. (2018). Different combinations of segmented thermoelectric legs were considered and the most efficient geometry with the best cost performance ratio were analysed. The thermoelectric figure of merit was argued by the authors as the top criterion to be considered when choosing TE materials.

2.6.3 Three-Dimensional Finite Optimization Method

A more accurate simulation could be obtained using three-dimensional modelling which also provides a better understanding of temperature distribution and heat transfer process in systems thereby enhancing performance predictions. Rezania et al. (2014) studied how thermoelectric footprint significantly affected the TEG performance. Finite element method (FEM) was used to perform the numerical study. Results revealed that when $A_n/A_p < 1$, maximum TEG output power and cost-performance could be obtained. Meng et al. (2016) presented a three-dimensional numerical study of helical TE module using finite volume method (FVM) and a comparison with conventional straight module was also presented. Comparing the helical module and straight module, they found that the power output of the helical

module was higher and the helical TEG power output and efficiency were positively influenced by increasing the pitch.

Ming et al. (2017a) studied a compact TEG numerically and analytically. The numerical study was conducted using ANSYS and results showed that the new compact TEG performed excellently. The authors argued that the newly designed TEG utilized space efficiently while maximizing output power; therefore it could be applied in areas such as automobile and aerospace. Ferreira-Teixeira et al. (2018) used FEM and COMSOL Multiphysics software to perform TEG geometric optimization. Cubic and cylindrical thermoelectric leg geometries were studied, and they observed an identical performance from both geometries under the same conditions. In addition, they observed an output power increase as the leg area increased and they recommended that the leg area and copper contact area should be the same for output power enhancement.

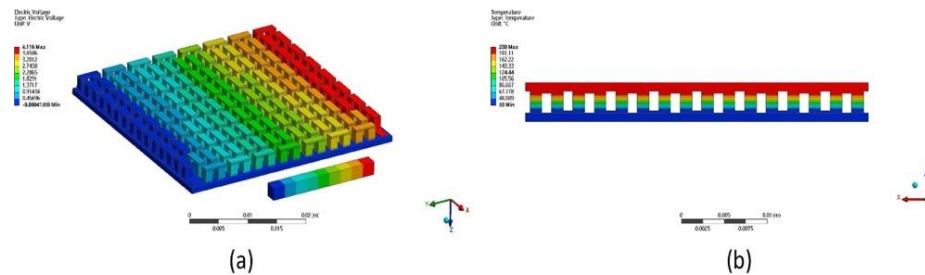


Figure 2.30: TEG (a) voltage and (b) temperature distributions (Liao et al., 2018)

Liao et al. (2018) presented a three-dimensional finite element model for a TEG with 127 thermocouples (shown in Figure 2.30) and an experiment was performed to validate the simulation. They found that both the temperature difference and maximum output power increased by 10.2% and 14.8% respectively by the use of TEG with fins in comparison to when fins were not used. Furthermore, Wang et al. (2019) optimized the geometry of a TEG and results showed that larger cross-sectional area ratio and lower leg height provided an enhanced power output. Lead telluride

thermoelectric material was used, and the authors argued that optimization of thermoelectric geometry was a very good approach to achieve performance enhancement.

2.6.4 Thermal Stress Optimization

Either in cooling/heating or power generation applications, the temperature difference in TE legs cause thermal stress due to the fact that the thermal expansion of the materials is different. Consequently, it is important to perform thermal stress analysis and optimization to provide information on locations of high stress in the legs. The main aim of thermal stress optimization study is to significantly decrease the thermoelectric legs thermal stress which in turn helps to increase the thermoelectric device life span. Clin et al. (2009) observed the high stress locations in the thermoelectric legs to be around the corners of the legs. Furthermore, they found that the stress at the thermoelectric leg corners could be reduced by soldering alloy plastic deformation. In addition, it was found that the distribution of stress in the thermoelectric legs was affected greatly by the boundary conditions and the mismatch of thermal expansion coefficient between the different materials in the TE module.

The effect of TE leg geometry on TEG thermal stress was investigated by Al-Merbati et al. (2013). Three different leg geometries were studied, and they found that TE geometry optimization could lower the stress developed in the thermoelectric legs greatly. The thermoelectric leg geometry shown in Figure 2.31 was found to provide the lowest thermal stress in the thermoelectric legs. Chen et al. (2013) used finite element method to investigate the stress developed in a bismuth telluride TEG and found that the use of elastic-plastic model provided a more accurate representation of the stress levels in the TEG compared to the linear elastic model. This is because in

the elastic-plastic model, copper and solder alloy undergo plastic deformation which reduces the stress level in the TEG.

Jia et al. (2014) estimated the mechanical performance of a STEG (Jia and Gao, 2014) and TEG (Jia and Guo, 2020). The effect of segment length on the TE materials maximum stress level was studied at different temperatures and results revealed the significant decrease in STEG stress due to the deformation of solder and copper (Jia and Gao, 2014). Furthermore, it was found that the maximum stress of TE legs occurs on the hot end face that contacts the welding strips and a reduction of thermoelectric leg length increases the maximum stress (Jia and Guo, 2020).

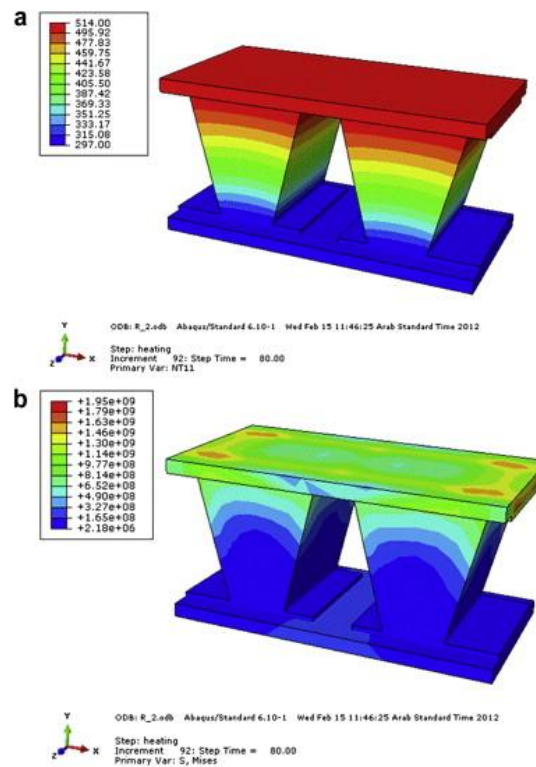


Figure 2.31: (a) 3D temperature distribution and (b) thermal stress distribution (Al-Merbati et al., 2013)

Erturun et al. (2014) presented a series of studies on the relationship between thermoelectric leg geometry and TEG mechanical performance. The results reveal a thermal stress of 43.3 MPa in the cylindrical legs and 49.9MPa in the rectangular legs

at a temperature difference of 100 °C (Erturun et al., 2014). Furthermore, it was found that the maximum TE legs stress decreased by 10% by the use of coaxial-leg configuration (Erturun and Mossi, 2015). In addition, the authors found that decreasing leg height, increasing leg width and spacing all led to an increase in thermal stress (Erturun et al., 2015). Ming et al. (2015) studied how heat flux with a non-uniform distribution affected the stress developed in a TEG (Ming et al., 2015) and STEG (Ming et al., 2017b). Results revealed that the TEG mechanical performance was negatively impacted by the non-uniform heat flux (Ming et al., 2015). In addition, it was found that an increase of heat concentration led to an increase in thermal stress (Ming et al., 2017b).

Fan and Gao (2018) studied the effect of geometric parameters on ATEG thermal stress. They found that increasing the thermoelectric leg angle ratio resulted in an initial stress decrease before it increased. In addition, results revealed the less impact of thermoelectric leg number on maximum stress in ATEG legs. It was also observed that the mechanical reliability of the ATEG could be improved by increasing the thermoelectric leg length although doing that will cause a decrease in the electrical performance of the ATEG. Ibeagwu (2019) performed a comprehensive investigation on the influence of variable leg geometry on TEG stress. The authors considered four different leg geometries and they found that the thermal stress in their new geometry was lower than that in the conventional geometries.

2.6.5 Finite Element Method

Finite element method (FEM) can be used to solve partial differential equations which are too complex to solve using analytical methods. Finite element method operates such that the spatial domain is broken up into a number of simple geometric elements such as triangles or quadrilaterals and a weighted residual concept

is then used to approximate the solution function over each finite element domain. The continuity of dependent variables and their first partials in moving from element to element must be ensured thus, partial differential equations are transformed into sets of ordinary differential equations in time (Ramirez, 1997). Furthermore, using finite element method for numerical solutions involves the discretization of a physical problem and the degree of discretization determines the accuracy of the solution. An example of the basic unit of a mesh-suitable finite element method is a triangle as shown in Figure 2.32 (Rapp, 2017). It can be seen from Figure 2.32 that the domain is subdivided into an arbitrary number of individual triangles which are indexed using Roman numerals while the corners of the triangles are indexed using Arabic numbers. In addition, regions where large changes of the dependent variable are expected should be resolved at a higher accuracy by using more and smaller triangles while regions where only slight changes are expected can be approximated using larger and few triangles (Rapp, 2017).

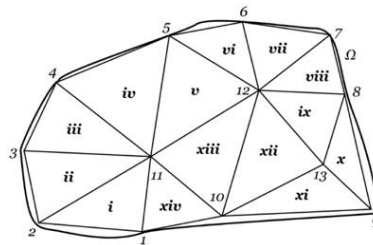


Figure 2.32: Mesh discretization used in finite element method (Rapp, 2017)

The finite element analysis process is shown in Figure 2.33 (Bathe, 2014). A physical problem is usually described with a mathematical model which would require certain assumptions that then produce a set of differential equations governing the mathematical model. Subsequently, finite element method is used to solve the mathematical model and the accuracy of the solution can be further enhanced by

refining solution parameters such as mesh size until the accuracy criteria are met (Bathe, 2014).

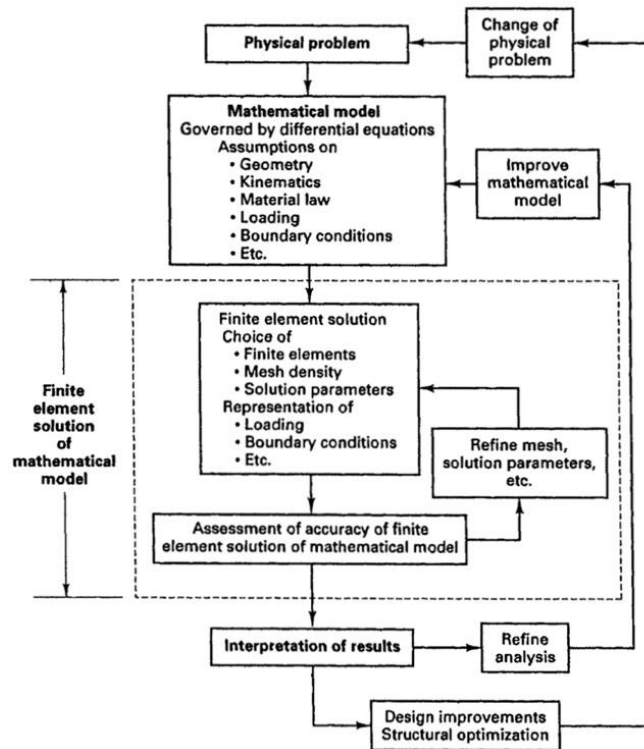


Figure 2.33: Finite element analysis process (Bathe, 2014)

2.6.6 Computational Procedure

The numerical study carried out in this research is performed using finite element method in COMSOL Multiphysics software and the simulation process is shown in Figure 2.34. Physical problems requiring multi-physics solutions can be solved using COMSOL which already has the governing equations for various physics inbuilt. The main steps involved in numerical simulation with COMSOL are briefly described below.

- 1) Geometry creation: This is the first step in the numerical simulation and in this research three-dimensional geometries are considered. The photovoltaic, thermoelectric generator and heat pipe geometries are created in COMSOL

while some of the innovative thermoelectric geometries studied are created in AutoCAD before being imported into COMSOL.

- 2) **Material selection:** Each domain in the model must be assigned a material corresponding to the physical entity being modelled. Materials can be assigned from the inbuilt material library in COMSOL while new materials can be assigned, and the values of the material properties can be modified as required. Furthermore, temperature dependent material properties can be assigned by using the interpolation function especially for thermoelectric material properties which are temperature dependent.
- 3) **Boundary conditions:** The initial and boundary conditions for the numerical model must be assigned before the model can be solved. Boundary conditions such as fixed temperature boundary, thermal contact, convective heat flux, radiative heat flux and fixed constraints can be assigned as required.
- 4) **Physics selection:** Depending on the system being studied, different physics interfaces are used together including heat transfer in solids and liquids, electric currents, laminar flow and electrical circuit. The Multiphysics considered are thermoelectric effect, electromagnetic heating and non-isothermal flow.
- 5) **Mesh creation:** Meshing is a very important part of the numerical solution using finite element method because it determines the accuracy of the model. Different mesh sizes can be used for different parts of the model geometry and COMSOL inbuilt mesh settings can be used to perform mesh independence test to ensure the numerical model converges.
- 6) **Study selection:** Different types of studies can be performed including stationary, time dependent/transient, eigenfrequency, eigenvalue and

frequency domain. In this research, stationary and transient studies are considered. After selecting a study, the relevant solvers are configured by COMSOL and the numerical model is solved by computing a solver configuration.

- 7) Postprocessing: Postprocessing tools help to understand the results obtained from the solved numerical model. The specific required results including temperature, voltage, current and von Mises stress must be extracted from the generated simulation results. In addition, three dimensional plots can be used to visualise the temperature, voltage and thermal stress distributions.

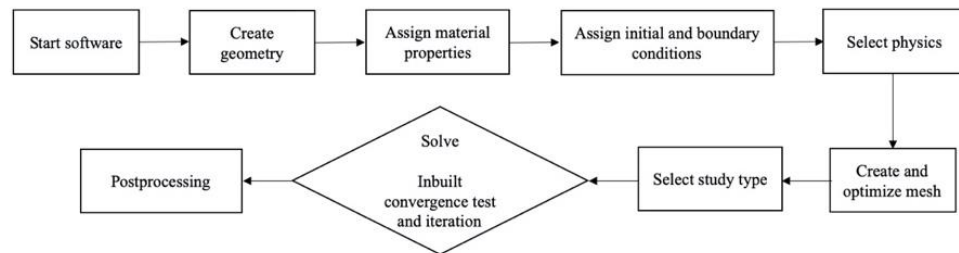


Figure 2.34: Simulation process in COMSOL

2.7 Discussion and Recommendations

This section presents a summary of the research achievement, research gaps and challenges, potential opportunities in the development of hybrid PV-TE systems and added value of present research relative to the current state-of-art.

2.7.1 Summary of Research Achievement

Several researchers (Li et al., 2019b; Mahmoudinezhad et al., 2019) have agreed that the performance of a thermoelectric generator in a hybrid system can be enhanced by material and structural optimization. A lot of material optimization efforts are being carried out on improving the efficiency of the PV and TE. Some of this research have obtained significant results as presented above. Improving the

thermoelectric figure of merit is the major research task for increasing the efficiency of the TE. A 50% increase in hybrid system efficiency could be achieved simply by using TEG with a higher figure of merit compared to the currently available ones (Van Sark, 2011). The use of nanostructured materials has also been gaining momentum recently due to the good results obtained thus, more research is encouraged on hybrid PV-TEG systems with nanostructure materials. In addition, more research is encouraged in the area of PV surface absorptivity. Increasing the absorptivity of PV could significantly increase its efficiency thus, more research on photon management of hybrid PV-TEG is highly recommended.

In spite of the plethora of research available on TEG optimization, its integration with PV necessitates new investigations be made due to the complex relationship between the PV and TEG. While one requires more temperature for higher performance (TEG), the other system (PV) prefers the opposite. Thus, more research on the efficient coupling of PV-TEG is needed especially considering the thermal contact resistance in the hybrid system. In addition, a lossless coupling would be very good for the hybrid system performance and it is very important to remember that results obtained from TEG only optimization is not sufficient for the hybrid system optimization. Therefore, the optimized load resistance and geometry of the TEG in a TEG only system is different from the one in a hybrid system due to the influence of the PV.

Due to the intermittent nature of solar energy, storage systems have been incorporated into the hybrid PV-TEG to store energy for use during periods of low irradiance. The use of phase change material (PCM) seems to be the best option due to its unique capability to store a significant amount of heat and thus mitigate the temperature fluctuations in the hybrid system. More research on the hybrid systems

with PCM is suggested however, again the extra cost must be considered. A limiting factor to the enhancement of hybrid system performance is the need for opportunity cost analysis. While there are obvious ways to easily improve the performance of the system, a trade-off must be made due to the high cost of such optimization. The use of concentrated solar energy is an easy way to improve the hybrid system efficiency however, care must be taken not to damage the PV by over applying high concentration. It is widely known that the performance of the PV reduces with temperature however, when high concentration is properly applied, the overall performance of the system could be increased. Thus, there is a need to properly determine the concentration ratio for optimized performance.

Thermoelectric geometry and structure optimization are hot research fields currently being paid a lot of attention due to the huge potential for performance enhancement. Regarding the optimization of thermoelectric leg length or height, it has been reported that the thermoelectric generator efficiency and power output have a linear and inverse relationship respectively, with the thermoelectric leg length. Furthermore, the optimum leg length ratios for maximum efficiency and output power in a segmented thermoelectric generator have been reported to be different. Therefore, optimizing the thermoelectric leg length for linear enhancement of power output and efficiency of TEG and STEG is a main issue which should be paid more attention in future. While the efficiency of a thermoelectric generator increases as the leg length increases, the hybrid photovoltaic-thermoelectric system efficiency decreases as the leg length increases.

2.7.2 Research Gaps and Challenges

Effective thermal management of photovoltaic (PV) with thermoelectric generator (TEG) typically requires the use of several thermoelectric generators to

completely cover the back surface of the photovoltaic in the direct coupling method. However, this is not cost effective as thermoelectric generators are expensive. In addition, the integration of thermoelectric generators to the back surface of the photovoltaic will enhance the heat extraction and improve thermal management however, the power generation cost will be increased because of the increased amount of thermoelectric generators needed to cover the photovoltaic back surface. Furthermore, the optimal operation of PV-TE systems depend on effective heat transfer from the photovoltaic to the thermoelectric generator thus, the PV and TEG must be thermally matched and the thermal resistances must be adjusted properly to ensure optimal hybrid system performance.

Cooling is an integral part of any TEG system as it directly affects the system performance significantly. Therefore, the hybrid PV-TEG system needs efficient cooling systems capable of creating a larger temperature difference across the TE while also reducing the temperature of the PV. Although there are several cooling systems currently available including free air, forced air, water and nanofluid cooling, the cooling and cost effectiveness must be considered before the cooling system is selected. Furthermore, very few research works on hybrid PV-TEG systems have been conducted with the use of three-dimensional finite element method (FEM). Contrarily, there is an abundance of research on the one-dimensional simulation using MATLAB/Simulink and two-dimensional simulation. Three-dimensional simulation provides greater information on temperature distribution in the system and it provides more accurate prediction of the actual system performance.

Results from thermoelectric geometry optimization in a thermoelectric generator only cannot be used as reference for TE geometry optimization in hybrid PV-TE systems due to the complex relationship between the photovoltaic and

thermoelectric generator therefore, new optimization studies need to be carried out. Furthermore, while a lot of attention has been paid to improving the conversion efficiency and power output of thermoelectric generators through geometry optimization, the mechanical performance (thermal stress) optimization has been neglected. Finally, the main drawback of all the interesting research being carried out on thermoelectric geometry optimization is the lack of experimental results to validate the numerical results and performance enhancement being predicted. There are few to none experimental research available on the effect of thermoelectric geometry on electrical and mechanical reliability of TEG.

2.7.3 Potential Opportunities in the Development of Hybrid PV-TE Systems

Passive cooling of photovoltaic-thermoelectric generator is an interesting research area being explored due to the effectiveness of passive cooling devices like heat pipe in significantly reducing the temperature of photovoltaic cells. Heat pipes are efficient heat transfer devices that can transport heat over a long distance with a small temperature gradient (Makki et al., 2016). Therefore, the use of heat pipes in a hybrid PV-TEG system could reduce the quantity of TEG used in the thermal management of photovoltaic cells while also providing an enhanced overall performance (Li et al., 2016b). Flat plate microchannel heat pipes are more efficient than cylindrical heat pipes because of the reduced thermal contact resistance between the surface of the PV and heat pipe due to the shape of the heat pipe. Therefore, more research on the integration of hybrid PV-TEG with flat plate microchannel heat pipes are strongly recommended especially because of the encouraging results reported from such heat pipe hybrid systems by (Li et al., 2016b; Makki et al., 2016).

From the detailed review carried out, the consensus is that water cooling is more effective than air cooling. However, the introduction of nanofluid cooling into

hybrid PV-TEG systems has resulted in significantly lower temperature on the TEG cold side compared to water cooling therefore, more research on PV-TEG using nanofluid is suggested. Nevertheless, the extra cost of nanofluid must be taken into consideration and a justification must be made in terms of overall performance compared to hybrid systems with cheap conventional cooling. More research on PV-TE using a three-dimensional finite element method is recommended instead of one-dimensional and two-dimensional simulation methods. The advantage of using FEM is that it can be used for three-dimensional study of the actual system. Thus, it provides more realistic results and better optimization efforts can be made using this method. Finite element method has Multiphysics capability thus it is highly suggested for deep research on hybrid PV-TEG. In addition, FEM allows the Thomson effect and temperature dependent thermoelectric properties to be easily coupled and it provides a user-friendly interface for easy visualization of results.

Furthermore, it was reported that the optimum leg cross-sectional area in a thermoelectric generator and hybrid photovoltaic-thermoelectric system is different. This difference is due to the presence of the photovoltaic in the hybrid system which contributes the greater percentage of the hybrid system efficiency and power output. Consequently, it is recommended to perform leg length and leg cross-sectional area optimization in both a thermoelectric only device and a hybrid system as the results might be different. In addition, more studies on the combined effects of thermoelectric leg length, area, number and shape on thermal stress in a thermoelectric generator are recommended. Only a few research has been conducted on spectrum splitting PV-TEG however, sufficient works have been done on direct coupling PV-TEG system. It is therefore recommended that more attention be paid to spectrum splitting hybrid systems due to their potentially high performance when properly optimized. A

profusion of literature exists on the steady state performance of hybrid PV-TEG systems however, the actual performance of the hybrid system is affected by the daily variations in weather conditions. Thus, more research is needed on the hybrid system performance under transient conditions.

Three-dimensional finite optimization studies are very important as they provide more information about temperature distribution in TEG as well as providing more accurate results close to real values. More three-dimensional parametric studies are encouraged for optimizing the TE geometry for the different geometry and structure types. Multi-objective optimization is an efficient method to perform comprehensive and simultaneous optimization of various thermoelectric geometry parameters. The combination of three-dimensional finite optimization and multi-objective optimization is very important and significant as it combines the advantages of each of the individual optimization methods. Therefore, research on combined three-dimensional and multi-objective optimization of TEG geometry for electrical and mechanical performance enhancement is recommended. Another major future research direction is experimental investigation of various thermoelectric geometries for electrical and mechanical performance enhancement.

2.7.4 Added Value of Present Research Relative to the Current State-of-Art

Considering the results from the detailed literature review carried out and the future potential opportunities in the development of hybrid PV-TE systems, this research will address the following aspects: (1) reducing the quantity of thermoelectric generators needed and cost of the hybrid system by the use of a flat plate microchannel heat pipe which also increases the heat transfer in the system by reducing thermal resistance; (2) using water cooling for the TEG cold side due to its better cooling and cost effectiveness, while the hybrid system feasibility for co-generation of electricity

and hot water is demonstrated; (3) developing detailed three-dimensional simulation models using finite element method to predict and optimize the performance of the hybrid PV-TE system with and without flat plate heat pipe; and (4) performing thermoelectric geometry optimization in a thermoelectric generator only and hybrid PV-TE system while also considering the mechanical performance optimization of TEG. These works are intended to enhance the development of a new hybrid PV-TE system and fill some of the gaps identified from the literature review. The research results will contribute significantly to the development of the hybrid PV-TE systems.

2.8 Chapter Summary

Owing to the fast rate at which the field of PV-TEG is growing and the numerous significant research being carried, this review was written to present and discuss the state-of-art in the field of PV-TEG. This review presented an explanation of basic operating principles of the technologies considered. In addition, a detailed overview of all research areas and optimization efforts relating to hybrid PV-TEG was provided. Key focus areas in the hybrid system research such as: concentrated hybrid system, hybrid system coupling, energy storage and TEG cooling were all discussed in detail. Niche applications of PV-TEG were also presented to show its wide applicability in various fields and not just electricity generation.

Optimization of thermoelectric generator is a key research objective to increase its conversion efficiency. This review also presented an in-depth analysis of thermoelectric geometry and structure optimization. The main significance of geometry and structure optimization is that quantity of material needed for optimum performance could be reduced thereby providing a dual function of increasing efficiency and reducing material cost. The four main parameters including leg length

or height, cross-sectional area, number of legs and leg shape which are paid attention to during optimization of thermoelectric geometry were discussed in detail.

In addition, a review of the different thermoelectric structure currently available was provided including flat plate, annular and segmented thermoelectric generators. Furthermore, three-dimensional finite optimization method was discussed. An in-depth review of thermal stress optimization studies was presented and the effect of thermal stress on mechanical reliability of thermoelectric generators was discussed. Finite element method was explained and the computational procedure using COMSOL Multiphysics software was presented.

Finally, a thorough investigation of hybrid PV-TEG systems and thermoelectric geometry optimization has been presented in this chapter in addition to recommendations for future research. It is envisaged that this review would serve as an indispensable literature on hybrid PV-TEG and thermoelectric geometry optimization.

CHAPTER 3 CONCEPTUAL DESIGN, MATHEMATICAL ANALYSIS AND SIMULATION MODEL DEVELOPMENT

3.1 Chapter Introduction

This chapter presents the conceptual design of the proposed hybrid photovoltaic-thermoelectric-flat plate microchannel heat pipe (PV-TE-MCHP) system for electricity generation and the computer simulation models for the hybrid system and individual components. The following tasks are addressed in this chapter:

- 1) Presenting the design of the PV-TE-MCHP system including sketch drawings.
- 2) Describing the basic operating principle and mathematical equations of the hybrid system.
- 3) Describing the components and dimensions of the hybrid system.
- 4) Simulating and analysing the performance of the system under steady state and transient conditions.

The conceptual design and computer simulation models presented in this chapter will provide the foundation for the research methodology which includes numerical simulation and experimental study.

3.2 System Design

The proposed hybrid system incorporates three main components including photovoltaic, thermoelectric generator and heat pipe as shown in Figure 3.1. The heat pipe is used for thermal management of the photovoltaic therefore it is placed directly behind the PV module while the thermoelectric generator is used for additional

electrical power generation thus, it is placed at the condenser section of the flat plate microchannel heat pipe. Furthermore, as shown in Figure 3.1a, the photovoltaic module is attached to the top surface of the heat pipe evaporator section therefore, the accumulated heat at the rear surface of the PV is extracted by the heat pipe thereby cooling the PV and improving its efficiency. Figure 3.1b shows the system design in three-dimension however, a single PV cell is shown instead of the actual four PV cells in the module which are shown in Figure 3.1a. This is because the drawings are to scale thus to ensure the components of the system are clearly seen, the figure is cut and just one PV cell is shown.

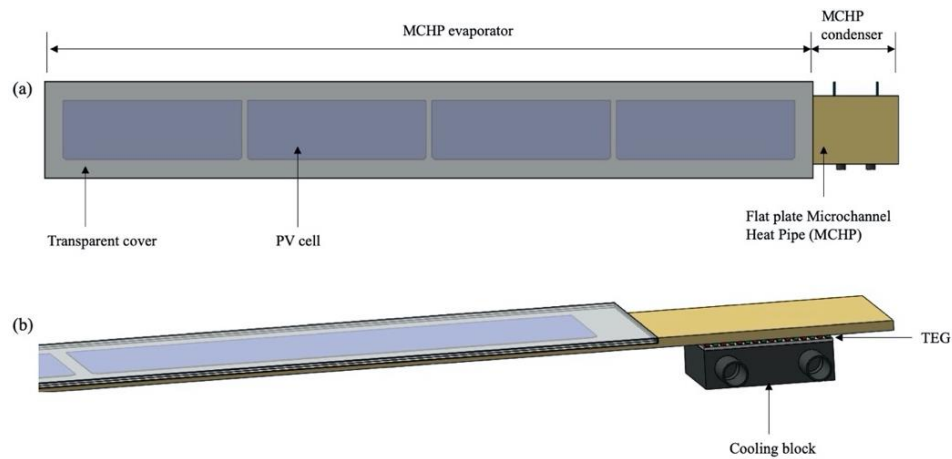


Figure 3.1: Schematic diagram of PV-TE-MCHP system in (a) 2-dimension and (b) 3-dimension

The proposed system can be divided into two main parts including the PV-MCHP and TEG-cooling block as shown in Figure 3.2. In this study, the effect of back surface insulation is considered therefore, the insulation layer which covers the back surface of the photovoltaic and flat plate microchannel heat pipe is shown in Figure 3.2a. Thermal insulation is placed at the back surface of the PV-MCHP to minimize thermal losses. In addition, the experimental study carried out in this research which will be presented in subsequent chapters considered the effect of back surface insulation on the hybrid system performance thus, results were obtained for the case

with and without insulation. Furthermore, the second part of the hybrid system is the TEG-cooling block which is shown in Figure 3.2b. Water cooling is used in this study due to its superior performance compared to air cooling as observed from the literature review conducted. Therefore, a cooling block which has an inlet and outlet was placed on the cold side of the thermoelectric generator to ensure sufficient temperature difference is maintained across the sides of the thermoelectric generator. The inlet and outlet of the cooling block are connected to the water tank via water pipes and a small pump for constant circulation. The external wires of the thermoelectric generator are connected to an external load resistance where voltage and current can be measured and thus, the TEG power output is obtained.

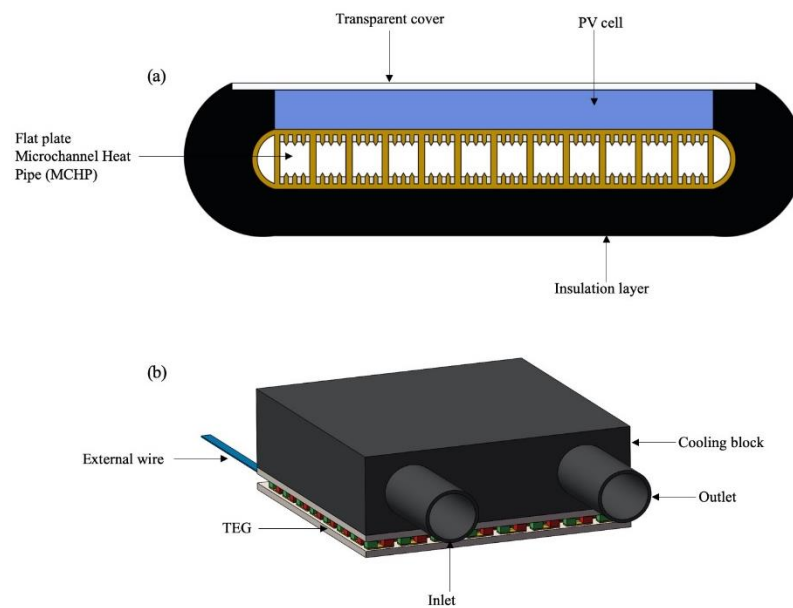


Figure 3.2: (a) PV-MCHP layout with back surface insulation and (b) TEG-cooling block layout

The incorporation of the thermoelectric generator and water-cooling block on the condenser section of the flat plate microchannel heat pipe is shown in Figure 3.3. The heat extracted from the PV back surface which is attached to the upper surface of the MCHP evaporator section is transferred via the vapour-condensation process to the condenser section of the heat pipe where the thermoelectric generator is attached.

As shown in Figure 3.3, the hot side of the TEG is attached to the lower surface of the MCHP condenser section which provides the heat input while the cooling block is attached to the cold side of the TEG to maintain a temperature difference. The thermoelectric generator utilizes the temperature difference to generate electricity directly thereby increasing the electrical output of the hybrid system.

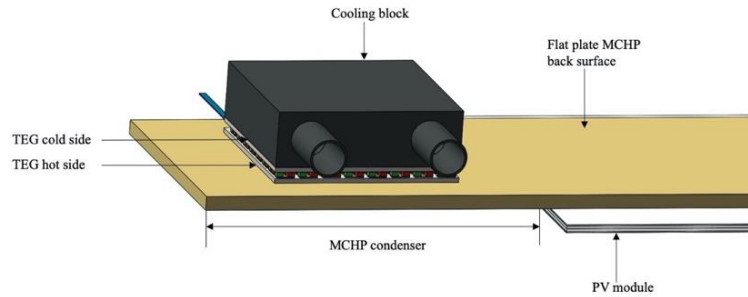


Figure 3.3: Layout of waste heat recovery system attached to MCHP condenser section

3.2.1 Research Questions

The following research questions are envisaged to be answered in this research:

- 1) What is an effective strategy to reduce the quantity of thermoelectric generators needed for effective photovoltaic thermal management?
- 2) What are the performance improvements achievable through the use of a thermoelectric generator and a flat plate heat pipe for photovoltaic thermal management?
- 3) What is the feasibility of the hybrid system for co-generation of electricity and hot water?
- 4) What is the optimum thermoelectric geometry in a thermoelectric generator only and hybrid photovoltaic-thermoelectric for performance enhancement?

3.2.2 Potential Solutions

Based on the research questions proposed, the following potential solutions will be explored:

- 1) A novel conceptual hybrid photovoltaic system with a single thermoelectric generator and flat plate microchannel heat pipe (MCHP) will be designed.
- 2) A PV-TE-MCHP prototype will be set up and tested under laboratory conditions to investigate the performance of the hybrid system in terms of overall system efficiency and power output.
- 3) Heat removed from the thermoelectric generator cold side will be recirculated into the water tank to increase the water temperature while the system generates electricity.
- 4) Thermoelectric geometry optimization will be performed in a thermoelectric generator only and in a hybrid PV-TE system using validated three-dimensional simulation models.

3.3 Operating Principle

This research is on solar energy harvesting therefore, solar energy is used as the input energy source. Solar radiation is impinged on the PV module and it is transmitted via the transparent cover of the PV and absorbed mainly by the photovoltaic cells. The PV cells convert part of the absorbed solar radiation into electricity directly via the photovoltaic effect while the remaining solar radiation is accumulated as waste heat at the back surface of the PV. As a result of the low conversion efficiency of most photovoltaic, a large part of the solar radiation is converted into waste heat while only a small part is converted into electricity. In addition, the increase in temperature of the photovoltaic causes a decrease in its

efficiency therefore, cooling of the PV is essential. Furthermore, the accumulated heat at the PV back surface will be transferred to the MCHP evaporator section since they are attached together. Subsequently, the absorbed heat vaporizes the working fluid inside the flat plate MCHP and this vaporized heat is transferred to the condenser section of the microchannel heat pipe. At the condenser section, condensation of the vapor occurs therefore, the latent heat of vaporization is released to the attached thermoelectric generator. Since a water-cooling block is attached to the TEG cold side, a temperature difference is achieved across the TEG due to the heat from the MCHP condenser and the water cooling at the bottom of the TEG. Therefore, the TEG generates additional electricity via the Seebeck effect.

3.4 Components and Dimensions

The main components of the hybrid system are described in this section including photovoltaic module, flat plate microchannel heat pipe, thermoelectric generator, cooling block and water tank. In addition, the dimensions of these components are provided.

3.4.1 Photovoltaic Module

The photovoltaic module considered in this research is shown in Figure 3.4. It consists of five layers as shown in Figure 3.4a which are laminated together to form a module. The top surface of the PV is the transparent cover sheet which is a transparent tedlar polyester tedlar (TPT) in this research. The PV used in this research is unglazed therefore instead of a glass cover, a transparent TPT is present at the top surface. The transparent TPT helps to prevent accumulation of dust and enhance solar radiation transmission to the solar cells because of its high transmittance and low reflectance. Furthermore, the ethylene vinyl acetate (EVA) is used to encapsulate the solar

photovoltaic cells therefore the EVA is present on top and bottom of the PV cells while it provides adhesion between the solar cell, transparent front cover and back sheet. The photovoltaic cells used in this research are crystalline silicon cells which absorb the solar radiation and generate electricity via the photovoltaic effect. There are four PV cells in the PV module used in this research as shown in Figure 3.4b. Furthermore, the TPT back sheet provides durability and reliability for the PV module under extreme weather conditions. The dimensions of the PV module and PV cell in millimetres are shown in Figure 3.4b and the height of the PV module is 2 mm.

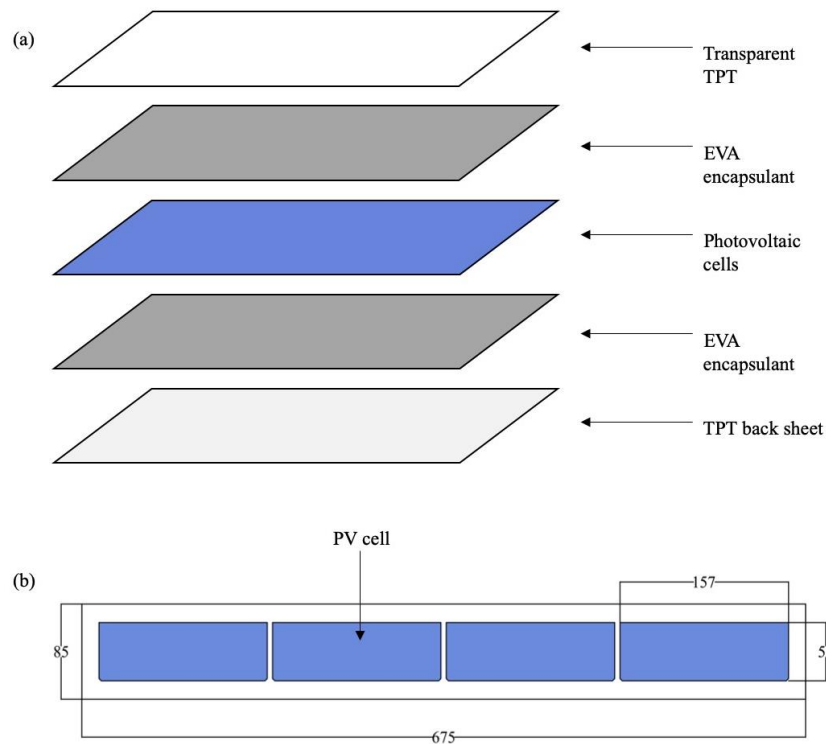


Figure 3.4: Photovoltaic module (a) layers and (b) dimensions

3.4.2 Flat Plate Microchannel Heat Pipe

The flat plate microchannel heat pipe used in this research is shown in Figure 3.5. The advantage of using a flat plate structure is that it can easily be integrated with the photovoltaic module which also has a flat structure thereby eliminating the thermal

contact resistance from geometry mismatch. The MCHP has the evaporator section which is attached to the photovoltaic and the condenser section where the thermoelectric generator is attached. As shown in Figure 3.5a, the working fluid is transferred from the evaporator section to the condenser section due to vaporization of the work fluid by the absorbed heat at the evaporation section. At the condenser section, the working fluid undergoes a phase change from vapour to liquid state and returns to the evaporator section after releasing its heat to the attached TEG. Furthermore, the inner structure of the MCHP is shown in Figure 3.5b including the channel, groove and fin. In addition, the dimensions of the flat plate microchannel heat pipe in millimetres are shown in Figure 3.5b and the height of the MCHP is 3 mm.

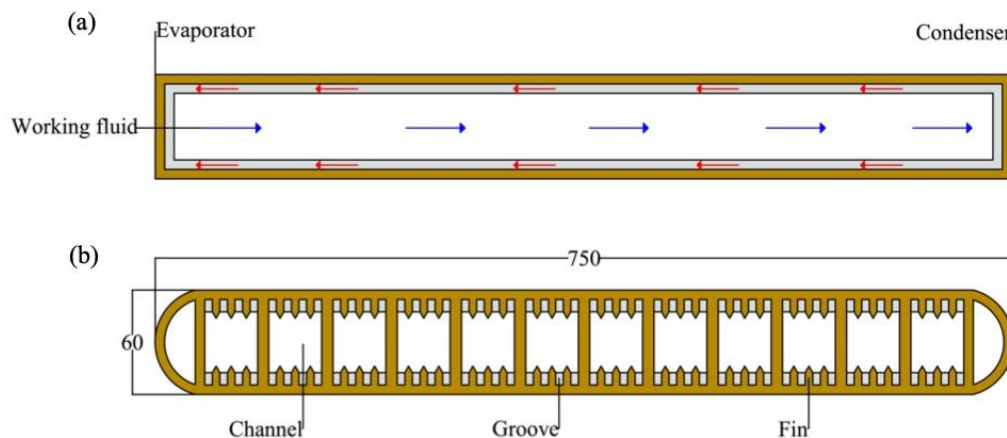


Figure 3.5: Flat plate microchannel heat pipe (a) outer structure and (b) inner structure

3.4.3 Thermoelectric Generator

The thermoelectric generator used in this research is shown in Figure 3.6. A typical thermoelectric generator is made up of several layers including ceramic, copper, n-type and p-type thermoelectric legs as shown in Figure 3.6a. In addition, two external wires (positive and negative) are used to connect the thermoelectric generator to the external load resistance. The ceramic layers enhance the heat transfer across the TEG and provide electrical insulation. Copper is the electrical conducting

material which allows an electrical circuit to be formed in the TEG. The n-type and p-type legs are made of bismuth telluride (Bi_2Te_3) thermoelectric material. Furthermore, the commercial TEG used (GM250-127-14-16) has 127 pairs of n-type and p-type legs therefore there are 254 legs in the module which are connected electrically in series and thermally in parallel as shown in Figure 3.6b. The dimensions of the thermoelectric generator in millimetres are shown Figure 3.6b and the height of the TEG is 3.4 mm.

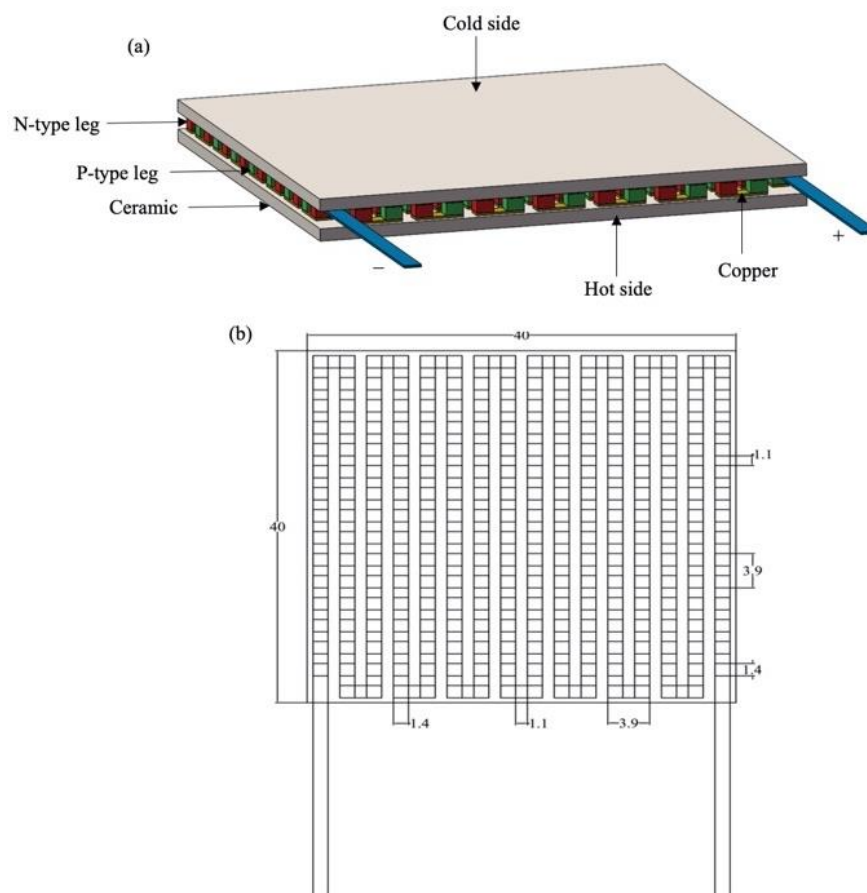


Figure 3.6: Thermoelectric generator in (a) 3-dimension and (b) 2-dimension

3.4.4 Cooling Block and Water Tank

The schematic and connection of the cooling block and water tank used in this research is shown in Figure 3.7. The dimensions of the cooling block in terms of length and width are exactly the same with those of the thermoelectric generator therefore, it

covers the entire surface of the TEG cold side thus, heat removal is more effective. Furthermore, the cooling block has an inlet and outlet where water pipes are connected to the outlet and inlet of the water tank respectively for water circulation as shown in Figure 3.7. Therefore, the thermoelectric generator is cooled by the water flowing through the cooling block and eventually, the heat removed from the TEG is circulated to the water tank which in turn increases the temperature of the water in the tank thus demonstrating the feasibility of the hybrid system for electricity generation and hot water production.

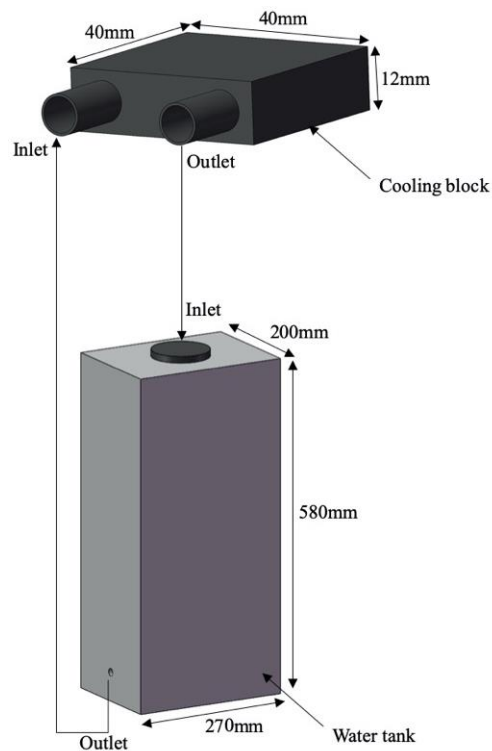


Figure 3.7: Schematic of cooling block and water tank

3.5 Computer Simulation Models

Numerical modelling approach is one of the methodologies applied in this research in addition to experimental investigation. In this section, the computer simulation models which describe the energy balance of the system components are

presented. The numerical investigation in this research is performed using COMSOL Multiphysics software and the equations used for the modelling are presented. The three main sub-systems in the hybrid system are the photovoltaic module, thermoelectric generator and heat pipe therefore, simulation models for each system is presented in addition to that of the hybrid system. In subsequent chapters, the models presented in this section will be validated with experimental results and published data.

3.5.1 Modelling Equations

The principles of heat transfer described above are applied to model the hybrid system and its individual subsystems. The modelling equations are based on the law of conservation of energy which is the principle underlying energy balance calculations. The photovoltaic, thermoelectric generator, heat pipe and hybrid system models used in this research are described below. The subsystems are firstly modelled separately before being integrated to form the hybrid PV-TE-MCHP system.

3.5.1.1 Photovoltaic Model

The governing equations for the temperature distribution in each layer of the PV are given as (Fallah Kohan et al., 2018):

$$\rho C_p \frac{\partial T}{\partial t} - \nabla \cdot (k \nabla T) = q_{sol} - P_{gen} - q_{rad} - q_{conv} \quad (3.1)$$

where ρ , C_p and k are density, specific heat capacity and thermal conductivity of each layer. q_{rad} is the radiative heat loss and q_{conv} is the convective heat loss. T is the temperature, q_{sol} can be defined as the volumetric solar energy absorption by each layer and P_{gen} is the electrical power generation per volume which is zero for all layers except the crystalline silicon cell layer.

The solar energy absorption and power generation in each layer of the PV can be modelled by firstly specifying the solar radiation intensity (G_0), after which the

energy absorption in each layer can then be calculated and considered as an internal heat generation. In this study, the cell surface is assumed to always be uniformly illuminated. The volumetric energy absorption of each layer is given as:

$$q_{sol,i} = \frac{G_{rec,i} \times \alpha_i \times A_i \times C}{V_i} \quad (3.2)$$

$$G_{rec,i} = G_{rec,i-1} \times [(1 - \alpha_{i-1}) - \rho_{i-1}] \quad (3.3)$$

where α_i , ρ_i and V_i are the absorptivity, reflectivity and volume of the i th layer respectively. $G_{rec,i}$ can be defined as the solar radiation intensity received at each layer, $q_{sol,i}$ is the associated volumetric heat source at each layer, A_i is the area of the i th layer and C is solar concentration ratio.

In the crystalline silicon layer, power generation is considered as an internal heat sink and can be defined as (Evans, 1981):

$$\eta_{pv} = \eta_{ref} [1 - \beta(T_{pv} - T_{ref})] \quad (3.4)$$

$$P_{gen} = q_{sol,3} \times \eta_{pv} \quad (3.5)$$

where η_{ref} is the reference efficiency of the crystalline silicon solar cell and β is the temperature coefficient. In addition, T_{pv} is the average temperature of the silicon layer, T_{ref} is the reference temperature of 298.15 K, $q_{sol,3}$ is the volumetric solar energy absorption at the silicon layer and η_{pv} is the efficiency of the PV.

The electrical power generation obtained from Eq. (3.5) is dependent entirely on the temperature distribution in each of the layers therefore, Eq. (3.1) – Eq. (3.5) are coupled together and solved simultaneously to obtain the temperature distribution using finite element method.

The radiative heat loss at the top surface of the photovoltaic is given as,

$$q_{rad} = \varepsilon \sigma_b (T_{sky}^4 - T_{ts}^4) \quad (3.6)$$

where σ_b is Stefan-Boltzmann's constant and T_{ts} is the temperature of the photovoltaic top surface.

The sky temperature is used for the radiative heat loss calculation and it is given as (G. Li et al., 2018b),

$$T_{sky} = 0.0552T_a^{1.5} \quad (3.7)$$

where T_a is the ambient temperature and T_{sky} is sky temperature.

The convective heat loss at the top surface of the photovoltaic is given as,

$$q_{conv} = h(T_a - T_{ts}) \quad (3.8)$$

The convective heat transfer coefficient of the PV is given in terms of the wind speed as (Zhou et al., 2015):

$$h = 5.82 + 4.07v \quad (3.9)$$

where h is the convective heat transfer coefficient v is the wind speed (m/s).

3.5.1.2 Thermoelectric Generator Model

The thermoelectric generator operation is governing by the following equations which are solved using finite element method (Xiao et al., 2012):

$$\rho C_p \frac{\partial T}{\partial t} + \nabla \cdot \vec{q} = \dot{q} \quad (3.10)$$

where C_p is specific heat capacity, \vec{q} is heat flux vector, ρ is the density, T is temperature and \dot{q} is the heat generation rate per unit volume.

Electric charge continuity equation is expressed as,

$$\nabla \cdot \left(\vec{J} + \frac{\partial \vec{D}}{\partial t} \right) = 0 \quad (3.11)$$

where \vec{D} is the electric flux density vector and \vec{J} is the electric current density vector.

The following thermoelectric constitutive equations are used to couple the Eq. (3.10) and (3.11) (Antonova and Looman, 2005),

$$\vec{q} = T[\alpha] \cdot \vec{J} - [\kappa] \cdot \nabla T \quad (3.12)$$

$$\vec{j} = [\sigma] \cdot (\vec{E} - [\alpha] \cdot \nabla T) \quad (3.13)$$

where $[\kappa]$ is the thermal conductivity matrix, $[\alpha]$ is the Seebeck coefficient matrix, and $[\sigma]$ is the electrical conductivity matrix.

$$\vec{E} = -\nabla\varphi \quad (3.14)$$

where φ is the electric scalar potential and \vec{E} is the electric field intensity vector.

The combination of the above equations results in the coupled thermoelectric equations which are expressed as,

$$\rho_d C_p \frac{\partial T}{\partial t} + \nabla \cdot (T[\alpha] \cdot \vec{j}) - \nabla \cdot ([\alpha] \cdot \nabla T) = \dot{q} \quad (3.15)$$

$$\nabla \cdot ([\varepsilon] \cdot \nabla \frac{\partial \varphi}{\partial t}) + \nabla \cdot ([\sigma] \cdot [\alpha] \cdot \nabla T) + \nabla \cdot ([\sigma] \cdot \nabla \varphi) = 0 \quad (3.16)$$

where $[\varepsilon]$ represents the dielectric permittivity matrix.

Rewriting Eq. (3.13) and (3.14) results in (Ezzat, 2011),

$$\nabla \cdot (T\alpha\vec{j}) - \nabla \cdot (\lambda\nabla T) = \dot{q} \quad (3.17)$$

$$\nabla \cdot (\sigma\alpha\nabla T) + \nabla \cdot (\sigma\nabla\varphi) = 0 \quad (3.18)$$

where ∇ is the vector differential operator and ∇^2 is the Laplace operator which is a scalar operator and is expressed as the divergence of the gradient of T and φ in the above equations.

The thermoelectric generator electrical performance (power output and efficiency) are derived from the equations below:

$$V_{OC} = \alpha\Delta T \quad (3.19)$$

where α is the Seebeck coefficient, V_{OC} is the open circuit voltage, and ΔT is the temperature difference between the hot and cold sides of the TEG.

$$V_L = V_{OC} - R_{in}I = R_L I \quad (3.20)$$

where R_{in} is the TEG internal resistance, V_L is the output load voltage, and I is the TEG current which is expressed as,

$$I = \frac{V_{OC}}{R_{in} + R_L} \quad (3.21)$$

The thermoelectric generator power output is expressed as,

$$P_{teg} = V_L I = R_L I^2 \quad (3.22)$$

The efficiency of the thermoelectric generator is given as,

$$\eta_{teg} = \frac{P_{teg}}{Q_h} \quad (3.23)$$

where Q_h is the input power at the top surface of the TEG and η_{teg} is the thermoelectric generator efficiency.

3.5.1.3 Flat Plate Heat Pipe Model

The flat plate heat pipe model used in this study is a simplified model given by (COMSOL Multiphysics, 2018a) and modified for this particular study.

The capillary pressure is given as:

$$\Delta p_c = \frac{2\sigma}{r_c} \quad (3.24)$$

where r_c is the capillary radius and σ is the surface tension.

The capillary pressure must be greater than all other pressure drops in the heat pipe therefore,

$$\Delta p_c \geq \Delta p_v + \Delta p_l + \Delta p_g \quad (3.25)$$

where Δp_v is the vapor pressure drop, Δp_c is capillary pressure drop, Δp_l is liquid pressure drop in wick and Δp_g is pressure drop due to gravitation and acceleration.

$$\Delta p_l = \left(\frac{\mu_l}{K A_w L_{vp_l}} \right) L_{eff} q \quad (3.26)$$

where μ_l is the liquid viscosity, K is wick permeability, A_w is wick area, L_{eff} is the heat pipe effective length and q is the capillary limit.

The vapor pressure drop Δp_v can often be neglected and if the effect of gravity is not considered then,

$$\Delta p_c = \Delta p_l \quad (3.27)$$

The capillary limit is given as:

$$q = \frac{2\sigma K A_w L_v p_l}{L_{eff} r_c \mu_l} \quad (3.28)$$

$$L_{eff} = \frac{L_{evap}}{2} + \frac{L_{conden}}{2} \quad (3.29)$$

where L_{evap} is the length of evaporator section and L_{conden} is the length of condenser section of the heat pipe.

The effective thermal conductivity of the sintered copper powder wick is given as (COMSOL Multiphysics, 2018a):

$$k_{eff} = \frac{k_f(k_f + k_s - (1-\varphi)(k_f - k_s))}{k_f + k_s + (1-\varphi)(k_f - k_s)} \quad (3.30)$$

where φ is porosity, taken as 0.5, k_f and k_s are thermal conductivity of fluid (water) and thermal conductivity of solid (copper) respectively, taken as 0.61 and 400 respectively.

The vapor density according to the Ideal gas law is given as:

$$\rho_v = \frac{p}{R_s T} = \frac{p \times M_n}{R_s T} \quad (3.31)$$

where p is pressure and M_n is the molar mass (18.01528[g/mol]).

Laminar compressible flow is used and the saturation pressure (from Clausius-Clapeyron) at the inlet/outlet at evaporator/condenser side of the wick/vapor interface is given as:

$$p = p_{sat}(T) = p_{ref} \cdot \exp\left(\frac{\lambda}{R_s} \left(\frac{1}{T_{ref}} - \frac{1}{T}\right)\right) \quad (3.32)$$

$$\lambda = h_{fg} \times M_n \quad (3.33)$$

where λ is the enthalpy of vaporization, M_n is the molar mass, h_{fg} is the latent heat (2473 [kJ/kg]), p_{sat} is saturation pressure, R_s is specific gas constant (8.3144621

[J/mol/K]), T_{ref} is reference temperature (100 °C), T is temperature and p_{ref} is reference pressure (1atm).

A global analytical function is used to define the saturation pressure and the vapor density is calculated from the equation.

The resulting normal mass flux of the evaporating/condensing water at the wick/vapor interface is given as,

$$\dot{m} = \rho_v(v \cdot n) \quad (3.34)$$

where ρ_v is vapor density, v is velocity field component and n is normal direction.

Viscous dissipation is included in this model and heat conduction is present in the container and wick. In the vapor chamber, heat transfer is via conduction and convection.

The boundary heat source that accounts for the heat of evaporation/condensation at the wick/vapor interface is given as:

$$q_{evap} = \dot{m}\lambda \quad (3.35)$$

where \dot{m} is normal mass flux and λ is the enthalpy of vaporization.

A global variable is used to define the heat of vaporization q_{evap} and a boundary heat source is used to apply it to the wick/vapor interface.

3.5.1.4 Hybrid System Model

In this research, the model for the hybrid PV-TE and PV-TE-MCHP are essentially the same because the heat pipe is simply a passive cooling device with no electrical contribution to the hybrid system. Instead, the heat pipe cools the PV thereby increasing the PV efficiency while also providing some heat flux at its condenser section for the TEG to generate electricity simultaneously.

The total power output of the hybrid system is a sum of the crystalline silicon cell layer power output and the TEG power output at matched load resistance. This is given as:

$$P_{hybrid} = P_{gen} + P_{teg} \quad (3.36)$$

Similarly, the overall efficiency of the hybrid system is given as the sum of the PV and TEG efficiencies.

$$\eta_{hybrid} = \eta_{pv} + \eta_{teg} \quad (3.37)$$

In the experimental study carried out, a pump is used to circulate the water for cooling the thermoelectric generator. Therefore, the overall power output of the experimental PV-TE-MCHP system is given as,

$$P_{pv-te-mchp} = P_{gen} + P_{teg} - P_{pump} \quad (3.38)$$

where P_{pump} is the power consumed by the pump.

The overall electrical efficiency of the experimental PV-TE-MCHP is given as,

$$\eta_{pv-te-mchp} = \frac{P_{gen} + P_{teg} - P_{pump}}{G \times A_c} \quad (3.39)$$

where G is the solar radiation and A_c is the area of the PV collector.

Since the heat removed from the TEG is transported back to the water tank which then increases the temperature of the water, the heating capacity obtained by the water in the tank can be expressed as (Guiqiang Li et al., 2015b),

$$\dot{Q}_{th} = m_{w_tank} c_w \frac{d\bar{T}}{dt} \quad (3.40)$$

where m_{w_tank} is the mass of water tank, c_w is the specific heat capacity of water and \bar{T} is the average temperature of water in the tank.

The thermal efficiency of the system is given as,

$$\eta_{th} = \frac{\int_{t_1}^{t_2} \dot{Q}_{th} dt}{A_c \int_{t_1}^{t_2} G dt} \quad (3.41)$$

where A_c is the area of the PV collector.

The exergy analysis is based on second law of thermodynamics and it is used to present the maximum quantity of work that can be produced in a given environment (Chow et al., 2009). The exergy efficiency of the PV-TE-MCHP is given as,

$$\eta_{xpv-te-mchp} = \frac{E_{xpv} + E_{xte} + E_{xw_tank} - P_{pump}}{E_{xin}} \quad (3.42)$$

where E_{xpv} , E_{xte} are the exergy outputs of PV and TE respectively and E_{xw_tank} is the exergy obtained in the water tank.

$$E_{xpv} = P_{gen} \quad (3.43)$$

$$E_{xte} = P_{teg} \quad (3.44)$$

Assuming that the temperature value in the water tank is the average of three thermocouple temperature values, E_{xw_tank} can be expressed as (Gang et al., 2012),

$$E_{xw_tank} = \dot{Q}_{th} \left(1 - \frac{T_a}{T} \right) \quad (3.45)$$

The exergy from the sun E_{xin} is given as (Gang et al., 2011),

$$E_{xin} = A_c G \varphi_{srad,max} \quad (3.46)$$

where $\varphi_{srad,max}$ is the maximum efficiency ratio for determining the exergy of thermal emission at temperature T_{sun} and it is expressed using Petela equation as (Petela, 2003),

$$\varphi_{srad,max} = 1 + \frac{1}{3} \left(\frac{T_a}{T_{sun}} \right)^4 - \frac{4}{3} \frac{T_a}{T_{sun}} \quad (3.47)$$

where T_a is ambient temperature and T_{sun} is the solar irradiance temperature which is taken as 6000 K (Li et al., 2016a).

The experimental error of the corresponding independent variables such as solar radiation, current, voltage and temperature are determined by the accuracy of the measuring instrument used. The relative error (RE) of the dependent variable y is given as (Ji et al., 2009),

$$RE = \frac{dy}{y} = \frac{\partial f}{\partial x_1} \frac{dx_1}{y} + \frac{\partial f}{\partial x_2} \frac{dx_2}{y} + \dots + \frac{\partial f}{\partial x_n} \frac{dx_n}{y} \quad (3.48)$$

$$y = f(x_1, x_2, \dots, x_n) \quad (3.49)$$

where $x_i (i = 1, \dots, n)$ is defined as variable of dependent variable y , and $\frac{\partial f}{\partial x}$ is defined as error transferring coefficient of the variables.

During test period, the experimental relative mean error (RME) is given as,

$$RME = \frac{\sum_1^N |Re|}{N} \quad (3.50)$$

3.5.2 Other Optimization Models

Asides the hybrid PV-TE-MCHP model which is described above, some other models are used in this research to optimize the performance of the thermoelectric generator and the hybrid photovoltaic-thermoelectric system while the results obtained will be presented in subsequent chapters. These models are used in conjunction with the sub-system models described above.

3.5.2.1 Solar TEG Model

At the top surface of the solar TEG, the input power is given as (P. Li et al., 2010)

$$Q_{in} = CGA_s \alpha_s \eta_{opt} \quad (3.51)$$

where A_s is the area of solar selective absorber which is placed on the top surface of the solar thermoelectric generator, α_s is the SSA absorptivity (0.95), η_{opt} represents the optical efficiency (0.90) and the SSA emissivity is 0.05 (Yin et al., 2018d). C represents the concentration ratio and G represents the solar radiation.

Heat loss due to radiation and convection at the top surface of the solar TEG are considered in this study. The sky temperature is used for the radiative heat loss calculation which is shown in Eq. (3.7) and the convective heat transfer coefficient is given in Eq. (3.9).

The Solar TEG efficiency is given as (Xiao et al., 2012):

$$\eta_{solarTEG} = \eta_{teg} \alpha_s \eta_{opt} \quad (3.52)$$

3.5.2.2 Phase Change Material Model

The phase change numerical model used in this study is based on the apparent heat capacity method. Initially, the phase change material (PCM) is in solid phase and the conduction equation in solid PCM is given as (Kylili et al., 2016):

$$\rho C_{eq} \frac{\partial T}{\partial t} + \nabla \cdot (-k_{eq} \nabla T) = Q \quad (3.53)$$

where C_{eq} is the effective heat capacity and k_{eq} is the effective thermal conductivity.

When the phase change material reaches its phase change temperature i.e. melting temperature (T_m), it is assumed that the phase change process occurs over a time period. Consequently, this time interval is defined between $T_m - \Delta T/2$ and $T_m + \Delta T/2$ and the phase of the PCM during this time period is defined by the function, θ . This function, θ is called the liquid fraction or phase transition function because it presents the fraction of the phase before the phase transition. Furthermore, the phase transition function is equal to 1 before $T_m - \Delta T/2$ (i.e. solid phase) and 0 after $T_m + \Delta T/2$ (i.e. liquid phase). Furthermore, the density, ρ and specific enthalpy, H are given as (COMSOL Multiphysics, 2018b):

$$\rho = \theta \rho_{ph1} + (1 - \theta) \rho_{ph2} \quad (3.54)$$

$$H = \frac{1}{\rho} (\theta \rho_{ph1} H_{ph1} + (1 - \theta) \rho_{ph2} H_{ph2}) \quad (3.55)$$

where $ph1$ and $ph2$ represent a material in phase 1 and phase 2 respectively.

The specific heat capacity is given as (COMSOL Multiphysics, 2018b):

$$C_p = \frac{1}{\rho} (\theta_1 \rho_{ph1} C_{p,ph1} + \theta_2 \rho_{ph2} C_{p,ph2}) + (H_{ph2} - H_{ph1}) \frac{d\alpha_m}{dT} \quad (3.56)$$

where $\theta_1 = \theta$ and $\theta_2 = 1 - \theta$.

The mass fraction α_m is given as:

$$\alpha_m = \frac{1}{2} \frac{\theta_2 \rho_{ph2} - \theta_1 \rho_{ph1}}{\rho} \quad (3.57)$$

The specific heat capacity is the sum of an equivalent heat capacity, C_{eq} (COMSOL Multiphysics, 2018b):

$$C_{eq} = \frac{1}{\rho} (\theta_1 \rho_{ph1} C_{p,ph1} + \theta_2 \rho_{ph2} C_{p,ph2}) \quad (3.58)$$

The distribution of latent heat C_L is given as:

$$C_L(T) = (H_{ph2} - H_{ph1}) \frac{d\alpha_m}{dT} \quad (3.59)$$

C_L is approximated so that the total heat per unit volume released during the phase transformation is equal to the latent heat L :

$$\int_{T_m - \frac{\Delta T}{2}}^{T_m + \frac{\Delta T}{2}} C_L(T) dT = L \int_{T_m - \frac{\Delta T}{2}}^{T_m + \frac{\Delta T}{2}} \frac{d\alpha_m}{dT} dT = L \quad (3.60)$$

In the heat equation, the apparent heat capacity, C_p used is given as:

$$C_p = \frac{1}{\rho} (\theta_1 \rho_{ph1} C_{p,ph1} + \theta_2 \rho_{ph2} C_{p,ph2}) + C_L \quad (3.61)$$

The effective thermal conductivity is given as:

$$k_{eq} = \theta_1 k_{ph1} + \theta_2 k_{ph2} \quad (3.62)$$

While the effective density is given as:

$$\rho = \theta_1 \rho_{ph1} + \theta_2 \rho_{ph2} \quad (3.63)$$

3.5.2.3 Contact Resistance Model

Thermal contact resistance can be defined as a ratio between the interface temperature drop and the interface average heat flow expressed as (Mahmoudinezhad et al., 2018b),

$$R_c = R_{pv_te} = R_{teg_hsink} = \frac{\Delta T^{interface}}{\dot{Q}/A} \text{ (mm}^2 \cdot \text{K/W)} \quad (3.64)$$

Interface heat transfer equation, which is given below, is used to evaluate the effect of thermal contact resistance between the thermoelectric copper-ceramic upper

and lower interface, photovoltaic-thermoelectric generator interface and thermoelectric generator-heat sink interface.

$$\dot{Q} = h_c A \Delta T_{interface} \quad (3.65)$$

where h_c is the thermal contact conductance which is simply the inverse of the thermal contact resistance and $\Delta T_{interface}$ is the effective temperature difference at the interface.

The thermal contact is implemented using COMSOL Multiphysics thermal contact boundary feature under the heat transfer in solids interface. Equivalent thin resistive layer contact model is used, and the thermal contact resistance is provided. Furthermore, the surface emissivity of the upper and lower interface layers is provided.

The electrical contact is implemented using the electrical contact boundary feature under the electric current interface. The constriction conductance is provided which is the inverse of the electrical contact resistance (R_{cont}) and it is solved using the equation from COMSOL Multiphysics shown below.

$$n \cdot J_1 = h_{co}(V_1 - V_2) \quad (3.66)$$

where h_{co} is the electrical contact conductance, $V_1 - V_2$ is the interface voltage difference, n is normal vector and J_1 is the current density.

3.5.2.4 Thermal Stress Model

Since the thermal conductivity of the materials considered are temperature dependent, the thermoelectric module is not entirely one-dimensional. Thus, thermodynamic and mechanical characteristics of the system in the z-axis direction are nonlinear. The temperature field is used to calculate the thermal stress field since temperature influences deformations in the system.

The thermodynamic equation can be express as (Wu et al., 2014),

$$\frac{\partial}{\partial x} \left[k \frac{\partial T}{\partial x} \right] + \frac{\partial}{\partial y} \left[k \frac{\partial T}{\partial y} \right] + \frac{\partial}{\partial z} \left[k \frac{\partial T}{\partial z} \right] = 0 \quad (3.67)$$

where $k = f(T)$ and $T = f(x, y, z)$. The temperature field is obtained by the numerical simulation and is used in the thermal stress analysis.

Thermal stress is generated due to the uneven expansion of the materials making up the thermoelectric generator. The equations governing the displacement-strain relations for the thermal stress can be expressed as (Ming et al., 2017b),

$$\bar{\varepsilon}_{xx} = \frac{\partial \bar{u}}{\partial \bar{x}}, \bar{\varepsilon}_{yy} = \frac{\partial \bar{v}}{\partial \bar{y}}, \bar{\varepsilon}_{zz} = \frac{\partial \bar{w}}{\partial \bar{z}} \quad (3.68)$$

$$\bar{\varepsilon}_{xy} = 0.5 \left(\frac{\partial \bar{u}}{\partial \bar{y}} + \frac{\partial \bar{v}}{\partial \bar{x}} \right), \bar{\varepsilon}_{yz} = 0.5 \left(\frac{\partial \bar{w}}{\partial \bar{y}} + \frac{\partial \bar{v}}{\partial \bar{z}} \right), \bar{\varepsilon}_{xz} = 0.5 \left(\frac{\partial \bar{w}}{\partial \bar{x}} + \frac{\partial \bar{u}}{\partial \bar{z}} \right) \quad (3.69)$$

The stress-strain relation can be expressed in a dimensionless form using a nonsymmetrical Jacobian matrix as,

$$\begin{Bmatrix} \bar{\sigma}_{xx} \\ \bar{\sigma}_{yy} \\ \bar{\sigma}_{zz} \\ \bar{\sigma}_{yz} \\ \bar{\sigma}_{zx} \\ \bar{\sigma}_{xy} \end{Bmatrix} = \frac{\bar{E}}{(1+\nu)(1-2\nu)} \begin{bmatrix} 1-\nu & \nu & \nu & 0 & 0 & 0 \\ \nu & 1-\nu & \nu & 0 & 0 & 0 \\ \nu & \nu & 1-\nu & 0 & 0 & 0 \\ 0 & 0 & 0 & 1-2\nu & 0 & 0 \\ 0 & 0 & 0 & 0 & 1-2\nu & 0 \\ 0 & 0 & 0 & 0 & 0 & 1-2\nu \end{bmatrix} \times \begin{Bmatrix} \bar{\varepsilon}_{xx} \\ \bar{\varepsilon}_{yy} \\ \bar{\varepsilon}_{zz} \\ \bar{\varepsilon}_{yz} \\ \bar{\varepsilon}_{zx} \\ \bar{\varepsilon}_{xy} \end{Bmatrix} - \begin{Bmatrix} 1 \\ 1 \\ 1 \\ 0 \\ 0 \\ 0 \end{Bmatrix} \frac{\bar{\alpha} \bar{E} \bar{T}}{1-2\nu} \quad (3.70)$$

The three principal stress are represented as σ_1 , σ_2 and σ_3 respectively. The von Mises equivalent stress can be obtained from the fourth strength theory of mechanics of materials also known as the distortion of energy theory. It describes the total combined stresses in all three dimensions as,

$$\sigma = \sqrt{\frac{[(\sigma_1 - \sigma_2)^2 + (\sigma_2 - \sigma_3)^2 + (\sigma_3 - \sigma_1)^2]}{2}} \quad (3.71)$$

The difficulty encountered in trying to solve the above equations analytical due to the temperature dependence of the material properties necessitates the need to use finite element method to obtain the solution to these equations. The electrical,

thermal and mechanical behaviours of the thermoelectric generator can be obtained from the coupled equations described above.

3.6 Modelling Results and Discussion

In this section, results obtained from the numerical simulation are presented and discussed in detail. Three different systems are studied under identical operating conditions and compared including photovoltaic (PV) only, photovoltaic-thermoelectric (PV-TE) and photovoltaic-thermoelectric-flat plate microchannel heat pipe (PV-TE-MCHP). The hybrid PV-TE system consists of a single thermoelectric generator which is directly coupled to the photovoltaic and positioned at the middle of the PV. Consequently, the PV-TE can be compared to the PV-TE-MCHP which also consists of a single thermoelectric generator placed at the condenser section of the MCHP. The photovoltaic only has no additional component attached to it therefore it represents the conventional PV module. The schematic diagram of the hybrid systems studied is shown in Figure 3.8 including PV-TE-MCHP (shown in Figure 3.8a) and PV-TE (shown in Figure 3.8b).

3.6.1 Boundary Conditions

To accurately model and simplify the hybrid system, the following boundary conditions and assumptions are considered.

- 1) PV reference efficiency at 298.15 K is 15% and temperature coefficient is 0.0045 1/K.
- 2) Steady state and transient conditions are considered.
- 3) Convective and radiative heat loss are considered at the top surface of the photovoltaic.

- 4) In terms of radiative heat loss, the front and back surface of the PV are taken to view the sky and ground respectively.
- 5) The initial temperature of the system is assumed to be equal to the ambient temperature.
- 6) Heat loss through convection and radiation on all surfaces of the TEG are assumed to be zero.
- 7) Thermoelectric electrical and thermal contact resistances are considered.
- 8) The heat sink of the TEG is considered as a thermal boundary condition with a fixed temperature value.
- 9) The copper on the n-type thermoelectric leg is assumed to be at zero potential while the one at the p-type leg is connected to the external load resistance circuit.
- 10) Effect of gravity is neglected (COMSOL Multiphysics, 2018a).
- 11) Heat transfer is mainly due to evaporation/condensation and convection of vapor. Therefore, heat transport in the wick is simplified as conduction with an effective heat transfer coefficient.
- 12) Constant material properties are used except for that of the vapor density.
- 13) This simplified model does not predict the operating limits of the heat pipe.
- 14) Convective heat transfer coefficient used at the top surface of the heat pipe is variable and dependent on the wind speed.

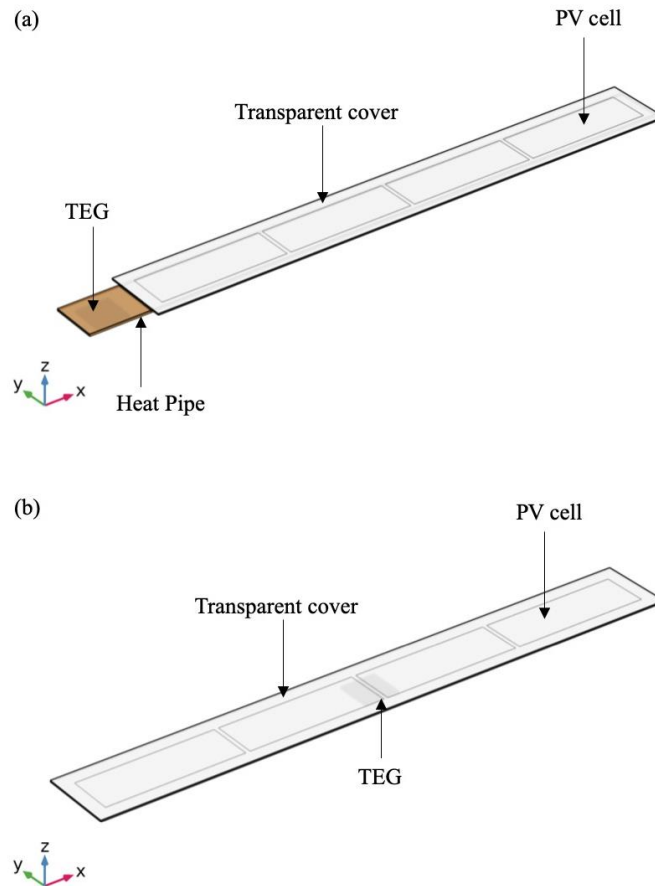


Figure 3.8: Schematic diagram of (a) PV-TE-MCHP and (b) PV-TE

3.6.2 Effect of Wind Speed

The effect of wind speed on the performance of the PV only and the hybrid PV-TE systems is studied at a constant solar radiation of 1000 W/m^2 , ambient temperature of $25 \text{ }^\circ\text{C}$ and thermoelectric cold side temperature of $20 \text{ }^\circ\text{C}$ under steady-state conditions. The electrical response of the studied systems to wind speed variation is shown in Figure 3.9. It can be seen from Figure 3.9a that the overall efficiency of the PV only, PV-TE and PV-TE-MCHP all increase as the wind speed is increased. This is because the wind speed affects the convective heat transfer coefficient which accounts for the convective heat loss from the surface of the photovoltaic. Therefore, increase in wind speed leads to an increase in the convective cooling of the photovoltaic thereby increasing the efficiency of the PV. There is an inverse

relationship between the temperature and efficiency of the photovoltaic therefore, thermal management of the PV is essential.

Furthermore, it can be seen from Figure 3.9a that the PV-TE-MCHP provides the highest overall efficiency at different wind speeds while the efficiency of the PV-TE is the lowest. In fact, at a wind speed of 0 m/s which is the assumed wind speed condition in a laboratory, the overall efficiency of the PV-TE-MCHP is 4.04% and 10.75% greater than that of the PV only and PV-TE systems respectively. Furthermore, it can be seen that the overall efficiency of the PV, PV-TE and PV-TE-MCHP all increase by 13.03%, 16.94% and 9.04% respectively when the wind speed increased from 0 m/s to 5 m/s .

The efficiency of the thermoelectric in the PV-TE and PV-TE-MCHP is shown in Figure 3.9b. It is obvious that the TE efficiency in PV-TE-MCHP is higher than that of the TE in PV-TE. This is because the single thermoelectric generator attached to the PV in the PV-TE system cannot sufficiently extract all the waste heat from the back surface of the PV. Therefore, several thermoelectric generators would be required to completely cover the back surface of the photovoltaic so as to enhance its thermal management capabilities. However, the use of flat plate microchannel heat pipe eliminates this challenge as the heat pipe can effectively extract the waste heat from the back surface of the PV and transfer this heat to its condenser section for additional electricity generation by the single thermoelectric generator attached. Consequently, the use of the flat plate microchannel heat pipe eliminates the need for a high quantity of thermoelectric generators thus, reducing the overall system cost and increasing the hybrid system performance.

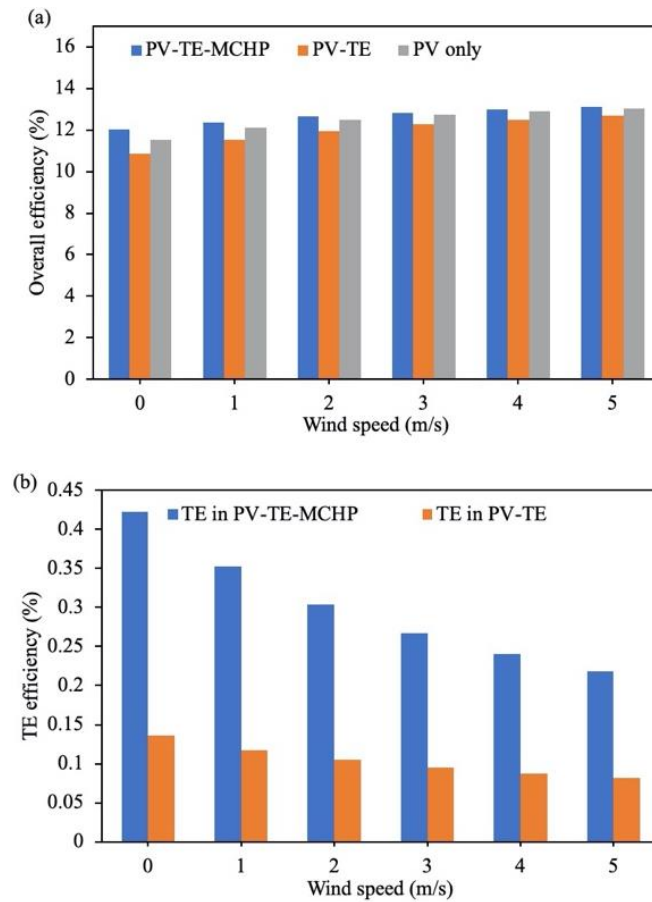


Figure 3.9: Variation of wind speed with (a) overall efficiency and (b) TE efficiency

The temperature response of the studied systems to wind speed variation is shown in Figure 3.10. It is clear from Figure 3.10a that the temperature of the photovoltaic sharply decreases as the wind speed is increased as a result of the improved convective cooling. Furthermore, the back surfaces of the PV-TE-MCHP and PV-TE are insulated besides the thermoelectric cold side. Consequently, the PV temperature in the PV only is slightly lower due to the absence of any insulation or additional component at the back surface therefore, convective heat loss occurs at the top and back surfaces of the PV only. Furthermore, Figure 3.10b shows that the temperature difference across the hot and cold sides of the thermoelectric generator in the PV-TE-MCHP and PV-TE decrease as the wind speed increases. This is because of the opposing relationship the PV and TE individually have with temperature. Since

the wind speed increase reduces the temperature of the PV, the input heat flux to the TE will thus be reduced thereby reducing its temperature difference.

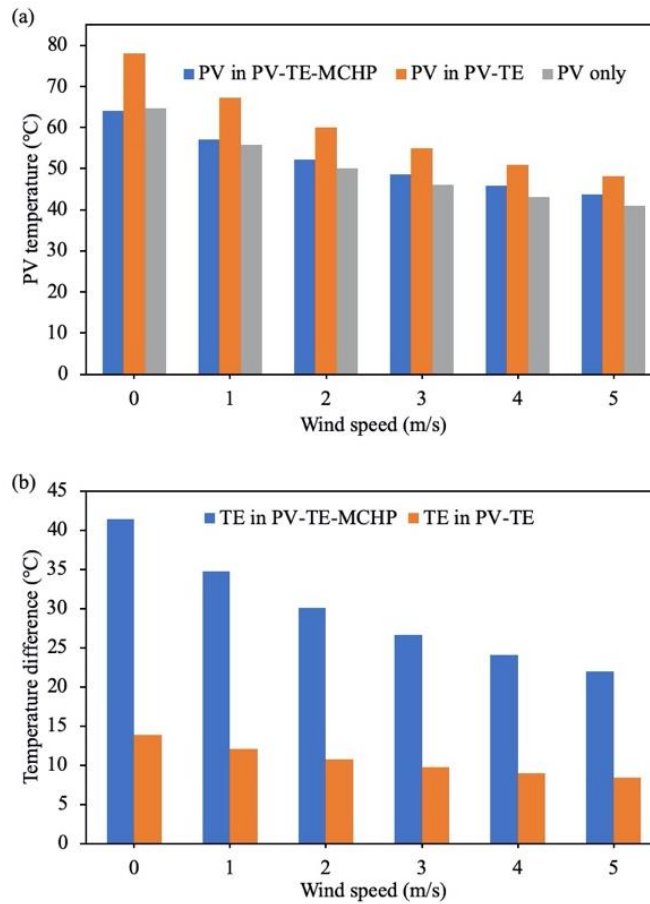


Figure 3.10: Variation of wind speed with (a) PV temperature and (b) TE temperature difference

3.6.3 Effect of Ambient Temperature

The effect of ambient temperature on the performance of the PV only and the hybrid PV-TE systems is studied at a constant solar radiation of 1000 W/m^2 , wind speed of 0 m/s and thermoelectric cold side temperature of $20 \text{ }^\circ\text{C}$ under steady-state conditions. The electrical response of the studied systems to wind speed variation is shown in Figure 3.11. It can be seen from Figure 3.11a that the overall efficiency of the PV only and hybrid systems all decrease as the ambient temperature increases. This decrease in overall efficiency is caused by the increase in temperature of the

photovoltaic as the ambient temperature is increased. Furthermore, it can be seen from Figure 3.11a that the PV-TE-MCHP provides the highest overall efficiency at different ambient temperatures while the efficiency of the PV-TE is the lowest. In fact, at an ambient temperature of 25 °C the overall efficiency of the PV-TE-MCHP is 4.04% and 10.75% greater than that of the PV only and PV-TE systems respectively. However, at a high ambient temperature of 50 °C, the PV-TE-MCHP overall efficiency is greater than that of the PV only and PV-TE systems by 9.76% and 14.46% respectively. Therefore, it is obvious that the hybrid PV-TE-MCHP system is better for sunny regions with high ambient temperature. Furthermore, it can be seen that the overall efficiency of the PV, PV-TE and PV-TE-MCHP all decrease by 12.80%, 10.50% and 6.91% respectively when the ambient temperature increased from 25 °C to 50 °C.

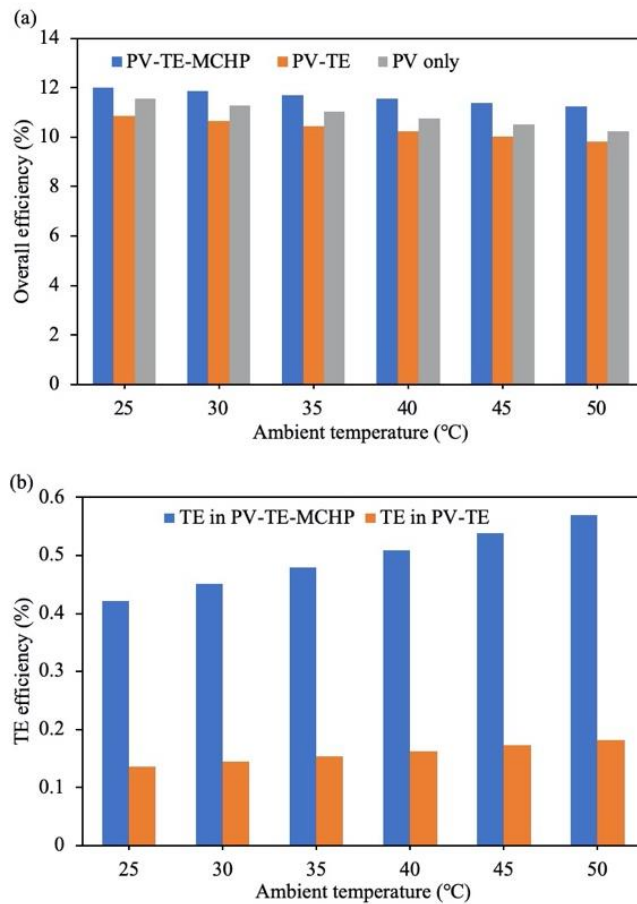


Figure 3.11: Variation of ambient temperature with (a) overall efficiency and (b) TE efficiency

Figure 3.11b shows the thermoelectric efficiency in the hybrid PV-TE-MCHP and PV-TE. It is clear that the TE efficiency increases as the ambient temperature increases. This is because, an increase in ambient temperature causes an increase in PV temperature thus, a greater amount of heat is available for the attached thermoelectric generator. Therefore, the ambient temperature increase has a positive effect on the thermoelectric generator and a negative effect on the photovoltaic module. Furthermore, it is clear from Figure 3.11b that the thermoelectric performs better in the PV-TE-MCHP compared to the PV-TE due to the greater amount of heat input to the TE in the PV-TE-MCHP.

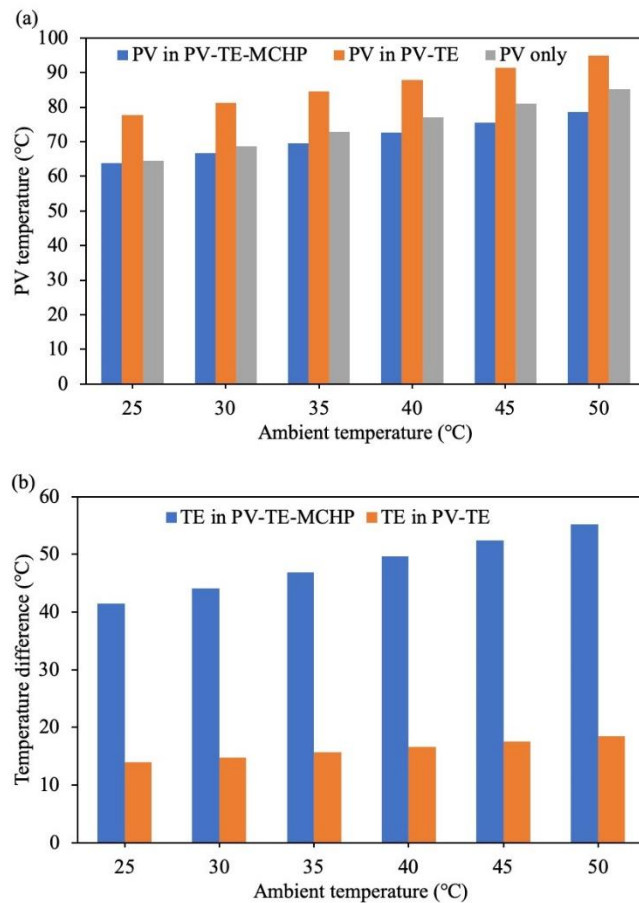


Figure 3.12: Variation of ambient temperature with (a) PV temperature and (b) TE temperature difference

The temperature response of the studied systems to ambient temperature variation is shown in Figure 3.12. The negative effect of the ambient temperature on the photovoltaic temperature is clearly seen in Figure 3.12a. The photovoltaic temperature in PV only, PV-TE and PV-TE-MCHP all increase by 32.08%, 21.88% and 22.88% respectively when the ambient temperature increased from 25 °C to 50 °C. In addition, it is obvious that the photovoltaic temperature in PV-TE-MCHP is the lowest for all ambient temperatures considered. Furthermore, Figure 3.12b shows the positive effect of ambient temperature on the thermoelectric temperature difference. The increase in TE temperature difference as ambient temperature increases is the reason for the thermoelectric efficiency increase explained above.

3.6.4 Transient Response

The transient response of the PV only and the hybrid PV-TE systems under a constant solar radiation of 1000 W/m^2 , ambient temperature of 25 °C, wind speed of 0 m/s and thermoelectric cold side temperature of 20 °C is studied for a period of 1800 s (30 mins). This test condition is similar to that of the experimental study in a laboratory which will be explained in subsequent chapters. The electrical performance of the studied systems in terms of conversion efficiency is shown in Figure 3.13. It can be seen from Figure 3.13a that the overall efficiency of the studied systems all decrease as the time increases. This is expected because, the longer the systems are studied under a constant solar radiation, the higher the total amount of energy absorbed by the photovoltaic and the higher its operating temperature becomes. Therefore, the efficiency of the photovoltaic which accounts for the larger percentage of the overall efficiency decreases as the temperature increases.

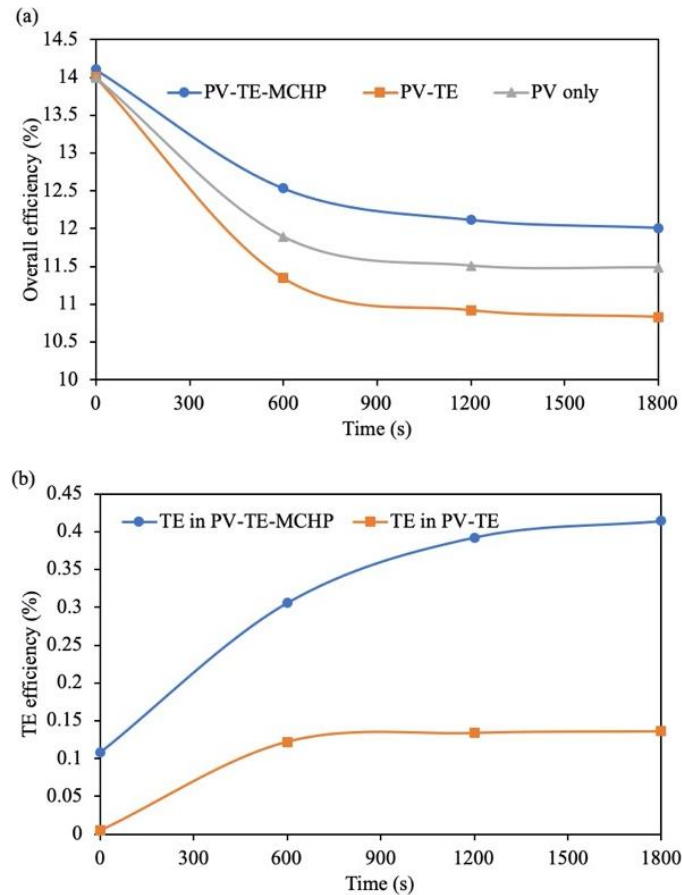


Figure 3.13: Time variation with (a) overall efficiency and (b) TE efficiency

Nevertheless, it is clear from Figure 3.13a that the hybrid PV-TE-MCHP provides the better electrical performance compared to the other studied systems. In fact, after 1800 s, the overall efficiency of the PV-TE-MCHP is greater than that of the PV-TE and PV only by 10.87% and 4.55% respectively. The reason for the low performance of the PV-TE system is due to the poor heat extraction capability of the single thermoelectric generator attached. However, if several TEGs are used to completely cover the back surface of the PV, its performance will be better than that of the PV only. In addition, it is important to note that efficiency enhancement achievable via the use of the hybrid systems especially the PV-TE-MCHP compared to the PV only becomes more significant under highly concentrated solar radiation.

Furthermore, the thermoelectric efficiency in the hybrid systems is shown in Figure 3.13b. It can be seen that the thermoelectric efficiency increases as the time is increased until it attains an optimum value at which it then becomes steady. This is because initially, as the time increases, the amount of heat input available to the thermoelectric generator increases thus, its efficiency increases.

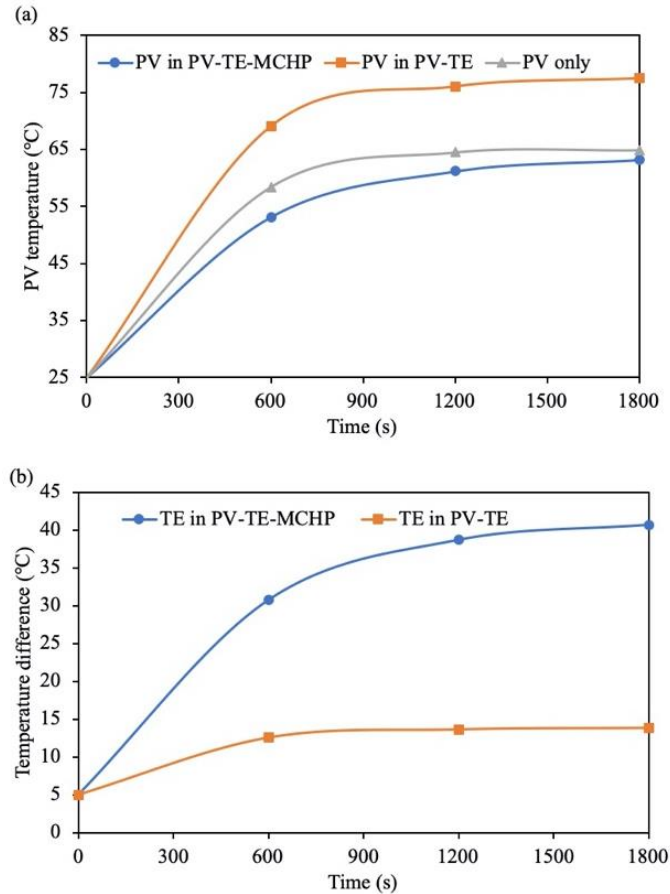


Figure 3.14: Time variation with (a) PV temperature and (b) TE temperature difference

The temperature response of the studied systems under transient conditions is shown in Figure 3.14. The temperature response of the systems explains the electrical response of the systems shown above. It can be seen from Figure 3.14a that the photovoltaic temperature in the PV-TE-MCHP is the lowest and this is the reason for its higher overall efficiency. In addition, it is obvious that the photovoltaic temperature increases as the systems are studied for longer time periods. Furthermore, it is clear

from Figure 3.14b that the thermoelectric temperature difference also increases as the systems are studied for longer time periods. However, both the electrical and temperature responses of the studied systems attain a steady state after a period of time.

3.6.5 Temperature and Voltage Distributions

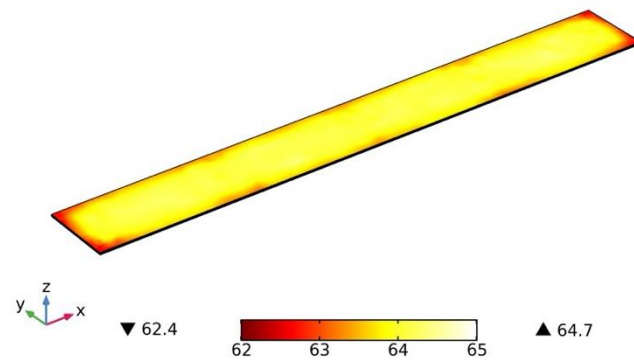
One of the advantages of the three-dimensional numerical study carried out with COMSOL Multiphysics is the ability to observe the temperature and voltage distributions in the systems. The PV temperature distributions in the three studied systems are shown in Figure 3.15. It can be seen from Figure 3.15a that the temperature is non-uniformly distributed across the photovoltaic surface due to the absence of any additional cooling component.

Furthermore, Figure 3.15b shows the PV temperature distribution in the PV-TE and it can be seen that the region where the thermoelectric generator is attached has the lowest temperature and this creates a non-uniform temperature distribution across photovoltaic surface. In addition, Figure 3.15c shows the PV temperature distribution in the PV-TE-MCHP and it can be seen clearly that the temperature is uniformly distributed across the photovoltaic cell surface due to the presence of the flat plate microchannel heat pipe. This is another advantage of using the MCHP in the hybrid system as it helps to prevent the development of hotspots across the photovoltaic cell surface.

CHAPTER 3 CONCEPTUAL DESIGN, MATHEMATICAL ANALYSIS AND SIMULATION MODEL DEVELOPMENT

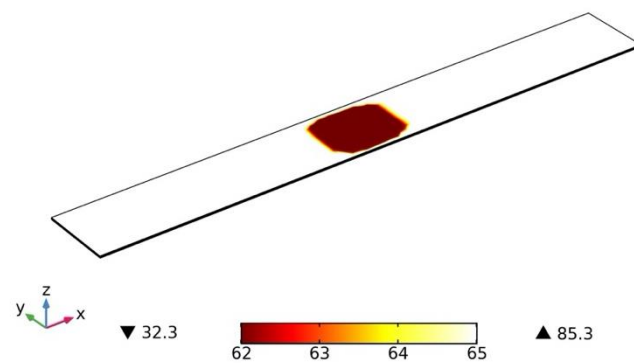
t_amb(1)=25 degC w_sp(1)=0 Volume: Temperature (degC)

(a)



t_amb(1)=25 degC w_sp(1)=0 Volume: Temperature (degC)

(b)



t_amb(1)=25 degC w_sp(1)=0 Volume: Temperature (degC)

(c)

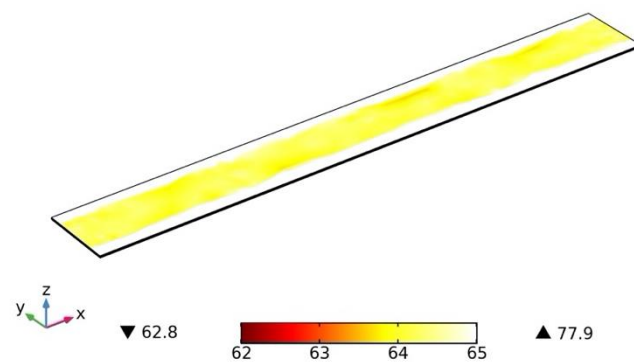
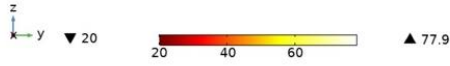


Figure 3.15: Three-dimensional PV temperature distribution in (a) PV only (b) PV-TE and (c) PV-TE-MCHP

CHAPTER 3 CONCEPTUAL DESIGN, MATHEMATICAL ANALYSIS AND SIMULATION MODEL DEVELOPMENT

t_amb(1)=25 degC w_sp(1)=0 Volume: Temperature (degC)

(a)



t_amb(1)=25 degC w_sp(1)=0 Volume: Temperature (degC)

(b)

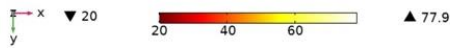
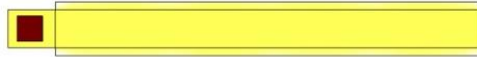
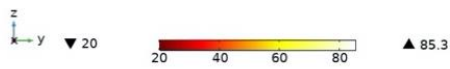


Figure 3.16: PV-TE-MCHP temperature distribution (a) side view and (b) back view

t_amb(1)=25 degC w_sp(1)=0 Volume: Temperature (degC)

(a)



t_amb(1)=25 degC w_sp(1)=0 Volume: Temperature (degC)

(b)

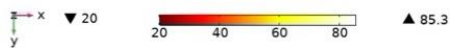


Figure 3.17: PV-TE temperature distribution (a) side view and (b) back view

The other views of the temperature distribution in the hybrid PV-TE-MCHP and PV-TE are shown in Figure 3.16 and Figure 3.17 respectively. The side view of the PV-TE-MCHP is shown in Figure 3.16a while its back view is shown in Figure 3.16b and the location of the thermoelectric generator at the condenser section of the flat plate microchannel heat pipe can be seen clearly. Furthermore, the side view of the PV-TE is shown in Figure 3.17a while its back view is shown in Figure 3.17b and the location of the thermoelectric generator at the centre of the photovoltaic can be seen clearly.

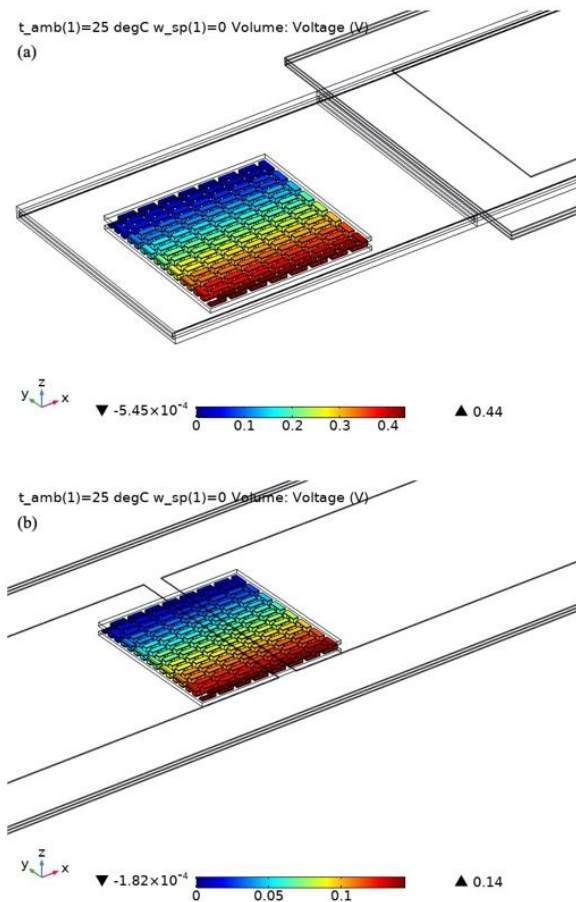


Figure 3.18: Voltage distribution in (a) PV-TE-MCHP and (b) PV-TE

The voltage distributions in the hybrid systems are shown in Figure 3.18. The use of COMSOL Multiphysics enables the coupling of different physics therefore, both temperature and voltage distributions can be obtained. In the hybrid systems, the

voltage distribution is clearly seen in the thermoelectric generator. The thermoelectric legs are connected electrically in series and thermally in parallel as shown in Figure 3.18. Furthermore, the voltage distribution in the PV-TE-MCHP is shown in Figure 3.18a while Figure 3.18b shows the voltage distribution in the PV-TE. In addition, the location of the thermoelectric generator in the hybrid systems can be clearly seen and it is obvious that the thermoelectric generator in the PV-TE-MCHP generates more voltage than that in PV-TE under similar conditions.

3.7 Chapter Summary

This chapter presented the conceptual design of the proposed hybrid system and the computer simulation models used for studying the system numerically. The design of the PV-TE-MCHP system including sketch drawings was presented. The proposed system design includes the use of flat plate microchannel heat pipe (MCHP) for thermal management of the photovoltaic (PV) by placing it directly behind the photovoltaic module and the use of thermoelectric generator for additional power generation by placing it at the condenser section of the flat plate MCHP. Furthermore, drawings for the two main parts of the hybrid system including the PV-MCHP and TEG-cooling block were provided. The operating principle of the proposed hybrid system was explained in detail while the components used in the hybrid system were presented including their dimensions and drawings.

Based on the conceptual design, system components and dimensions, the computer simulation models of the system were developed. The modelling equations for the three main components in the hybrid system including photovoltaic, thermoelectric generator and flat plate heat pipe were presented individually. Furthermore, the hybrid system model was presented and other optimization models

including solar thermoelectric generator, phase change material, contact resistance and thermal stress models were presented.

The performance of the proposed PV-TE-MCHP was simulated and compared to that of photovoltaic only and photovoltaic-thermoelectric (PV-TE) systems under steady state and transient conditions. Results showed that the overall efficiency of the PV-TE-MCHP was 4.04% and 10.75% greater than that of the PV only and PV-TE systems respectively at a wind speed of 0 *m/s*. Furthermore, it was found that the use of the flat plate microchannel heat pipe eliminates the need for a high quantity of thermoelectric generators thus, reducing the overall system cost and increasing the hybrid system performance. At a high ambient temperature of 50 °C, the PV-TE-MCHP overall efficiency was found to be greater than that of the PV only and PV-TE systems by 9.76% and 14.46% respectively. Therefore, the hybrid PV-TE-MCHP is recommended for sunny regions with high ambient temperature.

Under the transient conditions, the overall efficiency of the PV-TE-MCHP was found to be greater than that of the PV-TE and PV only by 10.87% and 4.55% respectively after 1800 s. In addition, the three-dimensional study carried out showed that in the hybrid PV-TE-MCHP, the temperature is uniformly distributed across the photovoltaic surface due to the presence of the flat plate microchannel heat pipe unlike the non-uniform temperature distribution observed in the photovoltaic only and photovoltaic-thermoelectric systems. Therefore, the use of the MCHP in the hybrid system prevented the development of hotspots across the photovoltaic surface.

CHAPTER 4 EXPERIMENTAL TESTING AND MODEL VALIDATION

4.1 Chapter Introduction

This chapter presents the experimental test rig setup and the experimental testing of the hybrid PV-TE-MCHP prototype under laboratory conditions. The following tasks are addressed in this chapter:

- 1) Describing the system and measuring components used in the experimental study.
- 2) Presenting the experimental setup and procedure for testing the system under laboratory conditions.
- 3) Presenting and discussing the experimental results obtained.
- 4) Validating the computer simulation models using the experimental results and published data.

The experimental study presented in this chapter along with the results will provide real data to assess the feasibility and performance of the proposed hybrid PV-TE-MCHP system.

4.2 System and Measuring Components

The experimental study is conducted to investigate the performance of the hybrid PV-TE-MCHP using several components which are listed in Table 4.1.

4.2.1 PV-TE-MCHP Prototype and Major Components

The PV-TE-MCHP comprises of three main components including, photovoltaic module, flat plate microchannel heat pipe and thermoelectric generator which are shown in Figure 4.1, Figure 4.2 and Figure 4.3 respectively. The flat plate MCHP and

the photovoltaic module which is an unglazed polycrystalline silicon module with 15% reference efficiency were manufactured by Guangdong Five-Star Solar Energy Ltd. The working fluid in the experimental MCHP is acetone which is compatible with the aluminium material of the MCHP. The operating temperature range of acetone is -40 °C to 140 °C and its pressure is between 0.01 to 10.49 bar (Byon, 2016). The thermoelectric generator used is a commercial TEG (GM250-127-14-16) which was manufactured by European thermodynamics and its manufacturer performance data is listed in Table 4.2. It is made up of 127 pairs of n-type and p-type bismuth telluride thermoelectric legs.

Table 4.1: Experimental test rig component specification

Component	Specification	Accuracy	Manufacturer	Quantity
Voltmeter	Pocket digital multimeter	±0.5%	Neoteck	1
Ammeter	Digital multimeter AN8009	±0.5%	Aneng	1
Solar module analyser	ISM 490	±1%	RS Pro	1
Resistor box	Variable decade resistor	±1%	Earlywish	1
DC power supply	KPS305D	-	Eventek	1
Water tank	Tower water tank	-	Tanks direct	1

Flowmeter	DigiFlow	±5%	Vyair	1
Pump	Water pump	-	RS Pro	1
Solar simulator	Solar constant MHG 4000/2500	-	Atlas	1
Pyranometer	SR20-D2	±1.2%	Hukseflux	1
Data logger	Memory HiLogger LR8400	-	Hioki	1
PV	Unglazed polycrystalline silicon	-	Guangdong five-star solar energy	1
MCHP	Flat plate	-	Guangdong five-star solar energy	1
TEG	Peltier module GM250-127- 14-16	-	European thermodynamics	1
Cooling block	Aluminium water block	-	Yeeco	1
Thermocouple	Type K	±0.5%	RS Pro	16



Figure 4.1: Photovoltaic module used in experiment



Figure 4.2: Flat plate microchannel heat pipe used in experiment



Figure 4.3: Thermoelectric generator module used in experiment

Table 4.2: Thermoelectric generator module manufacturer data

Parameter	Value
Matched load output power	6.99 W
Matched load resistance	3.65 Ω \pm 15%
Open circuit voltage	10.11 V
Matched load output	1.38 A
Matched load output voltage	5.05 V
Heat flow through module	\sim 139.8 W
Maximum compress (non-destructive)	1.2 MPa
Maximum operation temperature	Hot side - 250 $^{\circ}$ C Cold side - 175 $^{\circ}$ C

Parameters for hot side temperature 250 $^{\circ}$ C and cold side temperature 30 $^{\circ}$ C.

4.2.2 Test Rig and Major Components

Asides the three main components of the hybrid system described above, several components are used to setup the experimental test rig and these are briefly described in this section.

4.2.2.1 Solar Simulator

Since the experimental study is conducted in a laboratory, a solar simulator is used as the source of solar radiation impinged on the hybrid PV-TE-MCHP system. The solar simulator used is an Atlas SolarConstant MHG 4000/2500 which is specially designed for large luminaires for solar simulation. This solar simulator is typically used for photovoltaic module testing and it offers high irradiance efficiency and superior spatial irradiance uniformly over the target area. Figure 4.4 shows the actual solar simulator used in the experiment and it can be seen that large ventilation hoses are placed directly under the solar simulator to cool the simulator by extracting heat through a ventilator.



Figure 4.4: Solar simulator used in experiment

4.2.2.2 Water Tank

A 28-litre tower tank manufactured by Tanks direct is used in the experiment as shown in Figure 4.5. The outlet size of the tank is 1/2" British standard pipe (BSP) female and a valve was used to regulate the flow of water from the tank. Furthermore, a hose connector 1/2" BSP thread to Ø 8 mm was used to ensure the water tank can be connected to the cooling block through a water pipe/hose. The water tank without insulation is shown in Figure 4.5a while the insulated water tank is shown in Figure 4.5b. Insulation is used on the water tank to minimise heat loss since the temperature in the water tank is an important parameter which is measured. In addition, the water tank has an outlet and inlet through which water is circulated.

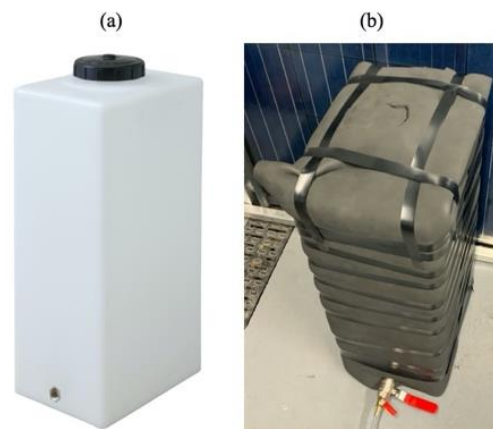


Figure 4.5: Water tank (a) without insulation and (b) with insulation

4.2.2.3 Cooling Block

An aluminium water-cooling block shown in Figure 4.6 is used in this experiment to cool the thermoelectric generator. The cooling block has an M-shape flow channel therefore, the hot and cold-water alternating area is maximized. Furthermore, the flat surface of the cooling block facilitates its integration with the flat surface of the thermoelectric generator used. In addition, the cooling block has an

inlet and outlet which is connected to the outlet and inlet of the water tank respectively via a water pipe/hose.



Figure 4.6: Cooling block used in experiment

4.2.2.4 Pump

A direct coupling water pump with maximum flow rate of 2L/min shown in Figure 4.7 is used to circulate the water from the water tank through the cooling block in order to continuously cool the thermoelectric generator. The pump is a high-quality miniature liquid pump which uses centrifugal principle to provide smooth pulseless flow. In addition, the pump provides a reliable and quiet operation.



Figure 4.7: Pump used in experiment

4.2.2.5 DC Power Supply

The direct current power supply which is used in this experiment to power the pump is shown in Figure 4.8. The output voltage and current of the power supply are

adjustable continuously at nominal value. Furthermore, it offers high accuracy and reliability. The output voltage is DC 0-30 V and output DC current is 0-5 A.

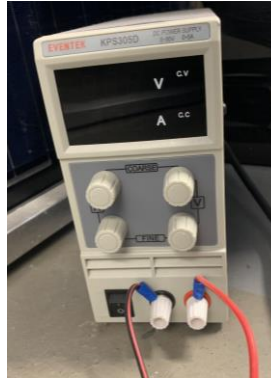


Figure 4.8: DC power supply used in experiment

4.2.2.6 Resistor Box

The thermoelectric generator output power can be obtained by connecting an external load resistor which is varied till the maximum power output is obtained. Therefore, a resistor box shown in Figure 4.9 is used for impedance matching and to close the circuit of the thermoelectric generator. The external wires of the thermoelectric generator are connected to the resistor box. The resistor box provides 0.1 to 99999.9 Ω variable resistance.



Figure 4.9: Resistor box used in experiment

4.2.2.7 Insulation

Figure 4.10 shows the insulation materials used in this experiment to minimise heat loss. Neoprene sponge foam rubber sheet roll is used as the insulation material

because it is durable, easy cut, non-slip and non-absorbent. The insulation material is 1/4" thick dense sponge foam which is waterproof. The water tank, the thermoelectric generator, cooling block and the connection pipes are insulated with the same material shown in Figure 4.10a while the back surface of the photovoltaic, MCHP are insulated using the insulation material shown in Figure 4.10b. .



Figure 4.10: Insulation material with (a) rubber and (b) foam

4.2.2.8 Thermal Grease and Adhesive

Thermal grease and adhesive shown in Figure 4.11 are used to couple the different components used in this experiment. Silicone thermal grease shown in Figure 4.11a and silicone thermal adhesive shown in Figure 4.11b are used to attach the flat plate microchannel heat pipe to the photovoltaic module. In addition, they are used to attach the thermoelectric generator to the cooling block and attach the thermoelectric generator-cooling block to the condenser section of the flat plate MCHP. They are used for thermal coupling of the components due to their excellent thermal conductivity.



Figure 4.11: Thermal (a) grease and (b) adhesive

4.2.3 Other Measurement Instruments and Elements

Several components are used to measure the performance of the hybrid system under laboratory conditions. These measuring components are briefly explained below.

4.2.3.1 Pyranometer

A pyranometer shown in Figure 4.12 is used in the experiment to measure the solar radiation intensity from the solar simulator. A SR20-D2 pyranometer manufactured by Hukseflux is used and it provides irradiance output in the form of analogue 4-20 mA current output. The pyranometer is fixed on the back board upon which the hybrid system is placed therefore, it is at the same inclination angle as the studied systems.



Figure 4.12: Pyranometer used in experiment

4.2.3.2 Thermocouple

Several thermocouples are used in this experiment to measure the temperature at different locations. The thermocouples are attached directly to the surface of the components measured while the other ends are connected to the data logger for data recording. The K-type thermocouples used in this experiment are shown in Figure 4.13 and they have a temperature range $-75\text{ }^{\circ}\text{C}$ to $+260\text{ }^{\circ}\text{C}$. The thermocouples with a 5

mm cable length are used for water tank temperature measurements while the other temperature measurements are obtained using the same thermocouple but with a 2 mm cable length due to the shorter distance required.



Figure 4.13: K-type thermocouples used in experiment

4.2.3.3 Data Logger

The data logger used to record the temperature readings from the thermocouples is a Hioki Memory Hilogger LR8400 shown in Figure 4.14. The data logger offers 30-channel standard capabilities which is expandable to 60 channels. Furthermore, it logs data at 10 ms speeds and can save data to a USB memory stick. Several thermocouples are connected to the data logger and temperature readings from different locations in the system are recorded.

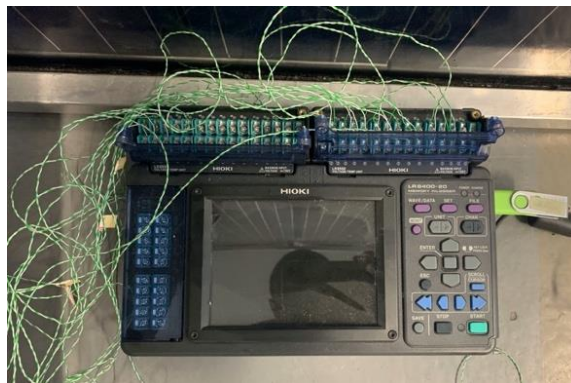


Figure 4.14: Data logger used in experiment

4.2.3.4 Solar Module Analyser

The performance of the photovoltaic module is measured using the RS Pro ISM 490 solar module analyser shown in Figure 4.15. It can be used to determine the efficiency of the photovoltaic module and its maximum voltage and current measurements are 60 V DC and 12 A respectively. Furthermore, the current and voltage accuracy of the solar module analyser are both $\pm 1\%$ while its operating temperature range is 0 – 50 °C. In addition, the two leads of the photovoltaic module are connected to the solar module analyser using kelvin clips. The solar module analyser is used to measure the electrical performance (open circuit voltage, short circuit current, maximum power, maximum voltage, maximum current and fill factor) of the PV.

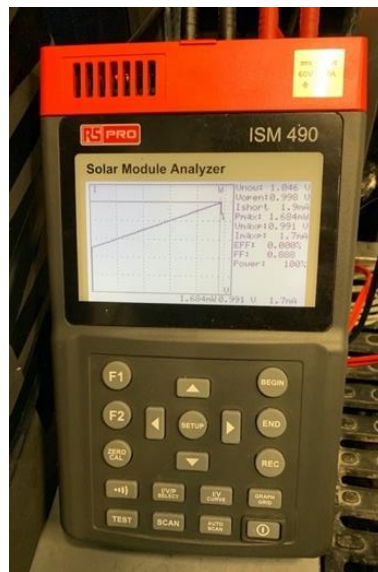


Figure 4.15: Solar module analyser used in experiment

4.2.3.5 Voltmeter and Ammeter

The voltage and current of the thermoelectric generator which is connected to an external load resistance box are measured using a voltmeter and an ammeter respectively as shown in Figure 4.16. The power output of the thermoelectric generator can be calculated easily from its voltage and current outputs. A Neoteck pocket digital

multimeter is used for the voltage measurement while an Aneng digital multimeter is used for the current measurement.



Figure 4.16: Voltmeter and ammeter used in experiment

4.2.3.6 Flowmeter

The water flow rate in the experiment is measured using a Vyair DigiFlow 6710M flowmeter shown in Figure 4.17. It has a flow rate display of 0.2 – 5L/min and operating temperature range of 0 – 80 °C. The flowmeter is connected to the outlet of the water tank after the pump so as to measure the water flow rate.



Figure 4.17: Flowmeter used in experiment

4.2.3.7 Computer

Computers shown in Figure 4.18 are used during the experiment to observe and analyse the data recorded from the data logger, solar module analyser, voltmeter and ammeter. In addition, the output data from the pyranometer is observed using a computer.

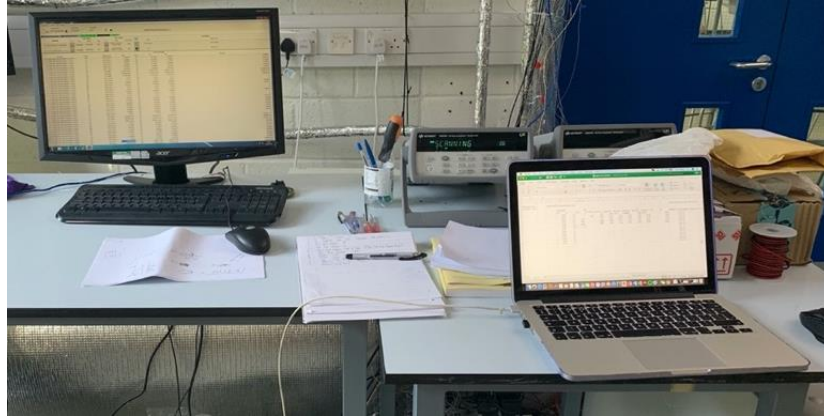


Figure 4.18: Computers used in experiment

4.3 Experimental Setup and Procedure

The arrangement of the PV, TEG, MCHP and cooling block is shown in Figure 4.19 and it can be seen that the MCHP is attached directly to the back surface of the PV. In addition, it can be seen that the hot side of the thermoelectric generator is attached to the condenser of the flat plate microchannel heat pipe while the cooling block is attached to the cold side of the TEG. Furthermore, the experimental setup of the hybrid PV-TE-MCHP is shown in Figure 4.20. Water is used to cool the thermoelectric generator in the hybrid system and the surfaces of the components are insulated to minimise heat loss. In this experimental study, two different test cases shown in Figure 4.21 are considered including PV-TE-MCHP with back surface insulation (Figure 4.21a) and without insulation (Figure 4.21b). The effect of the insulation on the performance of the hybrid system is studied and results are presented in subsequent section.



Figure 4.19: PV-TE-MCHP arrangement

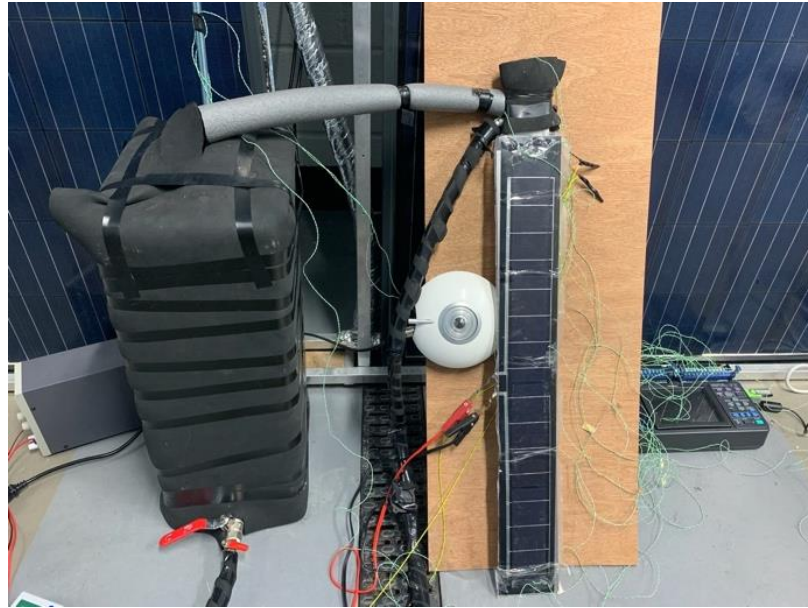


Figure 4.20: PV-TE-MCHP experimental setup

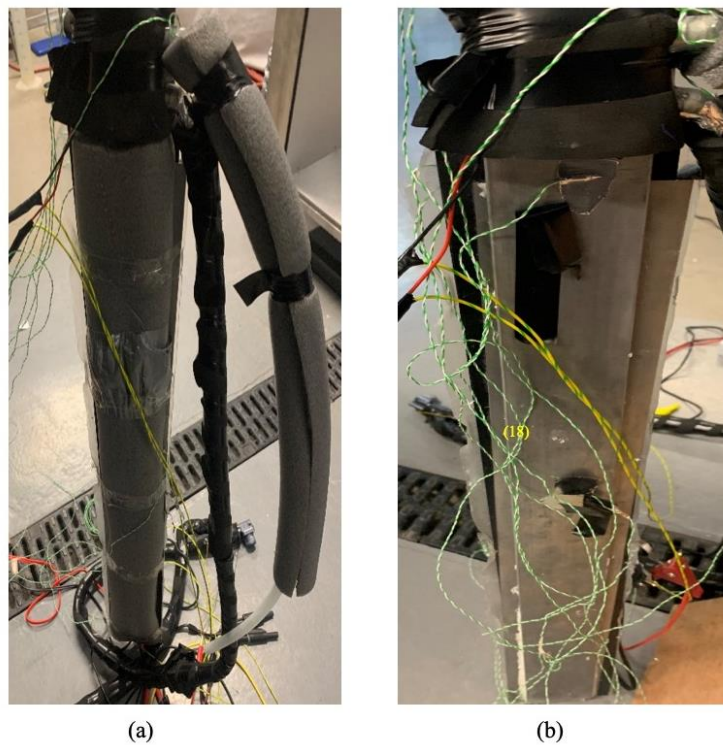


Figure 4.21: PV-TE-MCHP (a) with back surface insulation and (b) without insulation

The performance of the hybrid PV-TE-MCHP is compared to that of a conventional photovoltaic only system shown in Figure 4.22. The PV only system does not have any additional component attached to it. The complete experimental

setup can be seen in Figure 4.23 which consists of various components such as photovoltaic, thermoelectric generator, flat plate microchannel heat pipe, solar simulator, pyranometer, insulated water tank, direct current (DC) power supply, pump, flowmeter, solar module analyser, thermocouples, data logger, resistor box, cooling block, voltmeter and ammeter. Furthermore, several thermocouples are used to measure the temperature at different locations in the system and the position of the thermocouples in the experimental setup is listed in Table 4.3. In this experiment, three thermocouples are used to measure the average temperature of the PV while two thermocouples are used for obtaining the TEG cold side temperature. In addition, one thermocouple is used to obtain the TEG hot side temperature which is the same as the temperature of the MCHP condenser. Furthermore, three thermocouples are used to obtain the average temperature of the water in the tank and an additional thermocouple is used to measure the ambient temperature.



Figure 4.22: Photovoltaic experimental setup



Figure 4.23: Complete experimental setup for testing

Table 4.3: Position of thermocouples in experimental setup

Number	Position
PV-TE-MCHP	
1	PV front surface top
2	PV front surface middle
3	PV front surface bottom
4	TEG cold surface right
5	TEG cold surface left
6	TEG hot surface

7	Heat pipe surface middle
8	Water tank bottom
9	Water tank middle
10	Water tank top
11	Cooling block left
12	Cooling block right
13	Ambient temperature
PV only	
14	PV front surface top
15	PV front surface middle
16	PV front surface bottom

4.3.1 Experimental Procedure

An experimental methodology is utilized in this study therefore, the hypothesis that hybrid PV-TE-MCHP can provide enhanced performance compared to conventional PV only is tested experimentally. The experimental setup has been described in the section above while the experimental procedure is described here. This experiment is carried out in a laboratory at the University of Hull, UK in April and the testing is done for several days. The intensity of the solar radiation is varied for different test scenarios and all surfaces except the front surface of the PV are insulated. However, the insulation on the back surface of the MCHP was removed during a test scenario to investigate its effect on the performance of the hybrid system.

In addition, a comparison between the performance of the hybrid system and that of the PV only system is made. The electrical performance of the PV is measured every 10 minutes alongside the voltage and power output of the TEG. Therefore, the solar module analyser and multimeters are used simultaneously to obtain the electrical performance of the PV and TEG at an interval of 10 minutes.

Furthermore, a time interval of 20 seconds is used to record the temperature readings on the data logger. Depending on the test scenario, the systems are run for several hours to obtain valuable experimental data. The MCHP is placed directly behind the PV in parallel as shown in Figure 4.19. During the experiment, the PV-TE-MCHP and PV only systems are both placed at a title angle of 34° as shown in Figure 4.23. The pump is operated at a constant speed during the experiment therefore, throughout the system operation, the flow rate is maintained at 1 L/min while the water volume is kept constant at 10 L.

4.3.2 Laboratory Health and Safety

Since this experiment is carried out in a laboratory and it involves the use of a solar simulator, some health and safety procedures are observed to ensure the experiment is performed under safe conditions. Each of the components used in the experiment pose a unique safety concern therefore, risk assessment is performed. The laboratory condition when the system is in operation is shown in Figure 4.24. Furthermore, the routine start-up procedure for the experiment is as follows:

- 1) Put on the relevant personal protective equipment including ultraviolet glasses.
- 2) Check electrical connections for the photovoltaic, thermoelectric generator and pump.
- 3) Ensure the water connections have no signs of leakage, especially the water tank.

- 4) Check the bulb in the solar simulator for signs of damage or wear.
- 5) If any faults are noticed, perform relevant maintenance upon the piece of equipment and stop the start-up procedure.
- 6) Position the solar simulator and set experimental parameters.
- 7) Draw the lab curtains and fit with the interlock so that the light will be enclosed upon turning on.
- 8) Turn on the DC power supply for the pump and the pyranometer.
- 9) Turn on the ventilation system for the solar simulator.
- 10) Turn on the solar simulator and set the required radiation intensity.
- 11) Record and monitor the system parameters to ensure safe operation.



Figure 4.24: Laboratory condition during system operation

4.4 Results and Discussion

The experimental results from this study are presented in this section and analysed in detail. The experiment was carried out under laboratory conditions and the solar radiation is varied using a solar simulator. The relative mean error of all the experimental variables are obtained and shown in Table 4.4. Where T is temperature, G is solar radiation, I is electric current, U is electric voltage, P is power output and η is efficiency.

Table 4.4: Experimental relative mean error of variables

Variable	T	G	I	U	P	η
RME	0.33%	2%	$\pm 1\%$	$\pm 1\%$	$\pm 2\%$	$\pm 4\%$

4.4.1 Effect of Thermoelectric Load Resistance

The maximum power output of the thermoelectric generator can be obtained by impedance matching. Therefore, the external load resistance can be varied to obtain the maximum power output. Figure 4.25 shows the variation of load resistance with the current, voltage and power output of the TE in the hybrid system. The experiment was conducted using two different solar radiation values and the results obtained are shown in Figure 4.25. It can be seen from Figure 4.25a that the current of the thermoelectric decreases rapidly as the load resistance increases however, the voltage of the thermoelectric shows an opposing trend. A better understanding of the effect of external load resistance on thermoelectric power output is shown in Figure 4.25c. It can be seen that the power output firstly increases before decreasing as the load resistance is varied from 1 Ω to 10 Ω . In fact, the maximum power output of the thermoelectric is obtained at a load resistance value of 3 Ω . Therefore, it is important to investigate the optimum load resistance at which maximum power output can be

obtained. In addition, it can be seen from Figure 4.25c that the power output increases as the solar radiation increases because of the increase in absorbed energy by the thermoelectric and the greater temperature difference. Furthermore, the result in Figure 4.25b shows the rising tendency of the thermoelectric voltage as the load resistance is increased.

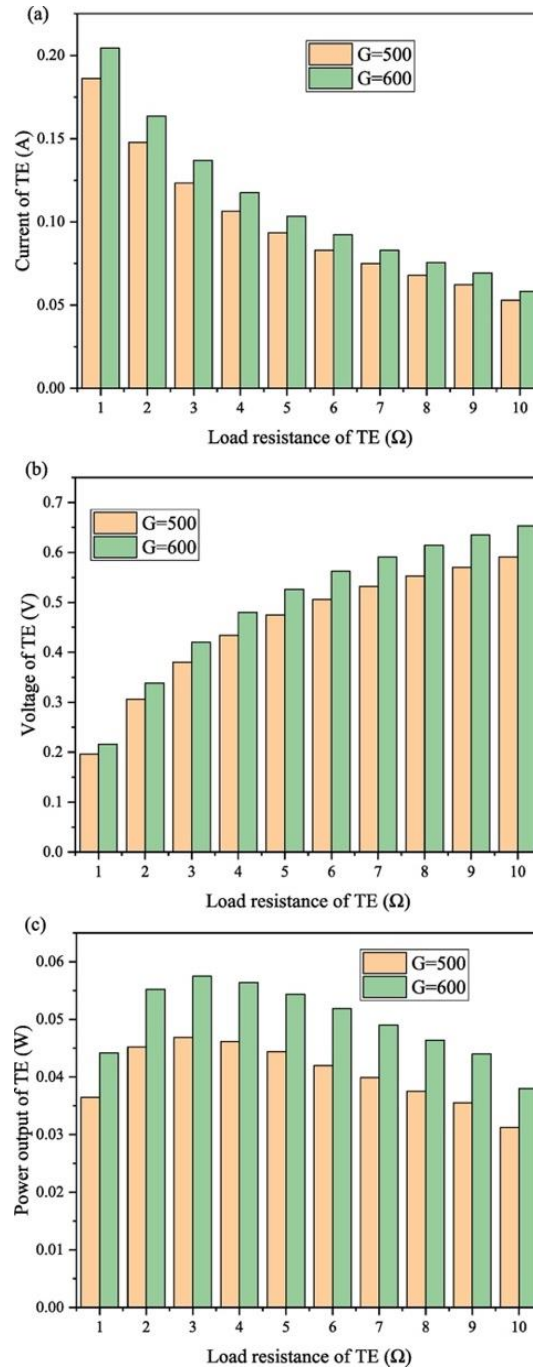


Figure 4.25: Variation of load resistance with (a) current (b) voltage and (c) power output of TE

4.4.2 Effect of Solar Radiation

Solar radiation is one of the most important parameters that significantly affects the performance of the hybrid system. Therefore, the effect of solar radiation variation on PV-TE-MCHP electrical performance is shown in Figure 4.26. It can be seen from Figure 4.26a that the open circuit voltage and short circuit current of the PV in the hybrid system show an opposing trend as the solar radiation is varied from 500 W/m² to 1000 W/m². While the short circuit current increases rapidly, the open circuit voltage decreases slowly as the radiation increases. In addition, it can be seen from Figure 4.26a that the voltage and current of the thermoelectric increases as the solar radiation increases. This shows that the PV and TE have a complex relationship as the photovoltaic performance (efficiency) decreases under high radiation values while that of the TE increases under high radiation values.

Furthermore, the average power output of the hybrid system is shown in Figure 4.26b. As expected, the power output of the hybrid system increases as the solar radiation increases. It is also important to note that the PV provides the greater percentage of the overall power output of the hybrid system. The power output of the PV-TE-MCHP increases from 1.86 W to 3.92 W as the solar radiation increases from 500 W/m² to 1000 W/m². Therefore, increased power output can be obtained from the hybrid system at high radiation values. However, the efficiency of the hybrid system decreases as the solar radiation increases as shown in Figure 4.26c.

The temperature response of the hybrid system to solar radiation variation is shown in Figure 4.27. The decrease in hybrid system efficiency as solar radiation increases can be explained by the increase in average PV temperature as the solar radiation increases as shown in Figure 4.27a. An increase in temperature of PV generally leads to a decrease in efficiency. In addition, Figure 4.27a shows the

temperature of the TE hot side increases rapidly with solar radiation increase and the cold side temperature also increases. The reason for the increase in cold side temperature is that the heat removed from the TE cold side is transported to the water tank, which is also recirculated back to the TE. As shown in Figure 4.27b, the temperature of water in the tank also increases as the solar radiation increases. Furthermore, the ambient temperature values recorded for the different test days the solar radiation was varied is shown in Figure 4.27b.

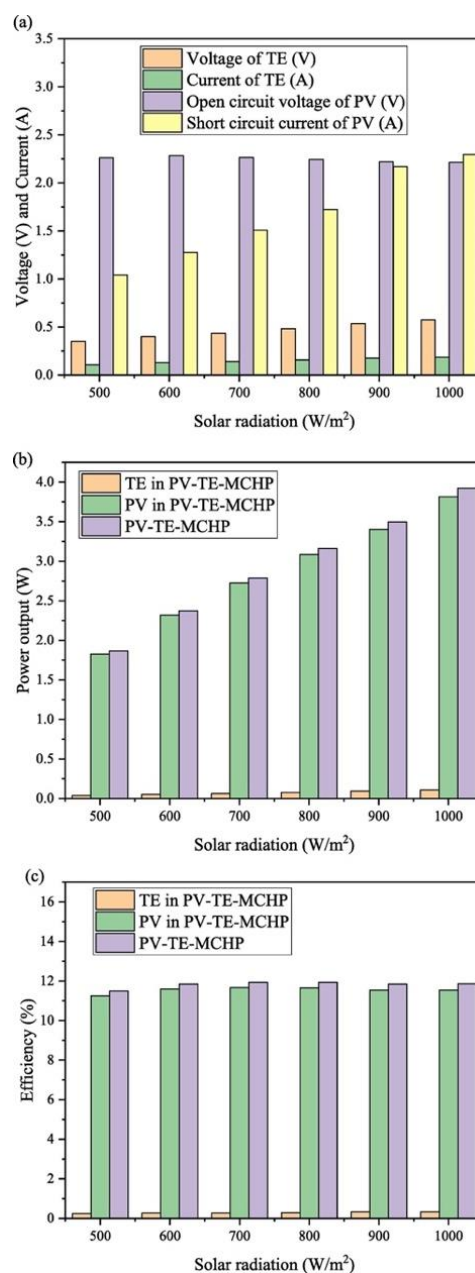


Figure 4.26: Solar radiation variation with (a) voltage, current (b) power output and (c) efficiency

The initial and final temperature of the water in the tank after a 5 h period is shown in Figure 4.27c. The hybrid system was run under a constant radiation value for 5 h to investigate the capacity of the system to increase the water temperature in the tank. In addition, the thermal efficiency of the system is calculated and shown in Figure 4.27c. It can be seen that the thermal efficiency gradually decreases as the solar radiation increases. This is because, although the difference between the initial and final water temperature increase with solar radiation increase, this difference is not significant enough to compensate for the increased solar energy absorbed therefore, the thermal efficiency which is a ratio between the useful thermal energy output and the input energy decreased as the solar radiation increased. Nevertheless, it can be seen from Figure 4.27c that the highest thermal efficiency of 69.53% is obtained for the day the system was run under a solar radiation value of 500 W/m². The lowest thermal efficiency value obtained is 56.57%, which is still very high thereby demonstrating the feasibility of the hybrid system for water heating and electricity production.

Furthermore, the exergy of the PV, TE and water tank in the hybrid system is calculated and shown in Figure 4.27d. It can be seen that the exergy of the TE in PV-TE-MCHP is very low although it increases from 0.13% to 0.18% as the solar radiation increases from 500 W/m² to 1000 W/m². In addition, the highest exergy efficiency of the PV in PV-TE-MCHP was 6.39% under a solar radiation of 700 W/m². The exergy efficiency of the PV and TE in the hybrid system are lower than their corresponding electrical efficiency because for the exergy efficiency calculation, the collector area is used while the PV cell area is used for the electrical efficiency calculation because the PV cells do not completely cover the surface. Furthermore, it can be seen from Figure 4.27d that the highest exergy efficiency obtained from the water tank is 1.63% at a

solar radiation of 1000 W/m^2 . The water tank exergy efficiency is highly dependent on the thermal efficiency and the environmental conditions, especially the ambient temperature.

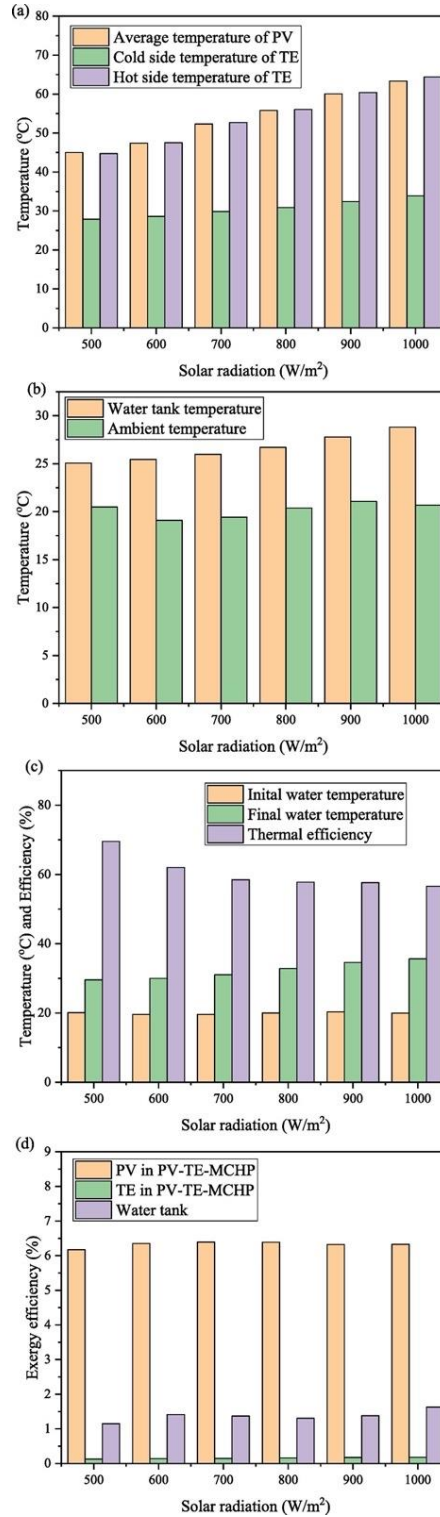


Figure 4.27: Variation of solar radiation with (a) PV, TE temperature (b) water tank, ambient temperature, (c) thermal efficiency and (d) exergy efficiency

4.4.3 Effect of Insulation and Comparison with Photovoltaic Only

To study the effect of insulation at the back surface of the MCHP on the performance of the hybrid system, two different cases were compared as shown in Figure 4.21a and Figure 4.21b respectively and the results obtained were compared to those of a PV only system as shown in Figure 4.28. It can be seen from Figure 4.28a that the presence of insulation at the back of the MCHP significantly lowers the efficiency of the hybrid system. The reason for this is that the presence of insulation at the rear of the microchannel heat pipe contributes to the additional increase of the photovoltaic temperature. In fact, after running the system for 1 h, the efficiency of the hybrid system with and without insulation is 11.98% and 12.19% respectively. In comparison, the efficiency of the PV only at that time is 11.94% thereby showing the advantage of the hybrid system over PV only system. In addition, as expected the efficiency of the hybrid system with and without insulation and that of the PV all decrease as the running time increases as shown in Figure 4.28a due to the increase in operating temperature.

Consequently, effective thermal management of photovoltaic is essential for maintaining high conversion efficiency during long operational periods. Furthermore, Figure 4.28a shows that the advantage of the hybrid system with insulation over PV only system is lost after running the system for a long period because of the ineffectiveness of the cooling system due to the increase in the water temperature in the tank. Therefore, the temperature of the cooling water in the tank must be maintained at a low value by introducing fresh cold water if only high electrical conversion efficiency is desired. Figure 4.28b shows that the PV-TE-MCHP without insulation provides the highest power output compared to the other systems. It can also be seen that the power output of the PV only stabilises after some time while those

of the PV-TE-MCHP with and without insulation continues to decrease due to the ineffectiveness of the cooling system after a long period of time. Consequently, there has to be a trade-off between obtaining increased power output or efficiency from the hybrid system and obtaining additional hot water as a by-product.

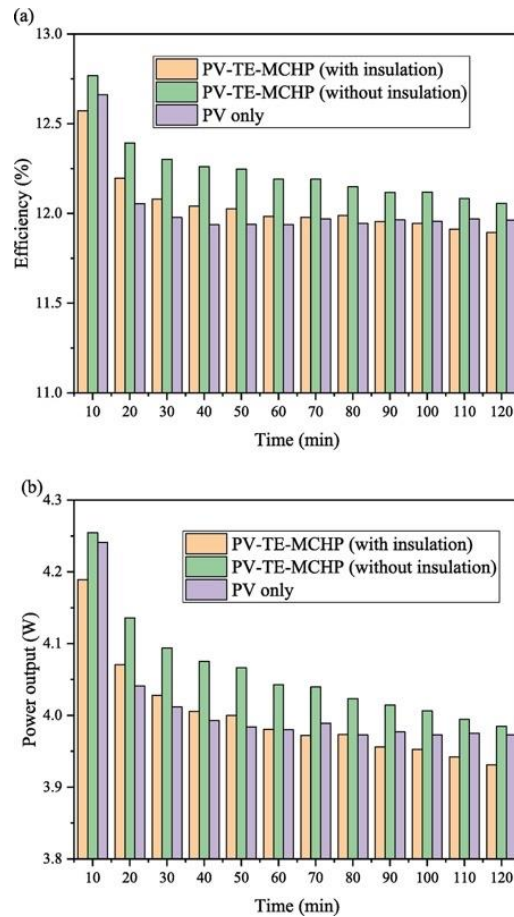


Figure 4.28: Time variation with (a) efficiency and (b) power output

The temperature response of the studied systems for a period of time is shown in Figure 4.29. The average temperature of the PV in the PV-TE-MCHP with and without insulation and the PV only is shown in Figure 4.29a. It can be seen clearly that the temperature of the PV in the PV only system is the highest therefore; the effectiveness of the hybrid system in providing reduced PV temperature is demonstrated. In fact, after running the system for 1 h, the PV temperature in the hybrid system with and without insulation is 62.2 °C and 61.9 °C respectively. In

comparison, the temperature of the PV in PV only at that time is 67.9 °C. Therefore, it can be concluded that the PV-TE-MCHP without insulation provides the lowest PV temperature. This is significant because there is an inverse relationship between the temperature and photovoltaic efficiency. Furthermore, the temperature difference across the hot and cold sides of the thermoelectric in the PV-TE-MCHP with and without insulation is shown in Figure 4.29b. As expected, the temperature difference of the TE in PV-TE-MCHP with insulation is higher than that without insulation due to the heat loss from absence of insulation. However, the contribution of the TE to the overall power output and efficiency of the hybrid system is not that significant to warrant the use of insulation.

In addition, it can be seen that the thermoelectric temperature difference gradually decreases as the time increases due to the reduction in the cooling effectiveness of the water tank with time. Similarly, as shown in Figure 4.29c, the temperature of the water in the tank when an insulation is used in the PV-TE-MCHP is higher than that without insulation because of better prevention of heat loss. Consequently, if water heating is the main requirement of the hybrid system, an insulation should be used, however, if enhanced electricity generation is desired, insulation should not be used on the back surface of the microchannel heat pipe. There is a direct relationship between the thermoelectric temperature difference and the water tank temperature because the water tank provides the cooling water for the thermoelectric cold side. Therefore, as the thermoelectric temperature difference in the hybrid systems decreases with increase in time (Figure 4.29b), the water tank temperature increases (Figure 4.29c). This means that the water tank is no longer effectively removing the waste heat from the thermoelectric cold side thus, the TE temperature difference decreases.

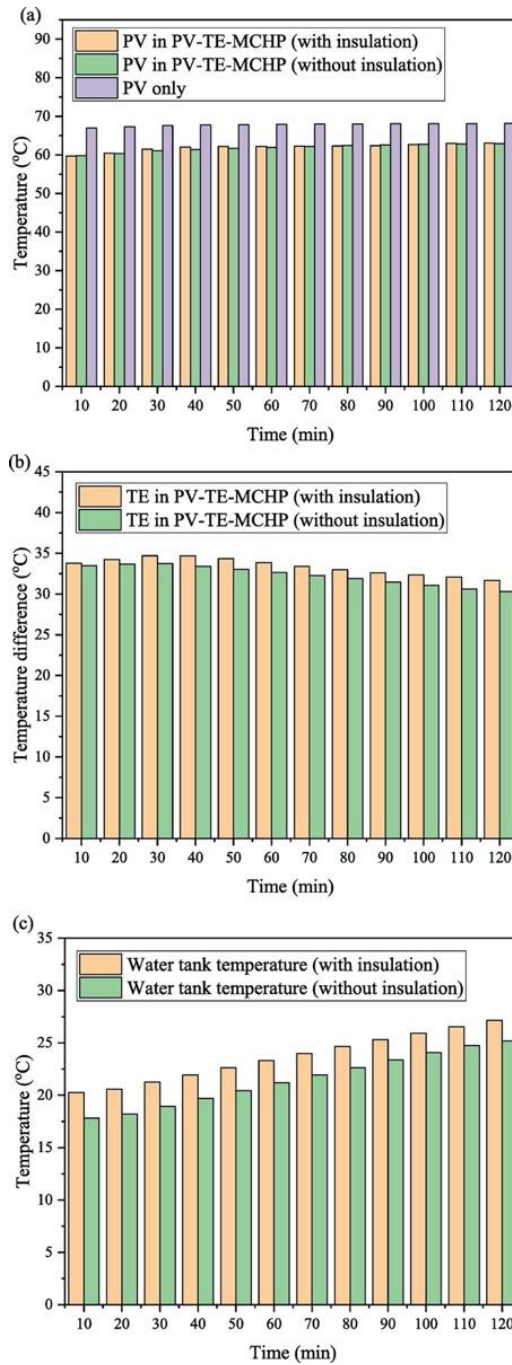


Figure 4.29: Time variation with (a) PV temperature (b) TE temperature difference and (c) water tank temperature

4.5 Model Validation/Refinement

The computer simulation models used in this research are validated with experimental results and published data. Results obtained from the hybrid PV-TE-

MCHP and PV only experiments carried out under laboratory conditions are used to validate the photovoltaic, thermoelectric generator and heat pipe models while the phase change material, contact resistance and thermal stress models are validated with published data obtained from literature. The modelling results are in very good agreement with the experimental results thereby showing the accuracy of the models without any need for refinement.

4.5.1 Validation with Experimental Results

The performance of a conventional photovoltaic module was measured during the laboratory experiment carried out under a solar radiation of 1000 W/m^2 for a period of time. Therefore, to validate the photovoltaic model, the simulation is performed using similar conditions as the experiment and results obtained are compared as shown in Figure 4.30.

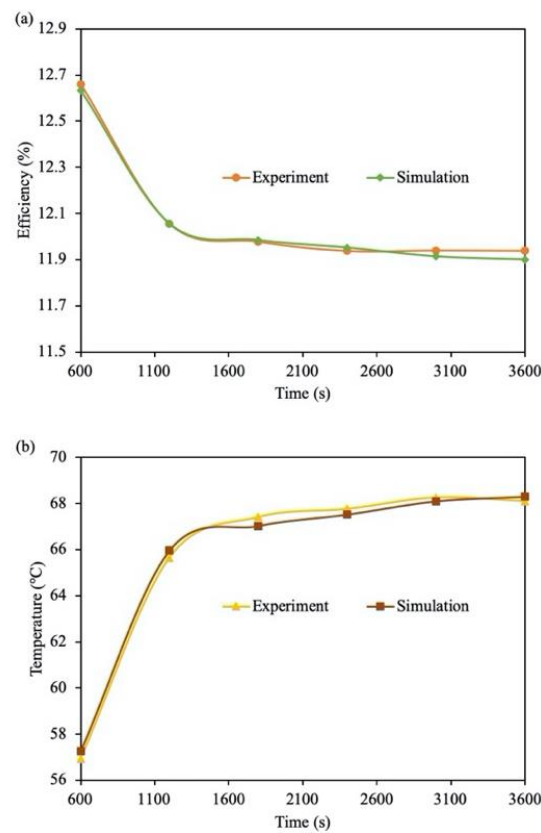


Figure 4.30: Variation of experimental and simulation (a) efficiency and (b) temperature of a conventional photovoltaic module

The electrical conversion efficiency of the photovoltaic module is shown in Figure 4.30a for a period of 3600 s (1 h). As expected, the photovoltaic efficiency decreases as the time increases due to the increase in temperature. Furthermore, it can be seen that the experimental and simulation results are in perfect agreement, with a root mean square error (RMSE) of 0.02. The temperature response of the photovoltaic module is shown in Figure 4.30b. It can be seen that the temperature of the photovoltaic increases as the time increases thereby leading to decrease in efficiency. In addition, the close agreement between the experimental and simulation results for the photovoltaic temperature response can be seen, with a RMSE of 0.28.

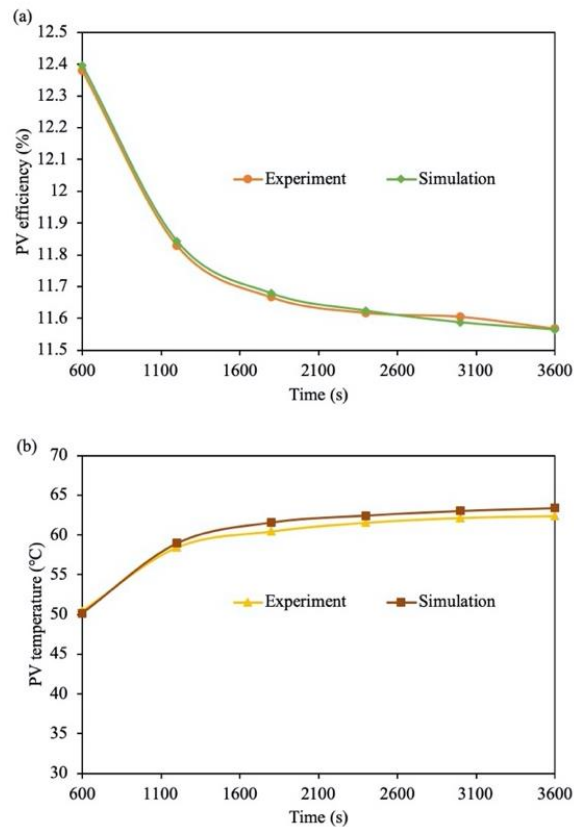


Figure 4.31: Variation of experimental and simulation (a) efficiency and (b) temperature of PV in PV-TE-MCHP

Furthermore, the performance of the photovoltaic in the hybrid PV-TE-MCHP system was measured during the laboratory experiment carried out under a solar

radiation of 1000 W/m^2 for a period of time and compared with the simulation results as shown in Figure 4.31. It can be seen from Figure 4.31a that the electrical efficiency of the PV in the PV-TE-MCHP reduces as the time increases. In addition, it can be seen that the experimental and simulation results follow the same trend and have a RMSE of 0.01. The temperature of the PV in the PV-TE-MCHP is shown in Figure 4.31b. A similar increasing trend in photovoltaic temperature is observed for both the experimental and simulation results as the system is studied for a longer period, with a RMSE of 0.84. Consequently, the photovoltaic simulation model is validated with experimental results and simulation results are justifiable.

The performance of the thermoelectric generator in the hybrid PV-TE-MCHP system was measured during the laboratory experiment carried out under a solar radiation of 1000 W/m^2 for a period of time and compared with the simulation results as shown in Figure 4.32. The electrical conversion efficiency of the TE in PV-TE-MCHP is shown in Figure 4.32a. A similar increasing trend is observed in the experimental and simulation thermoelectric efficiency in the hybrid PV-TE-MCHP, with a root mean square error (RMSE) of 0.05. In addition, it is obvious that the thermoelectric efficiency in the hybrid system increases initially as the time increases until it reaches a steady state. Furthermore, the temperature difference between the hot and cold sides of the thermoelectric generator in the hybrid PV-TE-MCHP is shown in Figure 4.32b. A good agreement between the experimental and simulation results is observed, with a RMSE of 1.33. Consequently, the thermoelectric generator simulation model is validated with experimental results and simulation results are justifiable.

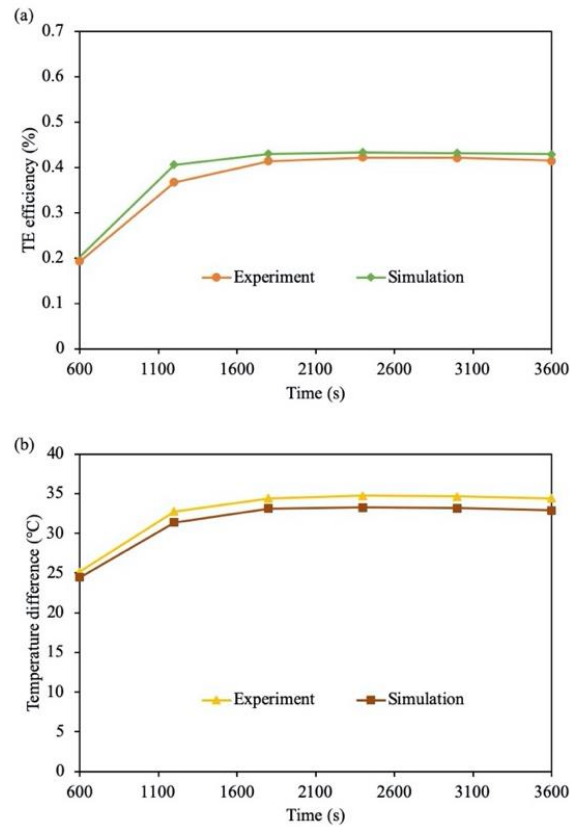


Figure 4.32: Variation of experimental and simulation (a) efficiency and (b) temperature difference of TE in PV-TE-MCHP

The performance of the flat plate microchannel heat pipe in the hybrid PV-TE-MCHP system was measured during the laboratory experiment carried out under a solar radiation of 1000 W/m^2 for a period of time and compared with the simulation results as shown in Figure 4.33. The average temperature of the MCHP back surface was measured during the experiment and this is compared to the simulation results obtained. As shown in Figure 4.33, the simplified heat pipe model is able to accurately predict the temperature at the back surface of the MCHP in the hybrid PV-TE-MCHP. A close agreement between the experimental and simulation results is observed, with a RMSE of 0.84. Furthermore, it is obvious that the temperature of the MCHP increases as time increases due to the increase in the waste heat transferred from the photovoltaic module which is attached to the top surface of the MCHP evaporator. In

addition, since the heat pipe is a passive device, it does not generate any electrical power output therefore, the MCHP model is validated with the experimental temperature results and the simulation results are justifiable.

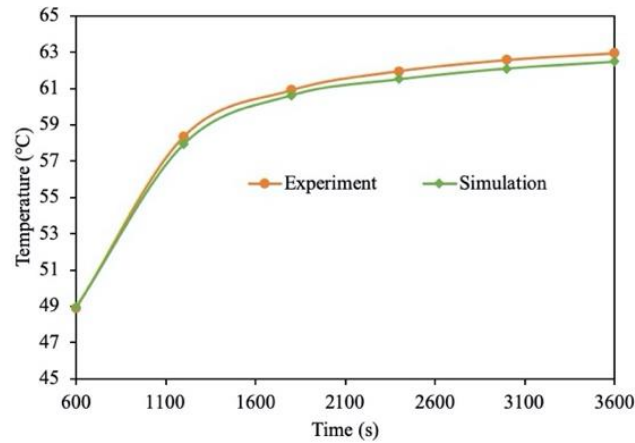


Figure 4.33: Variation of experimental and simulation temperature difference of MCHP in PV-TE-MCHP

4.5.2 Validation with Published Data

Firstly, the commercial thermoelectric generator module (GM250-127-14-16) used in this research is validated with the datasheet from the manufacturer, which contains the experimental results obtained. Therefore, the operating parameters of the thermoelectric generator including matched load power output at different hot and cold sides temperature is used to validate the simulation model and the result obtained is shown in Figure 4.34. It is obvious that the simulation results agree closely with the manufacturer data therefore, the thermoelectric generator model used in this research is accurate and justifiable.

Furthermore, the phase change material (PCM) model used in this research is validated with a similar PCM model used in the published paper (Manikandan et al., 2019). Since the objective is to ensure the simulation model is accurate, the material properties and simulation conditions are set to those in the referenced paper and the result obtained is shown in Figure 4.35. It can be seen clearly that the results obtained

in the previous study and this present study are in good agreement consequently, the PCM model is validated.

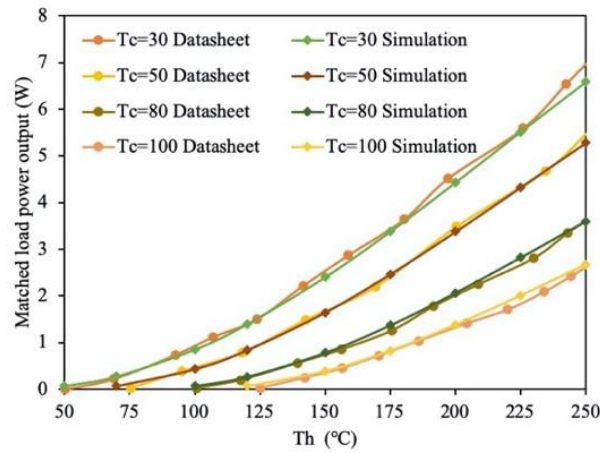


Figure 4.34: Validation of thermoelectric generator model with manufacturer datasheet

(European Thermodynamics Limited, 2014a)

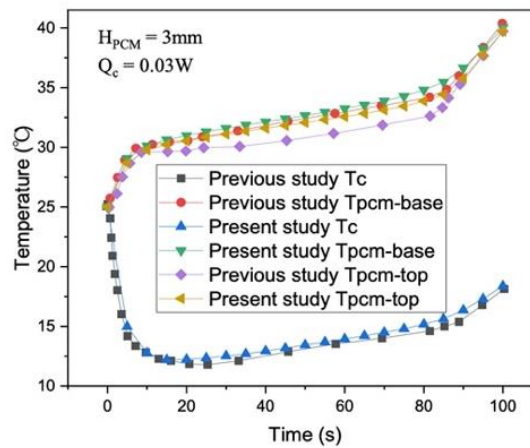


Figure 4.35: Validation of PCM model with previous study (Manikandan et al., 2019)

The contact resistance model used in this research is validated with a similar contact resistance model used in the published paper (He et al., 2019a). This model was for a thermoelectric generator which accounted for the thermoelectric thermal contact resistance (R_c) and electrical contact resistance (R_{cont}). In addition, simulation conditions are set to those in the referenced literature. The results obtained in the previous study [PS] and this current research are shown Figure 4.36 and it is

very clear that the results are closely matched therefore, the contact resistance model is validated.

Furthermore, the thermal stress model used in this research is validated with a similar thermal stress model used in the published paper (Yilbas et al., 2016) and simulation conditions are set to those in the referenced paper for proper comparison. The results obtained are shown in Figure 4.37. It can be seen clearly that both results are very identical and therefore, the thermal stress model is validated.

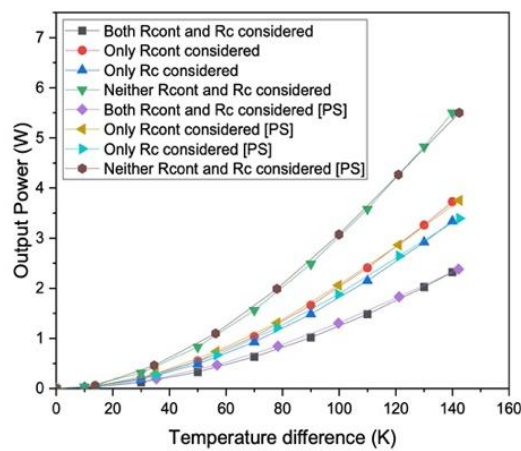


Figure 4.36: Validation of contact resistance model with previous study (He et al., 2019a)

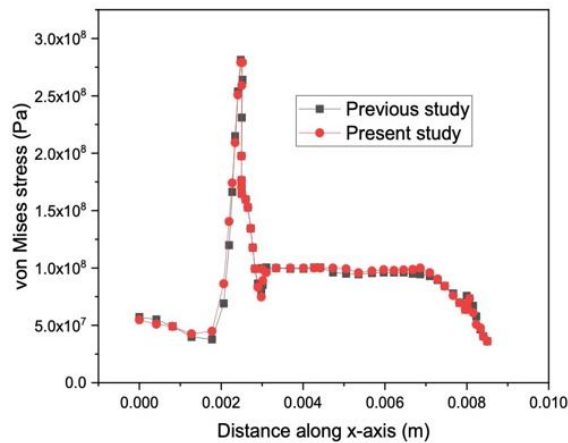


Figure 4.37: Validation of thermal stress model with previous study (Yilbas et al., 2016)

4.6 Chapter Summary

This chapter presented the experimental testing of the proposed hybrid system and computer simulation model validation. The main PV-TE-MCHP components including photovoltaic module, thermoelectric generator, flat plate microchannel heat pipe were described in addition to the other test rig components including solar simulator, water tank, cooling block, pump, DC power supply, resistor box, insulation, thermal grease and adhesive. Additional measurement instruments used in the experiment including pyranometer, thermocouple, data logger, solar module analyser, voltmeter, ammeter, flowmeter and computer were described in detail. The experimental setup and procedure followed were explained in addition to the laboratory health and safety procedures. Furthermore, the experimental results for a hybrid photovoltaic-thermoelectric with flat plate microchannel heat pipe and water cooling were presented and the feasibility of the hybrid system for electricity generation and hot water production was demonstrated.

Using a solar simulator, solar radiation was varied for different test scenarios and exergy analysis was performed. The effects of thermoelectric load resistance, insulation layer on the back surface of the flat plate microchannel heat pipe and solar radiation on the performance of the hybrid system were presented and a comparison with a photovoltaic only system was made. The experiment was carried out in a laboratory at the University of Hull, United Kingdom in April. Furthermore, the computer simulation models used in this research were validated with experimental results and published data. The main conclusions from the experimental study carried out are:

- 1) The efficiencies of the photovoltaic-thermoelectric-microchannel heat pipe with and without insulation and that of the photovoltaic only after 1 h were

11.98%, 12.19% and 11.94% respectively. Therefore, the hybrid system provided an enhanced performance.

- 2) There has to be a trade-off between obtaining increased power output or efficiency from the hybrid system and obtaining additional hot water as a by-product.
- 3) The photovoltaic temperature in the hybrid system with and without insulation (62.2 °C and 61.9 °C respectively) was lower than that in the photovoltaic only system (67.9 °C) after 1 h.
- 4) There is an optimum load resistance for obtaining maximum power output from the thermoelectric generator.
- 5) The average power output of the hybrid system increased from 1.86 W to 3.92 W when the solar radiation increased from 500 W/m² to 1000 W/m².
- 6) The highest and lowest thermal efficiencies obtained were 69.53% and 56.57% respectively under certain conditions.

CHAPTER 5 HYBRID PHOTOVOLTAIC- THERMOELECTRIC OPTIMIZATION RESULTS

5.1 Chapter Introduction

This chapter presents the results obtained using the validated simulation models for optimization of hybrid photovoltaic thermoelectric system and hybrid photovoltaic-thermoelectric-heat pipe system. Innovative asymmetrical thermoelectric geometry and conventional symmetrical thermoelectric geometry are utilized in the hybrid system for performance enhancement. The following tasks are addressed in this chapter:

- 1) Presenting steady state photovoltaic-thermoelectric optimization results.
- 2) Presenting transient state photovoltaic-thermoelectric optimization results.
- 3) Presenting photovoltaic-thermoelectric contact resistance optimization results.
- 4) Presenting photovoltaic-thermoelectric-heat pipe optimization results.

The optimization results presented in this chapter will provide valuable information on the feasibility of hybrid photovoltaic-thermoelectric systems with and without heat pipe. In addition, the results will provide useful insights into thermoelectric geometry optimization in hybrid systems and photovoltaic-thermoelectric accurate modelling.

5.2 Steady State Photovoltaic-Thermoelectric

The schematic diagrams of the different geometries of the hybrid system simulated are shown in Figure 5.1, Figure 5.2 and Figure 5.3 corresponding to the range $0.5 \leq R_A \leq 2$ and $0.5 \leq R_S \leq 2$. R_A is the cross-sectional area ratio of the thermoelectric element hot and cold junctions ($R_A = A_H/A_C$) and R_S is the area ratio

of the n-type and p-type thermoelectric elements ($R_S = A_n/A_p$). The system consists of a solar concentrator, PV module, tedlar, and TEG module. The PV module is a silicon cell and the TEG module consists of bismuth telluride thermoelectric elements which are connected electrically in series and thermally in parallel.

The nine different geometric configurations analysed are shown in Figure 5.1, Figure 5.2 and Figure 5.3. The geometric configurations when $R_A = 0.5$ are shown in Figure 5.1. For this case, Figure 5.1a, Figure 5.1b, Figure 5.1c show the configurations when $R_S = 0.5$, $R_S = 1$ and $R_S = 2$ respectively. Furthermore, the geometric configurations when $R_A = 1$ are shown in Figure 5.2. The configurations when $R_S = 0.5$, $R_S = 1$ and $R_S = 2$ are shown in Figure 5.2a, Figure 5.2b and Figure 5.2c respectively for this case. Finally, Figure 5.3 shows the geometric configurations when $R_A = 2$. For this case, Figure 5.3a, Figure 5.3b, Figure 5.3c show the configurations when $R_S = 0.5$, $R_S = 1$ and $R_S = 2$ respectively. The PV efficiency at standard test conditions is 10% for a PV cell with temperature coefficient of 0.001 K^{-1} (Cell A). The PV efficiency at standard test condition is 15% for a PV cell with temperature coefficient of 0.004 K^{-1} (Cell B).

Different geometrical configurations investigated are shown in Figure 5.1, Figure 5.2 and Figure 5.3. The temperature and voltage distributions corresponding to the maximum efficiency obtained are shown in Figure 5.4, Figure 5.5 and Figure 5.6 for $R_A = 0.5$, $R_A = 1$ and $R_A = 2$ respectively. These figures all correspond to the case when $R_S = 1$ and $\varphi_{PV} = 0.001/K$ (Cell A). Furthermore, temperature coefficient affects the temperature and voltage distributions in all the geometrical configurations investigated. Figure 5.4a, Figure 5.5a, and Figure 5.6a show the temperature distributions for $R_A = 0.5$, $R_A = 1$ and $R_A = 2$ respectively. While Figure 5.4b, Figure

CHAPTER 5 HYBRID PHOTOVOLTAIC-THERMOELECTRIC OPTIMIZATION RESULTS

5.5b and Figure 5.6b show the voltage distributions for $R_A = 0.5$, $R_A = 1$ and $R_A = 2$ respectively. In this study, a concentration ratio of 5 is used unless otherwise stated.

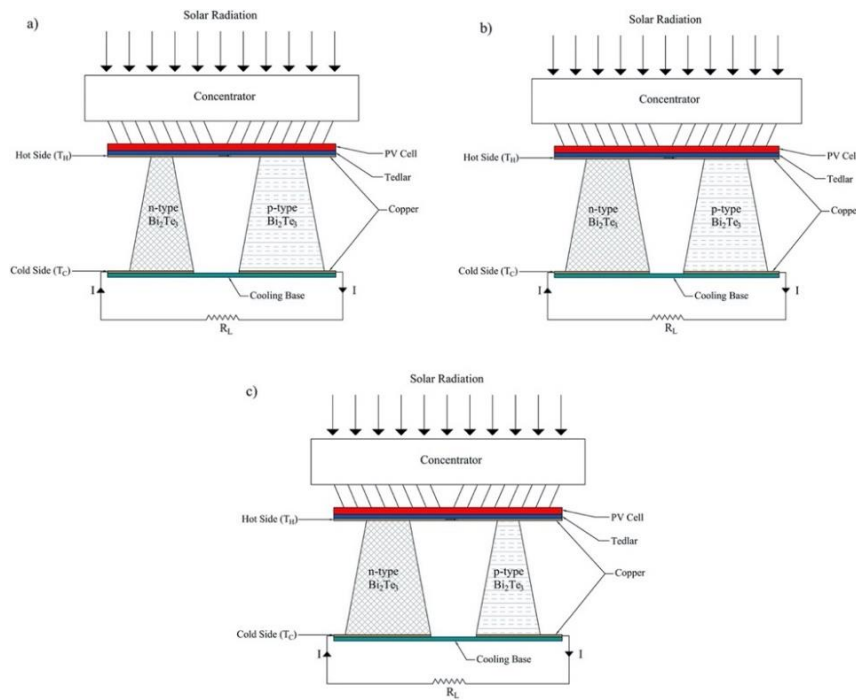


Figure 5.1: Schematic diagrams of a PV-TE with different leg geometries for $R_A = 0.5$ and a) $R_S = 0.5$ b) $R_S = 1$ c) $R_S = 2$

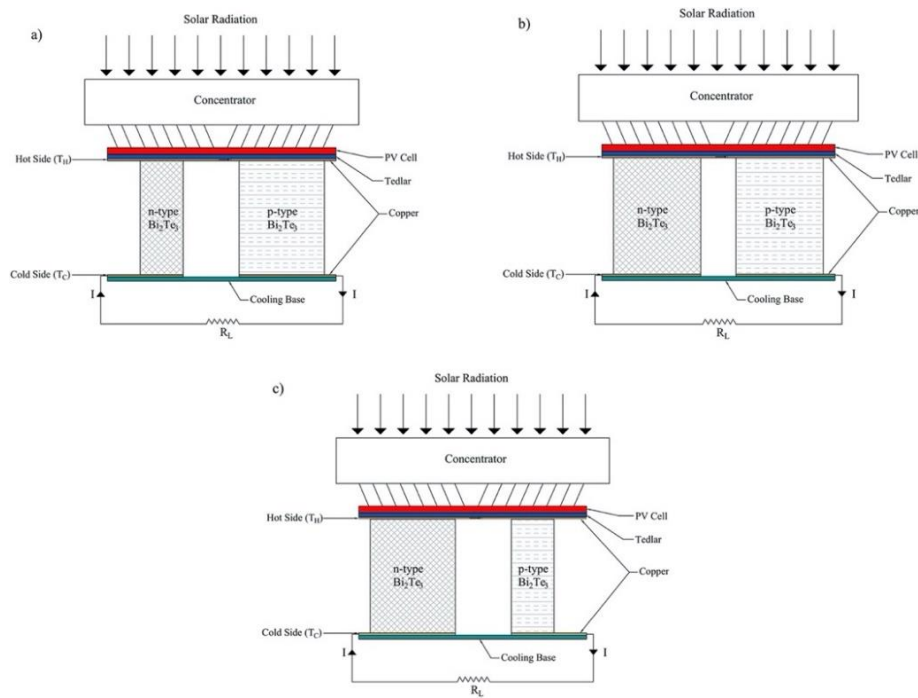


Figure 5.2: Schematic diagrams of a PV-TE with different leg geometries for $R_A = 1$ and a) $R_S = 0.5$ b) $R_S = 1$ c) $R_S = 2$

CHAPTER 5 HYBRID PHOTOVOLTAIC-THERMOELECTRIC OPTIMIZATION RESULTS

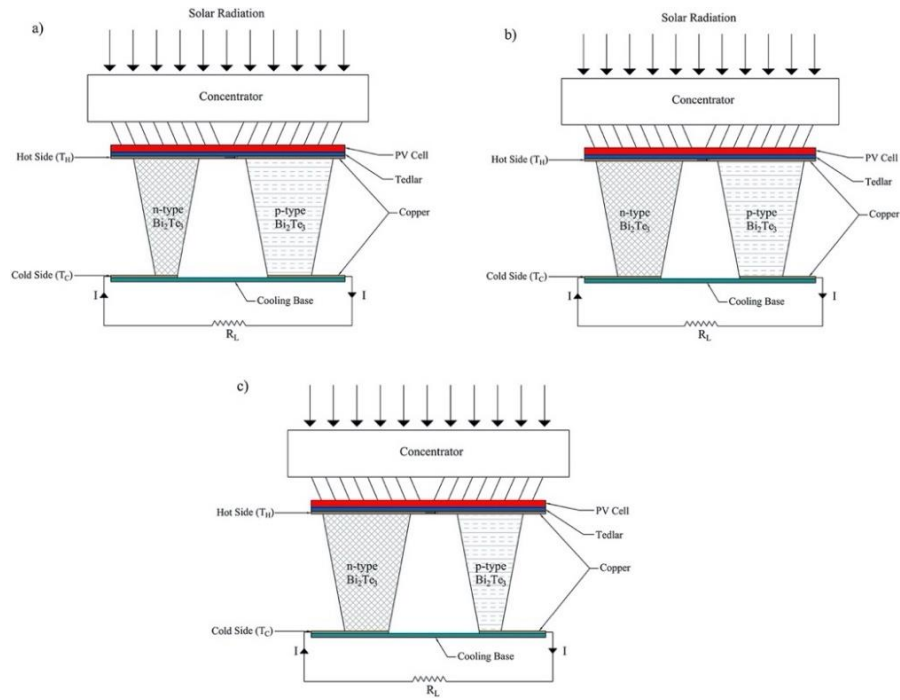


Figure 5.3: Schematic diagrams of a PV-TE with different leg geometries for $R_A = 2$ and a) $R_S = 0.5$ b) $R_S = 1$ c) $R_S = 2$

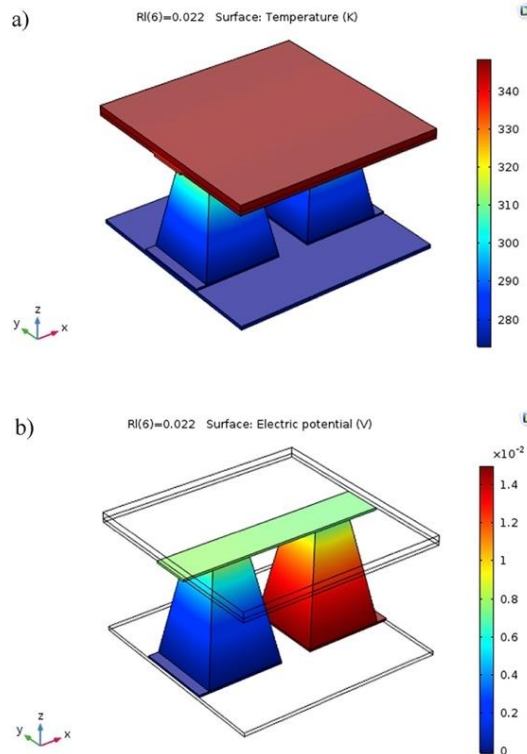


Figure 5.4: PV-TE 3-dimensional a) Temperature and b) Voltage distributions for $R_A = 0.5$

CHAPTER 5 HYBRID PHOTOVOLTAIC-THERMOELECTRIC OPTIMIZATION RESULTS

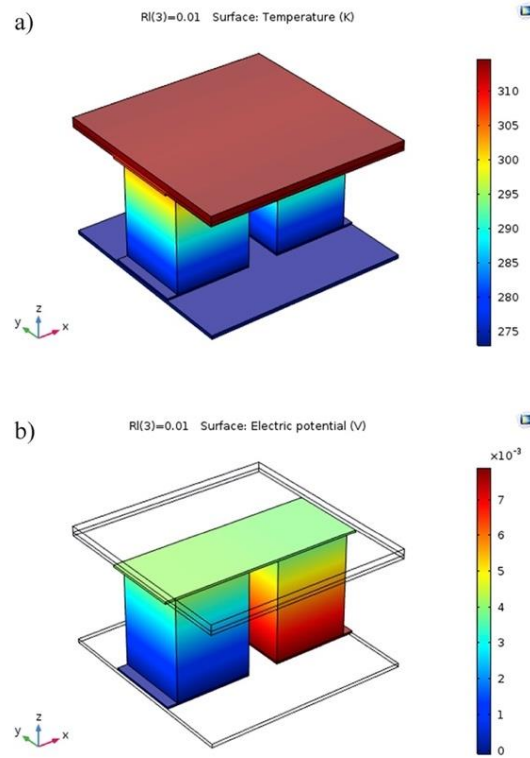


Figure 5.5: PV-TE 3-dimensional a) Temperature and b) Voltage distributions for $R_A = 1$

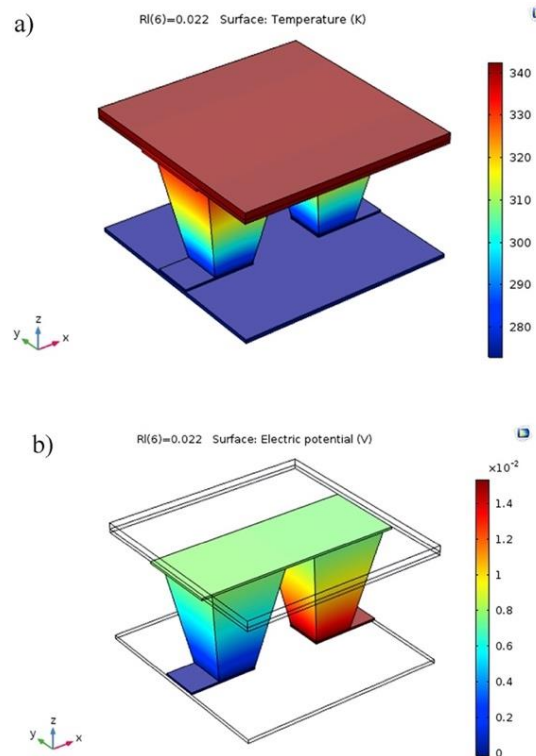


Figure 5.6: PV-TE 3-dimensional a) Temperature and b) Voltage distributions for $R_A = 2$

5.2.1 Boundary Conditions

To simplify the model used in this numerical study, the following assumptions have been taken:

- 1) Only steady state conditions are considered.
- 2) The cold side of the TEG is maintained at a constant temperature of 273 K.
- 3) Heat transfer occurs only in one dimension.
- 4) Two conversion efficiencies of PV (Cell A and Cell B) are considered (10% and 15%) for the two temperature coefficients used (0.001 K^{-1} and 0.004 K^{-1}) respectively and they change with temperature.
- 5) External heat flux is applied at the upper surface of the PV cell.
- 6) Convective and radiative loss are considered at the upper surface of the PV cell.

5.2.2 Geometry Area Ratios

The geometry of the thermoelectric elements in a hybrid PV-TE system influence the overall performance of the system which is measured in terms of its overall power output and conversion efficiency. Therefore, the two geometry area ratios which completely describe the geometry of thermoelectric elements in a hybrid PV-TE system are studied for the range $0.5 \leq R_A \leq 2$ and $0.5 \leq R_S \leq 2$ and optimized to obtain the maximum efficiency from the hybrid system. In addition, the geometry area ratios are investigated for the two different PV temperature coefficient values considered and the results obtained are shown in Figure 5.7 and Figure 5.8.

It can be seen clearly from Figure 5.7 and Figure 5.8 that the maximum hybrid PV-TE system efficiency depends greatly on the geometry of the thermoelectric elements in the hybrid system. Furthermore, it can be seen that the temperature coefficient value plays an important role in determining the optimum geometry for the

hybrid PV-TE system and consequently the maximum efficiency obtainable. The cross-sectional area ratio of the thermoelectric element hot and cold junctions ($R_A = A_H/A_C$) and the area ratio of the n-and p-type thermoelectric elements ($R_S = A_n/A_p$) are the two geometry area ratios analysed.

Figure 5.7 shows that when $\varphi_{PV} = 0.001/K$ (Cell A), the optimum geometry for the thermoelectric element in the hybrid PV-TE system is dissymmetrical i.e. $R_A = R_S \neq 1$. In essence, the optimum geometry of the TEG in the hybrid system is the same as its geometry in a TEG only system because the temperature coefficient value of the PV is too low to affect its geometry in the hybrid system. Rezanian et al. (2014) and Al-Merbati et al. (2013) found the optimum geometry of the thermoelectric elements in a TEG only system to be dissymmetrical. Furthermore, it can be seen that for all the values of R_S considered, the minimum efficiency all occurs when $R_A = 1$. In addition, efficiency increase can be observed for $R_A = R_S = 0.5$ and $R_A = R_S = 2$ thus, implying that the optimum geometry of the thermoelectric element in a hybrid system to obtain the maximum overall efficiency is dissymmetrical. Although the efficiency improvements might not be very significant now, the combination of several thermoelectric devices in series would lead to a more significant overall efficiency improvement.

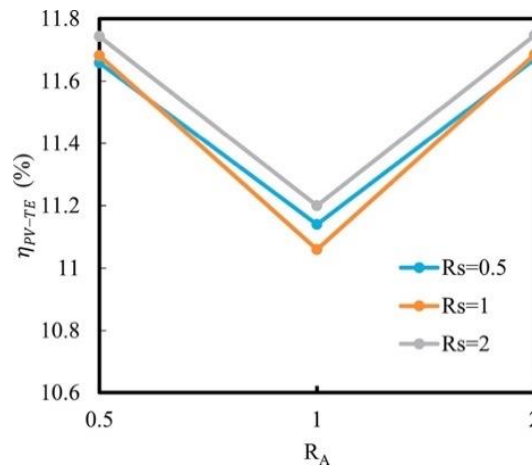


Figure 5.7: Overall PV-TE efficiency vs geometry area ratios for Cell A

Figure 5.8 shows an opposite trend to results from Figure 5.7 because the PV temperature coefficient has been increased to 0.004/K (Cell B). Furthermore, it is clear that the percentage increase in hybrid system efficiency values obtained for the different geometry area ratios in Figure 5.8 is lower than those obtained in Figure 5.7. This is because the efficiency of the hybrid PV-TE system decreases as the PV temperature coefficient increases (Yin et al., 2018b). In addition, the optimum geometry of the TEG in the hybrid system is symmetrical for this temperature coefficient value (0.004/K). Furthermore, it can be seen from Figure 5.8 that the maximum efficiency occurs when $R_A = 1$ for all the values of R_S considered. Therefore, it can be concluded that when a high temperature coefficient value is used, the optimum geometry of the TEG in a hybrid system is different from its geometry in a TEG only system. This is a very important finding that will help researchers accurately choose the PV temperature coefficient value and geometrical configuration to be used for obtaining maximum efficiency.

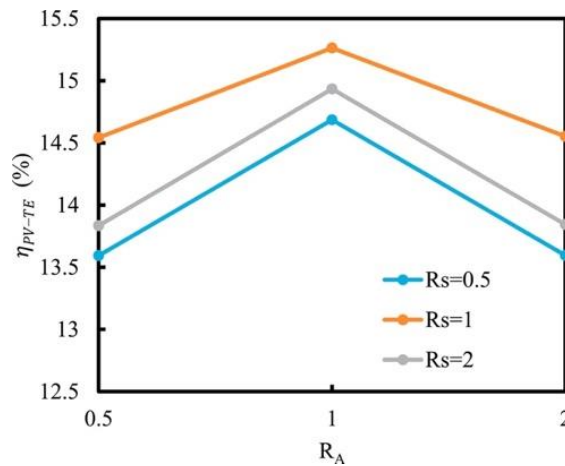


Figure 5.8: Overall PV-TE efficiency vs geometry area ratios for Cell B

5.2.3 Geometric Parameters

The thermoelectric element geometric parameters such as Height and Area can affect the maximum efficiency of the hybrid system. Furthermore, these geometric

parameters also affect the temperature difference across the thermoelectric device and consequently, the power output from these devices. The effects of these geometric parameters on the overall hybrid system efficiency and TE temperature difference are shown in Figure 5.9, Figure 5.10, Figure 5.11, Figure 5.12, Figure 5.14 and Figure 5.15 for $0.5 \leq R_A \leq 2$, $R_S = 1$, $\varphi_{PV} = 0.001/K$ (Cell A) and $\varphi_{PV} = 0.004/K$ (Cell B).

5.2.3.1 Case A ($R_A = 0.5$)

It can be seen from Figure 5.9a and Figure 5.9b that the overall efficiency of the hybrid system shows a decreasing trend as the thermoelectric element height increases. In addition, it is clear that the PV temperature coefficient value affects the steepness of the efficiency drop as thermoelectric element height increases. Therefore, shorter thermoelectric elements should be used to obtain improved hybrid PV-TE efficiency.

Furthermore, it can be seen from both Figure 5.9a and Figure 5.9b that the overall efficiency of the hybrid system increases as the cross-sectional area of the thermoelectric element increases. This is true no matter the temperature coefficient value used thus, there is an optimum thermoelectric element height and area which gives the maximum hybrid system efficiency. In addition, it can be seen from Figure 5.9b that the efficiency of the hybrid system for some thermoelectric element height and area is lower in comparison with the standard efficiency of the PV cell (15%). This can also be observed from Figure 5.9a where the standard efficiency of the PV cell (10%) is greater than that of the hybrid system for some thermoelectric element height and area. This implies that it is very important to find the optimum geometry for the thermoelectric element in the hybrid PV-TE system if high overall efficiency is desired.

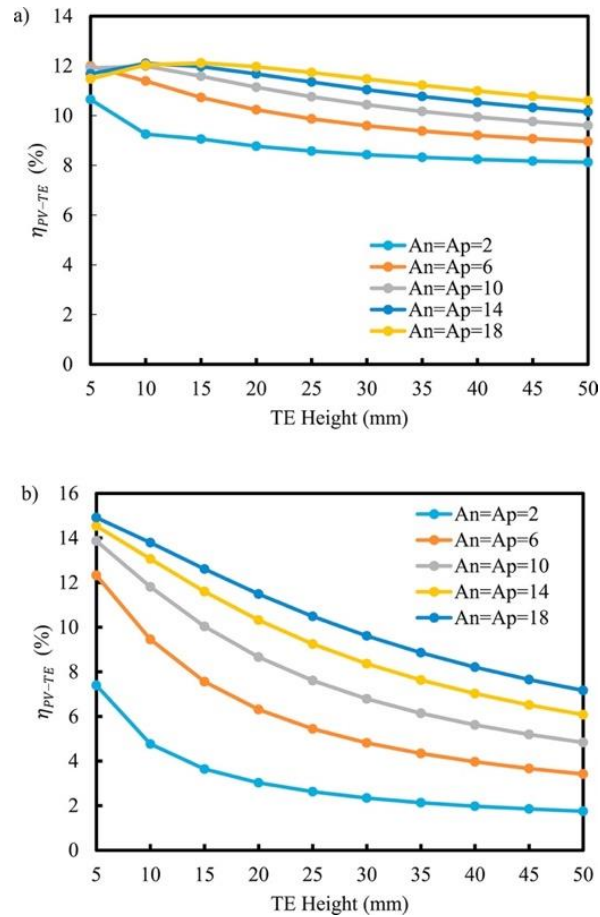


Figure 5.9: Hybrid system efficiency vs thermoelectric element height for $R_A = 0.5$ and a) Cell

A b) Cell B

5.2.3.2 Case B ($R_A = 1$)

Figure 5.10 shows the variation of overall system efficiency with thermoelectric element height and area. It can be seen from Figure 5.10b that the hybrid system efficiency shows a decreasing trend as the thermoelectric element height increases and an increasing trend as the thermoelectric element area increases when $\varphi_{PV} = 0.004/K$. However, Figure 5.10a shows that when $\varphi_{PV} = 0.001/K$, the overall efficiency initially increases before decreasing as the thermoelectric element height increases for some certain thermoelectric element area. This implies that maximum hybrid system efficiency can be obtained using some specific geometry parameters.

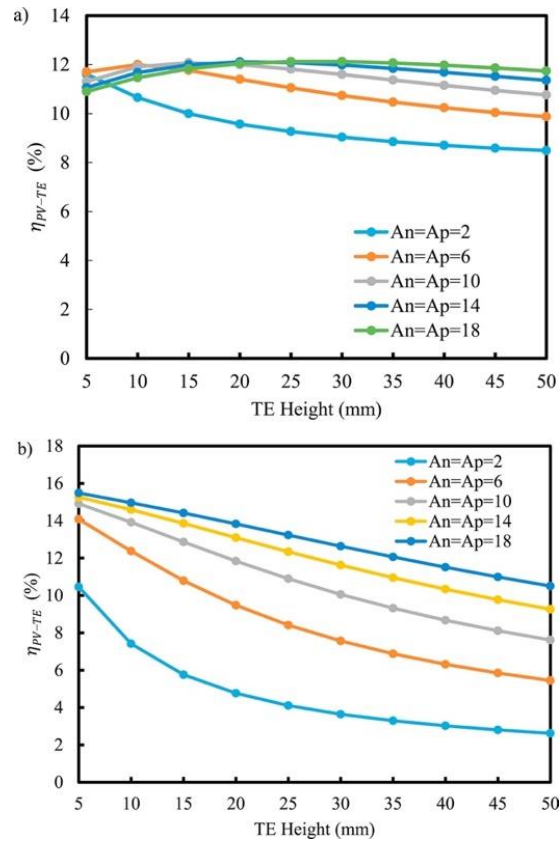


Figure 5.10: Hybrid system efficiency vs thermoelectric element height for $R_A = 1$ and a) Cell A
b) Cell B

5.2.3.3 Case C ($R_A = 2$)

The variation of overall hybrid system efficiency with thermoelectric element height and area is shown in Figure 5.11a and Figure 5.11b for both temperature coefficient values considered respectively. In addition, it can be seen from Figure 5.11a that the overall efficiency values obtained for this Case C are slightly higher than those obtained for Case A (Figure 5.9a). Therefore, the optimum geometry for a thermoelectric element in a hybrid PV-TE system when $\phi_{PV} = 0.001/K$ is $R_A = 2$. However, the optimum geometry when $\phi_{PV} = 0.004/K$ is $R_A = 1$.

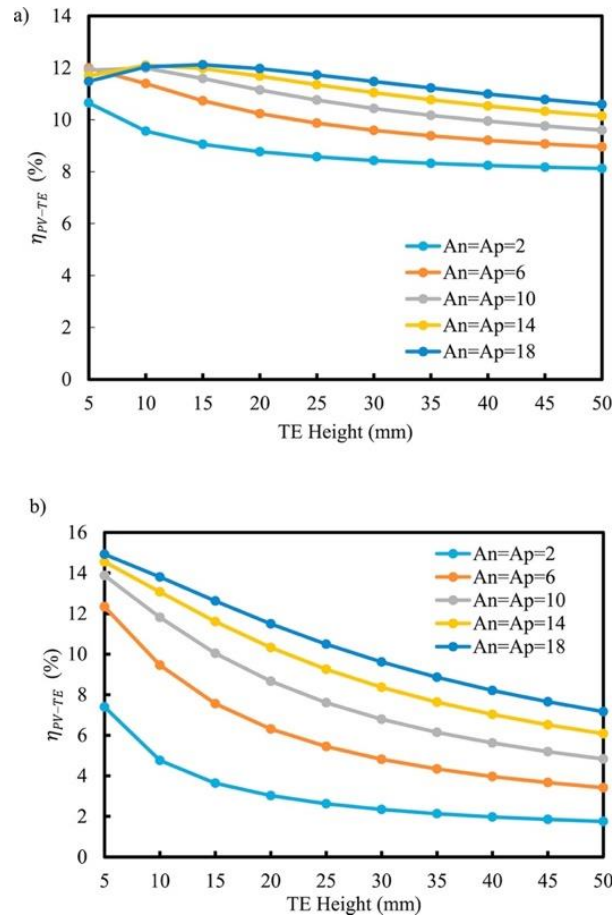


Figure 5.11: Hybrid system efficiency vs thermoelectric element height for $R_A = 2$ and a) Cell A
b) Cell B

5.2.4 Section Conclusion

The optimum geometry of a thermoelectric element in a hybrid PV-TE system has been investigated in this research using finite element method. Two geometry area ratios which completely describe the geometry of the thermoelectric element was investigated for the range $0.5 \leq R_A \leq 2$ and $0.5 \leq R_S \leq 2$. R_A is the cross-sectional area ratio of the thermoelectric element hot and cold junctions (A_H/A_C) while R_S is the area ratio of the n- and p-type thermoelectric elements (A_n/A_p).

Nine different geometric configurations were analysed for two different PV cells. The results obtained show that the PV temperature coefficient value affects the geometry and efficiency of the hybrid system. It was found that the hybrid PV-TE

system performs better with symmetrical TEG geometry ($R_A = R_S = 1$) if a PV temperature coefficient of 0.004/K (Cell B) is used. This is different from the optimum geometry for a TEG only system. However, the optimum geometry of the TEG in a hybrid system will be the same as that of a TEG only system (dissymmetrical i.e. $R_A = R_S \neq 1$) if a PV temperature coefficient of 0.001/K (Cell A) is used.

Geometric parameters such as thermoelectric element height and area were found to influence the performance of the hybrid PV-TE system. In general, thermoelectric element with shorter heights and higher cross-sectional area should be used to obtain maximum hybrid system efficiency.

5.3 Transient State Photovoltaic-Thermoelectric

The four different thermoelectric leg geometries which are considered in this study are shown in Figure 5.12. All layers of the photovoltaic are in direct contact and of equal area. A commercial bismuth telluride (Bi_2Te_3) thermoelectric generator (40mm x 40mm) manufactured by Thermonamic Co. (TEP1-1264-3.4) is used in this study. The TEG is made up of 126 n-type and p-type thermoelectric leg pairs which are connected in series electrically and thermally in parallel. Furthermore, air cooling is used in this study and the heat sink is made of copper material. Figure 5.12a shows the schematic of the hybrid system with symmetrical n-type and p-type thermoelectric leg geometry which corresponds to Case 1. Figure 5.12b corresponds to Case 2 which is asymmetrical n-type and symmetrical p-type thermoelectric leg geometry. Similarly, Case 3 shown in Figure 5.12c corresponds to symmetrical p-type and asymmetrical n-type TE leg geometry. Lastly, Case 4 shown in Figure 5.12d is the hybrid system with asymmetrical n-type and p-type TE leg geometry.

CHAPTER 5 HYBRID PHOTOVOLTAIC-THERMOELECTRIC OPTIMIZATION RESULTS

In all the cases, the leg dimensions are equal. However, the asymmetrical leg is obtained by the variation of cross-sectional area along the height of the thermoelectric leg. Therefore, the hot side (top) cross-sectional area of the asymmetrical leg is half that of the cold side (bottom). Between the thermoelectric legs and copper electrodes, thermoelectric electrical contact resistance is considered while thermoelectric thermal contact resistance is considered between the ceramic plates and copper electrodes. Furthermore, thermal contact resistance is considered between the tedlar and ceramic top surface, and between the ceramic lower surface and heat sink. The values of the thermoelectric electrical and thermal contact resistance are $6.5 \times 10^{-9} \Omega m^2$ and $2 \times 10^{-4} m^2 K/W$ respectively (Högblom and Andersson, 2014). The values of the other two thermal contact resistance are $2 \times 10^{-4} m^2 K/W$ each (Yin et al., 2017).

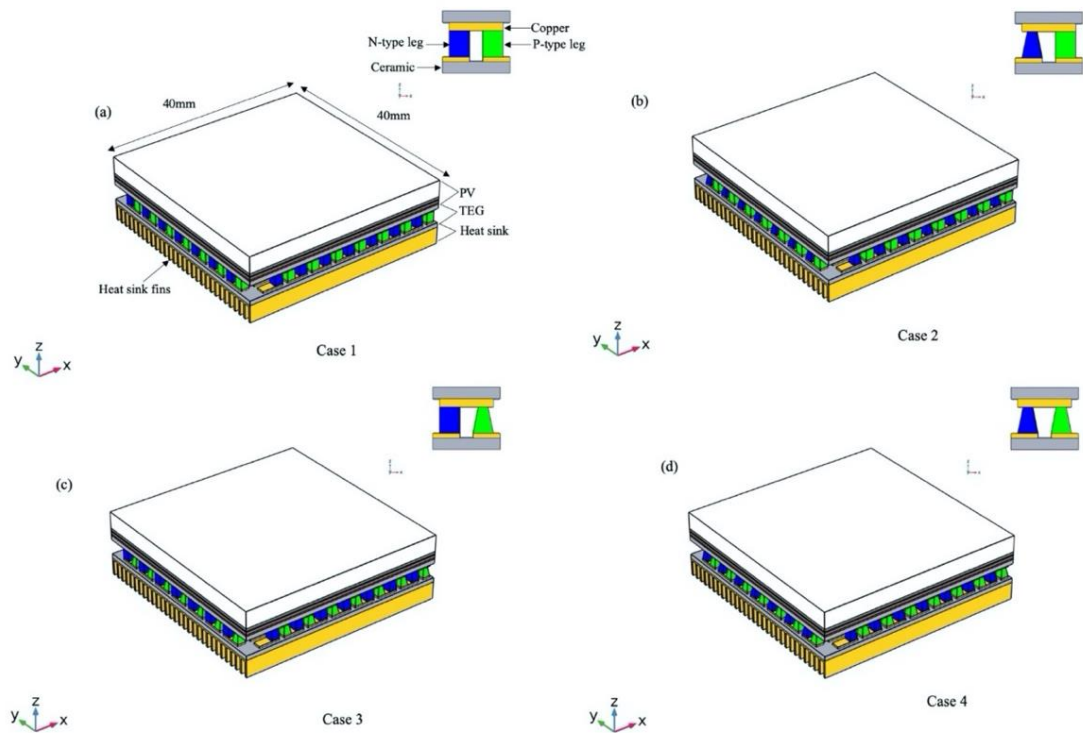


Figure 5.12: Schematic of hybrid system with different geometries (a) Case 1 (b) Case 2 (c) Case 3 and (d) Case 4

CHAPTER 5 HYBRID PHOTOVOLTAIC-THERMOELECTRIC OPTIMIZATION RESULTS

Actual variable weather conditions are considered in this study for summer climatic conditions in Heathrow, Greater London, United Kingdom for 2nd July 2017. The computation is run for 24 hours (one-day). The hourly solar radiation data is obtained from (Met Office, 2019a) and shown in Figure 5.13a while the hourly ambient temperature and wind speed are obtained from (Met Office, 2019b) and shown in Figure 5.13b. Furthermore, since this study involves the comparison of different thermoelectric leg geometries, the power output parameter will be expressed per volume as power output density to enable an adequate balance of material volume for the different leg geometries. In this study, a concentration ratio of 30 is used unless otherwise stated.

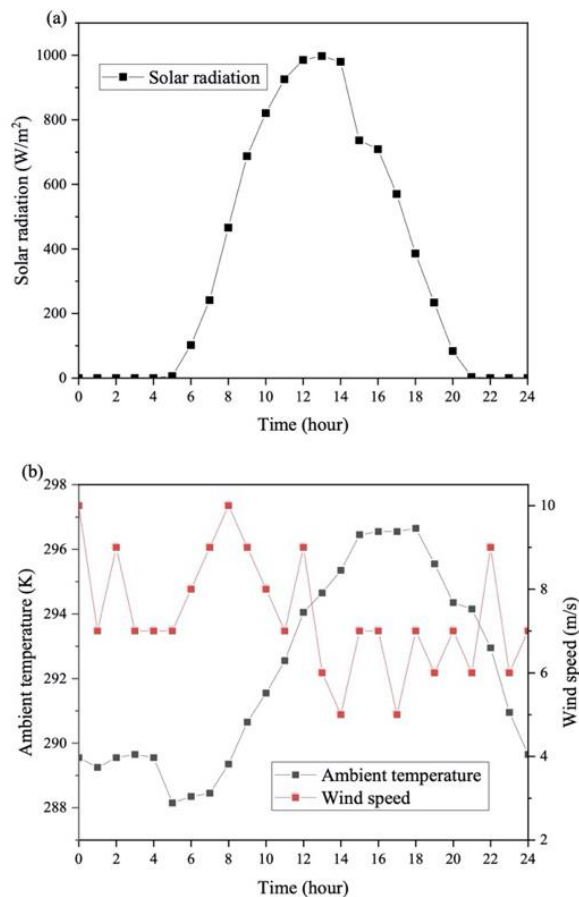


Figure 5.13: Hourly weather data (a) solar radiation (Met Office, 2019a) and (b) ambient temperature and wind speed (Met Office, 2019b)

5.3.1 Boundary Conditions

To simplify the model without much deviation from the actual reality, the following assumptions are made.

- 1) Transient conditions are assumed in this study.
- 2) The initial temperature of the system is assumed to be equal to the ambient temperature.
- 3) Convective and radiative heat loss are considered at the top glass surface of the photovoltaic.
- 4) For radiative heat loss calculation, the PV top glass surface is taken to view the sky while the bottom tedlar surface is taken to view ground/ambient.
- 5) Adiabatic conditions are assumed on the side surfaces of the thermoelectric generator.
- 6) Convective heat transfer coefficient is used to model the TEG cooling with heat sink.
- 7) Polycrystalline silicon solar cell is used with reference temperature of 298.15 K, reference efficiency of 17% and temperature coefficient of 0.0045 1/K (Zhou et al., 2017).

5.3.2 Effect of Thermoelectric Leg Height and Area

The height and cross-sectional area of thermoelectric legs significantly affect the thermoelectric generator performance. Therefore, the effect of thermoelectric leg height on the performance of the hybrid CPV-TE is shown in Figure 5.14 using the base values at a peak time of 13:00 pm. It can be seen from Figure 5.14a that the temperature of the concentrated photovoltaic cell in the hybrid system significantly increases linearly as the leg height is increased. This implies that long thermoelectric legs reduce the heat removal capacity of the thermoelectric generator which is attached

to the concentrated photovoltaic. Furthermore, from Figure 5.14a, it can be seen that the CPV-TE system with a thermoelectric geometry of Case 4 has the highest CPV cell temperature while Case 1 provides the lowest CPV cell temperature. Consequently, it is clear that in a hybrid CPV-TE, the asymmetrical n-type and p-type thermoelectric leg geometry (Case 4) provides the worst heat removal performance.

Furthermore, the most important performance parameter considered in this study is the power output density of the concentrated photovoltaic-thermoelectric system, which is shown in Figure 5.14a. It can be seen clearly that the power output density of the hybrid system for all the four cases considered decreases as the leg height increases. Nevertheless, the hybrid system with Case 1 geometry still provides the highest power output density for all the leg heights considered while the lowest power output density is provided by Case 4. Therefore, even though the volume of the thermoelectric legs for Case 1 is the highest for all leg height, its power output density is actually the highest thereby making it cost effective and optimum geometry for the hybrid system. Furthermore, Figure 5.14a shows that short thermoelectric legs are better than long legs as they provide the highest power output density due to better heat removal capacity. At the optimum leg height of 1 mm, the hybrid system power output density for Case 1 is higher than that of Case 2, Case 3 and Case 4 by 6.46%, 6.30% and 15.08% respectively. This shows that the concentrated photovoltaic-thermoelectric system has a superior performance with symmetrical n-type and p-type thermoelectric legs (Case 1). However, even for Case 1, the hybrid system power output density decreased by 50.93% when the thermoelectric leg height increased from 1mm to 6mm. Therefore, it is imperative to use short thermoelectric legs in a hybrid concentrated photovoltaic-thermoelectric system.

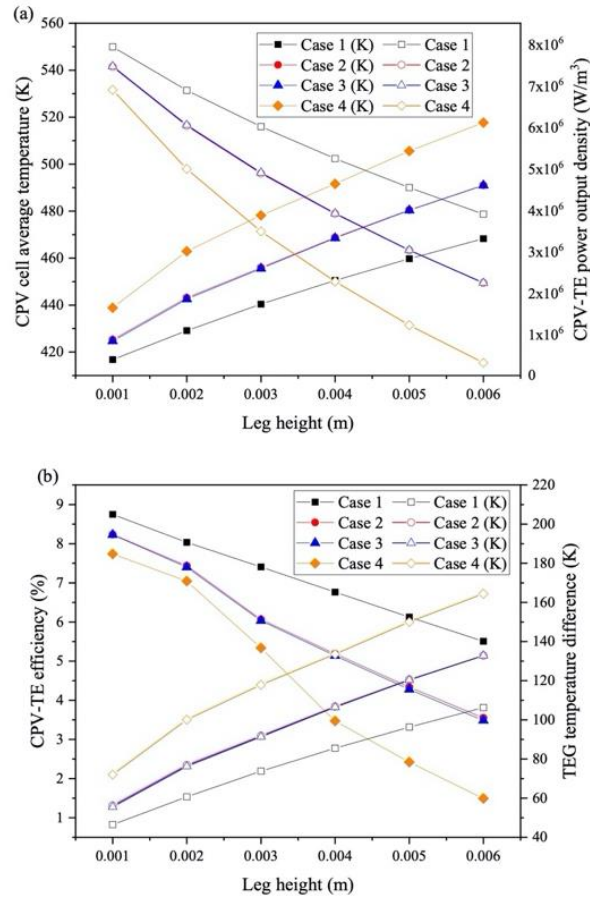


Figure 5.14: Variation of leg height with (a) CPV cell temperature, CPV-TE power output density and (b) CPV-TE efficiency, temperature difference

The hybrid system efficiency variation with leg height is shown in Figure 5.14b. A decreasing trend is observed for the CPV-TE efficiency as the leg height is increased for all the four cases considered. Notwithstanding, the hybrid system with Case 1 provides the highest efficiency for all leg height while Case 4 is the least efficient system. This decrease in efficiency as leg height increased is a resultant effect of the sharp rise in CPV cell temperature shown in Figure 5.14a. Since the CPV contributes the larger percentage of the hybrid system efficiency, increase in leg height will lead to a decrease in hybrid system efficiency because the CPV temperature will increase speedily. However, as shown in Figure 5.14b, the temperature difference across the thermoelectric generator in the hybrid system increases linearly as the leg

height is increased. Therefore, leg height increase is beneficial for the thermoelectric generator however; it is harmful for the hybrid CPV-TE system because of the presence of photovoltaic. Furthermore, Figure 5.14b shows that the hybrid system with Case 4 has the highest TEG temperature difference while the lowest temperature difference is provided by Case 1. This is very significant as the TEG performance is highly dependent on the temperature difference across its hot and cold sides. Consequently, it can be inferred that the asymmetrical n-type and p-type thermoelectric legs (Case 4) is better for the TEG only while the symmetrical n-type and p-type thermoelectric legs (Case 1) is better for the CPV-TE system. This shows the importance of geometry optimization as the optimum geometry in a thermoelectric generator is not necessarily the same as that in a hybrid CPV-TE system.

The effect of thermoelectric leg area on the hybrid system performance for an optimum leg height of 1 mm is shown in Figure 5.15 for a peak time of 13:00 pm. Firstly, Figure 5.15a shows that the CPV cell temperature decreases almost linearly as the leg area increases which in turn leads to an increase in the CPV-TE power output density. It can also be seen that although the CPV cell temperature decreases with an increase in leg area, Case 4 geometry still provides the highest values while Case 1 provides the lowest values. Case 2 and Case 3 provide very similar results as the geometries are very similar. Since the thermoelectric generator area (40 mm x 40 mm) is kept constant, the increase in leg area simply means a decrease in the leg spacing. Although the thermoelectric legs volume increases as the leg area is increased, Figure 5.15a shows that the hybrid system power output density still increases. The power output density is an important parameter because it considers the volume of material used. When the leg area increased from $1 \mu\text{m}^2$ to $4 \mu\text{m}^2$, the CPV cell temperature for Case 1, Case 2, Case 3 and Case 4 decreased by 10.46%, 12.42%, 12.30% and 14.93%

CHAPTER 5 HYBRID PHOTOVOLTAIC-THERMOELECTRIC OPTIMIZATION RESULTS

respectively. Furthermore, at the optimum leg area of $4 \mu\text{m}^2$, the hybrid system power output density for Case 1 is higher than that of Case 2, Case 3 and Case 4 by 4.44%, 4.27% and 11.55% respectively.

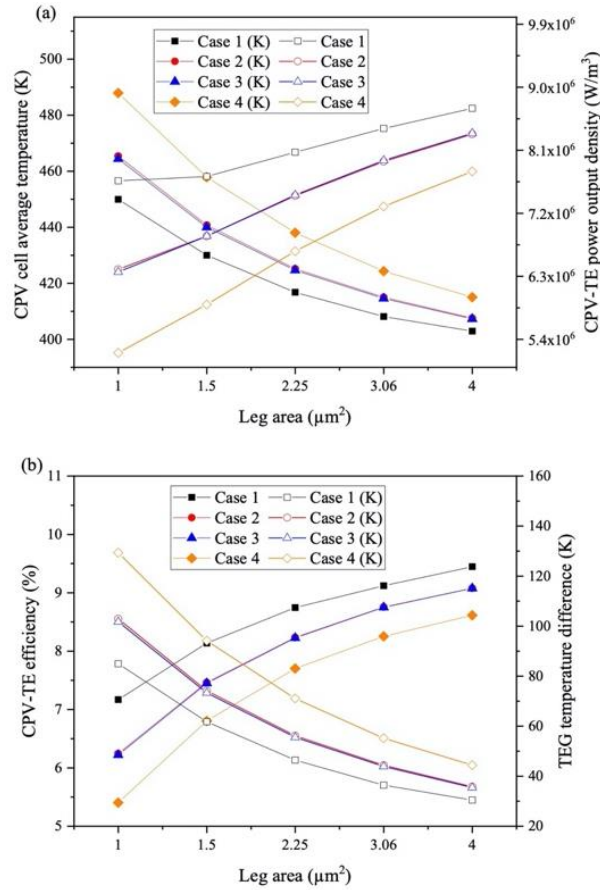


Figure 5.15: Leg area variation with (a) CPV cell temperature, CPV-TE power output density and (b) CPV-TE efficiency, temperature difference

Figure 5.15b shows the CPV-TE efficiency variation with leg area and the thermoelectric generator temperature difference. Furthermore, it is obvious that the efficiency of the CPV-TE increases as the leg area increases while Case 2 and Case 3 provide identical efficiency values and Case 1 provides the highest hybrid system efficiency. In addition, Figure 5.15b shows that Case 4 provides the highest thermoelectric generator temperature difference for all leg areas while Case 1 provides the lowest temperature difference. The reason for this is that the asymmetrical leg

geometry provides a decrease in the overall TEG thermal conductance, which causes a higher temperature difference to be built across the thermoelectric generator, which in turn leads to a higher CPV cell temperature as shown in Figure 5.15a. Consequently, Case 4 would provide enhanced TEG only performance because of its higher temperature difference compared to the others however, it is not suitable for the hybrid system.

5.3.3 Effect of Ceramic Height

Asides the thermoelectric leg height and area, the ceramic height of the thermoelectric generator is another important factor that significantly affects the TEG performance. This is because the ceramic is used to enhance thermal concentration in the thermoelectric generator. Figure 5.16 shows the performance of the CPV-TE for an optimum leg height of 1 mm and leg area of $4 \mu\text{m}^2$ at a peak time of 13:00 pm. Furthermore, Figure 5.16a presents the variation of thermoelectric ceramic height with CPV cell temperature and CPV-TE power output density. The CPV cell temperature increase as the ceramic height increased can be seen clearly. The reason for this is that the long ceramic height/thickness decreases the amount of heat transferred to the cold side of the TEG through the thermoelectric legs. Thus, for a hybrid CPV-TE, short thermoelectric ceramic height is beneficial. Furthermore, it can be seen from Figure 5.16a that the CPV cell temperature for Case 1 is significantly lower than the others. It can also be seen that the ceramic height variation reduces the CPV cell temperature more for Case 3 compared to Case 2 although the results are closely related. The decrease of CPV-TE power output density with ceramic height increase can be seen in Figure 5.16a. At an optimum ceramic height of 0.2 mm, the CPV-TE power output density for Case 1 is greater than that of Case 2, Case 3 and Case 4 by 3.90%, 3.72% and 10.21% respectively.

CHAPTER 5 HYBRID PHOTOVOLTAIC-THERMOELECTRIC OPTIMIZATION RESULTS

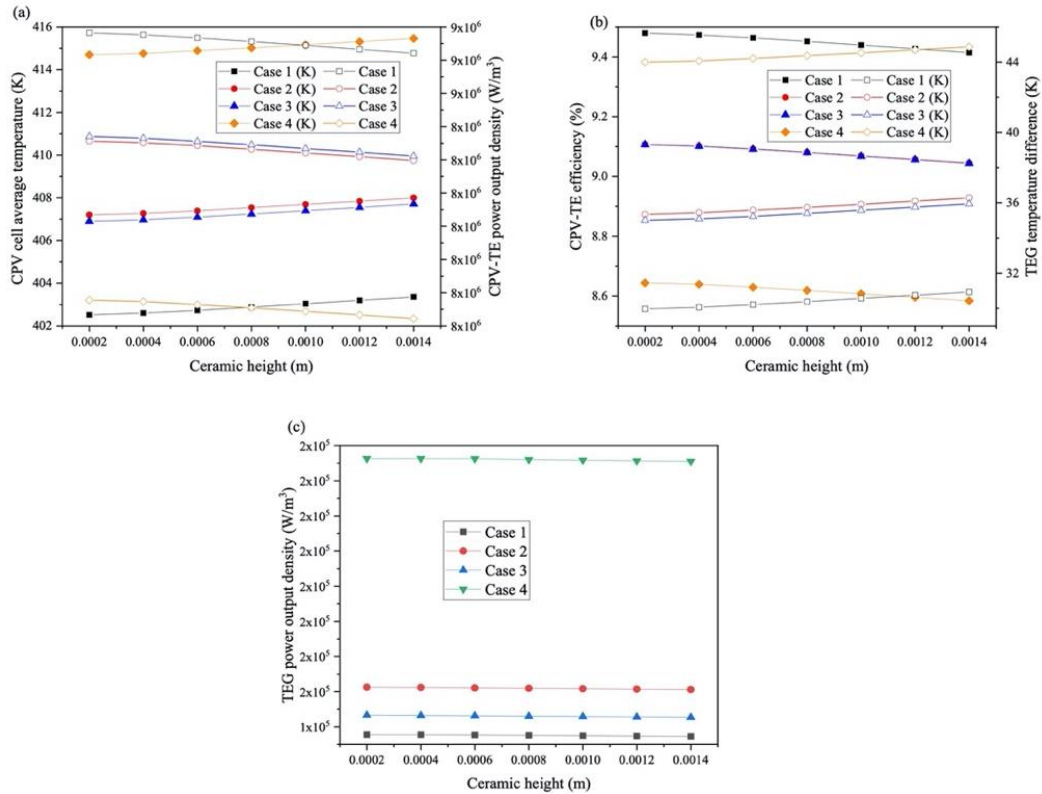


Figure 5.16: Variation of ceramic height with (a) CPV cell temperature, CPV-TE power output density (b) CPV-TE efficiency, temperature difference and (c) TEG power output density

Similarly, Figure 5.16b shows the hybrid system efficiency using Case 1 is the highest while that of Case 4 is the lowest. In addition, it is clear that the efficiency of the hybrid system decreases as the ceramic height increases although the thermoelectric generator temperature difference is increased. This is because of the increased thermal concentration obtained by the increase in ceramic height which leads to an increase in temperature difference. Furthermore, Figure 5.16c shows the power output density of the thermoelectric generator in the CPV-TE. It can be seen clearly that the highest TEG power output density is obtained from Case 4 followed by Case 2, Case 3 and the lowest is obtained from Case 1. This echoes the observation that asymmetrical n-type and p-type thermoelectric legs (Case 4) significantly enhance the TEG only performance. Basically, the asymmetrical geometry provides enhanced

TEG performance compared to the symmetrical geometry although the reverse is the case when the CPV is integrated to form a hybrid CPV-TE system.

5.3.4 Effect of Thermoelectric Geometry Optimization

The results shown in Figure 5.17 are very important because the significance of TE geometry optimization in a CPV-TE system can be seen clearly. Two systems are compared including, CPV-TE system with Case 1 and original geometry using the base values (leg height of 1.96 mm, leg area of $2.25 \mu\text{m}^2$ and ceramic height of 0.86 mm) and CPV-TE system with Case 1 and optimized geometry (leg height of 1 mm, leg area of $4 \mu\text{m}^2$ and ceramic height of 0.2 mm). Case 1 is used for both hybrid systems because of its superior performance compared to the others as explained in the sections above. Furthermore, the values for the optimized geometry are obtained from the parametric studies above. Using the base values for concentration ratio 30, which has been kept constant throughout this study, heat transfer coefficient value of $500 \text{ W/m}^2\text{K}$, the two systems are studied under the variable weather conditions shown in Figure 5.13 for a duration of 24 hours. It can be seen clearly from Figure 5.17a that the hybrid system with the optimized geometry provides the highest power output density which is significantly higher than that of the hybrid system with the original geometry.

Furthermore, it can be seen from Figure 5.17a that the variable weather conditions have a lower negative effect on the hybrid system with the optimized geometry compared with the hybrid system with original geometry, which experiences a sharp decrease in power output density at high solar radiation values. Consequently, it is obvious that thermoelectric geometry optimization can significantly reduce the negative impact of variable weather conditions. The maximum CPV-TE power output density with the optimized geometry decreased by 48.29% when the original geometry

is used. This is a very significant value, which shows the importance of thermoelectric geometry optimization in a hybrid system. Furthermore, Figure 5.17b shows that even the lowest CPV-TE efficiency obtainable from the CPV-TE with optimized geometry (7.62%) is still higher than that of the CPV-TE with original geometry (2.55%). In addition, Figure 5.17c shows that the peak CPV cell temperature of the CPV-TE with original geometry and CPV-TE with optimized geometry are 509.01 K and 426.26 K respectively. Therefore, it is obvious that the average temperature of the CPV cell can be reduced significantly by thermoelectric geometry optimization.

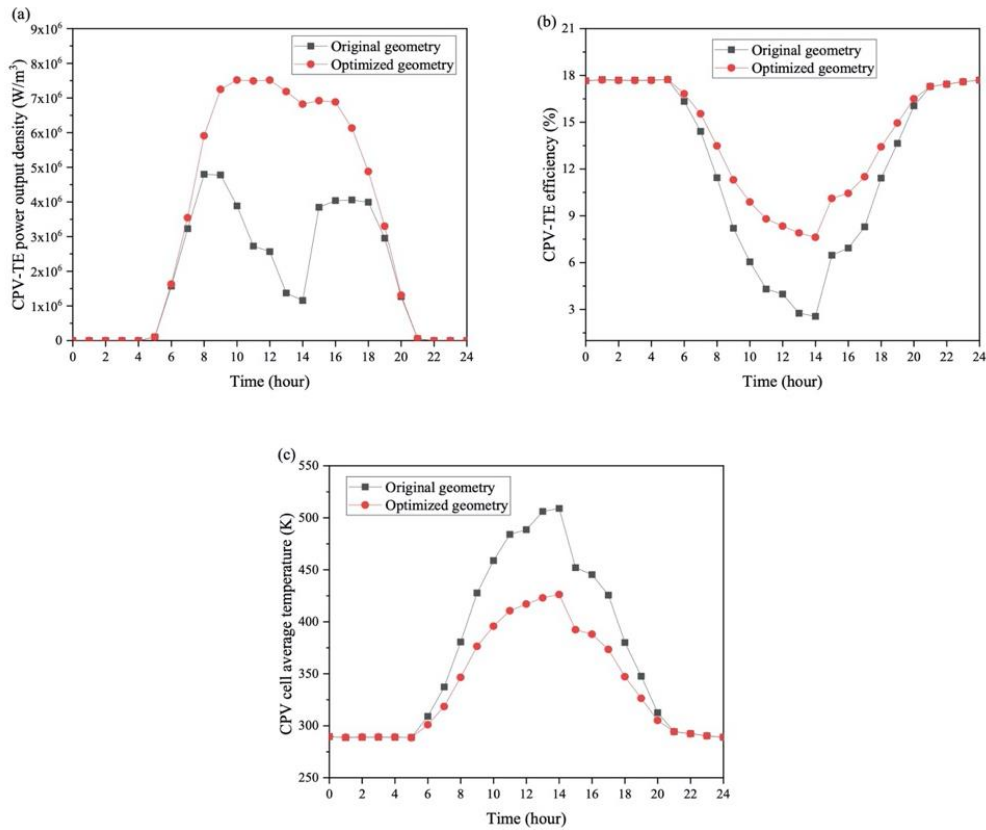


Figure 5.17: Variation of time with CPV-TE (a) power output density (b) efficiency and (c) CPV cell temperature

5.3.5 Three-Dimensional Temperature and Voltage Distributions

To better understand the temperature and voltage distributions in the CPV-TE system, three-dimensional plots are provided. Figure 5.18 shows the surface

CHAPTER 5 HYBRID PHOTOVOLTAIC-THERMOELECTRIC OPTIMIZATION RESULTS

temperature plots for different leg heights for Case 1 and Case 4. Figure 5.18 shows the visual representation of the results shown explained earlier in Figure 5.14b. Comparing Figure 5.18a and Figure 5.18b, it is clear that the maximum temperature across the thermoelectric legs increase significantly when the leg height is increased from 1mm (352 K) to 6 mm (435 K). This therefore means that the temperature difference would be increased since the cooling is constant. Furthermore, it is obvious that heat is transferred from the top of the legs to the bottom linearly because of the presence of a cooling system at the bottom and CPV which acts as the heat source at the top of the TEG. Similarly, comparing Figure 5.18c and Figure 5.18d, it can be seen that the maximum temperature across the legs increases from 378 K to 489 K when the leg height is increased from 1 mm to 6 mm. Also, the superior advantage of the asymmetrical n-type and p-type legs (Case 4) over the symmetrical n-type and p-type legs (Case 1) for the TEG only can be seen by comparing the maximum temperature in Figure 5.18a and Figure 5.18c or Figure 5.18b and Figure 5.18d.

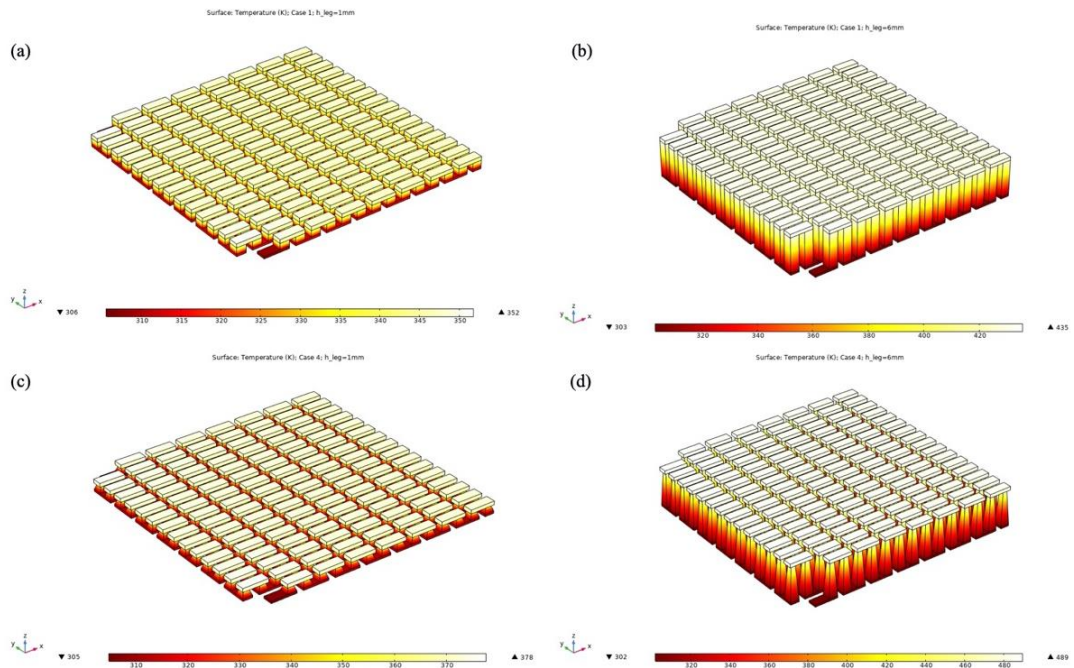


Figure 5.18: Surface temperature plots for leg height of (a, c) 1 mm and (b, d) 6 mm

CHAPTER 5 HYBRID PHOTOVOLTAIC-THERMOELECTRIC OPTIMIZATION RESULTS

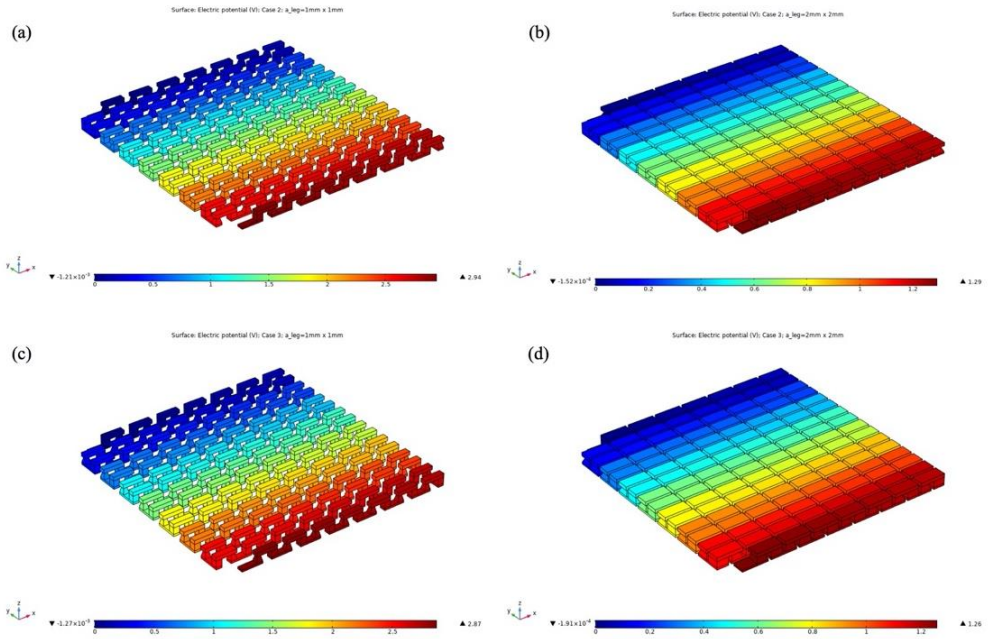


Figure 5.19: Electric potential plots for leg area of (a, c) 1 mm² and (c, d) 4 mm²

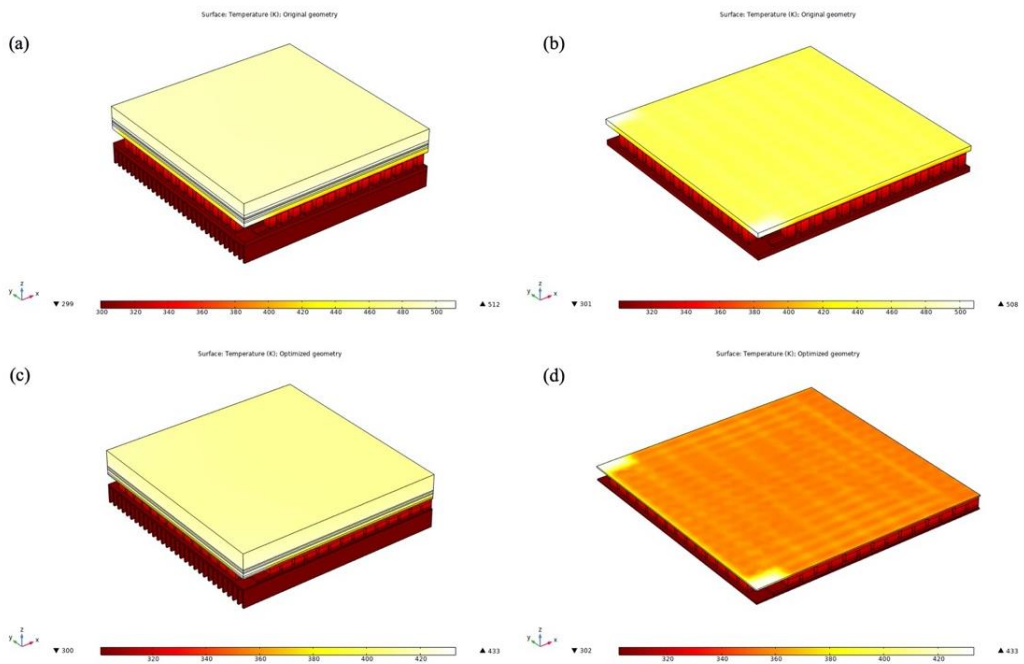


Figure 5.20: CPV-TE temperature distribution plots for (a, b) original geometry and (c, d) optimized geometry

Furthermore, Figure 5.19 shows the electric potential plots for different leg areas at a constant leg height for Case 2 and Case 3. It can be seen that the electric

potential is reduced as the leg area is increased for the same geometry as shown in Figure 5.19a and Figure 5.19b. In addition, Figure 5.19c and Figure 5.19d show that the electric potential decreases along the electrically series connected thermoelectric legs.

Figure 5.20 presents the temperature distribution plots in three-dimension for the Case 1 CPV-TE with original geometry and optimized geometry at a peak time of 13:00 pm. The hybrid system with original geometry can be seen in Figure 5.20a and Figure 5.20b while that with optimized geometry is shown in Figure 5.20c and Figure 5.20d. It is important to note that in this study, only the thermoelectric geometry is optimized and not the photovoltaic geometry as it is out of the scope of this particular study. Comparing Figure 5.20a and Figure 5.20c it can be seen that the maximum temperature in the hybrid system with original geometry is higher than that with optimized geometry. Figure 5.20b and Figure 5.20d show respectively the original and optimized TEG geometry in the hybrid system. Comparing both figures, it can be seen that the ceramic height/thickness in the optimized geometry (Figure 5.20d) is lower than that in the original geometry (Figure 5.20b). In addition, it can be seen that the leg height and leg area in the optimized geometry are lower and higher respectively compared to that in the original geometry. Consequently, the optimized thermoelectric geometry in the hybrid system in this study is obtained when the leg height is 1 mm, leg area is $4 \mu\text{m}^2$ and ceramic height is 0.2 mm.

5.3.6 Section Conclusion

Thermoelectric geometry optimization in a hybrid concentrated photovoltaic-thermoelectric system has been presented in this study. A detailed three-dimensional numerical investigation of the optimum TE geometry in a hybrid system under varying weather conditions was performed. The main conclusions from this study are:

- 1) Thermoelectric geometry optimization can significantly reduce the negative impact of variable weather conditions on concentrated photovoltaic-thermoelectric system performance.
- 2) The maximum concentrated photovoltaic-thermoelectric system power output density with the optimized thermoelectric geometry decreased by 48.29% when the original geometry is used.
- 3) At the optimum leg height of 1 mm, the hybrid system power output density for Case 1 is higher than that of Case 2, Case 3 and Case 4 by 6.46%, 6.30% and 15.08% respectively.
- 4) At the optimum leg area of $4 \mu\text{m}^2$, the hybrid system power output density for Case 1 is higher than that of Case 2, Case 3 and Case 4 by 4.44%, 4.27% and 11.55% respectively.
- 5) The asymmetrical n-type and p-type leg geometry (Case 4) provides enhanced thermoelectric generator only performance compared to the symmetrical n-type and p-type leg geometry (Case 1) although the reverse is the case for the hybrid concentrated photovoltaic-thermoelectric system.

5.4 Photovoltaic-Thermoelectric Contact Resistance

A direct coupling approach is used in this study for the concentrated photovoltaic-thermoelectric system (CPV-TE). As shown in Figure 5.21a, the thermoelectric generator is directly attached to the back of the photovoltaic (PV) module and a heat sink is coupled to the TEG for cooling. The five layers of the PV including glass, ethylene vinyl acetate (EVA) top layer, polycrystalline silicon cell, EVA bottom layer and tedlar polyester tedlar (TPT) are shown in Figure 5.21b. All the layers of the PV are of equal dimensions and in direct contact. Furthermore, the

thermoelectric generator (TEG) is made up of a ceramic top and bottom layer which provides thermal conductivity, copper electrode which provides electrical connection and semiconductor thermoelectric materials (p-type and n-type) as shown in Figure 5.21c.

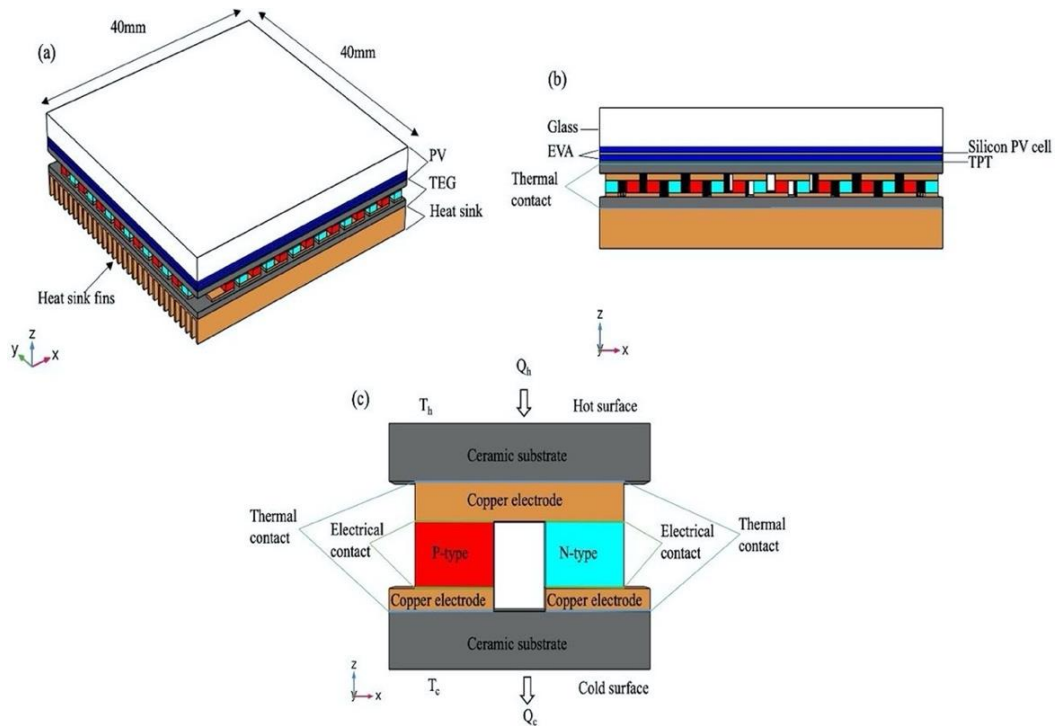


Figure 5.21: Schematic diagram of (a) PV-TE three-dimensional view (b) PV-TE front view and (c) TE uni-couple

An external load resistance is connected across the terminals of the TEG to obtain its power output and the thermoelectric legs are of equal dimension. Convective cooling is used in this study therefore; copper heat sink with fins is attached to the cold side of the thermoelectric generator. The location of the first thermal contact between the PV back sheet (TPT) and the TEG top surface (ceramic) is shown in Figure 5.21b. The second thermal contact between the TEG bottom surface (ceramic) and the heat sink is also shown in Figure 5.21b. Furthermore, Figure 5.21c shows the locations of the top side and bottom side thermoelectric thermal and electrical contacts.

Therefore, in this study, the effect of four different contact resistances are investigated including thermal contact resistance between PV back surface and TEG top surface (R_{pv_te}), thermal contact resistance between TEG bottom surface and heat sink (R_{teg_hsink}), thermoelectric thermal contact resistance (R_c) and electrical contact resistance (R_{cont}). This study is carried out using commercial bismuth telluride (Bi_2Te_3) TEG device manufactured by Thermonamic Co. (TEP1-1264-3.4). The TEG is $40\text{ mm} \times 40\text{ mm}$ in dimension and it consists of 126 pairs of p-type and n-type thermoelectric legs, which are connected, thermally in parallel and electrically in series. In this study, a concentration ratio of 30 is used unless otherwise stated.

5.4.1 Boundary Conditions

The boundary conditions and assumptions considered in the hybrid system are listed below.

- 1) Steady state conditions are assumed throughout this study.
- 2) Adiabatic conditions are assumed on surfaces of the thermoelectric generator.
- 3) Fins are attached to completely cover the cold surface of the TEG and an equivalent convective heat transfer coefficient is used to model the heat transfer from the TEG to ambient.
- 4) Both the n-type and p-type leg coppers are connected to the different ends of an external load resistance.
- 5) Convective and radiative heat loss are considered on the glass surface of the PV.
- 6) The initial temperature of the system is equal to the ambient temperature (298.15 K).
- 7) PV reference efficiency is 17% at 298.15 K reference temperature and temperature coefficient of 0.0045 1/K (Zhou et al., 2017).

- 8) For radiative heat loss calculation, the glass surface of the PV is taken to view the sky.
- 9) The thermal and electrical contacts considered in this study are modelled as boundary conditions.
- 10) The reference irradiance used throughout this study is 1000 W/m^2 .

5.4.2 Contact Resistance Study

Contact resistance between the interfaces of the hybrid system can significantly affect its performance therefore their effects are studied in this section. The effects of four different contact resistances are studied including, thermoelectric thermal contact resistance (R_c), thermoelectric electrical contact resistance (R_{cont}), photovoltaic-thermoelectric interface thermal contact resistance (R_{pv_te}) and thermoelectric generator-heat sink interface thermal contact resistance (R_{teg_hsink}).

5.4.2.1 Effect of Thermoelectric Thermal and Electrical Contact Resistance

The effect of the thermoelectric thermal contact resistance on the performance of the hybrid system is shown in Figure 5.22. The base values are used for this study except the TE thermal contact resistance which is varied from $1\text{E-}6$ to $1\text{E-}3 \text{ m}^2 \cdot \text{K/W}$ as reported in (Ouyang and Li, 2016). The TE thermal contact resistance is applied at the interface between the top and bottom electrical conductor and the top and bottom ceramic plates. It can be seen from Figure 5.22a that the TE thermal contact affects the system performance as the efficiency and power output of the PV-TE, PV and TE all decrease when the contact resistance increases. In addition, an almost steady trend is noticed in Figure 5.22a for low values of contact resistance however, as the value increases, a sharp decrease is noticeable therefore; the thermoelectric thermal contact resistance should be kept minimal. Thermal contact resistance results from surface roughness at the related interfaces and this leads to an increase in temperature as

shown in Figure 5.22b. Similar to the trend in Figure 5.22a, the effect of the thermal contact is not that significant for low values however, once the TE thermal contact resistance attains a high value such as $1E-4 \text{ m}^2 \cdot \text{K}/\text{W}$ and upward, its drastic effect on the hybrid system performance becomes very clear. This is in agreement with the reported findings in (Ouyang and Li, 2016). In addition, Figure 5.22 shows that there is an acceptable range ($1E-6 - 1E-4 \text{ m}^2 \cdot \text{K}/\text{W}$) of TE thermal contact resistance that has little influence on the hybrid system performance however, beyond this range, the concentrated PV-TE efficiency and power output decrease significantly.

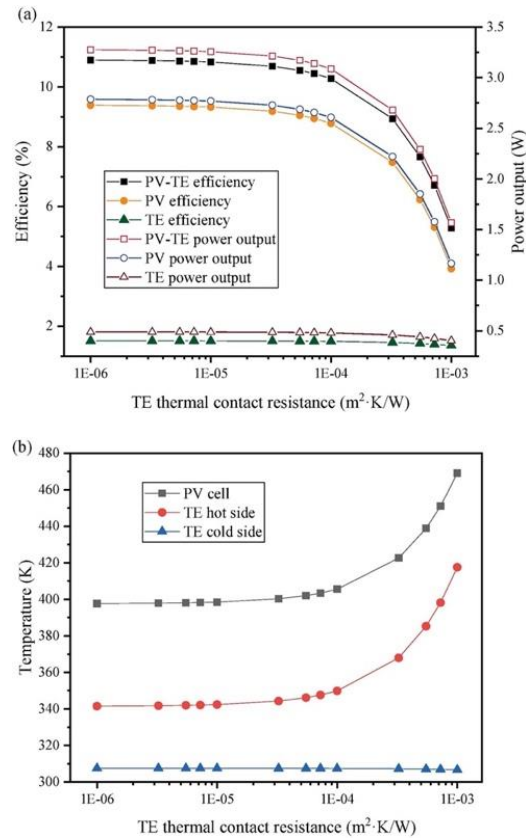


Figure 5.22: Relationship between TE thermal contact resistance and (a) efficiency, power output and (b) temperature

Figure 5.23 shows the effect of thermoelectric electrical contact resistance on concentrated PV-TE performance. The electrical contact resistance is varied from $1E-9$ to $1E-6 \Omega \cdot \text{m}^2$ which is an acceptable range obtained from (Ouyang and Li, 2016)

while other parameters are kept at base values. The TE electrical contact is applied at the interface between the p-type, n-type legs and the top and bottom electrical conductor. It can be seen from Figure 5.23a that the efficiency and power output of the hybrid system decrease as the electrical contact resistance increased. However, the decrease in performance becomes insignificant from $1\text{E-}7 \Omega \cdot \text{m}^2$. The reason for this is shown in Figure 5.23b where it can be seen that the PV cell temperature increase and TE temperature difference reaches a plateau from $1\text{E-}7 \Omega \cdot \text{m}^2$ consequently, the performance of the hybrid system is no longer severely affected. The effect of contact resistance is more significant for short thermoelectric legs, which are used in this study. Furthermore, large values of electrical contact resistance allow a lower current density therefore, increase in electrical contact resistance leads to decrease in current flow and a subsequent decrease in power output and efficiency.

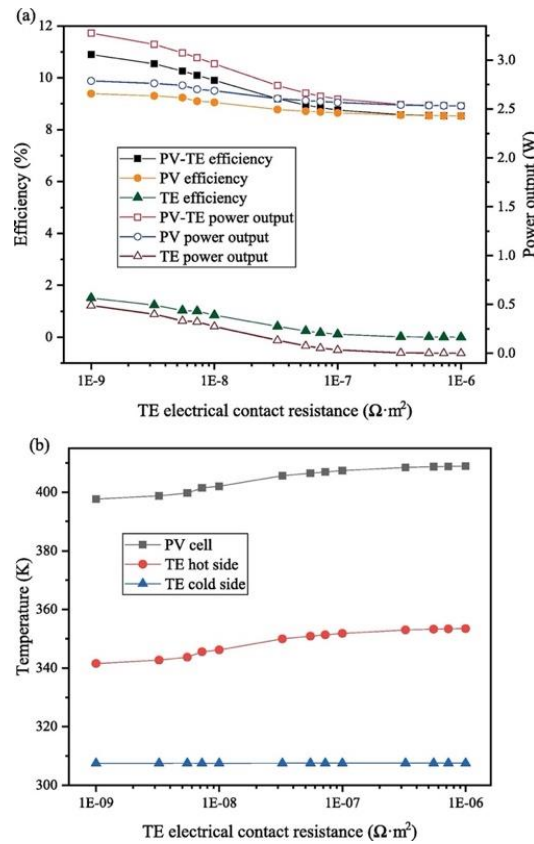


Figure 5.23: Effect of TE electrical contact resistance on (a) efficiency, power output and (b) temperature

5.4.2.2 Effect of Coupling Interface Thermal Contact Resistance

The effect of thermal contact resistance between the PV lower layer and the TEG top surface on the performance of the hybrid system is shown in Figure 5.24. Base values of concentration ratio 30, convective heat transfer coefficient $500 \text{ W/m}^2 \cdot \text{K}$ are used while the thermal contact resistance between the PV and TEG (R_{pv_te}) is varied from 0 to $1000 \text{ mm}^2 \cdot \text{K/W}$. As shown in Figure 5.24a, the efficiency of the PV-TE, PV and TE all decrease as the thermal contact resistance increases. This is expected as the increase in thermal contact resistance leads to a decrease in heat transfer from the PV to the TEG and a subsequent increase in temperature as shown in Figure 5.24b. The TEG heat removal capability from the PV is decreased as the thermal contact resistance increases. The efficiency of the hybrid system decreases by about 12.6% when R_{pv_te} increases from 0 to $1000 \text{ mm}^2 \cdot \text{K/W}$. Therefore, it is imperative to reduce this contact resistance as low as possible in a hybrid system.

Figure 5.25 shows the variation of the hybrid system performance with the thermal contact resistance between the TEG and heat sink (R_{teg_hsink}). A similar trend to the one observed in Figure 5.24 is shown in Figure 5.25 as the increase in thermal contact resistance between the TEG and heat sink reduces the cooling effectiveness of the heat sink. Since the performance of the TEG and the hybrid system is greatly affected by the temperature distribution in the system, Figure 5.25a shows that the efficiency of the hybrid system will reduce as the thermal contact is increased. This reduction in efficiency is caused by the increase in temperature shown in Figure 5.25b. The efficiency of the hybrid system decreases by about 13.23% when R_{teg_hsink} increases from 0 to $1000 \text{ mm}^2 \cdot \text{K/W}$. Figure 5.24 and Figure 5.25 show that the effect of the thermal contact resistances (R_{pv_te} and R_{teg_hsink}) on the efficiency and power output of the hybrid system is not that significant at values less than $200 \text{ mm}^2 \cdot$

K/W therefore, there is no significant advantage to reducing the thermal contact resistance to $0 \text{ mm}^2 \cdot K/W$. This is in agreement with the reported findings in (Zhang et al., 2014).

A comparison between the effects of R_{pv_te} and R_{teg_hsink} on the power output of the hybrid system and TE temperature difference is shown in Figure 5.26. It can be seen clearly that the thermal contact resistance between the TEG and heat sink (R_{teg_hsink}) has a greater effect on the system performance compared to that between the PV and TE. Therefore, as shown in Figure 5.26, decreasing R_{teg_hsink} should take precedence over R_{pv_te} as it is more important.

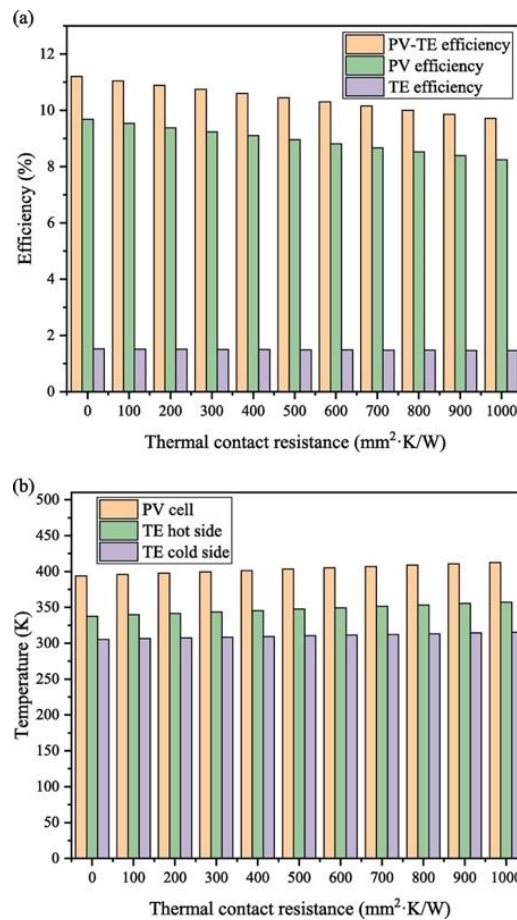


Figure 5.24: Relationship between PV-TE interface thermal contact resistance and (a) efficiency and (b) temperature

CHAPTER 5 HYBRID PHOTOVOLTAIC-THERMOELECTRIC OPTIMIZATION RESULTS

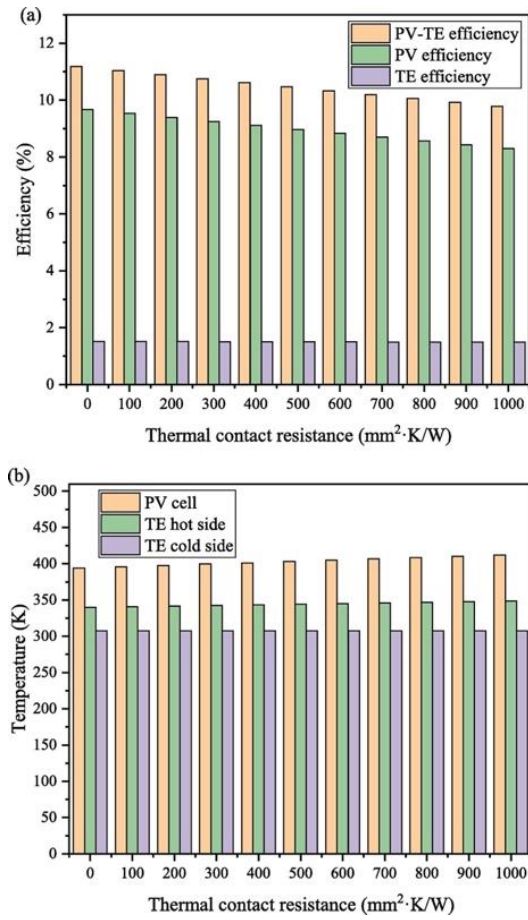


Figure 5.25: Variation of TEG-heat sink thermal contact resistance with (a) efficiency and (b) temperature

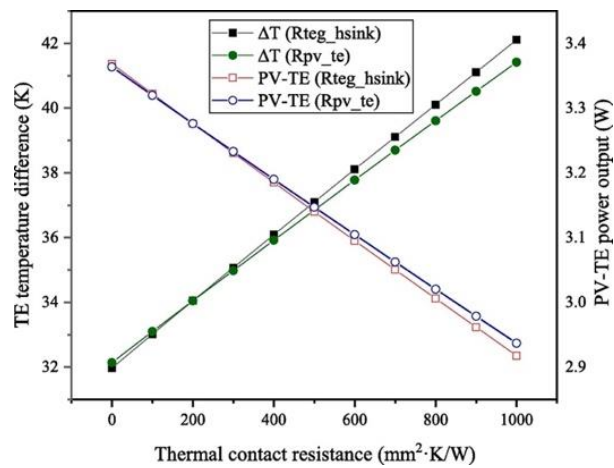


Figure 5.26: Comparison of PV-TE interface and TEG-heat sink thermal contact resistance effect

5.4.2.3 Three-Dimensional Temperature and Voltage Distributions

The three-dimensional nature of this study allows valuable temperature and voltage distribution information to be obtained to better understand the performance of the hybrid system. The temperature and voltage distributions in the hybrid system using the base values are shown in Figure 5.27a and Figure 5.27b respectively. As expected, Figure 5.27a shows that the PV has the highest temperature value since it is directly receiving the concentrated solar radiation while the TEG cold side has the lowest temperature value because of the convective cooling via heat sink. Figure 5.27b shows the voltage distribution through the total 252 legs of the thermoelectric generator.

The distributions of temperature and voltage at the thermal and electrical contact interfaces in the thermoelectric generator are shown in Figure 5.28. As shown in Figure 5.28a and Figure 5.28b, the temperature of the interface layers increases significantly when the TE thermal contact resistance increases from $1\text{E-}6$ to $1\text{E-}3 \text{ m}^2 \cdot \text{K}/\text{W}$. This is the reason for the decrease in hybrid system performance observed in Figure 5.22a. Furthermore, Figure 5.28c and Figure 5.28d show that the voltage at the electrical contact interface of the TEG decreases as the electrical contact resistance increases from $1\text{E-}9$ to $1\text{E-}6 \Omega \cdot \text{m}^2$ consequently, the efficiency and power output of the hybrid system decrease as shown in Figure 5.23a.

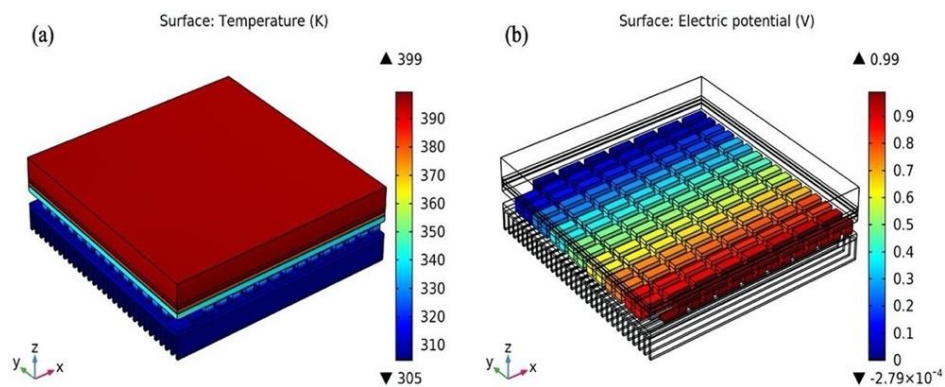


Figure 5.27: (a) Temperature and (b) voltage distribution for base values

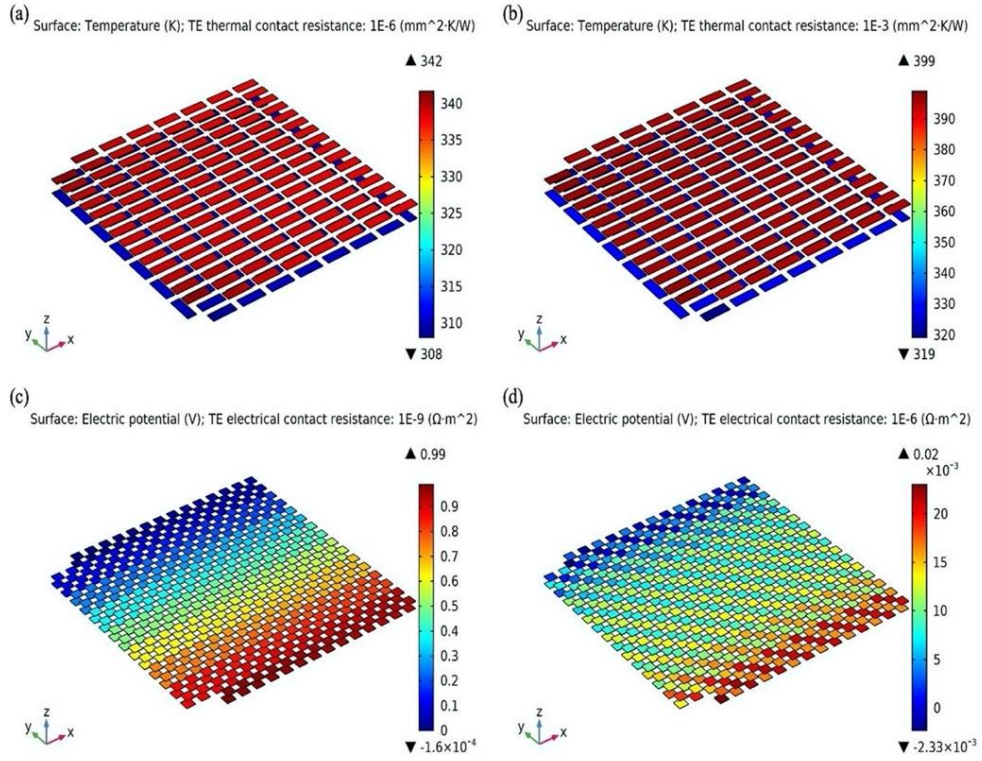


Figure 5.28: (a, b) Temperature distribution for TE thermal contact resistance interface and (c, d) voltage distribution for TE electrical contact resistance interface

5.4.3 Comparison of Contact Resistance Effects

This section is very important as it provides valuable insights into the significance of each contact resistance considered in this study. Twelve different cases are discussed in this section corresponding to different contact resistance scenarios as shown in Table 5.1. Since there are four contact resistances ($R_c, R_{cont}, R_{pv_te}, R_{teg_hsink}$) considered in this study, 12 combinations are possible which are explained in the sections below. When a specific contact resistance is not considered, that means perfect contact condition is assumed.

Table 5.1: Contact resistance case description

Case number	Description
-------------	-------------

CHAPTER 5 HYBRID PHOTOVOLTAIC-THERMOELECTRIC OPTIMIZATION RESULTS

- 1 No contact resistance is considered.
 - 2 Only TE thermal contact resistance is ignored.
 - 3 Only TE electrical contact resistance is ignored.
 - 4 Only PV-TE interface thermal contact resistance is ignored.
 - 5 Only TEG-heat sink interface thermal contact resistance is ignored
 - 6 TE thermal and electrical contact resistances are ignored.
 - 7 PV-TE and TEG-heat sink thermal contact resistances are ignored.
 - 8 Only TE thermal contact resistance is considered.
 - 9 Only TE electrical contact resistance is considered.
 - 10 Only PV-TE interface thermal contact resistance is considered.
 - 11 Only TEG-heat sink thermal contact resistance is considered.
 - 12 All contact resistances are considered.
-

5.4.3.1 Different Contact Resistance Case

Firstly, the variation of hybrid system efficiency with different contact resistance case number is shown in Figure 5.29a. It can be seen clearly that when no contact resistance is considered (Case 1), the highest hybrid system efficiency is obtained. This is expected as the presence of contact resistance of any kind reduces the efficiency of the hybrid system. In addition, it is obvious from Figure 5.29a that the TE electrical contact resistance is more significant than the TE thermal contact resistance because the magnitude of efficiency decrease when each one is ignored is

different. Case 2 implies that all other contact resistances are considered except the TE thermal contact resistance and since the efficiency is still as low as the efficiency for Case 12 where all contact resistance are considered, it can be concluded that the effect of the TE thermal contact resistance is not that significant. However, it is very important to note that this comparison is carried out using the base values.

Furthermore, Figure 5.29a shows that the TEG-heat sink interface thermal contact resistance is more important than the PV-TE interface resistance. In fact, it is the most important contact resistance that needs to be decreased. The same trend observed in hybrid system can be seen in the PV as shown in Figure 5.29b. In addition, it can be seen that an increase in convective heat transfer coefficient generally improves the efficiency of the system.

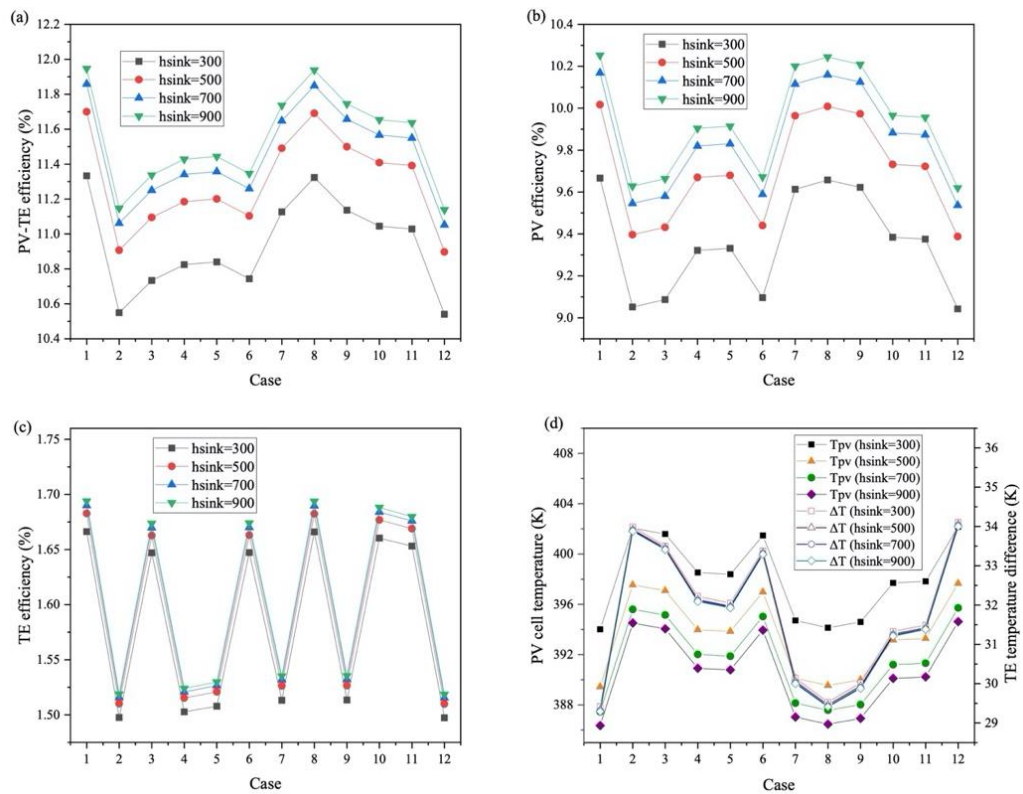


Figure 5.29: Effect of different contact resistance case with (a) PV-TE efficiency (b) PV efficiency (c) TE efficiency and (d) temperature

Figure 5.29c better explains the significance of thermoelectric thermal and electrical contact resistance. As can be seen from Figure 5.29c, the thermoelectric electrical contact resistance is the most important contact resistance in the TEG. The trends shown in Figure 5.29a and Figure 5.29b are because of the temperature distribution in the system, which is shown in Figure 5.29d. It can be seen from Figure 5.29d that the increase in heat sink heat transfer coefficient leads to a significant decrease in the PV cell temperature. Consequently, effective cooling of the thermoelectric is essential for adequate thermal management of photovoltaic. Furthermore, it is clear that from Figure 5.29d that the PV cell temperature in Case 1 is the lowest compared to all the other cases because the presence of contact resistance leads to an increase in temperature. This is the reason for the highest efficiency obtained for Case 1 shown in Figure 5.29a.

5.4.3.2 Overestimation Calculation

To quantify the effect of the contact resistances on the hybrid system performance, an overestimation calculation is made using the base values. Overestimation simply means the percentage increase in efficiency and power output resulting from ignoring one or more contact resistance. Since contact resistances are essential parameters that need to be considered in any numerical study, the values obtained when all the contact resistances are considered (Case 12) is taken as the actual correct value. Therefore, the overestimation percentage is calculated only for Case 1 to Case 11 and the result is shown in Figure 5.30.

It can be seen from Figure 5.30a that ignoring all contact resistances (Case 1) leads to an overestimation of the PV-TE power output and efficiency by about 7.6% and 7.4% respectively. In addition, it can be seen that ignoring both the PV-TE interface and TEG-heat sink contact resistance causes an overestimation of PV-TE

CHAPTER 5 HYBRID PHOTOVOLTAIC-THERMOELECTRIC OPTIMIZATION RESULTS

power output and efficiency by 5.5% and 5.4% respectively. Furthermore, Figure 5.30b shows that the PV efficiency and power output are mainly affected by the PV-TE interface and TEG-heat sink thermal contact resistances. While Figure 5.30c shows that the thermoelectric thermal and electrical contact resistances are the main resistances affecting the performance of the TEG. It is important to note that the overestimation calculation is specifically based on the base values therefore, the use of parametric values will definitely alter the results and higher overestimation percentage could be obtained.

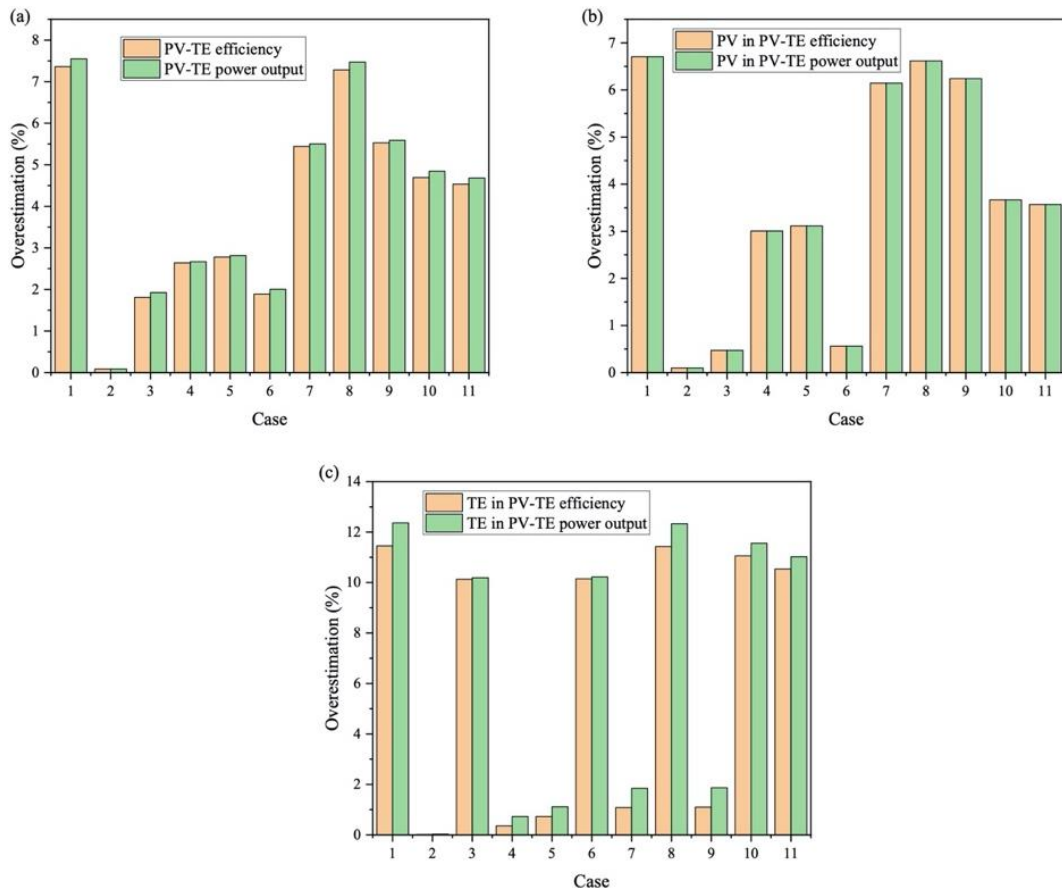


Figure 5.30: Overestimation calculation for (a) PV-TE (b) PV and (c) TE

5.4.4 Section Conclusion

A comprehensive three-dimensional investigation on the effects of contact resistances on hybrid concentrated photovoltaic-thermoelectric performance has been carried out in this study. The main conclusions from this study are listed below.

- 1) Ignoring all contact resistances in the hybrid system leads to an overestimation of hybrid concentrated photovoltaic-thermoelectric power output and efficiency by about 7.6% and 7.4% respectively.
- 2) The thermal contact resistance between the thermoelectric generator and heat sink, and that between the photovoltaic-thermoelectric interface are the most important contact resistances in the hybrid system that need to be reduced.
- 3) The hybrid system efficiency decreased by 12.6% and 13.23% when the photovoltaic-thermoelectric interface thermal contact resistance and thermoelectric generator-heat sink thermal contact resistance increased from 0 to $1000 \text{ mm}^2 \cdot \text{K}/\text{W}$ respectively.

5.5 Photovoltaic-Thermoelectric-Heat Pipe

The structure of each of the systems studied is shown in Figure 5.31. The schematic of the PV only can be seen in Figure 5.31a. All the layers of the PV are assumed to be of equal dimension of 40 mm x 40 mm. The hybrid PV-TE system studied is designed using the direct coupling PV-TE design. Therefore, the TEG module is attached directly to the back of the PV as shown in Figure 5.31b. The dimension of the TEG module is 40 mm x 40 mm with 128 p and n thermoelectric legs and it is attached to the back of the PV.

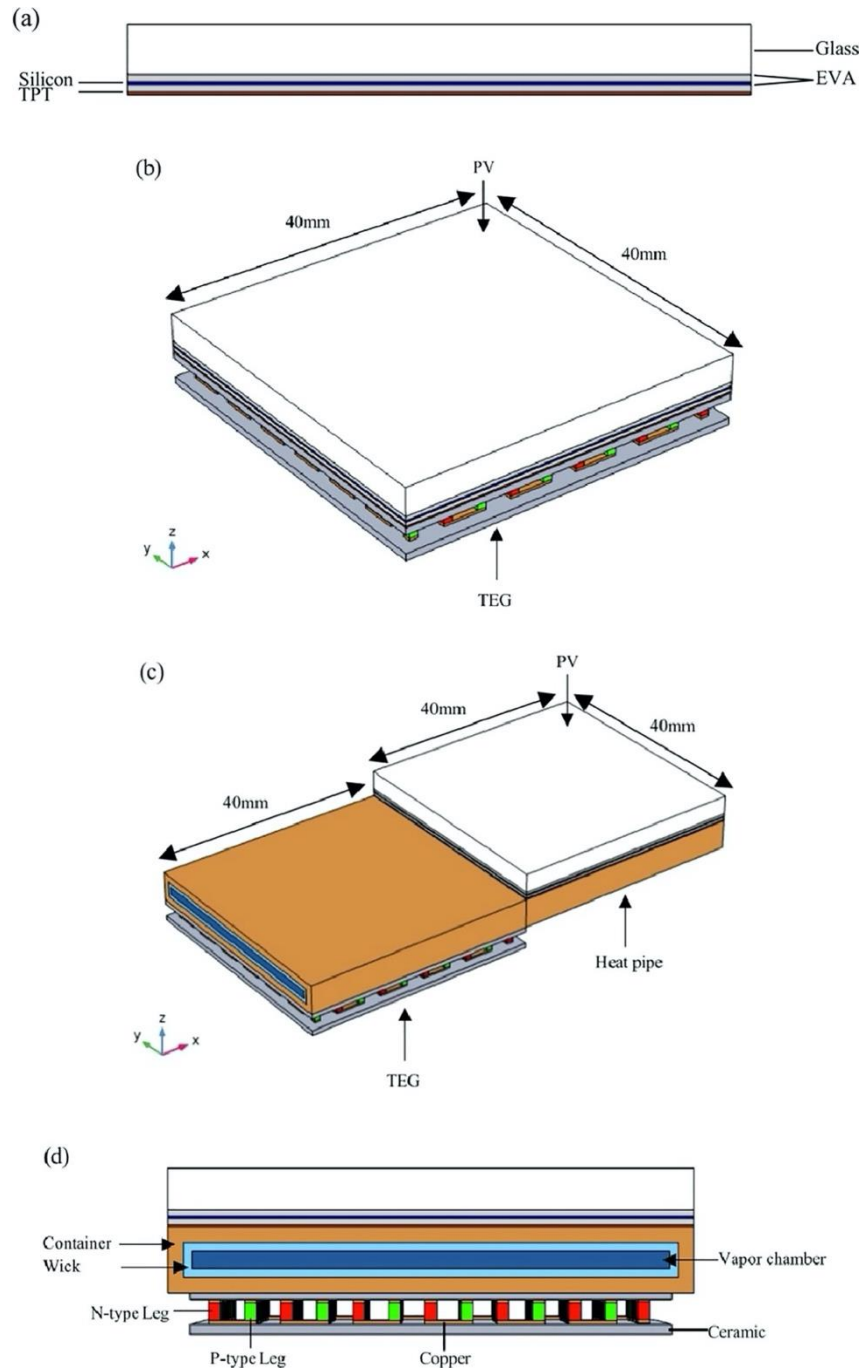


Figure 5.31: Schematic diagram of (a) PV front view (b) three dimensional PV-TE (c) three dimensional PV-TE-Heat pipe (d) PV-TE-Heat pipe side view

A three-dimensional schematic diagram of the hybrid PV-TE-Heat pipe system studied in this paper is shown in Figure 5.31c. The PV is attached directly to the evaporator section of the flat plate heat pipe while the TEG is attached to the bottom surface of the heat pipe condenser section. The dimensions of the evaporator section

of the heat pipe are exactly the same with that of the PV (40 mm x 40 mm) while the dimensions of the condenser section of the heat pipe is the same with that of the TEG (40 mm x 40 mm). The flat plate heat pipe consists of a solid container, wick and vapor chamber as shown in Figure 5.31d. In this study, a concentration ratio of 6 is used unless otherwise stated.

5.5.1 Boundary Conditions

To accurately model the hybrid system, the following boundary conditions are applied, and some assumptions are considered to simplify the model with minimal deviation from the real case.

- 1) Solar cell conversion efficiency at 298.15 K is assumed to be 17% and temperature coefficient to be 0.0045 K^{-1} (Zhou et al., 2017).
- 2) Steady state conditions are assumed.
- 3) All layers are assumed to be of equal area and in direct contact.
- 4) Heat loss via convection and radiation are considered at the upper surface (glass) and back surface (tedlar) of the PV.
- 5) Thermal properties of all materials are assumed to be isotropic and constant.
- 6) Ambient temperature is equal on all sides of the PV and adiabatic condition is assumed.
- 7) Convective heat transfer at the back surface of the PV is assumed to be half of that of the front surface.
- 8) In terms of radiative heat loss, the front and back surface of the PV are taken to view the sky and ground respectively.
- 9) Heat loss through convection and radiation on all surfaces of the TEG are assumed to be zero.
- 10) Electrical and thermal contact resistances are ignored.

- 11) The heat sink of the TEG is considered as a thermal boundary condition with a fixed temperature value.
- 12) The copper on the n-type thermoelectric leg is assumed to be at zero potential while the one at the p-type leg is connected to the external load resistance circuit.
- 13) Effect of gravity is neglected.
- 14) Heat transfer is mainly due to evaporation/condensation and convection of vapor. Therefore, heat transport in the wick is simplified as conduction with an effective heat transfer coefficient.
- 15) Constant material properties are used except for that of the vapor density.
- 16) This simplified model does not predict the operating limits of the heat pipe.
- 17) Convective heat transfer coefficient used at the top surface of the heat pipe is assumed to be $1200 \text{ W/m}^2/\text{K}$ (COMSOL Multiphysics, 2018a).
- 18) Sintered copper powder wick is used with porosity $\varphi = 0.5$.

5.5.2 Influence of Solar Concentration Ratio

Since the average solar radiation intensity (G_0) is kept constant (1000 W/m^2) all through this study, the solar concentration ratio is the determining factor for the total radiation impinged on the PV surface and absorbed by each later. Therefore, an increase in solar concentration ratio simply means an increase in radiation intensity since only uniform illumination is considered throughout this study. The influence of concentration ratio on the performance of the PV only, PV-TE and PV-TE-Heat pipe systems when the ambient temperature is 298.15 K and wind speed is 1 m/s is shown in Figure 5.32. As expected, the efficiency of the systems decreases as the concentration ratio increases as shown in Figure 5.32a. This is because, the increase in concentration ratio raises the temperature of the PV which in turn leads to a reduced

overall efficiency in all the systems. However, it can be seen clearly from Figure 5.32a that the PV-TE-Heat pipe system offers the highest conversion efficiency and slowest efficiency decline as the concentration ratio increases. In comparison, the efficiency of the PV only system shows a sharp decline as the concentration ratio increases. This can be attributed to the poor natural cooling of the PV only. On the other hand, the heat pipe provides a better and more efficient passive cooling of the PV thereby offering an increased overall efficiency.

The advantage of the PV-TE-Heat pipe system over the PV-TE and PV only systems becomes clearer as the concentration ratio increases. In fact, when the concentration ratio is 6, the PV-TE-Heat pipe efficiency is higher by 3.31% and 58.01% compared to that of the PV-TE and PV only systems respectively. Similarly, the maximum power output from the PV-TE-Heat pipe is enhanced by 1.31% and 57.23% compared to that of the PV-TE and PV only systems respectively when the concentration ratio is 6. Although the efficiency enhancement of the PV-TE-Heat pipe system compared to the PV-TE system is not much, it is important to note that the entire back surface of the PV is covered by the TEG in the PV-TE configuration. This is the only reason why the PV-TE system is efficient enough to compete with the PV-TE-Heat pipe system. However, in larger PV systems, the amount of TEG that will be required to cover the entire back surface of the PV will be a lot thus, the overall system cost will be high. This is where the PV-TE-Heat pipe system offers a superior advantage as the use of a heat pipe can reduce the quantity of TEG needed to cool the PV.

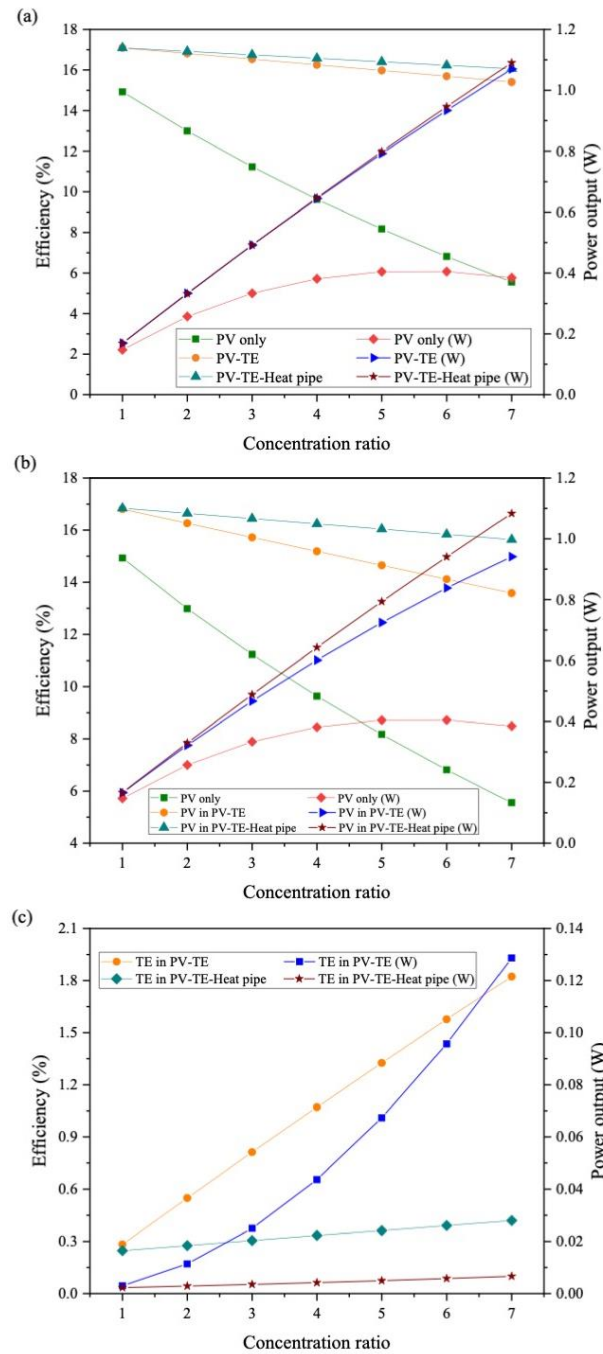


Figure 5.32: Variation of concentration ratio with (a) overall (b) PV (c) TE efficiency and power output

Furthermore, Figure 5.32a shows that the PV-TE-Heat pipe system is better for highly concentrated system operation. It can also be seen from Figure 5.32a that the power output of the PV only system first shows a rising tendency after which it starts decreasing. This shows that there is an optimum concentration ratio for the PV

only system. As seen from Figure 5.32a, the optimum concentration ratio for maximum power output from the PV only system is 6. Figure 5.32b shows the comparative performance of the PV in the PV only system, PV-TE and PV-TE-Heat pipe. It is obvious from Figure 5.32b that the PV in PV-TE-Heat pipe possesses the highest efficiency and power output due to the aforementioned cooling effectiveness of the heat pipe. Considering the efficiency and power output of the TE in the PV-TE and PV-TE-Heat pipe, Figure 5.32c shows the comparative performance results obtained. One glaring observation is that the efficiency and power output of the TE in the PV-TE is significantly greater than that of the TE in PV-TE-Heat pipe. However, this is not surprising because the TE's performance is highly dependent on the amount of input heat flux into the system since both systems have the same cold side temperature.

Therefore, the performance of the TE in PV-TE is significantly higher because there is a higher intensity of heat transferred from the PV to the TE due to the absence of any other cooling device behind the PV as is in the case of the PV-TE-Heat pipe. Moreover, the TE in the PV-TE-Heat pipe is attached to the condenser of the heat pipe which is at a much lower temperature. However, the contribution of the TE to the overall efficiency of the PV-TE and PV-TE-Heat pipe is not that significant because the PV contributes the greater share of the overall hybrid system efficiency. Consequently, the performance of the PV-TE-Heat pipe is still better than that of the PV-TE because the PV is better cooled.

5.5.3 Influence of Ambient Temperature

The influence of the ambient temperature on the performance of the PV only and hybrid PV-TE systems when the concentration ratio is 6 and wind speed is 1 m/s is shown in Figure 5.33.

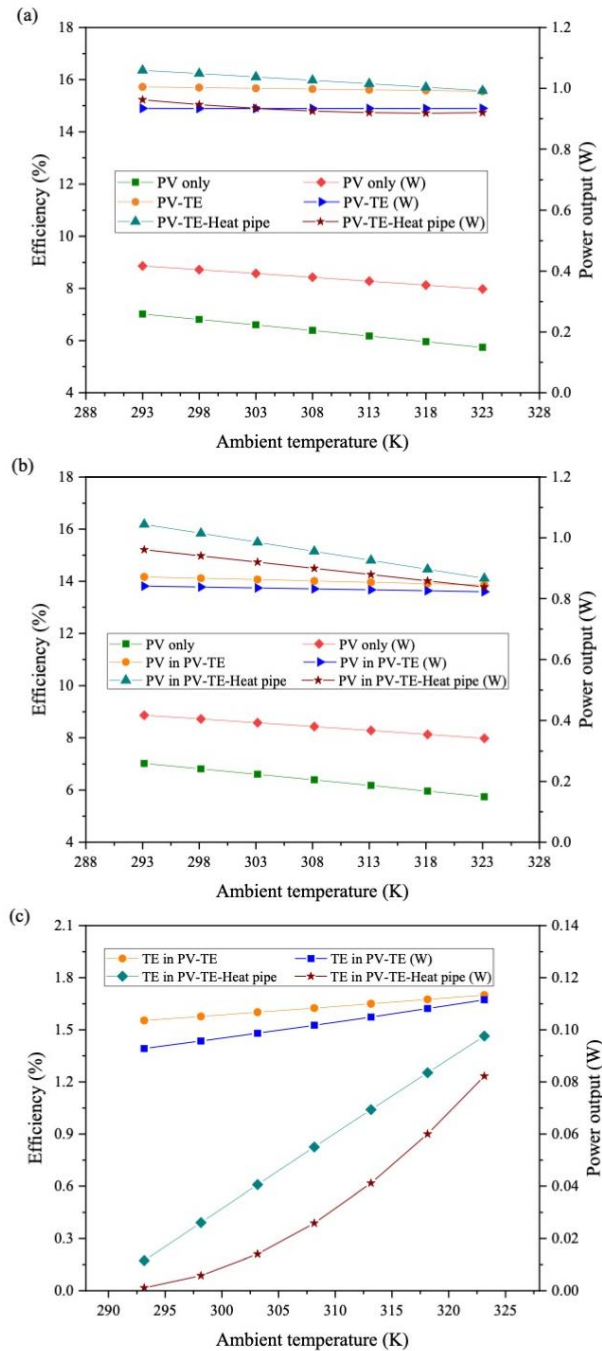


Figure 5.33: Ambient temperature variation with (a) overall (b) PV (c) TE efficiency and power output

It can be seen from Figure 5.33a that the efficiency and power output of the PV, PV-TE, PV-TE-Heat pipe all decrease as the ambient temperature increases. This trend is similar to the one reported in (Li et al., 2016b; Makki et al., 2016). The reason for this is that the ambient temperature influences the amount of heat loss due to

convection and radiation from the systems therefore, an increase in ambient temperature will ultimately lead to a decrease in heat loss and a decrease in performance. Nevertheless, the PV-TE-Heat pipe still offers the best performance in that its efficiency is higher by 1.47% and 61.01% compared to that of the PV-TE and PV only systems at a high ambient temperature of 313.15 K.

In addition, Figure 5.33b shows the performance of the PV in the PV only, PV-TE and PV-TE-Heat pipe systems. It can be seen that the power output and efficiency of the PV decreases as the ambient temperature increases due to the heat losses to the environment. Furthermore, Figure 5.33c shows the performance of the TE in the hybrid systems as the ambient temperature is varied. It can be seen that the power output and efficiency of the TE in the hybrid systems increase as the ambient temperature increases. This is because the increase in ambient temperature leads to a rise in the temperature of the PV therefore, the input heat flux to the TE is increased consequently, its power output and efficiency is increased as shown in Figure 5.33c.

5.5.4 Influence of Wind Speed

When the ambient temperature is 298.15 K and concentration ratio is 6, the influence of the wind speed on the performance of the PV only and hybrid PV-TE systems is shown in Figure 5.34. It can be seen that an increase in wind speed leads to a rapid increase in the efficiency and power output of the PV only system and a slight increase in those of the hybrid systems. This is because the wind speed affects the convective heat transfer coefficient which accounts for the convective cooling of the PV therefore, an increase in wind speed ultimately leads to a decrease in PV temperature and an increase in performance. In addition, Figure 5.34a shows that the PV-TE-Heat pipe performs better than the PV-TE and PV only systems. However, it can also be seen from Figure 5.34a that the efficiency and power output increase

CHAPTER 5 HYBRID PHOTOVOLTAIC-THERMOELECTRIC OPTIMIZATION RESULTS

offered by the PV-TE and PV-TE-Heat pipe as the wind speed increases is not that significant. This is because, unlike the PV only system in which natural convective cooling is applied to front and back surfaces of the PV, the PV-TE system only has convective cooling at the front surface of the PV due to the presence of TEG which covers the entire back surface of the PV.

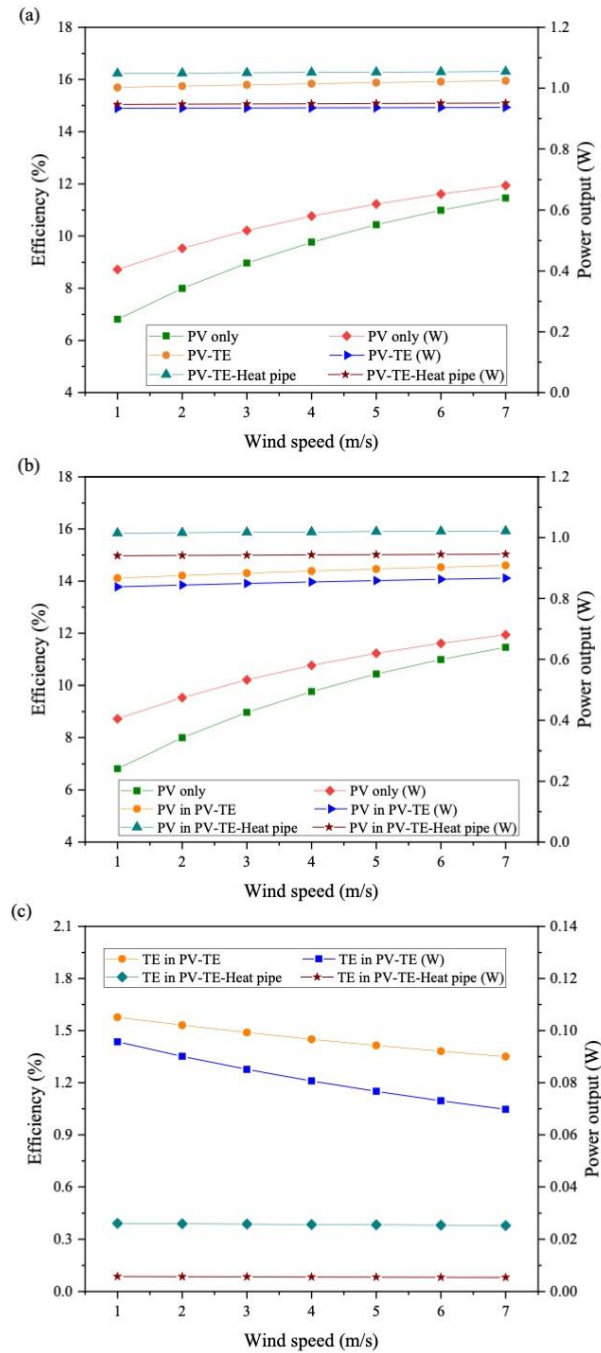


Figure 5.34: Variation of wind speed with (a) overall (b) PV (c) TE efficiency and power output

Similarly, the PV-TE-Heat pipe system also only has convective cooling at the front surface of the PV due to the presence of the heat pipe which covers the entire back surface of the PV. Therefore, the influence of the wind speed on the efficiency and power output of the PV-TE and PV-TE-Heat pipe is not that significant. In fact, the back surface of the PV-TE-Heat pipe is assumed to be insulated besides the TEG so as to create sufficient temperature gradient for the TEG to operate. Figure 5.34b shows the efficiency and power output variation of the PV in PV only, PV-TE and PV-TE-Heat pipe systems as the wind speed is increased. It can be seen clearly from Figure 5.34b that the PV-TE performs better than the PV only although its performance is second only to that of the PV-TE-Heat pipe. Figure 5.34c shows the performance of the TE in PV-TE and PV-TE-Heat pipe as the wind speed increases. It is obvious that the efficiency and power output of the TE in PV-TE decreases as the wind speed increases. This is due to the fact that an increase in wind speed leads to a better cooling of the PV and thus a reduced temperature and the input heat flux to the TE is reduced.

5.5.5 Influence of Thermoelectric Generator Cold Side Temperature

Asides the amount of input heat flux available to the TEG, the TEG cooling effectiveness is the other most important factor that influences the performance of the device. This is because, effective cooling at the cold side of the TEG creates a larger temperature difference across the TEG thus, more power can be generated.

Figure 5.35 shows the performance of the PV-TE and PV-TE-Heat pipe as the cold side temperature of the TEG is varied when the ambient temperature is 298.15 K, wind speed is 1 m/s and concentration ratio is 6. It can be seen from Figure 5.35a that the efficiency and power output of both hybrid PV-TE systems decrease as the TEG cold side temperature increases because the contribution of the TEG to the overall

CHAPTER 5 HYBRID PHOTOVOLTAIC-THERMOELECTRIC OPTIMIZATION RESULTS

efficiency will decrease significantly due to the lesser temperature difference available to the device.

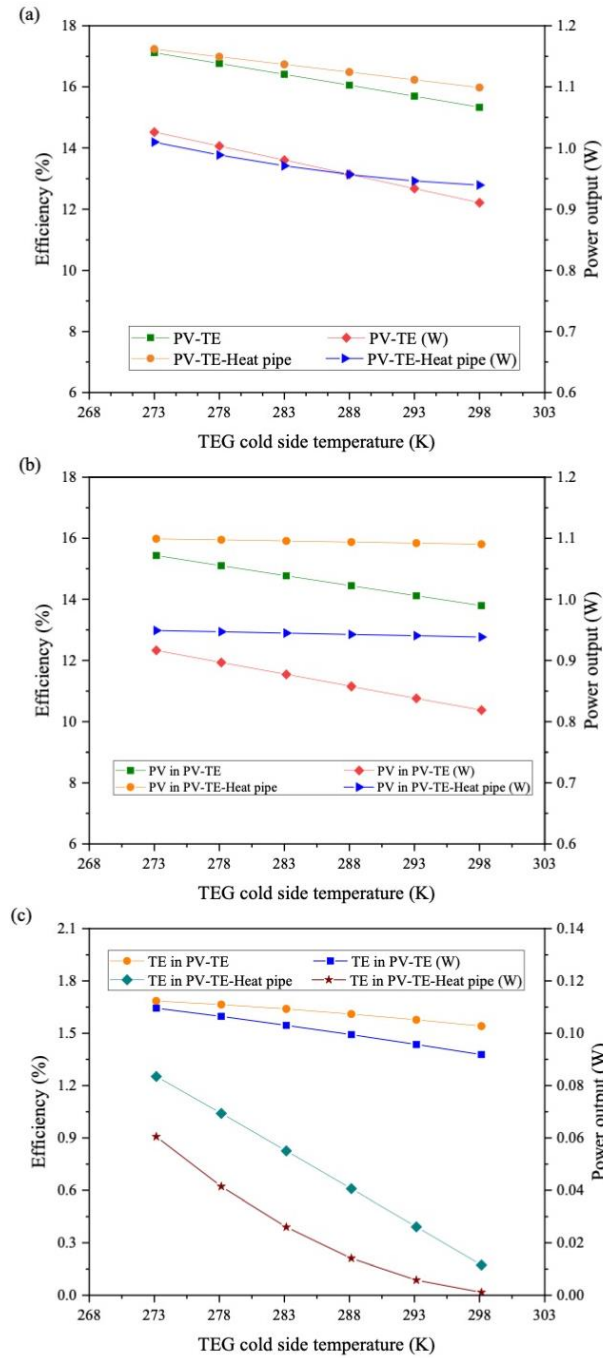


Figure 5.35: TEG cold side temperature variation with (a) overall (b) PV (c) TE efficiency and power output

In addition, Figure 5.35b shows that the power output and efficiency of the PV in PV-TE and PV-TE-Heat pipe decrease as the TEG cold side temperature increases

because of the inadequate cooling provided. As expected, Figure 5.35c shows that the TE in PV-TE provides a better performance compared to the TE in PV-TE-Heat pipe because of the lesser temperature gradient. However, in both cases, the TE power output and efficiency sharply decrease as the TEG cold side temperature increases thereby showing how highly important effective cooling of TEG is.

5.5.6 Temperature and Voltage Distributions

The temperature and voltage distribution in the PV-TE are shown in Figure 5.36 when ambient temperature is 298.15 K, wind speed is 1 m/s, concentration ratio is 6 and TEG cold side temperature is 293.15 K. The three-dimensional temperature distribution of the PV-TE can be seen from Figure 5.36a. Under the aforementioned conditions, the maximum temperature in the PV-TE is 337 K.

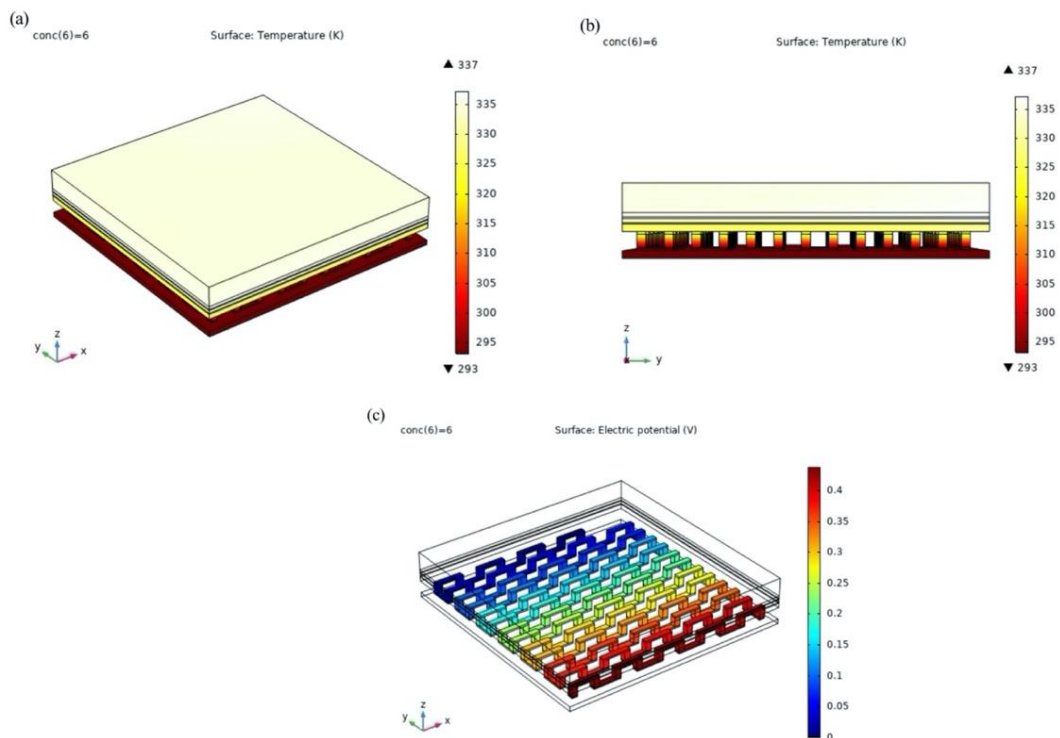


Figure 5.36: PV-TE temperature distribution in (a) three-dimension (b) side view (c) voltage distribution

CHAPTER 5 HYBRID PHOTOVOLTAIC-THERMOELECTRIC OPTIMIZATION RESULTS

Figure 5.36b shows the temperature distribution from the side view of the PV-TE while Figure 5.36c shows the voltage distribution in the PV-TE. It can also be seen that the highest temperature in the hybrid PV-TE system is generated at the polycrystalline silicon layer. Considering the PV-TE-Heat pipe, its temperature and voltage distribution are shown in Figure 5.37 when ambient temperature is 298.15 K, wind speed is 1 m/s, concentration ratio is 6 and TEG cold side temperature is 293.15 K. Figure 5.37a shows the three-dimensional temperature distribution of the PV-TE-Heat pipe.

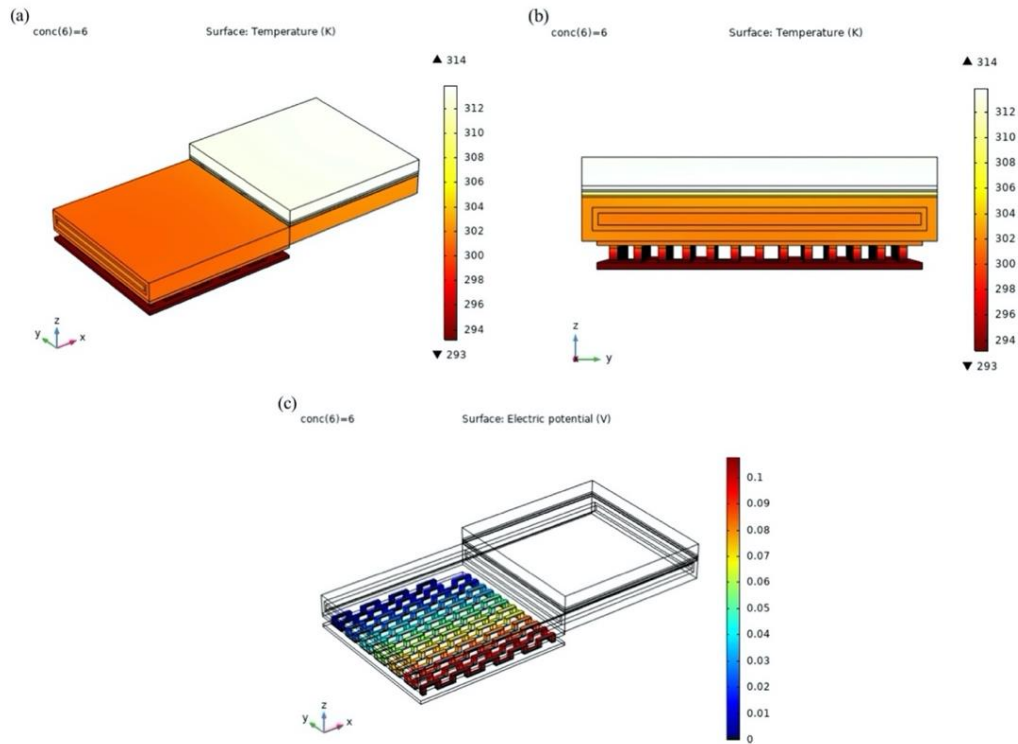


Figure 5.37: PV-TE-Heat pipe temperature distribution in (a) three-dimension (b) side view (c) voltage distribution

It can be seen clearly from Figure 5.37a that the maximum temperature under the aforementioned conditions is 314 K which is 23 K lower than that in the PV-TE as shown in Figure 5.36a. This shows the superiority of the flat plate heat pipe in cooling the PV compared to the TE. In addition, Figure 5.37b shows the temperature

distribution from the side view of the PV-TE-Heat pipe and it can be seen that the lowest temperature is from the TEG cold side. Finally, the TEG voltage distribution in the PV-TE-Heat pipe is shown in Figure 5.37c. The thermoelectric legs are connected in series therefore, current flows across all the legs and voltage can be measured across the negative and positive terminals.

5.5.7 Section Conclusion

This study presented a detailed comparative analysis of the performance of a PV only, PV-TE and PV-TE-Heat pipe under varying ambient conditions. The main conclusions from this study are as follows:

- 1) The PV-TE-Heat pipe system is recommended for highly concentrated systems because of its superior performance at high concentration ratios.
- 2) Efficiency of the PV-TE-Heat pipe is 3.31% and 58.01% higher compared to that of the PV-TE and PV only systems respectively at a concentration ratio of 6.
- 3) Ambient temperature increase is not beneficial to the performance of the PV, PV-TE and PV-TE-Heat pipe. Nevertheless, the PV-TE-Heat pipe efficiency is 1.47% and 61.01% higher than that of the PV-TE and PV only systems at a high ambient temperature of 313.15 K.
- 4) Increase in wind speed enhances the performance of the PV, PV-TE and PV-TE-Heat pipe although the enhancement is not significant in the PV-TE and PV-TE-Heat pipe.
- 5) Although the PV-TE-Heat pipe system is recommended because of its superior performance, it is worth noting that the PV-TE system is also a better alternative to the PV only system because its performance is better compared to the PV only system.

- 6) The PV and TE have a complex relationship in that some ambient conditions are beneficial to the performance of the PV while harming that of the TEG and vice versa.
- 7) Ineffective cooling of the TEG could cause a negative effect on the performance of the hybrid systems.

5.6 Chapter Summary

The validated simulation models are used to optimize the hybrid photovoltaic-thermoelectric system and photovoltaic-thermoelectric-heat pipe system. Results obtained from the four different studies were presented in this chapter. Furthermore, thermoelectric geometry optimization in a hybrid photovoltaic-thermoelectric system under steady state and transient conditions was presented in addition to contact resistance optimization. Optimization of the hybrid photovoltaic-thermoelectric system with flat plate heat pipe was also presented. COMSOL Multiphysics software was used to perform the three-dimensional numerical studies with finite element method. The main findings from each study carried out were presented in the section conclusions while the general summary of the optimization results from the four studies carried out are respectively:

- 1) The results showed that a hybrid PV-TE system will perform better with symmetrical TEG geometry ($R_A = R_S = 1$) if a PV temperature coefficient of 0.004/K (Cell B) is used. This is different from the optimum geometry for a TEG only system. However, the optimum geometry of the TEG in a hybrid system will be the same as that of a TEG only system (dissymmetrical i.e. $R_A = R_S \neq 1$) if a PV temperature coefficient of 0.001/K (Cell A) is used.

- 2) Results showed that thermoelectric geometry optimization can reduce significantly the negative impacts of the variable weather conditions on the hybrid system performance. Furthermore, results showed that the maximum hybrid system power output density with the optimized thermoelectric geometry decreased by 48.29% when the original geometry was used.
- 3) Results showed that ignoring all contact resistances in the hybrid system causes an overestimation of overall power output and efficiency by 7.6% and 7.4% respectively using the base values considered in this study. In addition, the thermal contact resistance between the thermoelectric generator and heat sink, and that between the photovoltaic-thermoelectric interface were found to be the most important contact resistances, which should be reduced.
- 4) Results showed that the photovoltaic-thermoelectric-heat pipe efficiency was 1.47% and 61.01% higher compared to that of the photovoltaic-thermoelectric and photovoltaic only systems respectively at a concentration ratio of 6. In addition, the photovoltaic-thermoelectric-heat pipe is recommended for highly concentrated systems because of its superior performance. Furthermore, the photovoltaic-thermoelectric system is a better alternative to the photovoltaic only system because of its enhanced performance which is second only to that of the photovoltaic-thermoelectric-heat pipe system. Results also showed that ineffective cooling of the thermoelectric generator can adversely affect the performance of the hybrid systems.

CHAPTER 6 THERMOELECTRIC GENERATOR OPTIMIZATION AND RESULTS DISCUSSION

6.1 Chapter Introduction

This chapter presents the results obtained using the validated simulation models for optimization of thermoelectric generator. Furthermore, results obtained from the optimization studies carried out on thermoelectric generator electrical and mechanical performance enhancement using innovative geometries such as annular, segmented and asymmetrical geometries are presented alongside optimization of the thermoelectric generator with phase change material. The following tasks are addressed in this chapter:

- 1) Presenting segmented annular thermoelectric generator optimization results.
- 2) Presenting segmented asymmetrical thermoelectric generator optimization results.
- 3) Presenting segmented solar thermoelectric generator optimization results.
- 4) Presenting solar thermoelectric generator with phase change material optimization results.

The optimization results presented in this chapter will provide valuable information on enhancing the performance of the thermoelectric generator and influence the design and optimization of the thermoelectric generator.

6.2 Segmented Annular Thermoelectric Generator

The segmented annular thermoelectric generator (SATEG) geometry is shown in Figure 6.1, and it consists of alumina ceramics, copper, welding layer and thermoelectric legs. In Figure 6.1a, θ_1 represents the angle of a single thermoelectric

leg, θ_2 represents half of the angle between two legs and θ_3 represents the angle between the cold side (outer) copper and the thermoelectric legs. The total leg angle of the thermoelectric generator is $\theta = \theta_1 + \theta_2$. The radius of each of the components of the SATEG are represented by r_1 to r_{10} as shown in Figure 6.1a. In addition, the length of the thermoelectric leg can be obtained from: $L = r_7 - r_6 = r_5 - r_4$. For simplification purposes, the lengths of the p-type and n-type thermoelectric materials are assumed equal. Also, the lengths of the thermoelectric elements (n-type and p-type) in the cold segment are assumed to be equal to those of the hot segment. In order to increase the speed of calculation, only one uni-couple is analysed as shown in Figure 6.1b.

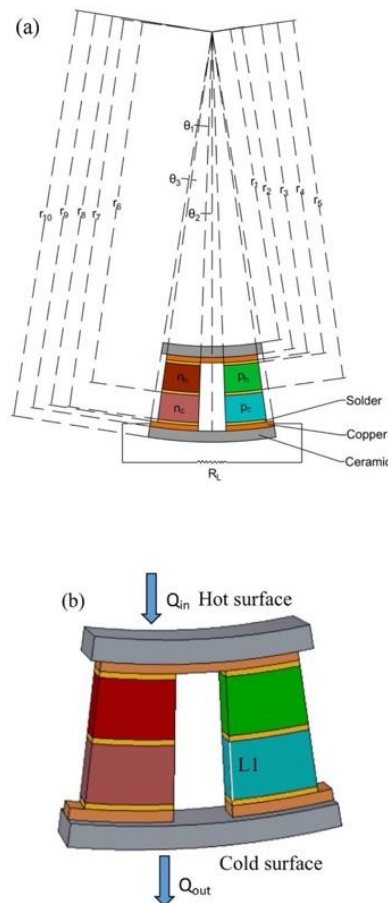


Figure 6.1: SATEG geometry; (a) schematic diagram and (b) three-dimensional view

Different geometries analysed corresponding to the different leg length and leg angle of the SATEG and ATEG studied are drawn with AutoCAD software and imported into COMSOL individually. Each geometry is then analysed under similar conditions and the performance is observed. Furthermore, the geometry of the non-segmented annular thermoelectric generator analysed in this study is shown in Figure 6.2. For all of the drawings (SATEG, ATEG) the radius of the cold side ceramic is kept constant and is the beginning of each drawing. The only difference between the SATEG and ATEG studied is the segmentation of the TEG into two different thermoelectric pairs and materials. All other components, leg angle and leg length are exactly the same with those of the SATEG. This is to ensure similarity between the SATEG and ATEG so that proper comparison in performance can be made. In addition, Bismuth telluride (Bi_2Te_3) is the material (n-type and p-type) used on the cold segment (n_c and p_c) while CoSb_3 Skutterudite material (n-type and p-type) is used on the hot segment (n_h and p_h). The addition of an external load resistance R_L helps to close the electric circuit so that the output power can be measured.

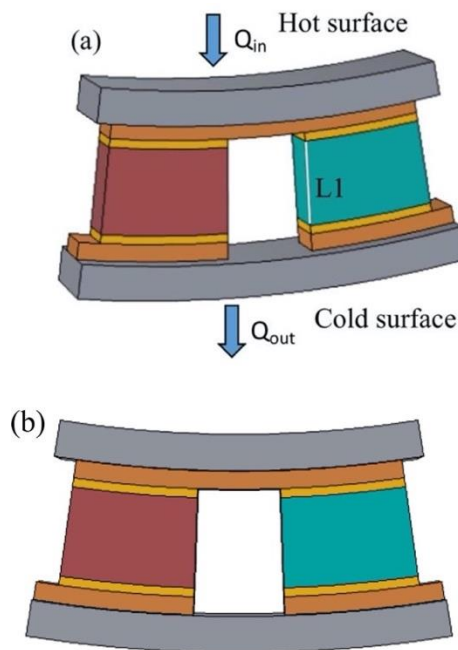


Figure 6.2: ATEG geometry; (a) three-dimensional view and (b) front view

6.2.1 Boundary Conditions

The basic assumptions made in this numerical simulation to simplify the model without significant deviations from the real condition are:

- 1) All other surfaces except the hot and cold surfaces are adiabatic.
- 2) Electrical contact resistance and thermal contact resistance are ignored.
- 3) Heat losses due to convection and radiation on all surfaces are neglected.
- 4) The heat source (hot surface) and heat sink (cold surface) are considered as thermal boundary conditions with fixed temperature values.
- 5) A fixed constraint boundary condition is applied on the hot surface of the thermoelectric generator while all other boundaries are free.
- 6) No difference in properties as a function of position exist.
- 7) A fixed temperature value of 298 K is applied to the cold surface to cool the thermoelectric generator.

6.2.2 Effect of Heat Source Temperature

Due to the fact that the input heat flux (Q_{in}) is dependent on the load resistance, there is a variation between the optimum load resistance for maximum output power and efficiency for different segmentation cases (Jia and Gao, 2014). Therefore, to better observe the effect of segmentation on the conversion efficiency which is the most important performance indicator considered in this study, the calculations are carried out at a constant load resistance condition. Since the heat sink temperature is kept constant throughout this study, the effect of the heat source temperature on the electrical performance of the SATEG and ATEG can be seen in Figure 6.3. Increase in temperature difference leads to an increase in the efficiency and output power of the SATEG and ATEG. This is a normal and expected phenomenon. However, the advantage of the SATEG over the Bismuth telluride ATEG in terms of efficiency can

be clearly seen when the temperature difference starts increasing from 100 K as shown in Figure 6.3a.

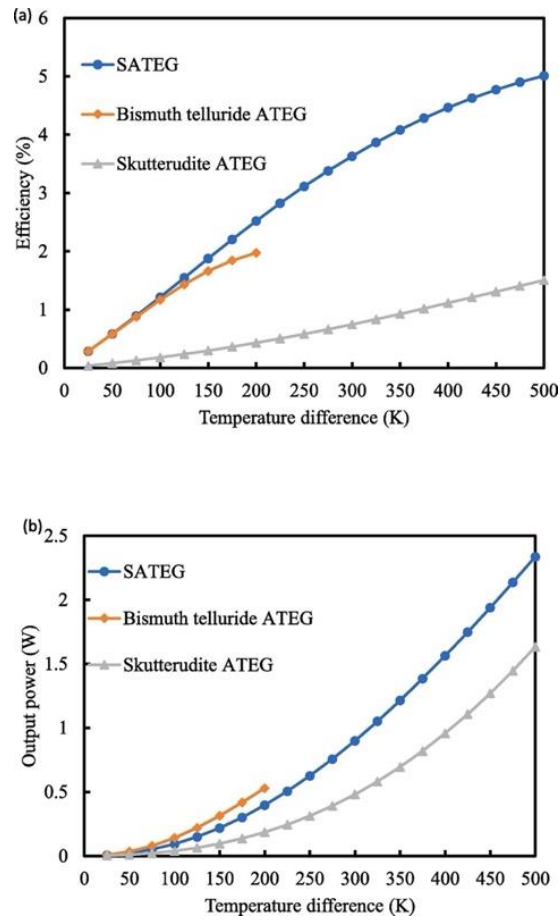


Figure 6.3: Variation of SATEG and ATEG (a) efficiency and (b) output power with temperature difference when $L = 2$, $\theta_1 = 6$, $\theta_2 = 2$ and $R_L = 0.01 \Omega$

It is also obvious that the Skutterudite ATEG's efficiency is lower than the other two and the SATEG is the best performing device in all temperature ranges. The conversion efficiency of the SATEG is 21.7% and 82.9% greater than that of the Bismuth telluride ATEG and Skutterudite ATEG respectively at a temperature difference of 200 K as shown in Figure 6.3a. Furthermore, Figure 6.3b proves the point that the optimum load resistance for efficiency and output power are different. It can be seen that although the SATEG has the highest efficiency at that load resistance, its output power is actually lower than that of the Bismuth telluride ATEG. However, the

advantage of the SATEG is its better performance over a higher temperature range compared to the limited temperature range of Bismuth telluride. Therefore, the SATEG can be used beyond the maximum temperature range for Bismuth telluride (498 K) thus, it has a higher potential compared to the other two single-material ATEG for recovering waste at a large temperature difference.

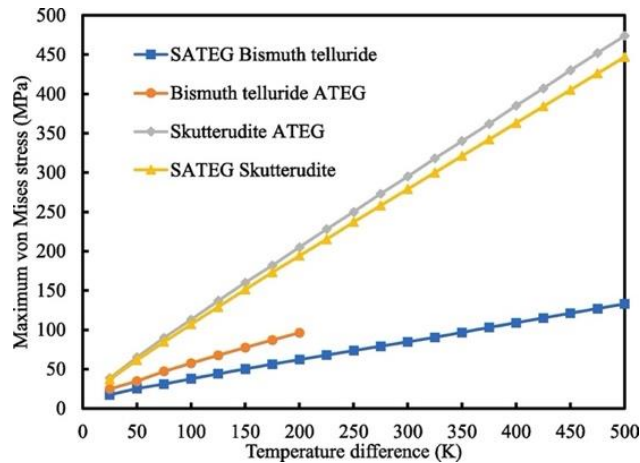


Figure 6.4: Variation of maximum von Mises stress in legs of SATEG and ATEG with temperature difference when $L = 2$, $\theta_1 = 6$ and $\theta_2 = 2$

The mechanical performance of the SATEG and ATEG under different heat source temperatures can be seen from Figure 6.4. The figure clearly shows the significance of segmentation as the maximum von Mises stress in the legs of the SATEG is lower than that in the ATEG. It can also be seen that the heat source temperature and maximum von Mises stress in the legs of both the SATEG and ATEG have a linear relationship. The maximum stress level in the legs of the Bismuth telluride ATEG is below the yield stress of the material even at its maximum allowable temperature range. However, the Bismuth telluride material in the SATEG will fail the mechanical strength test once the temperature difference applied on the SATEG is greater than 400 K. At a temperature difference of 200 K, the maximum von Mises stress in the legs of the Bismuth telluride material in the SATEG is lower by 35.4% compared to that of the Bismuth telluride ATEG. While at 500 K temperature

difference, the maximum von Mises stress in the legs of the Skutterudite material in the SATEG is lower by 5.7% compared to that of the Skutterudite ATEG. Therefore, SATEG has a better mechanical performance compared to the ATEG as shown in Figure 6.4.

6.2.3 Effect of Thermoelectric Leg Length

The effect of thermoelectric leg length on the electrical performance of Bismuth telluride ATEG, Skutterudite ATEG and SATEG can be seen in Figure 6.5, Figure 6.6 and Figure 6.7 respectively. It can be seen that the efficiency and output power for each of the devices follow the same trend.

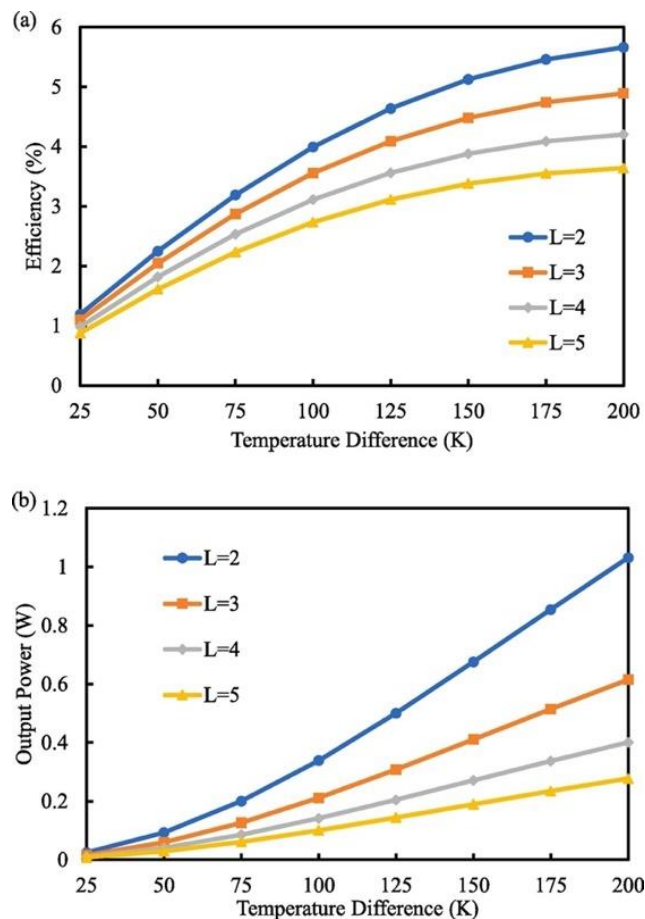


Figure 6.5: Variation of Bismuth telluride ATEG leg length with (a) Efficiency and (b) Output power when $\theta_1 = 3$, $\theta_2 = 3$, and $R_L = 0.001 \Omega$

The length of the thermoelectric leg has a significant influence on the performance, and it is found that short thermoelectric leg length provides better electrical performance than longer thermoelectric leg length. From Figure 6.5a, it can be seen that the efficiency of the device using the shortest leg length ($L = 2$) considered in this study is 35.7% greater than that of the device using the longest leg length ($L = 5$) considered in this study. Similarly, the output power when $L = 2$ is 73.1% greater than the output power when $L = 5$ as shown in Figure 6.5b. This shows how significant the influence of the leg length is on the electrical performance.

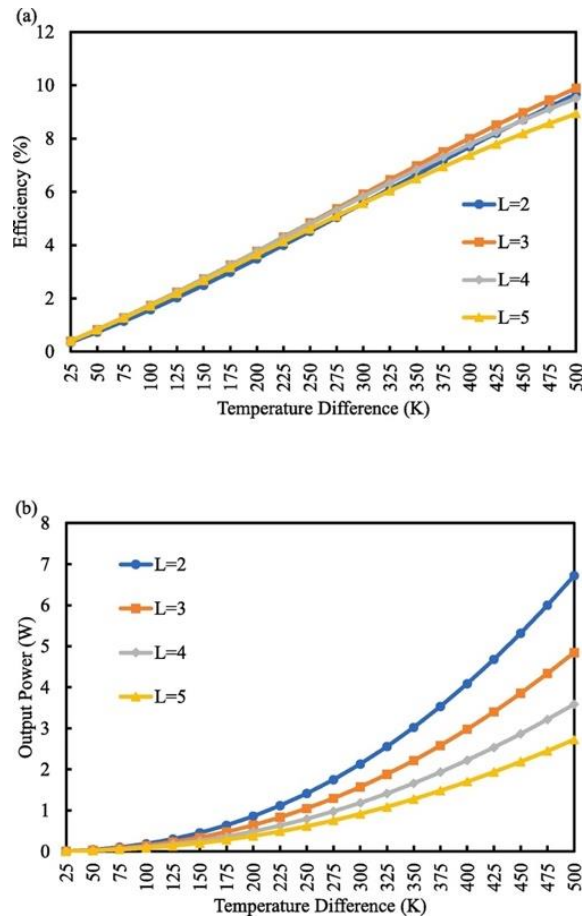


Figure 6.6: Variation of Skutterudite ATEG leg length with (a) Efficiency and (b) Output power when $\theta_1 = 3$, $\theta_2 = 3$, and $R_L = 0.001 \Omega$

In the case of the Skutterudite ATEG, the influence of the leg length over the device efficiency is not that obvious (Figure 6.6a) unlike when its output power is

considered as shown in Figure 6.6b. The output power of the Skutterudite ATEG when $L = 2$ is 59.4% greater than its output power when $L = 5$ as seen in Figure 6.6b. The same trend is observed in Figure 6.7a and Figure 6.7b for the efficiency and output power of the SATEG. In addition, an efficiency and output power enhancement of 45.3% and 79.1% respectively is observed when the SATEG thermoelectric leg length is reduced from $L = 5$ to $L = 2$.

The effect of the thermoelectric leg length on the mechanical performance of the thermoelectric devices is shown in Figure 6.8 and Figure 6.9. Increase in thermoelectric leg length has a positive effect on the von Mises stress developed in the leg. As shown in Figure 6.8, the lowest von Mises stress is observed when the leg length is high ($L = 5$) for both the SATEG and ATEG. The maximum von Mises stress in the Bismuth telluride material is reduced by 20.4% and 7.9% for the ATEG and SATEG respectively when the thermoelectric leg length is increased from $L = 2$ to $L = 5$. This shows that increasing the thermoelectric leg length can improve the mechanical reliability but reduce the electrical performance of the thermoelectric devices and this finding is in agreement with (Fan and Gao, 2018). The advantage of segmentation can also be seen from Figure 6.8 as the maximum von Mises stress in the Bismuth telluride material of the SATEG is lower than that of the ATEG for all leg length. In addition, Figure 6.9 also shows the effect of leg length on the mechanical performance of the SATEG and ATEG. However, the trend observed is slightly different due to the difference in the material and its mechanical properties. It can be seen from Figure 6.9 that the thermoelectric leg length of $L = 4$ provides the lowest von Mises stress in the legs of the Skutterudite material of the SATEG.

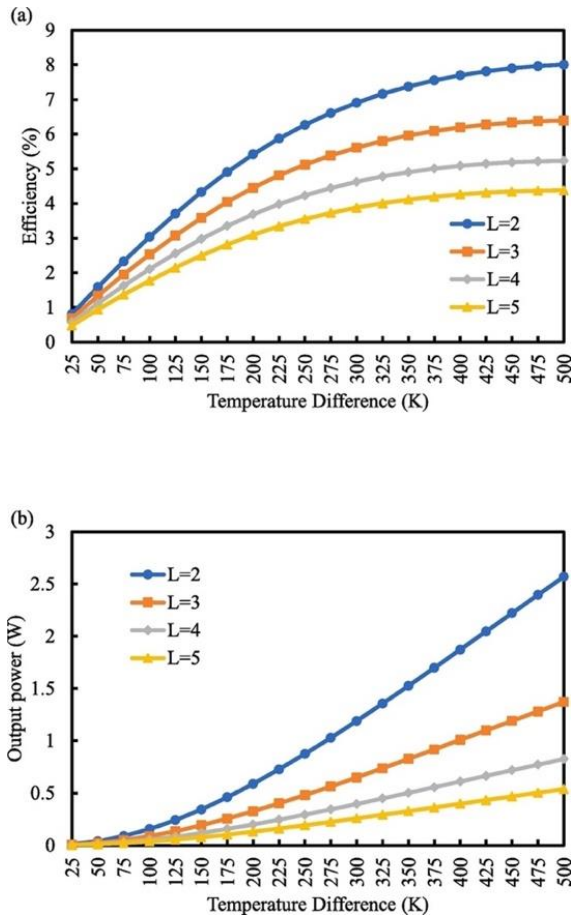


Figure 6.7: Variation of SATEG leg length with (a) Efficiency and (b) Output power when $\theta_1 = 3$, $\theta_2 = 3$, and $R_L = 0.001 \Omega$

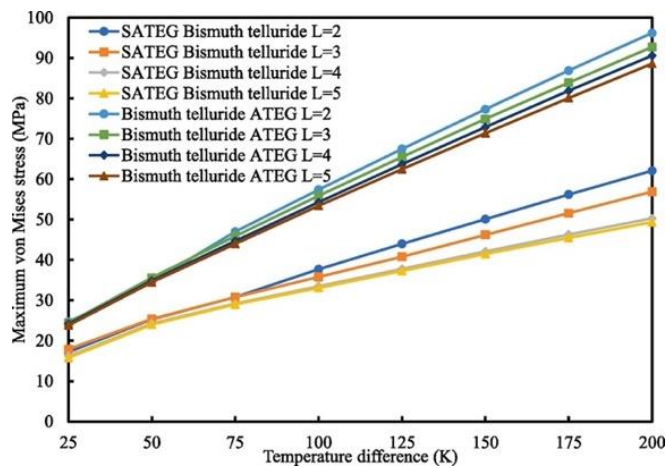


Figure 6.8: Effect of Bismuth telluride thermoelectric leg length in SATEG and ATEG when $\theta_1 = 6$ and $\theta_2 = 2$

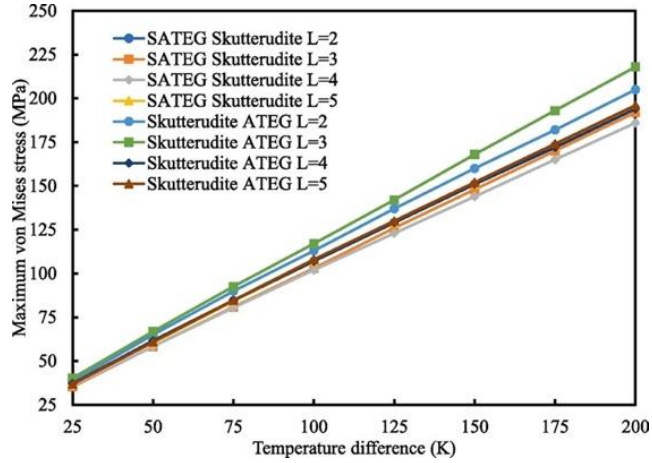


Figure 6.9: Effect of Skutterudite thermoelectric leg length in SATEG and ATEG when $\theta_1 = 6$ and $\theta_2 = 2$

6.2.4 Effect of Thermoelectric Leg Angle

The effect of the thermoelectric leg angle on the efficiency and output power of the SATEG is shown in Figure 6.10a and Figure 6.10b respectively. It can be seen from both figures that the efficiency and output power decreases when θ_2 increases. This implies that a small angle between the SATEG thermoelectric legs (n-type and p-type) can enhance the efficiency and output power of the device. Also, it can be seen that short thermoelectric legs provide the best performance in terms of efficiency and output power. Figure 6.10a and Figure 6.10b show that the optimum geometry of the SATEG for maximum electrical performance is when $L = 2$, $\theta_2 = 2$ and $\theta = 8$. It can be seen from Figure 6.10a and Figure 6.10b that at optimum length ($L = 2$), an efficiency and output power enhancement of 17.8% and 55.5% can be achieved respectively just by reducing the angle between the thermoelectric legs from $\theta_2 = 5$ to $\theta_2 = 2$.

The effect of the leg length on the maximum von Mises stress in the Bismuth telluride material of the SATEG can be seen in Figure 6.11a. For all the thermoelectric leg lengths considered, the maximum von Mises stress decreases as the angle between

the thermoelectric legs increases from $\theta_2 = 2$ to $\theta_2 = 5$. This shows that the electrical and mechanical performance of the SATEG have an inverse relationship when leg length and/or leg angle is being varied. Therefore, an optimum geometry must be obtained which will satisfy both the electrical requirement and mechanical reliability of the SATEG.

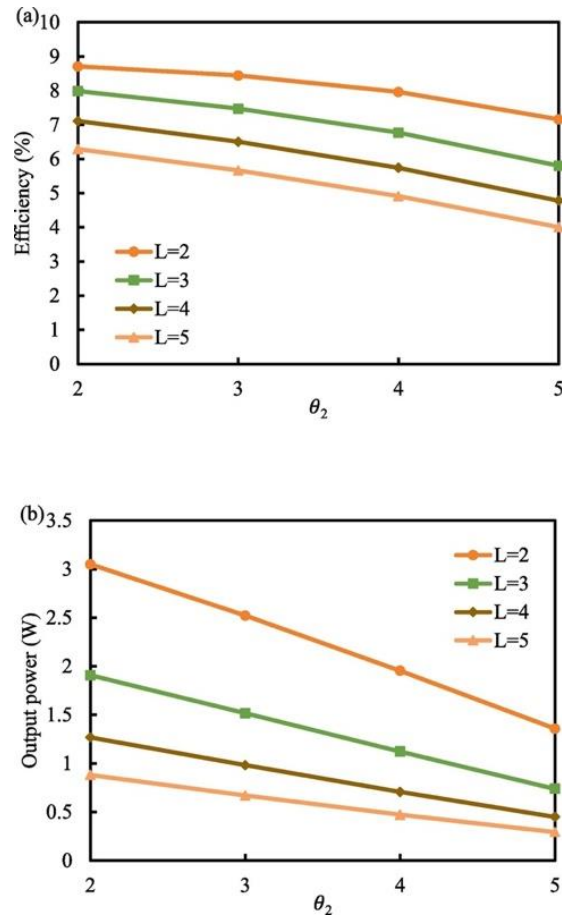


Figure 6.10: Variation of leg angle with SATEG (a) efficiency and (b) output power when $\theta = 8$, $T_h = 623K$ and $R_L = 0.001$

In addition, Figure 6.11a shows that at optimum mechanical reliability length ($L = 5$), a thermal stress decrease of 5.67% can be achieved just by increasing the angle between the thermoelectric legs from $\theta_2 = 2$ to $\theta_2 = 5$. Figure 6.11b shows the effect of leg angle on the maximum von Mises stress present in the Skutterudite material of the SATEG. The trend observed in this case (Figure 6.11b) is opposite to

that in Figure 6.11a. This implies that while an increase in the angle between the thermoelectric legs from $\theta_2 = 2$ to $\theta_2 = 5$ leads to a decrease in the maximum von Mises stress present in the Bismuth telluride material (cold segment) of the SATEG, an opposite effect is created in the Skutterudite material (hot segment). Therefore, the leg angle and leg length of the segmented annular thermoelectric generator must be carefully chosen to satisfy low stress requirements in both segments of the device.

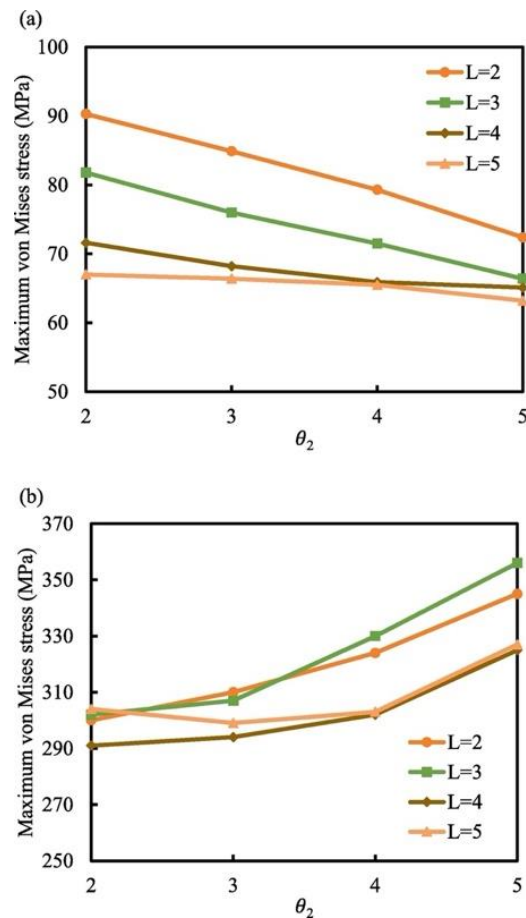


Figure 6.11: Variation of leg angle with maximum von Mises stress in (a) Bismuth telluride and (b) Skutterudite materials of the SATEG when $\theta = 8$ and $T_h = 623 K$

6.2.5 SATEG von Mises Stress Nephogram

The von Mises stress nephogram in the cold and hot segment of the segmented annular thermoelectric generator can be seen in Figure 6.12 and Figure 6.13 respectively. It can be seen clearly that the maximum von Mises stress occurs at the

hot surface of the thermoelectric legs which is in direct contact with the solder. It can also be seen that the maximum von Mises stress occurs at the edge of the thermoelectric legs thus, that region can easily break off. Thermal stress intensity is a very important factor that influences the lifecycle of a thermoelectric generator. Since the mechanical material properties (e.g. Young's modulus, Coefficient of thermal expansion) of each of the components in the TEG are different, thermal stress will be generated whenever a large temperature gradient is applied. As seen from Figure 6.12 and Figure 6.13, the positions that are most likely to crack are the contact areas between the hot surface of the thermoelectric legs and the solder strips, and the edges of the legs. It should be noted that the stress values shown in Figure 6.12 and Figure 6.13 are obtained while considering the elastoplastic characteristics of the copper and solder materials. If this is not considered, the maximum von Mises stress in the legs will be higher.

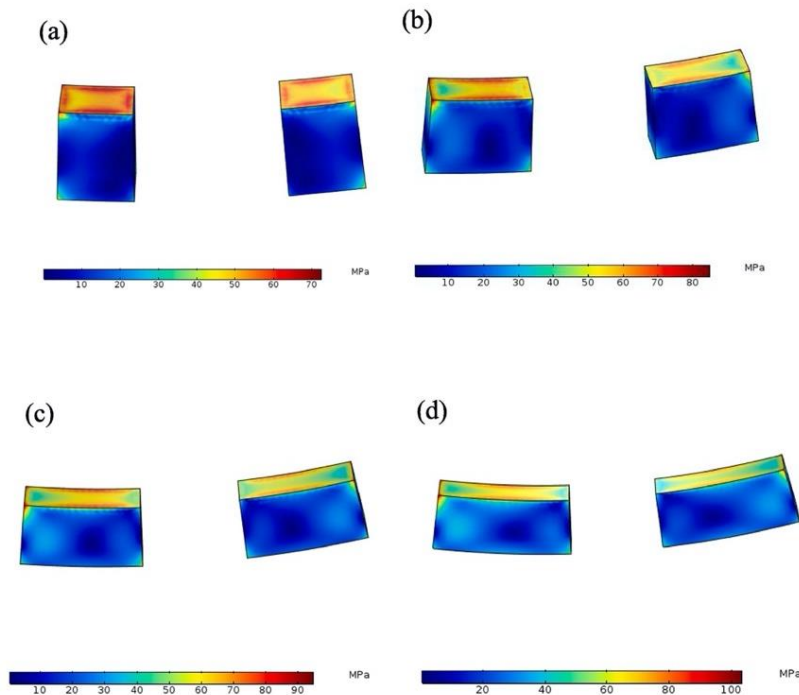


Figure 6.12: Nephogram of the von Mises stress in Bismuth telluride material of the SATEG

when $L = 2$, $T_h = 623\text{ K}$, $\theta_2 = 3$, (a) $\theta_1 = 3$, (b) $\theta_1 = 5$, (c) $\theta_1 = 7$ and (d) $\theta_1 = 9$

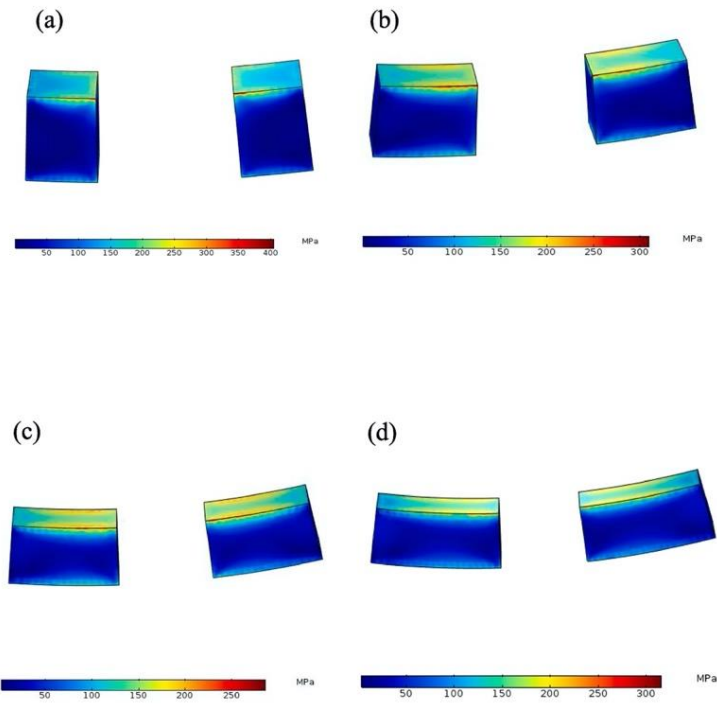


Figure 6.13: Nephogram of the von Mises stress in Skutterudite material of the SATEG when $L = 2$, $T_h = 623\text{ K}$, $\theta_2 = 3$, (a) $\theta_1 = 3$, (b) $\theta_1 = 5$, (c) $\theta_1 = 7$ and (d) $\theta_1 = 9$

6.2.6 Section Conclusion

In this study, the thermoelectric and mechanical performance of a segmented annular thermoelectric generator has been investigated using finite element analysis. Some of the important conclusions from this research are:

- 1) The efficiency of the SATEG is 21.7% and 82.9% greater than the efficiency of the Bismuth telluride ATEG and Skutterudite ATEG respectively at 200 K temperature difference.
- 2) The maximum von Mises stress in the legs of the Bismuth telluride material in the SATEG is 35.4% lower than that of the Bismuth telluride ATEG at 200 K temperature difference.

- 3) Efficiency and output power enhancement of 45.3% and 79.1% respectively were observed when the SATEG leg length was reduced from $L = 5$ to $L = 2$. Therefore, shorter thermoelectric legs provide better electrical performance.
- 4) Increase in thermoelectric leg length leads to decrease in thermal stress and an increase in electrical performance. Therefore, increasing thermoelectric leg length can improve the mechanical reliability but reduce the electrical performance of the thermoelectric generator.
- 5) The optimum geometry for maximum electrical performance of the SATEG studied is when $L = 2$, $\theta_2 = 2$ and $\theta = 8$. This geometry provides the best electrical performance for the system.
- 6) The Maximum von Mises stress in the SATEG decreases as the angle between the thermoelectric legs increases from $\theta_2 = 2$ to $\theta_2 = 5$ for all leg lengths considered.

6.3 Segmented Asymmetrical Thermoelectric Generator

The geometry of a typical thermoelectric generator (TEG) is shown in Figure 6.14a while that of the segmented asymmetrical thermoelectric generator (SASTEG) is shown in Figure 6.14b. The optimized geometry of the SASTEG is shown in Figure 6.14c and the rectangular heat flux pulse applied to the hot side of the TEG and SASTEG is shown in Figure 6.14d. Transient and steady state heating conditions are applied to the hot side of the TEG and SASTEG while the cold side is maintained at a constant temperature. In the case of the SASTEG, two different thermoelectric materials are used for the p-type leg as shown in Figure 6.14b. The dimensions of the TEG and SASTEG are exactly the same so as to ensure accurate comparison of

performance. The total height of the thermoelectric legs remains the same in both the TEG and SASTEG therefore,

$$H = H_1 + H_2 = H_3 + H_4 \quad (6.1)$$

where H_1 is the height of the hot segment p-type thermoelectric material, H_2 is that of the cold segment p-type material, H_3 is the height of the hot segment n-type thermoelectric material and H_4 is that of the cold segment n-type material.

For the sake of simplicity, the n-type and p-type thermoelectric legs are of the same dimensions. In this study, only the n-type leg is asymmetrical because the n-type materials are universally weaker compared to their p-type counterparts (Ouyang and Li, 2016). In addition, asymmetrical legs have been reported to perform better than the rectangular legs (Fabián-Mijangos et al., 2017). Therefore, to improve the performance of the n-type leg and consequently optimize the SASTEG performance, the n-type leg is made asymmetrical. The effect of asymmetrical p-type leg is beyond the scope of this present study and would be considered in future works. The asymmetrical n-type leg used in the SASTEG is achieved by varying the cross-sectional area across the leg height. Again, to simplify the analysis, the hot side cross-sectional area of the asymmetrical leg is half of that of the cold side therefore,

$$W_{le} = W_c = W_h \times 2 \quad (6.2)$$

where W_{le} is the width of the leg, W_h is the width of the hot side n-type asymmetrical thermoelectric leg and W_c is that of the cold side thermoelectric leg. This ratio is kept constant throughout the study. However, the height ratio of the segmented thermoelectric materials is varied to find the optimum value. Thus,

$$H_p = \frac{H_1}{H_2} \quad (6.3)$$

$$H_n = \frac{H_3}{H_4} \quad (6.4)$$

where H_p is height ratio of the SASTEG p-type material and H_n is that of the n-type materials.

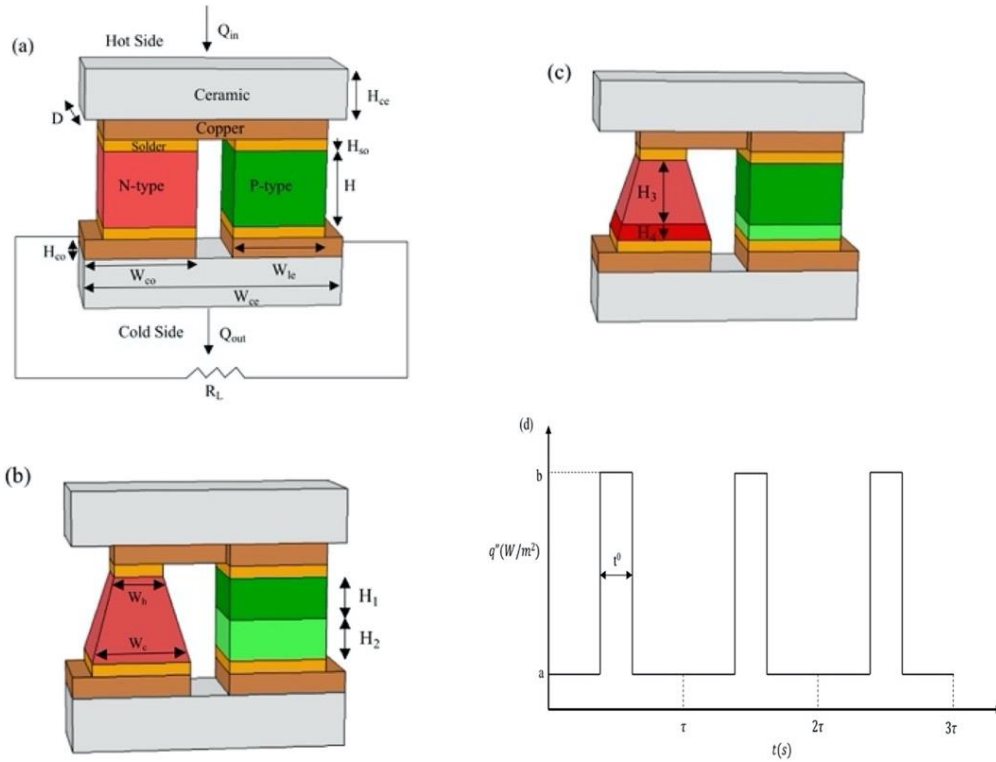


Figure 6.14: Schematic diagram of (a) thermoelectric generator (b) segmented asymmetrical thermoelectric generator and (c) optimized SASTEG geometry (d) rectangular heat flux pulse

Considering the optimum operating temperature range of thermoelectric materials, Bismuth telluride (Bi_2Te_3) and Skutterudite (CoSb_3) have been chosen for the cold segment/side and hot segment/side of the SASTEG respectively. While for the TEG, only Skutterudite thermoelectric material is used so as to ensure accurate comparison can be made with the SASTEG in the high temperature conditions under which both systems are studied.

In this study, steady-state heating (SSH) and pulsed heating (PH) are applied to both the SASTEG and the TEG. Duty cycle and period time (τ) are used to characterize the pulsed heat flux. Duty cycle ($\frac{t^0}{\tau}$) is defined as the ratio of heating time (t^0) to period time. Throughout the simulations, the overall heat input in the

pulsed heating case is equal to that of the steady state heating case. Rectangular function is used to model the pulsed heat input flux and considering Figure 6.14d, the input time-average heat flux for the rectangular function is given as (Asaadi et al., 2018):

$$q'' = a + (b - a) \times \frac{t^0}{\tau} \quad (6.5)$$

where b/a is the ratio of maximum input heat flux to minimum input heat flux for a time period. Throughout this study, $b/a = 12$ and $q'' = 60 \text{ kW} \cdot \text{m}^{-2}$.

Considering six continuous time periods ($6\tau = 720\text{s}$), the transient heat input is given as

$$q'' = (b - a) \times f(t) + a \quad (6.6)$$

where $f(t)$ is the rectangular input function.

6.3.1 Boundary Conditions

To simplify the analysis, some basic assumptions are made while still ensuring there is no significant deviation from the real conditions. These assumptions are:

- 1) The input heat flux is applied to the top surface (hot side) of the TEG with temperature T_h while the bottom surface (cold side) is maintained at a constant temperature (T_c) of 300 K.
- 2) Adiabatic condition is assumed therefore, no heat losses from all the other surfaces.
- 3) The hot side of the TEG is constrained during the thermal stress analysis while other boundaries are free.
- 4) Anisotropic material properties are not considered.
- 5) The lower left copper electrode is grounded while the lower right copper electrode is connected to the external resistor circuit.
- 6) Electrical and thermal contact resistance are not considered.

6.3.2 Thermal and Electrical Responses to Pulsed Heat Flux

The responses of temperature, open circuit voltage, current and maximum power output of the SASTEG and TEG to transient rectangular pulsed heating and steady state heating for five continuous time periods are shown in Figure 6.15a, Figure 6.15b, Figure 6.15c and Figure 6.15d respectively. The steady state heating is represented by a straight line while the rectangular pulsed heating is represented by dotted and dashed lines for the SASTEG and TEG respectively. The spatially averaged heat flux used in all simulations is $60 \text{ kW} \cdot \text{m}^{-2}$ and this is kept constant for both the pulsed heating and the steady state heating. Maximum power output can be obtained when the load resistance is matched to the TEG's internal resistance. Therefore, the external load resistance is varied till maximum power output is obtained which represents the matched load condition. The matched load under steady state heating for the SASTEG is found to be 0.012Ω and that of the TEG is found to be 0.006Ω .

To simplify the analysis, the load resistance is kept constant throughout this study for both the steady state heating and the pulsed heating. Figure 6.15a shows the spatially average temperature on the hot surface of the SASTEG and TEG while Figure 6.15b shows the open circuit voltage obtained from both devices at steady state and pulsed heating conditions. It can be seen from Figure 6.15 that the temperature, voltage, current and power output follow the same trend and transient heating provides a better performance compared to steady state heating due to the fact that the rectangular pulsed heating allows for a greater temperature difference across the thermoelectric generator. Another clear observation from Figure 6.15 is that the performance of the SASTEG is almost twice better than that of the TEG. This shows that the new design for thermoelectric generator incorporating the segmented

CHAPTER 6 THERMOELECTRIC GENERATOR OPTIMIZATION AND RESULTS DISCUSSION

materials and asymmetrical legs provides better electrical performance compared to the conventional TEG design.

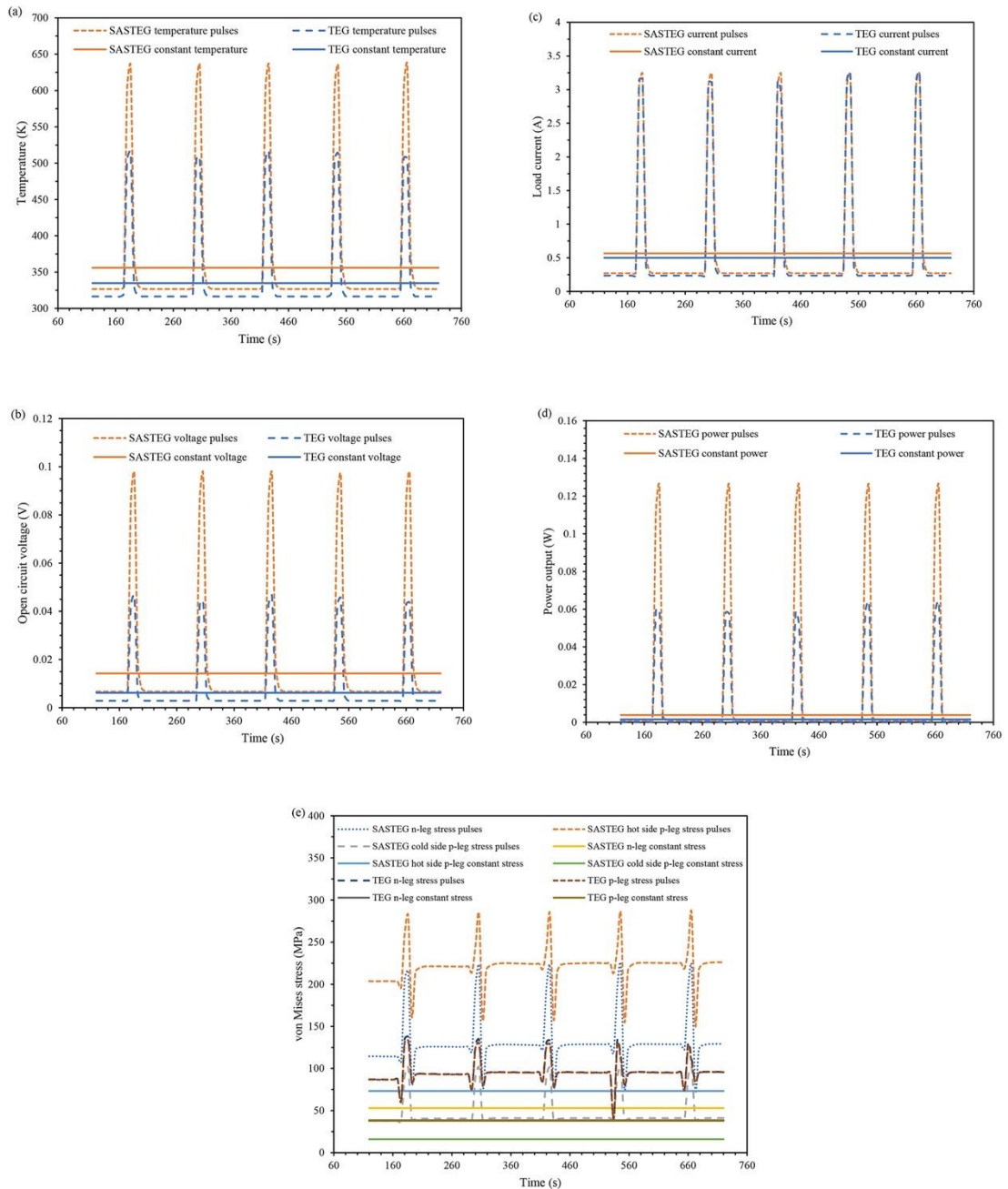


Figure 6.15: Transient and steady state responses of the SASTEG and TEG (a) temperature (b) open circuit voltage (c) load current (d) power output and (e) von Mises stress

The variation of the load current with time shown in Figure 6.15c is identical for the SASTEG and TEG because of the difference in load resistance used to attain the maximum power output. The load current simply obeys the ohms law therefore, it

is given as the output load voltage divided by the load resistance. Although the load current in both the SASTEG and TEG is identical, the power output of each device is clearly different because of the difference in their open circuit voltage and corresponding output load voltage when the external resistance is matched. It can be seen from Figure 6.15d that the maximum power output of the SASTEG at steady state condition is 0.0038469 W while that of the TEG is 0.0015034 W under the same condition. Therefore, a power output improvement of about 155.88% is observed under steady state condition simply by using the new design of the thermoelectric generator (i.e. SASTEG design).

Furthermore, the application of transient rectangular pulsed heat power is shown in Figure 6.15d to enhance the power output of the SASTEG and TEG significantly compared to the steady state heating. In fact, it can be seen that for the transient heating, the areas above the straight line (steady state heating) are larger than the areas below the straight line therefore, it can be concluded that the performance enhancement offered by the transient heating is significantly greater than that of the steady state heating. This finding is in agreement with (Asaadi et al., 2018; Chen and Lee, 2015).

The maximum von Mises stresses developed in the n-type and p-type thermoelectric legs of the SASTEG and TEG under transient and steady state heating conditions are shown in Figure 6.15e. Although the SASTEG offers a significant power enhancement compared to the TEG, it can be seen that the maximum von Mises stress developed in the legs of the SASTEG are greater than that of the TEG under both heating conditions. This is an expected trend because the thermal stress developed is directly proportional to the temperature distribution in the TEG. Therefore, since the SASTEG operates at a significantly higher temperature compared

to the TEG, its von Mises stress is expected to be higher. Also, it is obvious that the maximum von Mises stress under transient heating will be greater than that under the steady state heating due to the difference in operating temperature. The trend observed during the transient heating for the SASTEG and TEG shown in Figure 6.15e is simply because of the periodic switching on and off of the pulse heat and this is why the von Mises stress goes to a minimum value and then it starts rising again as the rectangular pulse is applied. A solution to reduce the maximum von Mises stress developed in the SASTEG while maintaining its enhanced power output compared to the TEG is to optimize the SASTEG geometry.

6.3.3 Optimization of SASTEG

Two stages of optimization are carried out on the SASTEG including the p-type leg optimization and the n-type leg optimization. Firstly, the optimum height ratio for the segmented p-type leg (H_p) is found by varying this ratio for the range $0.2 \leq H_p \leq 0.5$. This range was considered because of the ease of manufacturing. If smaller ratios are considered like below 0.2, the material size for the low segment will be so small that it might be difficult to manufacture. In addition, since it might be difficult to consider all possible ratios that could be used, a sample range is chosen for analysis in this study. Figure 6.16a shows the maximum von Mises stress developed in the hot and cold side legs of the p-type leg as the height ratio is varied. It is clear from Figure 6.16a that the optimum height ratio for the segmented p-type leg (H_p) is 0.2. This is because, when $H_p = 0.2$, for all time periods and for both the hot side and cold side of the p-type leg, the von Mises stress developed is the lowest compared to other height ratios.

Furthermore, as expected, the von Mises stress in the hot side p-type leg is greater than that of the cold side p-type leg due to the higher temperature impinged on

the hot side. In addition, it is clear that the height ratio $H_p = 0.5$ provides the worst performance in terms of maximum von Mises stress developed thus, the need for the optimization of the initial geometry used in this study is shown. Figure 6.16b shows the variation of the maximum von Mises stress in the SASTEG with the optimized p-type leg ($H_p = 0.2$) and it can be seen that compared to the thermal stress in the initial geometry shown in Figure 6.15e, the maximum von Mises stress in the SASTEG hot side p-leg has been reduced by about 20.95% while that of the cold side p-leg has been reduced by about 21.16% due to the optimization of the height ratio under transient heating condition.

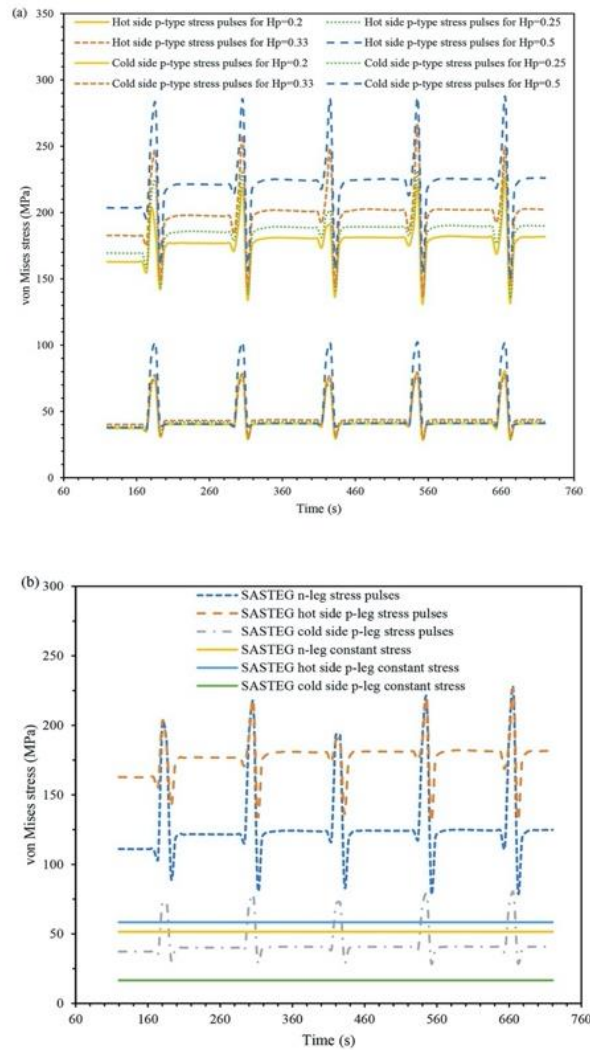


Figure 6.16: (a) Variation of von Mises stress with SASTEG p-type height ratio (H_p) and (b) first optimized SASTEG p-type leg

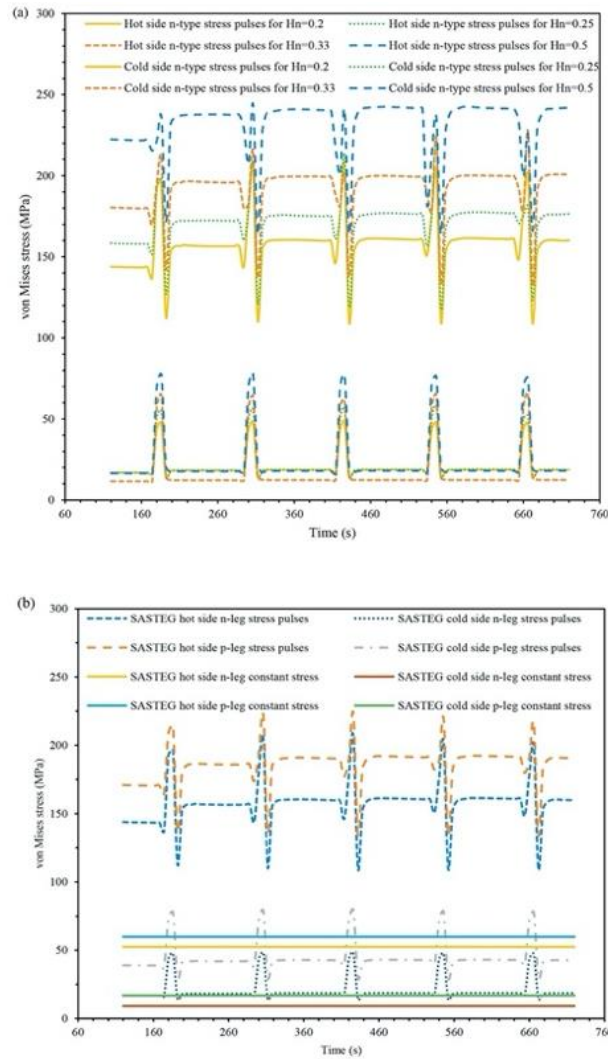


Figure 6.17: (a) Variation of von Mises stress with SASTEG n-type height ratio (H_n) and (b) second stage optimized SASTEG

In the second optimization stage, the n-type leg of the SASTEG is optimized while keeping the p-type leg at the optimized height ratio ($H_p = 0.2$) obtained from the first optimization stage. Thus, the n-type leg is segmented similar to the p-type leg in the initial geometry then the optimum height ratio (H_n) for the newly segmented n-type leg is then found. Similar to the findings in Figure 6.16a, Figure 6.17a shows that the optimum height ratio for the n-type leg is also 0.2 and the worst height ratio is 0.5. Thus, the lowest von Mises stress can be obtained in the n-type segmented leg when the height ratio (H_n) of 0.2 is used. This again proves the benefit of geometry

optimization of thermoelectric generators as lower von Mises stress means the lifespan of the TEG can be increased. Figure 6.17b shows the variation of the maximum von Mises stress in the SASTEG with optimized p-type leg ($H_p = 0.2$) and optimized n-type leg ($H_n = 0.2$). It is clear that for both the hot side and the cold sides, the asymmetrical thermoelectric leg (n-type) possessed a lower von Mises stress compared to the symmetrical thermoelectric leg (p-type). In fact, the maximum von Mises stress in the hot side asymmetrical leg (n-type) is lower by about 7.45% compared to that of the symmetrical leg (p-type). While in the cold side, the maximum von Mises stress in the asymmetrical leg is lower by about 39.21% compared to that of the symmetrical leg. This finding clearly shows that the thermal stress in a thermoelectric generator can be reduced by the use of asymmetrical legs and this resonates well with the findings in (Al-Merbaty et al., 2013).

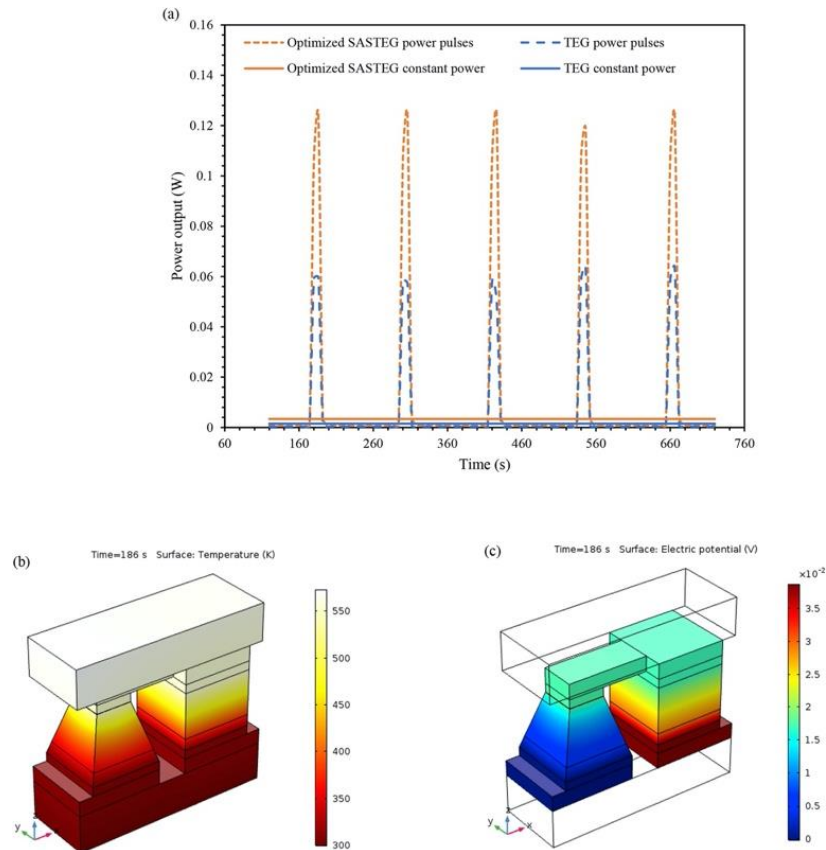


Figure 6.18: Second stage optimized SASTEG (a) power output response comparison with TEG (b) three-dimensional temperature distribution and (c) voltage distribution

Due to the results obtained from both optimization stages, the final optimized geometry in this study is found to be when $H_p = H_n = 0.2$. Thus, the power output of this optimized geometry is compared to that of the conventional TEG. As shown in Figure 6.18a, under transient response condition, the power output of the optimized SASTEG is greater than that of the conventional TEG by about 117.11%. This huge power output enhancement is obtained at a reduced thermal stress condition in the legs of the SASTEG thus, the device's reliability is improved. In addition, the three-dimensional temperature and voltage distribution in the optimized SASTEG is shown in Figure 6.18b and Figure 6.18c respectively.

6.3.4 Thermal Stress Distribution in SASTEG and TEG

Figure 6.19 shows the thermal stress distribution in the segmented asymmetrical thermoelectric generator and the TEG especially, the areas with high thermal stress concentrations. The maximum von Mises stress developed in the n-type and p-type legs of the conventional TEG, SASTEG and optimized SASTEG are shown in Figure 6.19a, Figure 6.19b and Figure 6.19c respectively. It can be seen clearly from all the figures that the maximum von Mises stress occurs at the hot surface of the thermoelectric legs and it is highly concentrated at the edges of the thermoelectric legs which are the positions most likely to crack. The lifespan of a thermoelectric generator is affected by the intensity of thermal stress developed in its legs therefore, it is important to reduce this stress.

Comparing the initial SASTEG geometry in Figure 6.19b to the optimized geometry in Figure 6.19c, it is obvious that the maximum von Mises stress in the legs has been reduced due to the geometry optimization. Besides changing the height ratio in the SASTEG to reduce the thermal stress, an increase in thermoelectric leg length can also reduce the thermal stress in a thermoelectric generator (Fan and Gao, 2018).

In addition, the use of asymmetrical legs can lead to reduced thermal stress developed in the thermoelectric generator (Al-Merbaty et al., 2013).

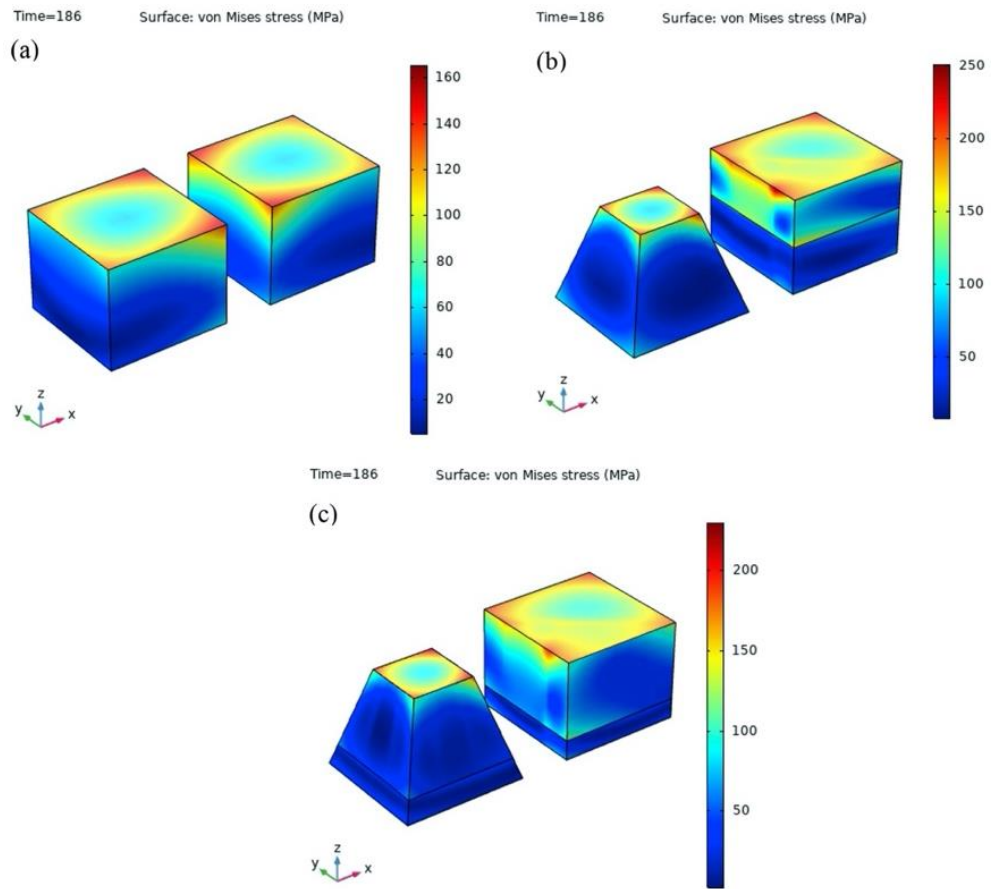


Figure 6.19: Thermal stress distribution in (a) thermoelectric generator (b) segmented asymmetrical thermoelectric generator and (c) optimized SASTEG geometry

6.3.5 Section Conclusion

A comprehensive numerical investigation of a segmented asymmetrical thermoelectric generator (SASTEG) and a conventional thermoelectric generator (TEG) was performed in this study. Rectangular pulsed heat input flux was applied to both devices and the temperature dependency of thermoelectric material properties was accounted for. The major conclusions from this study are summarized as follows:

- 1) Rectangular pulsed heat power enhances the performance of SASTEG and TEG significantly compared to steady state heating.

- 2) Under transient condition, the maximum von Mises stress in the SASTEG hot side p-leg reduced by about 20.95% while that of the cold side p-leg reduced by 21.16% simply because of the optimization of the height ratio (H_p).
- 3) Asymmetrical leg geometry (n-type) optimization reduced the thermal stress developed in the leg by 7.45% and 39.21% for the SASTEG hot side and cold side respectively compared to the values of the symmetrical leg geometry (p-type).
- 4) The power output of the optimized SASTEG with optimum height ratio $H_p = H_n = 0.2$ was greater than that of the conventional TEG by 117.11%.
- 5) The optimized SASTEG geometry provided an enhanced electrical performance at a reduced thermal stress condition thereby increasing the SASTEG's reliability.

6.4 Segmented Solar Thermoelectric Generator

The schematic of the segmented thermoelectric generator and non-segmented thermoelectric generator analysed in this study is shown in Figure 6.20a and Figure 6.20b respectively. A commercial thermoelectric generator (GM250-71-14-16) with 71 pairs of thermoelectric legs connected electrically in series and thermally in parallel is used in this study. The only difference between Figure 6.20a and Figure 6.20b is the presence of segmented p-type and n-type thermoelectric materials. However, the total length of the thermoelectric legs in both cases is kept constant throughout this study at a value of 2 mm. Bismuth telluride is used as the cold segment (P1-type and N1-type) thermoelectric material while Skutterudite is used as the hot segment (P2-type and N2-type) thermoelectric material. In both the segmented and non-segmented TEG, a solar selective absorber (SSA) is assumed to be present at the top of the ceramic.

CHAPTER 6 THERMOELECTRIC GENERATOR OPTIMIZATION AND RESULTS DISCUSSION

The ceramic enhances thermal conductivity, copper provides electrical connection and solder helps to alleviate the effect of thermal stress.

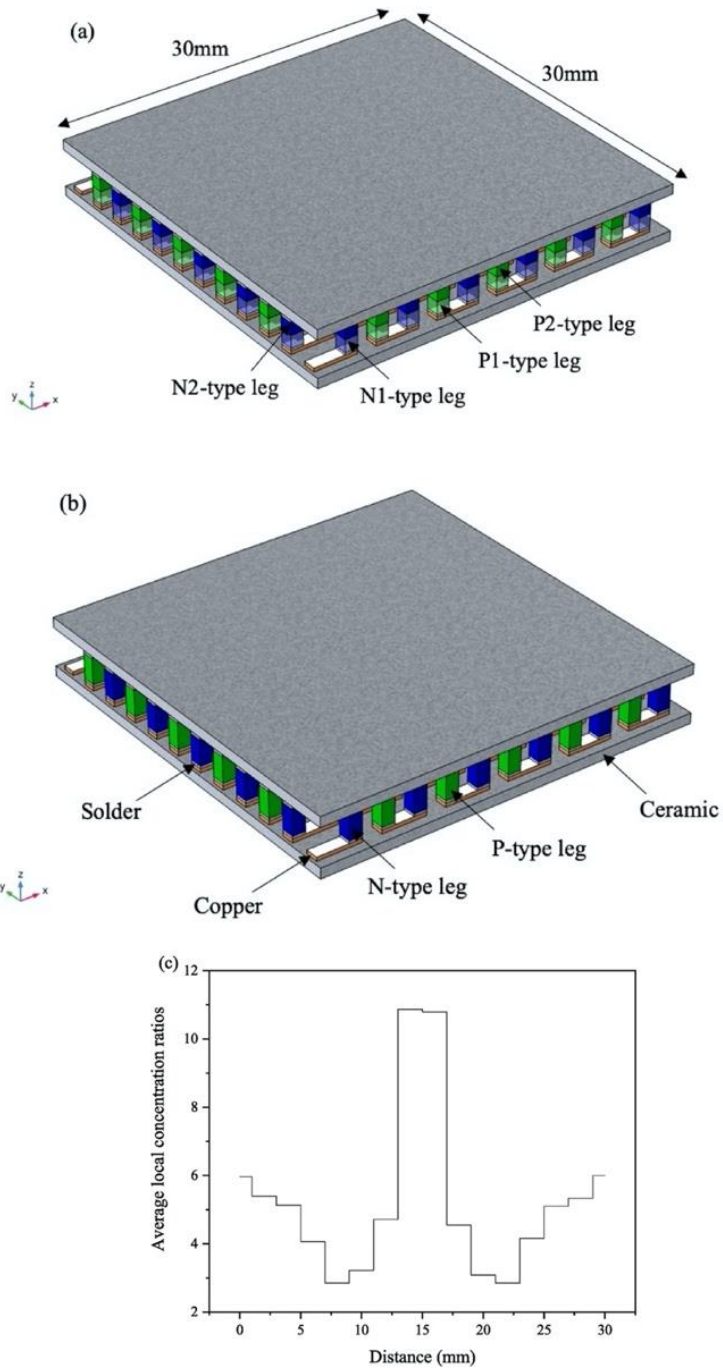


Figure 6.20: Schematic of (a) segmented thermoelectric generator (b) thermoelectric generator and (c) CPC flux distribution

In this study, the solar concentrator used is a compound parabolic concentrator (CPC) with a concentration ratio of 6. Firstly, SolidWorks is used to build the

geometric model of the CPC before being transferred into Lighttools for the ray tracing simulation. For avoidance of repetition, details about the simulation parameters and the model for the CPC can be found in our published paper (Xuan et al., 2017). The flux distribution from the compound parabolic concentrator is shown in Figure 6.20c. The emissivity and absorptivity of the SSA are 0.05 and 0.95 respectively. For the thermal stress analysis, copper and solder are considered as elastoplastic materials with yielding stress and tangential modulus of 70 MPa, 24 GPa and 26 MPa, 8.9 GPa respectively (Fan and Gao, 2018). Furthermore, the tensile strength of the hot segment material (Skutterudite) is 142 MPa (Fan and Gao, 2019) while the yielding stress of the cold segment material (Bismuth telluride) is 112 MPa (Al-Merbati et al., 2013).

In this study, five different design cases for the segmented and non-segmented solar thermoelectric generator shown in Table 6.1 are analysed. As shown in Table 6.1, Case 1 and Case 2 correspond to non-segmented solar thermoelectric generators with single material while Case 3, Case 4 and Case 5 correspond to the segmented solar thermoelectric generators with two different materials. It is important to note that the total thermoelectric length for the different cases is kept constant (2 mm) throughout this study and only the length ratio is optimized. The electrical and mechanical performance of the different design cases are analysed, and results are presented in this section.

Table 6.1: Material proportions in different design cases

Material	Case 1	Case 2	Case 3	Case 4	Case 5
Bi ₂ Te ₃	100%	0	75%	50%	25%
(P1/N1)					

Skutterudite	0	100%	25%	50%	75%
(P2/N2)					

6.4.1 Boundary Conditions

The three-dimensional numerical model used in this study is simplified using the following assumptions,

- 1) Steady state conditions are assumed throughout the study.
- 2) Lower copper electrodes on the n-type and p-type legs are connected to an external load resistance.
- 3) Electrical and thermal contact resistance are ignored.
- 4) A fixed constraint is assumed at the hot side of the segmented and non-segmented solar thermoelectric generator.
- 5) Adiabatic condition is assumed on all side surfaces.
- 6) Constant temperature of 25 °C is assumed at the cold side of the TEG unless otherwise stated.

6.4.2 Effect of Solar Radiation

Variation of solar radiation affects the amount of input energy absorbed by the thermoelectric generator and consequently its power output and efficiency. For the different cases, Figure 6.21a shows the effect of solar radiation variation on the power output of the solar thermoelectric generator under non-uniform heat flux. As expected, the power output for most cases increases as the solar radiation increases due to the increase in temperature difference across the module. However, for Case 1 and Case 3 in which the percentage of bismuth telluride material proportion is high (100% and 75% respectively), it can be seen that the power output shows a decreasing trend after an initial increase. This is because; bismuth telluride material is a low temperature

range ($< 200\text{ }^{\circ}\text{C}$) thermoelectric material therefore, once the operating temperature is exceeded, it becomes less efficient and its power output decreases. Contrarily, Skutterudite material is a medium temperature range ($< 500\text{ }^{\circ}\text{C}$) thermoelectric material therefore, the power output in Case 2 and Case 5 where the Skutterudite material proportion is high (100% and 75% respectively) increases linearly as solar radiation increases. This finding is in agreement with the previous finding of Ma et al. (2019).

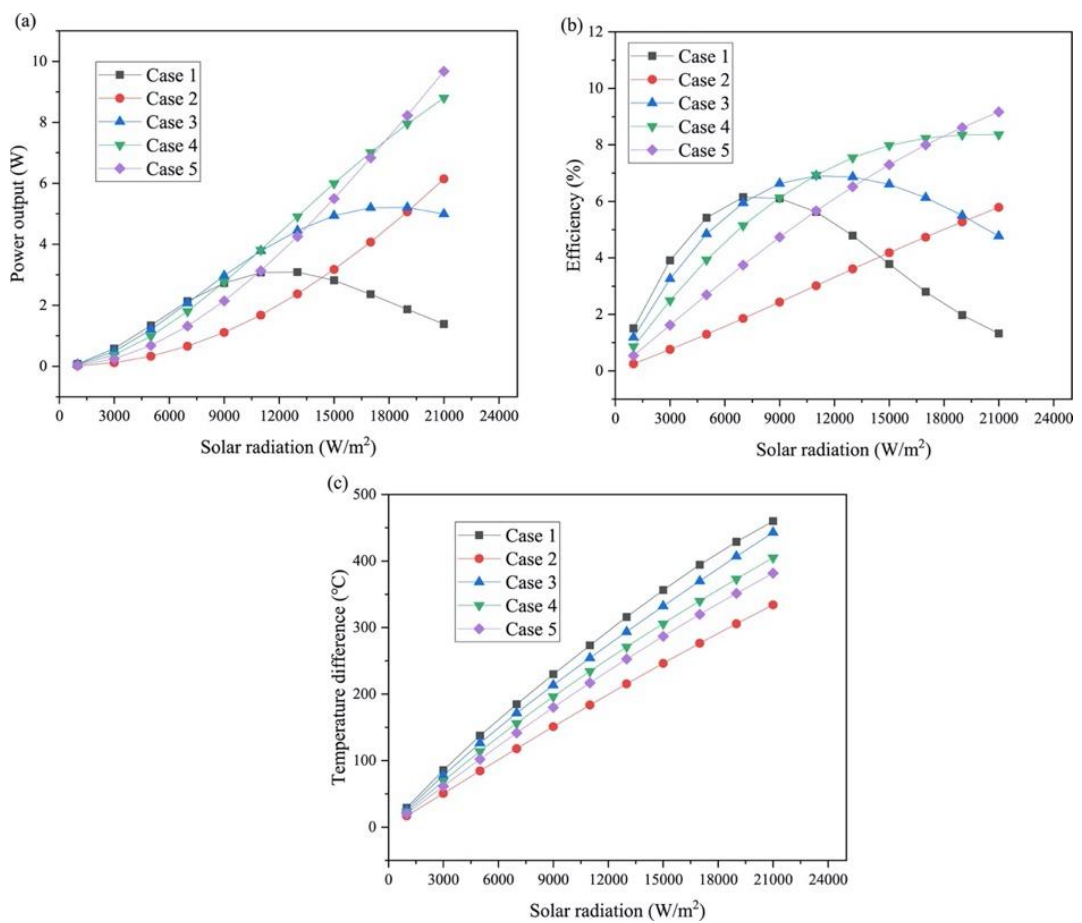


Figure 6.21: Effect of solar radiation on (a) power output (b) efficiency (c) temperature difference

Consequently, it is important to consider the operating temperature range before choosing an appropriate thermoelectric material. Furthermore, it can be seen from Figure 6.21a that the solar radiation, which influences the operating temperature,

determines the most appropriate design case for the solar thermoelectric generator. For example, when the solar radiation was between 11000 W/m² to 17000 W/m², Case 4 provides the highest power output, which also increases from 3.81 W to 7.01 W at that range. However, at a solar radiation value greater than 17000 W/m², it can be seen that Case 5 provides the highest power output. This is because, at such high radiation value, the operating temperature of the module will be high consequently; Case 5, which has a high proportion of Skutterudite, provides the highest power output.

The significance of segmentation can also be seen from Figure 6.21a in terms of power output. Comparing the highest power output obtained from Case 1 (bismuth telluride non-segmented solar TEG) which is 3.09 W at 13000 W/m², to the power output of the segmented thermoelectric generator (Case 3, Case 4 and Case 5). It can be seen that the power output of Case 3, Case 4 and Case 5 increased by 44.07%, 59.12% and 37.9% respectively compared to that of Case 1 at 13000 W/m². Similarly, comparing the highest power output obtained from Case 5 (Skutterudite non-segmented solar TEG) which is 6.15 W at 21000 W/m², to that from the segmented cases. It can be seen that the power output of Case 4 and Case 5 increased by 43.18% and 57.4% respectively compared to that of Case 5 at 21000 W/m² while that of Case 3 decreased by 18.76% because of the higher proportion of bismuth telluride material. As expected, Figure 6.21b shows that Case 1 provides the highest efficiency at low temperature range corresponding to solar radiation values of 1000 W/m² to 7000 W/m².

However, the advantage of the segmented design becomes more obvious at high radiation values. In addition, the trends observed in Figure 6.21a and Figure 6.21b are similar consequently, operating temperature is a critical parameter to be considered in designing highly efficient solar thermoelectric generators. Furthermore, Figure

6.21c shows that the temperature difference across the thermoelectric legs increases as the solar radiation increases. This is an expected phenomenon since the cold side temperature is maintained at a fixed value. In addition, Figure 6.21c shows that Case 1 provides the highest temperature difference because it is made up of 100% bismuth telluride material, which has low thermal conductivity that helps maintain the temperature gradient between the hot and cold side. Generally, thermoelectric materials with high electrical conductivity, low thermal conductivity and high Seebeck coefficient are desirable.

A comparison between the performance of the solar thermoelectric generators under non-uniform and uniform heat flux at different solar radiation values is shown in Figure 6.22. The trends for both non-uniform and uniform heat flux are similar however, a slight difference still exists. It can be seen from Figure 6.22a that the power output under uniform heat flux is higher than that under non-uniform heat flux however, after a saturation point is reached, the module under uniform heat flux suffers a steeper decrease in power output compared to that under non-uniform heat flux. This is because, under uniform heat flux, a higher amount of solar energy is absorbed by the solar TEG compared to that under non-uniform heat flux. Consequently, once the optimum operating temperature for bismuth telluride is exceeded, the power output under uniform heat flux decreases faster than that under non-uniform heat flux because of its higher operating temperature. However, at a solar radiation value of 11000 W/m^2 , the power output of Case 1 under uniform heat flux increased by 1.53% compared to that under non-uniform heat flux.

CHAPTER 6 THERMOELECTRIC GENERATOR OPTIMIZATION AND RESULTS DISCUSSION

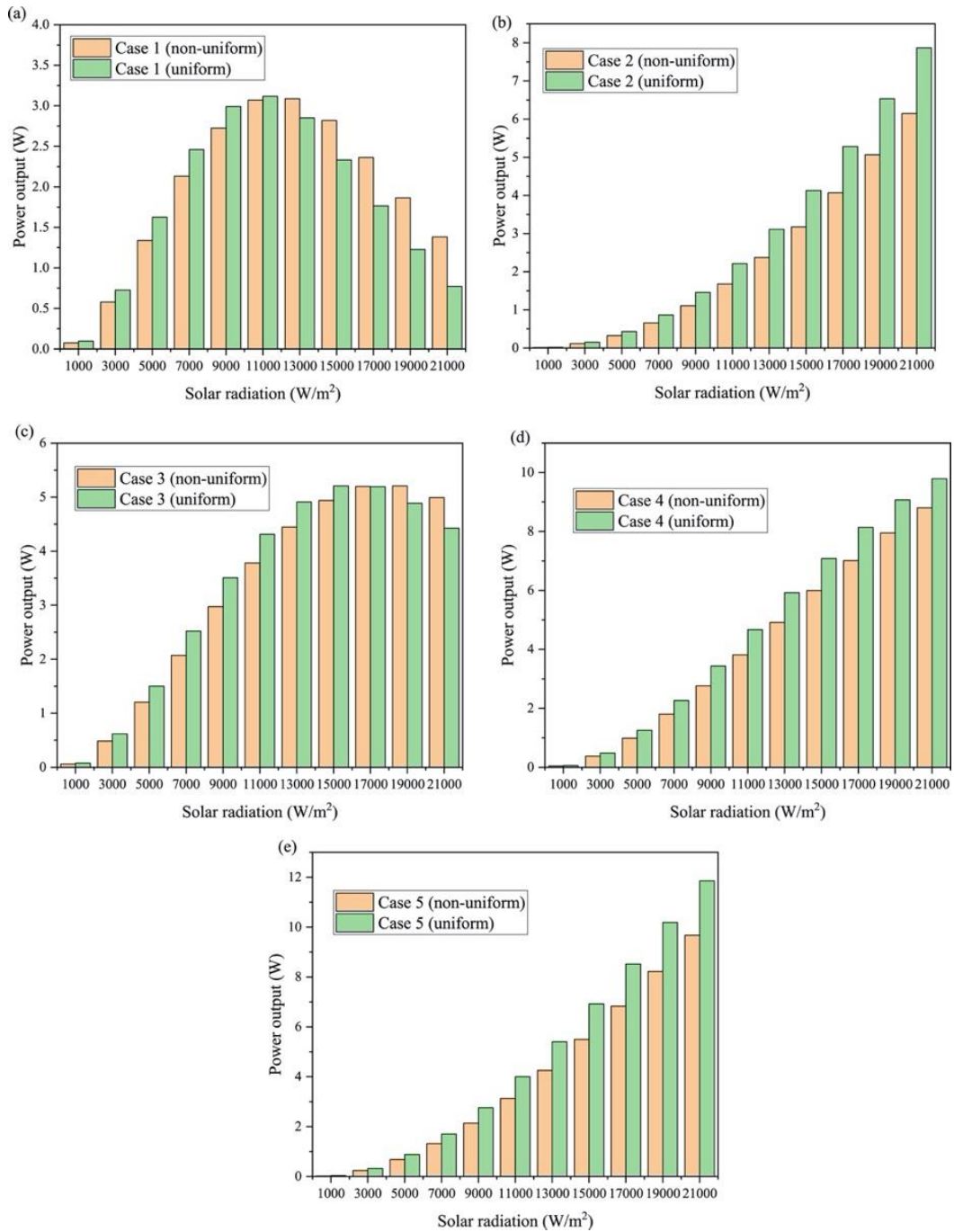


Figure 6.22: Comparison of non-uniform and uniform heat flux power output for (a) Case 1 (b) Case 2 (c) Case 3 (d) Case 4 and (e) Case 5

Furthermore, Figure 6.22b shows that the power output of Case 2 increases as solar radiation increases under both non-uniform and uniform heat flux. In fact, the significance of uniformity becomes very clear at higher radiation values. For example, at a radiation value of 11000 W/m², the power output of Case 2 under uniform heat

flux increased by 31.81% compared to that under non-uniform heat flux. At the same radiation value of 11000 W/m^2 , the power output of Case 3, 4 and 5 under uniform heat flux increased by 14.05%, 22.47% and 27.81% respectively, compared to that under non-uniform heat flux. Consequently, uniform heat flux is beneficial for enhanced power output.

6.4.3 Thermal Stress Analysis

Thermal stress is inevitable in a solar thermoelectric generator because of its high operating temperature consequently; this section presents the results from thermal stress analysis. The effect of solar radiation on the maximum von Mises stress in the solar thermoelectric generators is shown in Figure 6.23. Firstly, the maximum von Mises stress in the thermoelectric legs of all the different design cases is shown in Figure 6.23a in addition to the tensile strength of Skutterudite material (142 MPa) and the yielding stress of bismuth telluride material (112 MPa). It is clear that for all solar radiation values, the maximum von Mises stress in the non-segmented solar TEG (Case 1 and Case 2) is lower than that in the segmented solar TEG. Furthermore, it is clear from Figure 6.23a that for the segmented solar thermoelectric generator, Case 5 provides the lowest thermal stress in the legs while Case 3 provides the highest thermal stress. As expected, the maximum von Mises stress in the thermoelectric legs for all the cases increases as the solar radiation increases due to the increase in operating temperature. This may lead to a reduction in the service life of the thermoelectric generator or even damage the device. This finding is in agreement with that of Fan et al. (2019).

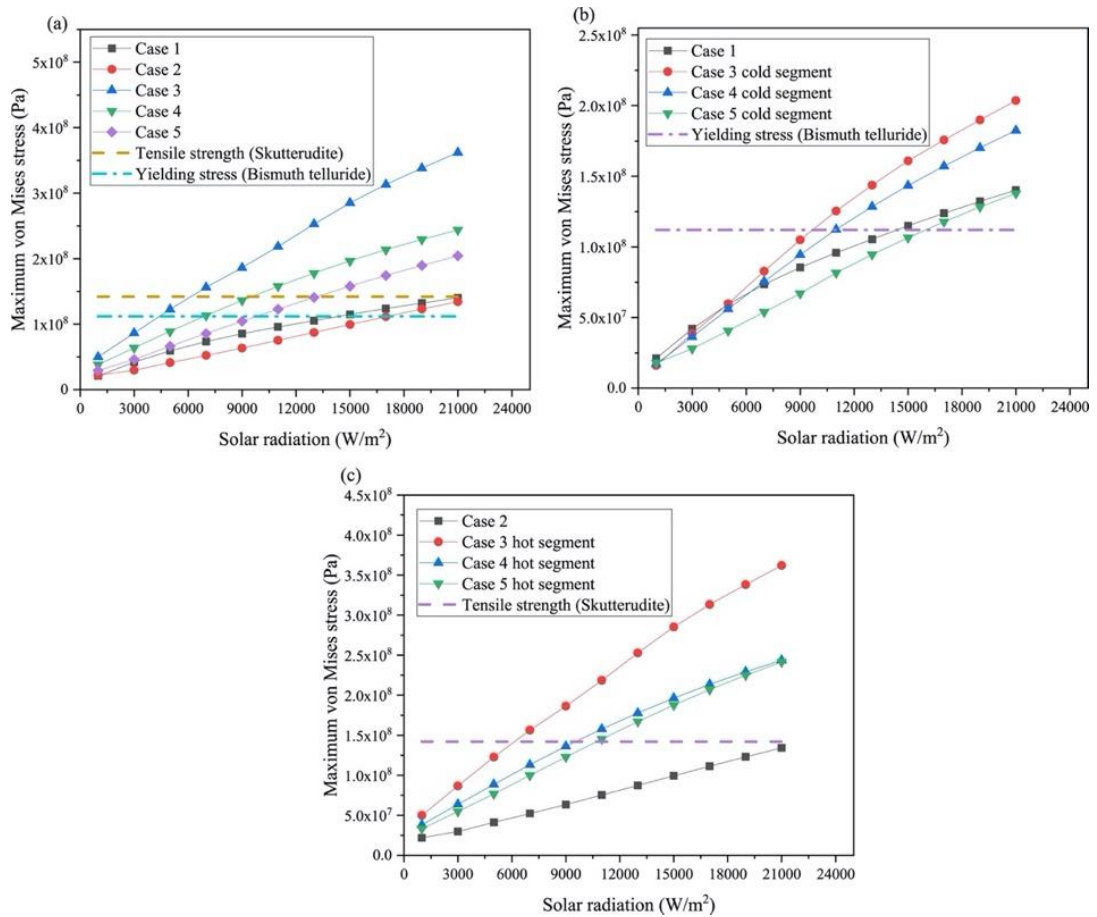


Figure 6.23: Effect of solar radiation on maximum von Mises stress in (a) different cases (b) bismuth telluride TEG and (c) Skutterudite segment

It is also important to note that for the highest solar radiation value considered in this study (21000 W/m²), the thermal stress in the legs of Skutterudite non-segmented solar TEG (Case 2) is within the acceptable tensile strength of the Skutterudite material, therefore, it can operate safely and reliably at such high solar radiation value. However, for the bismuth telluride non-segmented solar TEG (Case 1), it is clear that the module can only be guaranteed to operate safely and reliably at solar radiation values lower than 15000 W/m², beyond which the yielding stress of the material will be exceeded. However, from Figure 6.21a, the highest power output of Case 1 was obtained at a radiation value of 13000 W/m², thus; if the module is used

within its optimum operating temperature, it will provide a reliable and efficient operation in terms of both mechanical and electrical performance.

Comparing the segmented design cases, the maximum von Mises stress at a high radiation value of 21000 W/m^2 , in Case 5 decreases by 43.58% and 16.18% compared to Case 3 and Case 4 respectively. This shows the importance of leg length ratio optimization for thermal stress reduction. The reason for the better mechanical performance of Case 5 is its higher proportion of Skutterudite material compared to Case 3 and Case 4. Skutterudite material provides a better mechanical performance compared to bismuth telluride material however, the reverse is the case in terms of electrical performance. Consequently, it is imperative to optimize solar thermoelectric generators in terms of both electrical and mechanical performance.

Figure 6.23b provides a better understanding of the maximum von Mises stress in the thermoelectric legs made of bismuth telluride material only. In addition, the advantage of segmentation is shown in this figure. It can be seen clearly that for all solar radiation values considered, the maximum von Mises stress in Case 5 is the lowest, even lower than that in the non-segmented solar TEG (Case 1). For example, at a solar radiation value of 11000 W/m^2 , the maximum von Mises stress in the bismuth telluride material (cold segment) of Case 5 decreases by 14.85%, 34.93% and 27.36% compared to that in Case 1, Case 3 and Case 4 respectively.

Furthermore, it can be seen from Figure 6.23b that Case 3 attains the yielding stress quicker than the remaining cases, followed by Case 4, Case 1 and finally Case 5. This implies that a higher solar radiation value can be used for Case 5 compared to the others within which the module will still be reliable and will provide increased power output. To understand the stress distribution in the legs made of Skutterudite material, Figure 6.23c shows the maximum von Mises stress in different cases. It can

be seen that Case 2 provides the lowest thermal stress, which is still within the tensile strength of the Skutterudite material even at a high radiation value of 21000 W/m^2 . Comparing the segmented solar TEG, it is obvious that Case 5 provides the lowest thermal stress while Case 3 provides the highest thermal stress. A combination of Figure 6.23b and Figure 6.23c gives the results shown in Figure 6.23a.

6.4.4 Three-Dimensional Distributions

One of the advantages of this study is that it provides three-dimensional information about the actual temperature and stress distributions in a full-scale solar thermoelectric generator. Figure 6.24 shows the temperature distribution of the segmented solar thermoelectric generator (Case 4) under non-uniform and uniform heat flux. It can be seen from Figure 6.24a that the maximum temperature in the module is distributed in the middle of the module due to the non-uniformity of the heat flux from the compound parabolic concentrator used. The temperature distribution on the surface of the module shown in Figure 6.24a follows the trend of the CPC heat flux shown in Figure 6.20c.

Furthermore, Figure 6.24b shows the temperature distribution under uniform heat flux. It is clear that the temperature is evenly distributed across the surface of the module and the maximum temperature under uniform heat flux is $162 \text{ }^\circ\text{C}$ while that under non-uniform heat flux is $148 \text{ }^\circ\text{C}$. This difference in temperature is the main reason for the power output improvement observed under uniform heat flux and the reduced mechanical reliability also observed.

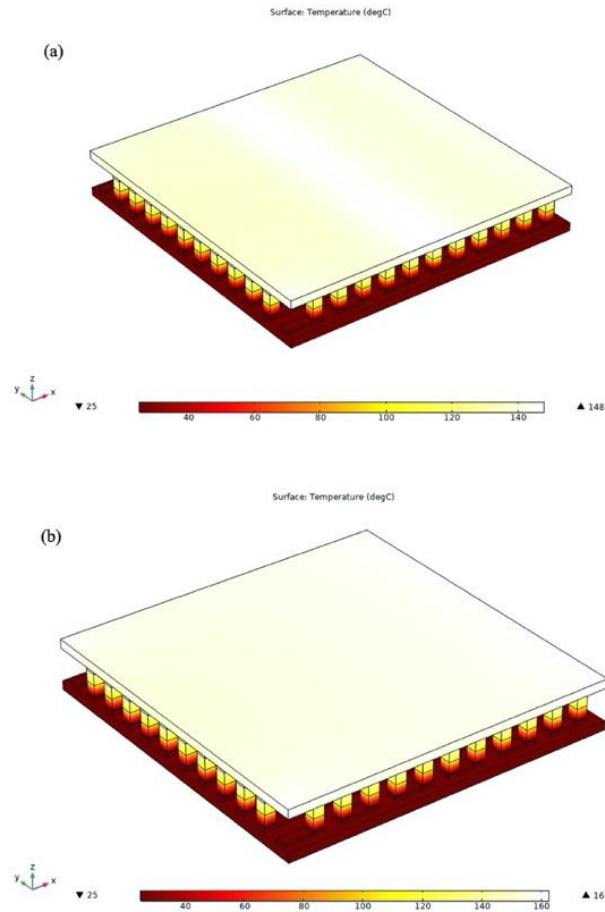


Figure 6.24: Three-dimensional temperature distribution for (a) non-uniform and (b) uniform heat flux at solar radiation of 5000 W/m²

To properly understand the locations of maximum von Mises stress in the thermoelectric legs of the different design cases, Figure 6.25 provides a three-dimensional thermal stress distribution. Figure 6.25a, Figure 6.25b, Figure 6.25c, Figure 6.25d and Figure 6.25e provide the stress distribution for Case 1, Case 2, Case 3, Case 4 and Case 5 respectively. One obvious trend seen from all the figures is that the maximum von Mises stress all occur at the edge of the thermoelectric legs, thus that region can break off easily. In addition, the other region most likely to crack are the contact areas between the thermoelectric legs hot surface and solder strips. The development of thermal stress in the legs of the solar thermoelectric generator is due to the difference in mechanical material properties of the solar TEG components.

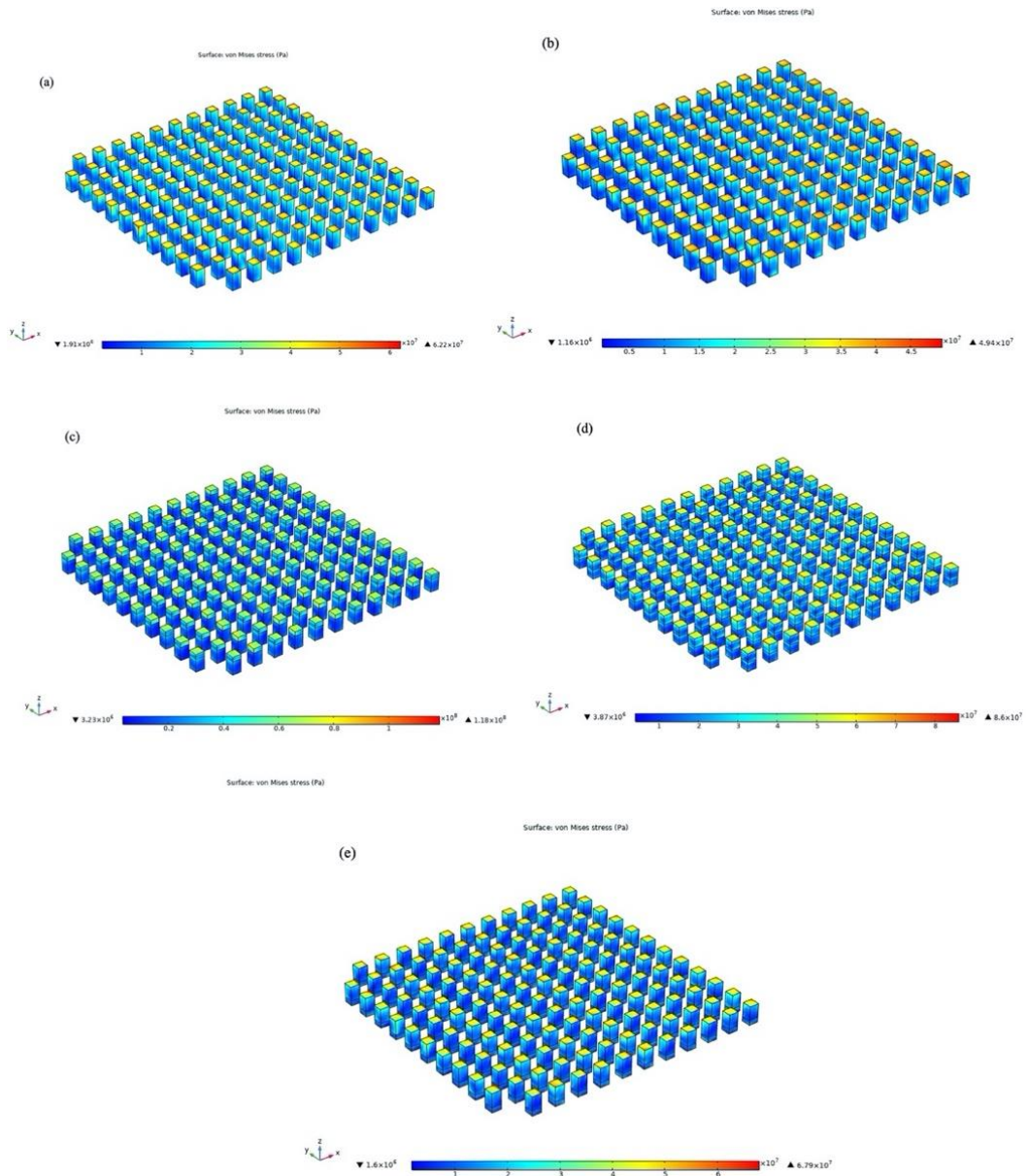


Figure 6.25: Thermal stress nephogram for (a) case 1 (b) case 2 (c) case 3 (d) case 4 and (e) case 5 at solar radiation of 5000 W/m^2

6.4.5 Section Conclusion

A detailed three-dimensional numerical study on electrical and mechanical performance of segmented and non-segmented solar thermoelectric generator under non-uniform and uniform heat flux was provided in this study. The main conclusions from this study are:

- 1) The required operating temperature range is a very important parameter which must be considered before choosing an appropriate thermoelectric material and design case.
- 2) The power output of the segmented solar thermoelectric generators in Case 3, Case 4 and Case 5 increased by 44.07%, 59.12% and 37.9% respectively compared to that of Case 1 (bismuth telluride non-segmented solar TEG) at 13000 W/m².
- 3) The maximum von Mises stress at a high radiation value of 21000 W/m², in Case 5 decreased by 43.58% and 16.18% compared to Case 3 and Case 4 respectively thereby showing the importance of leg length ratio optimization in segmented solar TEG.
- 4) Segmented and non-segmented solar thermoelectric generator must be optimized in terms of both electrical and mechanical performance rather than just electrical performance.
- 5) At a solar radiation value of 11000 W/m², the maximum von Mises stress in the bismuth telluride material (cold segment) of Case 5 decreased by 14.85%, 34.93% and 27.36% compared to that in Case 1 (non-segmented solar TEG), Case 3 and Case 4 respectively.

6.5 Solar Thermoelectric Generator with Phase Change Material

The solar thermoelectric generator considered in this study is shown in Figure 6.26 without the solar concentrator. A comparison study between a solar thermoelectric generator with and without phase change material is performed. The solar TEG with PCM is shown in Figure 6.26a while that without PCM is shown in Figure 6.26b. In this study, a commercial thermoelectric generator (GM250-71-14-16)

consisting of 71 pairs of thermoelectric legs connected in series electrically and thermally in parallel is used. Aluminum oxide is used as the ceramic material, which enhances heat transfer across the TEG and provides electrical insulation. Copper is used as the conducting material and bismuth telluride (Bi_2Te_3) is the n-type and p-type thermoelectric material. In addition, as shown in Figure 6.26a, the PCM is placed in a container made of copper material and copper fins are used to enhance the heat transfer between the container and the PCM. In both Figure 6.26a and Figure 6.26b, a solar selective absorber (SSA) is assumed to be present at the top surface. Furthermore, the solar radiation variation under typical partly cloudy weather conditions for a period of time in wet season is considered in this study as shown in Figure 6.27 (Mahmoudinezhad et al., 2018b). Temperature dependent thermoelectric material properties (European Thermodynamics Limited, 2014b) are used. The phase change material used in this study undergoes phase change from solid to liquid by absorbing the incident non-uniform solar radiation from the compound parabolic concentrator.

The properties of a PCM including, melting temperature, cost, availability and chemical stability determines its suitability for specific applications. Therefore, the PCM used in this study is chosen based on its melting temperature and the hot side temperature of the thermoelectric generator. Throughout this study, RT25HC is used as the phase change material. The PCM used in this study is a commercially available PCM manufactured by Rubitherm Technologies GmbH. It is a pure PCM that is capable of storing and releasing large quantities of thermal energy at a nearly constant temperature. The melting range according to the manufacturer datasheet is between $22\text{ }^\circ\text{C} - 26\text{ }^\circ\text{C}$ while its main peak is at $25\text{ }^\circ\text{C}$. Recently, Mankel et al. (Mankel et al., 2019) performed a differential scanning calorimetry (DSC) tests for RT25HC phase change material and the result obtained is shown in Figure 6.28. The DSC curve

justifies the manufacturer data and it can be seen that the melting interval is $4\text{ }^{\circ}\text{C}$ or 4 K . The PCM undergoes endothermic reaction at an onset temperature and the phase change from solid to liquid begins gradually. Furthermore, a large quantity of heat energy is absorbed during the phase change process, which is later released at the end of the phase change.

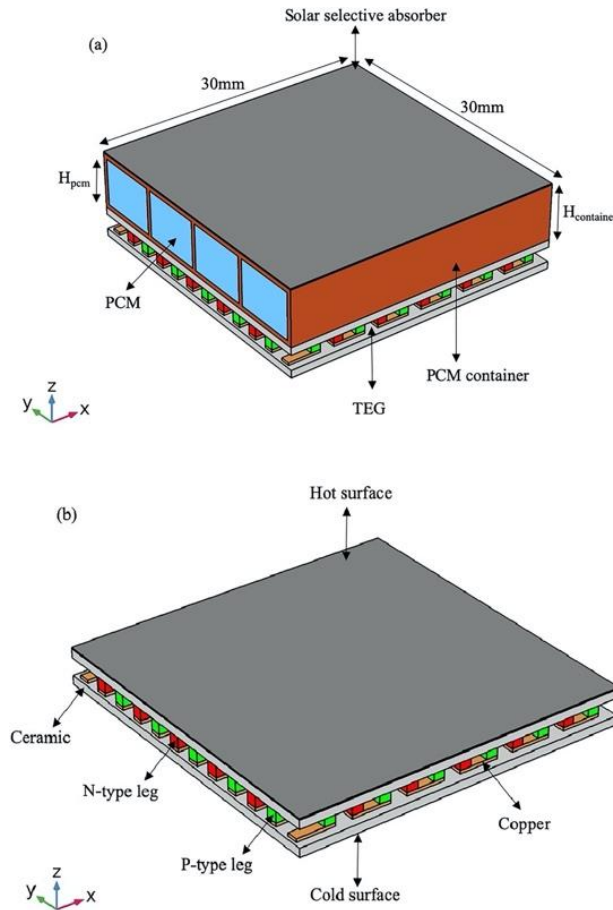


Figure 6.26: Solar thermoelectric generator (a) with PCM and (b) without PCM

In this study, the PCM absorbs the concentrated solar radiation, which raises its temperature, and when the onset temperature is reached, the phase change process begins. During this process, the PCM helps to maintain the temperature on the solar thermoelectric generator at an almost constant value thereby stabilizing the transient and non-uniform radiation, which in turn leads to a more stable power output from the solar thermoelectric generator. Furthermore, even during periods of low solar

radiation, the STEG is still able to provide some power output because of the stored heat released from the phase change material. Transient simulations are performed for the solar thermoelectric generator with and without phase change material. The CPC flux distribution profile and solar radiation shown in Figure 6.20c and Figure 6.27 respectively are combined and used for the numerical study. Consequently, each simulation is performed for a period of 15 minutes.

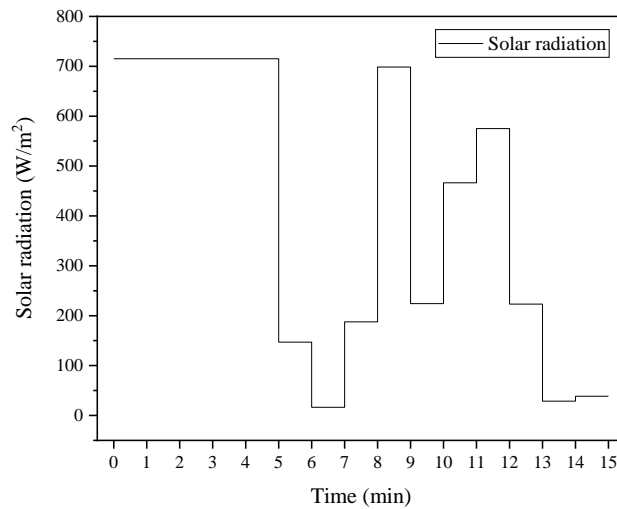


Figure 6.27: Variation of solar radiation with time (Mahmoudinezhad et al., 2018b)

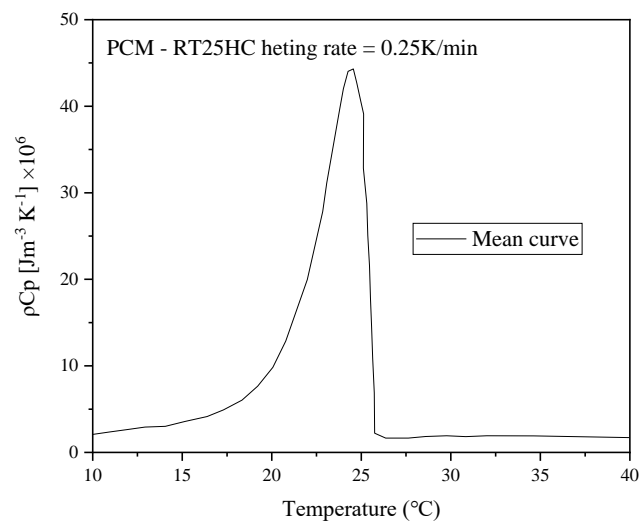


Figure 6.28: DSC curve of RT25HC PCM (Mankel et al., 2019)

6.5.1 Boundary Conditions

The boundary conditions and assumptions considered in this study are listed below:

- 1) Transient conditions are assumed.
- 2) A constant temperature (20 °C) boundary condition is assumed on the cold surface of the solar TEG.
- 3) The copper electrodes on the n-type and p-type legs are connected to the ends of an external load.
- 4) The external surfaces of the PCM container are insulated.
- 5) Initial temperature on all surfaces is zero.
- 6) Convective and radiative heat loss are considered at the SSA top surface.
- 7) Initial thermoelectric electric potential is zero.
- 8) An assumed value of $200 \text{ mm}^2 \cdot \text{K}/\text{W}$ is used in this study for the thermal contact resistance between the lower surface of the PCM container and the TEG ceramic top surface.

6.5.2 Effect of PCM Fin Number

In this study, fins are attached to the PCM container to enhance the heat transfer between the container and the PCM. The variation of the PCM fins with the power output, temperature difference and efficiency of the solar TEG with PCM for the time period considered is shown in Figure 6.29a, Figure 6.29b and Figure 6.29c respectively. A similar trend is observed in Figure 6.29a, Figure 6.29b and Figure 6.29c due to the solar radiation pattern shown in Figure 6.27. Solar radiation is one of the most important parameters that influence the performance of the solar thermoelectric generator. It can be seen from the figures that peak power output, temperature difference and efficiency of the solar TEG with PCM is achieved after 5

min after which a sharp decline is observed due to the drastic reduction in solar radiation.

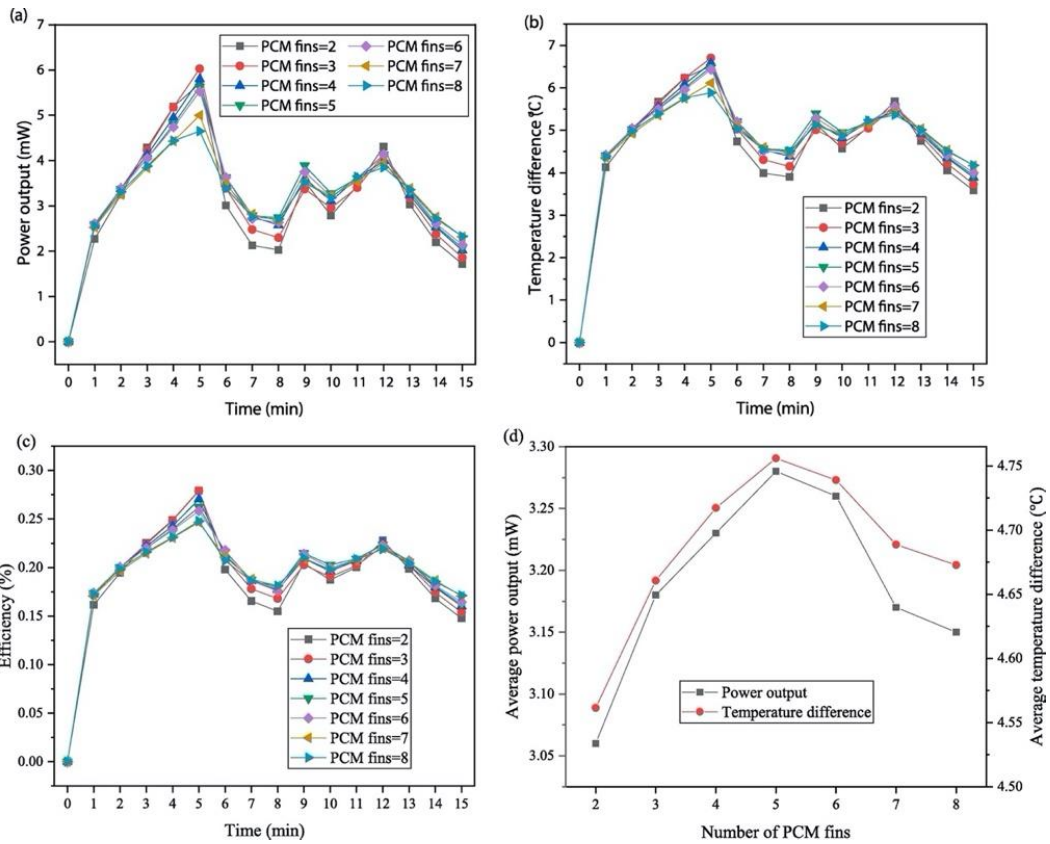


Figure 6.29: Number of PCM fins variation with (a) power output (b) temperature difference (c) efficiency and (d) average power output and average temperature difference

Furthermore, because the solar radiation at the initial time is high and is maintained for 5 min, the solar TEG with PCM quickly responds therefore, it takes just 1 min for the power output, temperature difference and efficiency shown in Figure 6.29a, Figure 6.29b and Figure 6.29c respectively, to significantly increase from the initial zero value. However, although the solar radiation is constant for the first 5 min, the power output, temperature difference and efficiency of the solar TEG are not constant but rather increase gradually due to the presence of the PCM on the top surface. During the first 5 min, the PCM receives the concentrated solar radiation and when its melting temperature is attained, it gradually begins to melt and this is the

reason for the gradual increase observed between 1 min – 5 min in Figure 6.29a, Figure 6.29b and Figure 6.29c.

For the sake of PCM fin number selection, the average values for the power output and temperature difference across the solar TEG over a period of 15 min is considered as shown in Figure 6.29d. This provides a clearer understanding of the effect of the number of PCM fins on the performance of the solar thermoelectric generator. It can be seen clearly from Figure 6.29d that the highest values for average power output and average temperature difference are obtained at fin number 5. Furthermore, a gradual increase is observed initially as the PCM fin number is increased before it sharply declines thereby showing the importance of fin optimization. The average power output of the solar TEG with PCM increased by 7.19% when the fin number increased from 2 to 5 while it decreased by 3.96% when the fin number increased from 5 to 8.

Similarly, the average temperature difference across the hot and cold sides of the solar TEG increased by 4.26% when the fin number increased from 2 to 5 whereas it decreased by 1.75% when the fin number increased from 5 to 8. Consequently, it is obvious that proper selection of PCM fin number could enhance the performance of the solar TEG with PCM. Therefore, throughout this study, a fin number of 5 (shown in Figure 6.26a) is used. Since the actual concentrated solar radiation is incident on the PCM container, the fin optimization is important to enhance the heat transfer from the container to the PCM and subsequently to the solar TEG.

6.5.3 Effect of PCM Height

The height of the PCM on the solar thermoelectric generator could affect its performance therefore; the effect of different PCM height on the solar TEG performance is shown in Figure 6.30. The variation of the PCM height with the power

output, temperature difference and efficiency of the solar TEG with PCM for the time period considered is shown in Figure 6.30a, Figure 6.30b and Figure 6.30c respectively. It is very clear from Figure 6.30a, Figure 6.30b and Figure 6.30c that the power output, temperature difference and efficiency of the solar TEG respectively decrease as the PCM height is increased.

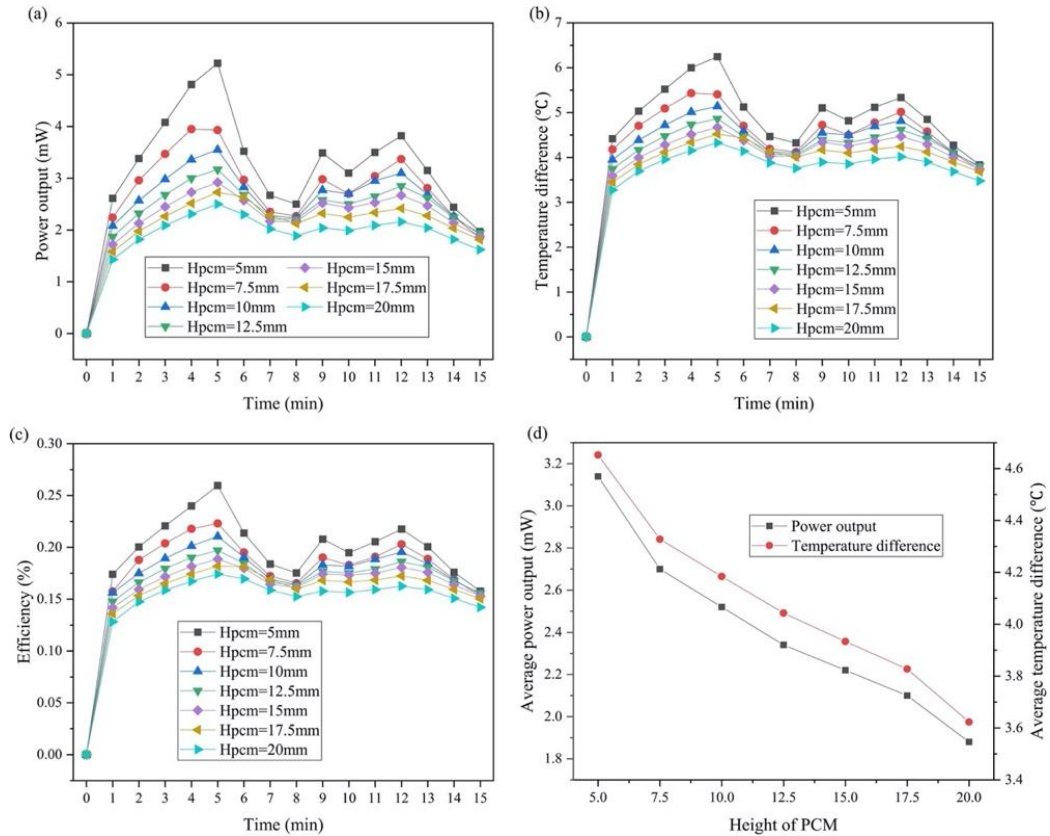


Figure 6.30: Height of PCM variation with (a) power output (b) temperature difference (c) efficiency and (d) average power output and average temperature difference

Furthermore, it is clear that peak performance is obtained after 5min due to the solar radiation pattern. From Figure 6.30a, Figure 6.30b and Figure 6.30c, it can be seen that the peak power output, temperature difference, and efficiency of the solar TEG decrease respectively by 52.11%, 30.71% and 32.87% when the PCM height is increased from 5 mm to 20 mm. The reason for the decrease in performance of the solar TEG is the position of the PCM. Unlike the conventional arrangement whereby

the PCM is used as the heat sink, in this study, the preference is to reduce the temperature fluctuations due to the transient solar radiation and to unify the non-uniform heat flux from the solar concentrators. Therefore, in this study, the PCM is positioned at the top surface of the solar TEG. Consequently, an increase in PCM height, which leads to an increase in volume, simply increases the time required to completely melt the PCM.

Since the area of the PCM is constant, an increase in height corresponds to an increase in volume of the PCM. Furthermore, if a small PCM height is used such as 5 mm, the PCM can melt quicker and the corresponding increase in temperature will enhance the performance of the solar TEG by increasing the temperature difference across it. Consequently, the PCM in this study is performing a dual function of stabilizing and unifying the transient non-uniform heat flux from the solar concentrator and increasing the temperature difference across the solar TEG when it melts. However, it can also be seen from Figure 6.30a, Figure 6.30b and Figure 6.30c that the increase in PCM height provides a more stable performance in terms of power output, temperature difference and efficiency respectively. The reason for this is because, the increase in PCM height leads to an increase in the time required to melt the phase change material. Furthermore, the average power output and average temperature difference across the solar TEG is shown in Figure 6.30d for different PCM height. A decreasing trend is observed from Figure 6.30d because of the reasons explained above. The average power output and average temperature difference across the solar TEG decrease by 40.13% and 22.13% respectively when the PCM height is increased from 5 mm to 20 mm. Consequently, a PCM height of 5 mm is used for the remainder of this study.

6.5.4 Effect of PCM and Thick Copper Plate

In this section, the significance of using phase change material at the top surface of the solar TEG is presented and a comparison is made with a solar TEG, which has a thick copper plate (5 mm) at the top surface instead of PCM. In addition, the two systems are compared with a solar thermoelectric generator without PCM or thick copper plate at the top surface. The variation of the power output obtained from the three systems studied with time is shown in Figure 6.31a. Since the solar radiation at the initial time is high and maintained at a constant value for 5 min, the solar TEG without PCM and thick copper plate responds the quickest followed by the solar TEG with copper plate while the solar TEG with PCM provides the lowest response. In addition, it can be seen from Figure 6.31a that the power output of the solar TEG without PCM varies significantly with time because of the solar radiation pattern.

This kind of unstable power output with very high peaks and low values could significantly affect the performance and life span of the device being powered. For several applications in which the solar thermoelectric generator could be useful, stable power output is required and beneficial. This is specifically why the use of PCM at the top surface of the solar TEG is important. As shown in Figure 6.31a, the power output of the solar TEG with PCM RT25HC gradually increases with time after which it stabilizes. Although the solar TEG with PCM cannot provide the peak power outputs provided by the solar thermoelectric generator without phase change material, it is still very useful for providing a stable power output, which is more important for specific applications and under transient conditions.

Between 1 min and 15 min, the difference between the maximum and minimum power output of the solar thermoelectric generator without PCM is 15.88 mW while that of the solar TEG with thick copper plate is 15.65 mW and that of the

solar TEG with PCM is 3.25 mW. This is very significant because it shows that the use of phase change material on the solar thermoelectric generator can provide a more stable power output over a long period. In addition, it can be seen from Figure 6.31a that the solar TEG with PCM outperforms the solar TEG without PCM and that with thick copper plate at very low solar radiation periods such as between 7 min - 8 min and 13 min - 15 min. In fact, after 15 min, the solar TEG with PCM still provides a power output of 1.97 mW while the solar TEG without PCM provides an almost zero (0.04 mW) power output and the solar TEG with thick copper plate provides a 0.23 mW power output, which is significantly lower compared to that of the solar TEG with PCM. This is one of the advantages of using phase change material because it can help the solar TEG provide power output during periods of zero or very low solar radiation.

Furthermore, the hot side temperature of the solar TEG with and without PCM is shown in Figure 6.31b. Since the cold side temperature is kept constant, the transient and non-uniform heat flux from the solar concentrator mainly affects the hot side temperature of the solar thermoelectric generator. It is clear from Figure 6.31b that the hot side temperature of the solar TEG without PCM is very unstable because of the solar radiation pattern. In addition, Figure 6.31b shows that after 1 min, the solar thermoelectric generator without PCM quickly attains its highest hot side temperature of 30.63 °C. This could be harmful to the solar thermoelectric generator if very high concentrated solar radiation is used. This is because, each thermoelectric generator has a maximum temperature it can tolerate consequently, this limit could be exceeded which would damage the device. However, using a PCM at the top surface of the solar TEG would prevent such occurrence from happening as shown in Figure 6.31b.

Therefore, the results confirm that the phase change material has a great potential for protecting the solar thermoelectric generator when high solar radiation is utilized.

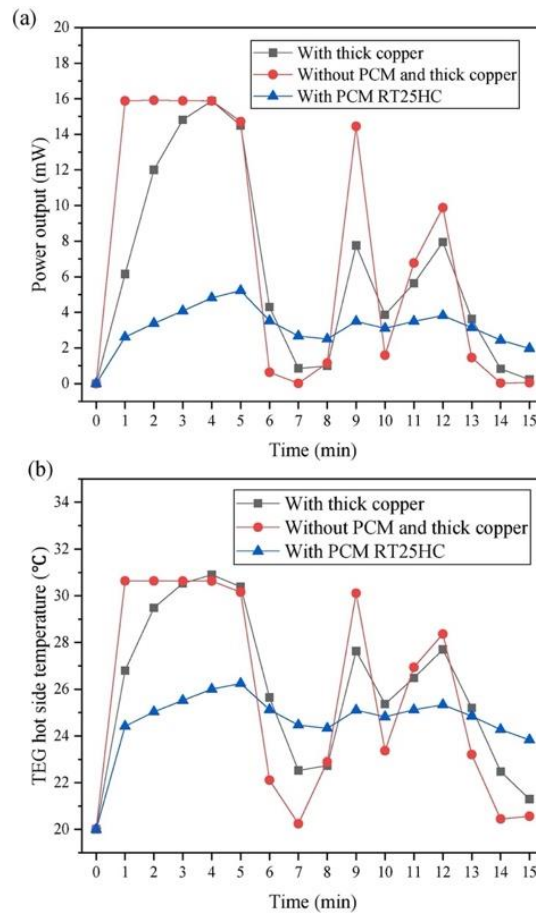


Figure 6.31: Variation of time with (a) power output and (b) temperature difference for solar TEG with and without PCM

In addition, Figure 6.31b shows that the use of PCM at the top surface of the solar TEG could significantly reduce the effect of transient and non-uniform heat flux fluctuations on the solar TEG temperature. Furthermore, after 15 min, the hot side temperature of the solar TEG with PCM is greater than that of the solar TEG without PCM and solar TEG with thick copper plate by 15.90% and 11.90% respectively. Consequently, the PCM can provide the hot side temperature for the solar TEG during periods of zero or very low solar radiation.

6.5.5 Temperature Distribution and Liquid Fraction

To better understand the behavior of the solar TEG with and without PCM, three-dimensional temperature distribution is presented for both cases. Figure 6.32 shows the three-dimensional temperature distribution of the solar TEG without PCM. The effect of the non-uniform heat flux distribution from the compound parabolic concentrator (CPC) used in this study, which is presented in Figure 6.20c on the temperature distribution of the solar TEG without PCM, is shown in Figure 6.32. As expected, the middle region of the solar TEG attains the highest temperature due to the flux distribution being higher in that region as shown in Figure 6.20c.

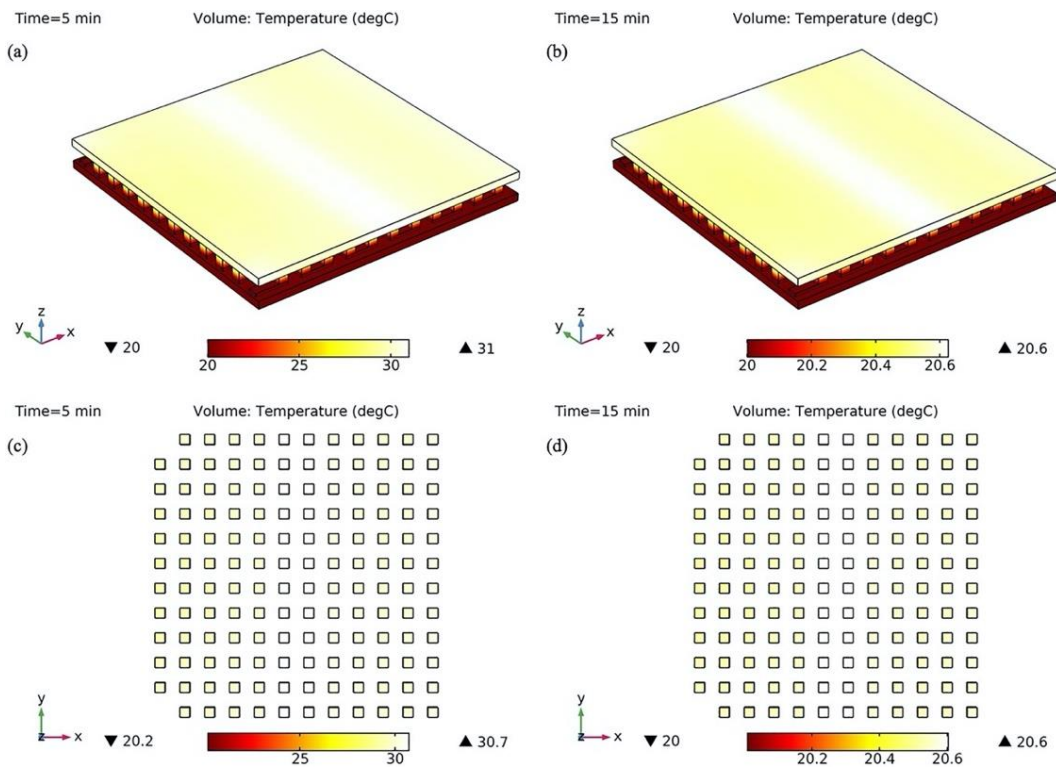


Figure 6.32: Temperature distribution of solar TEG at (a) 5 min (b) 15 min and front view of thermoelectric legs at (c) 5 min (d) 15 min

While Figure 6.32a shows the temperature distribution of the solar TEG without PCM at 5 min, Figure 6.32b shows the temperature distribution at 15 min. It can be seen that the temperature difference across the solar TEG without PCM

CHAPTER 6 THERMOELECTRIC GENERATOR OPTIMIZATION AND
RESULTS DISCUSSION

decreased from 11 °C (Figure 6.32a) to 6.6 °C (Figure 6.32b) due to the decrease in solar radiation. Furthermore, Figure 6.32c and Figure 6.32d show the actual temperature distribution at the top surface of the thermoelectric legs. The non-uniform heat flux from the solar concentrator affects the temperature distribution on the thermoelectric legs as shown in Figure 6.32c and Figure 6.32d at 5 min and 15 min respectively. In addition, it can be seen from Figure 6.32c and Figure 6.32d that the highest temperature is in the middle thermoelectric legs.

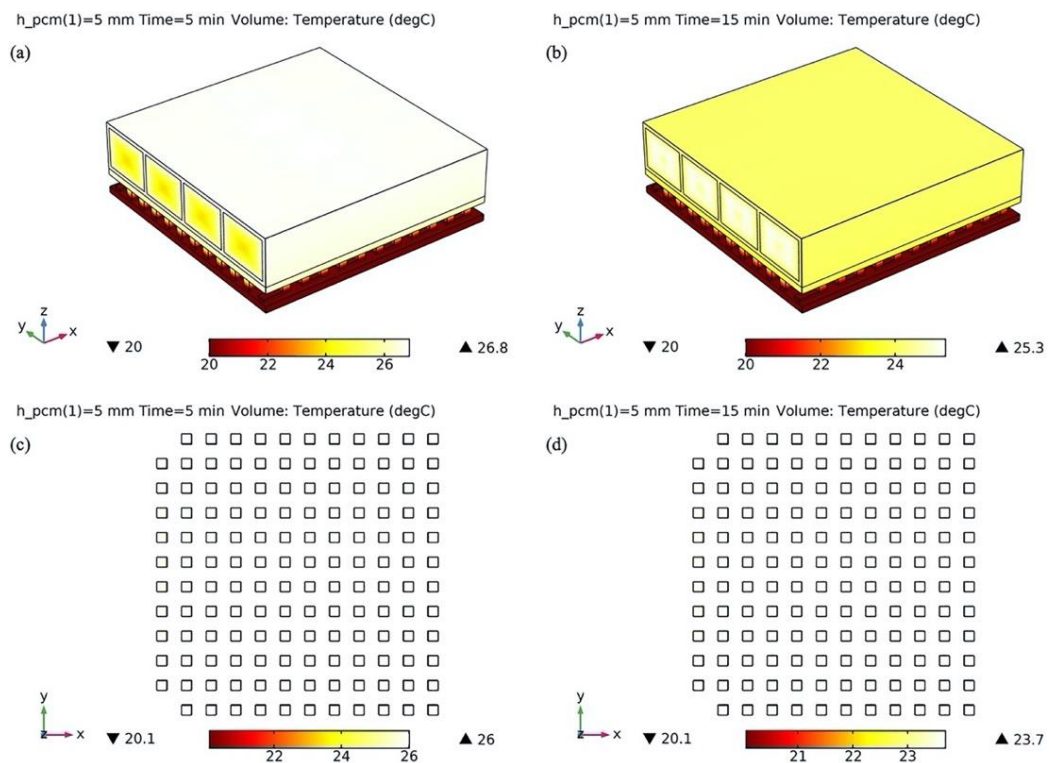


Figure 6.33: Temperature distribution of solar TEG with PCM at (a) 5 min (b) 15 min and front view of thermoelectric legs at (c) 5 min (d) 15 min

The three-dimensional temperature distribution of the solar TEG with PCM is shown in Figure 6.33. It can be seen clearly that the temperature difference across the solar TEG with PCM decreased from 6.8 °C (Figure 6.33a) to 5.3 °C (Figure 6.33b) due to the decrease in solar radiation during the period of 5 min to 15 min. This smaller decrease in temperature difference compared to that in Figure 6.32 shows the

capability of the PCM in providing stable performance for the solar TEG. In addition, Figure 6.33c and Figure 6.33d show the temperature distribution on the thermoelectric legs at 5 min and 15 min respectively. It is obvious that a uniform temperature distribution is achieved due to the presence of the PCM at the top surface of the solar thermoelectric generator. Consequently, the use of PCM provides a more stable performance from the solar TEG and nullifies the effects of non-uniform heat flux from solar concentrators especially at high radiation levels.

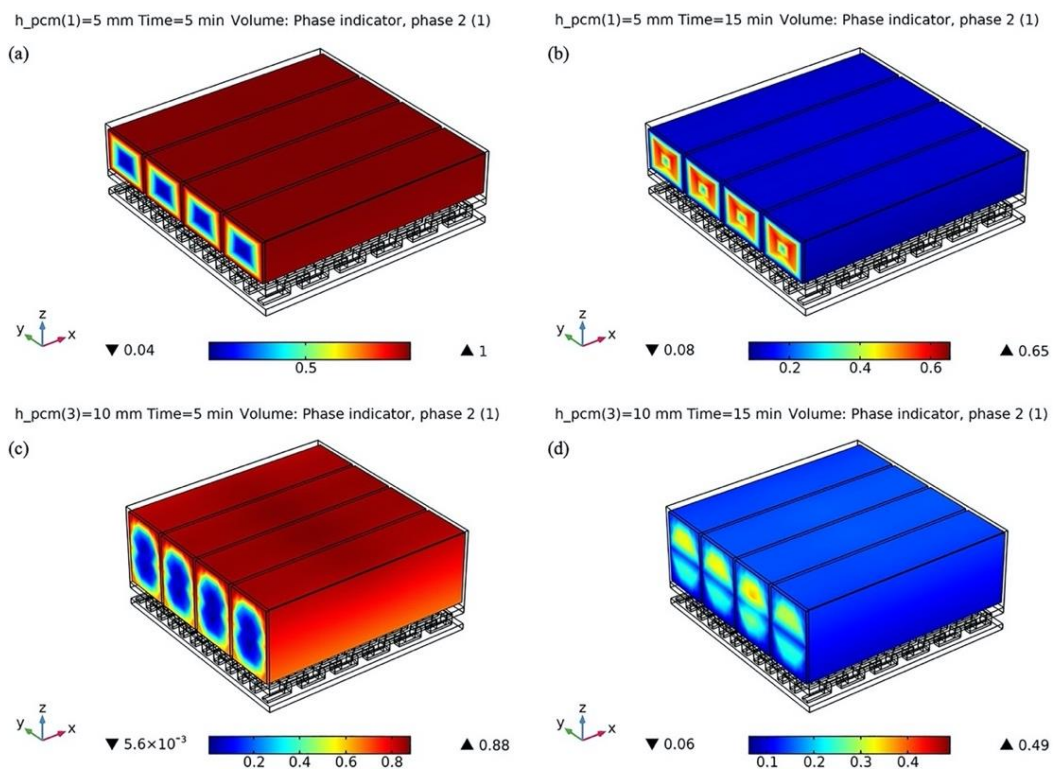


Figure 6.34: Liquid fraction of PCM with (a) 5 mm height, 5 min (b) 5 mm height, 15 min and (c) 10 mm height, 5 min (d) 10 mm height, 15 min

Furthermore, the liquid fraction of the PCM with 5 mm height at 5 min and 15 min is shown in Figure 6.34a and Figure 6.34b respectively. It is obvious that a higher percentage of the PCM melts at 5 min compared to 15 min because of the fluctuations in solar radiation. In addition, at 5 min, more than half of the PCM has melted while at 15 min, most of the PCM is back in solid form. Similarly, the liquid fraction of the

PCM with 10 mm height at 5 min and 15 min is shown in Figure 6.34c and Figure 6.34d respectively. It can be seen that although a larger percentage of the PCM melts at 5 min than at 15 min, this percentage is still lower than that of the PCM with 5 mm height. Furthermore, Figure 6.34 shows that the phase change starts close to the wall of the PCM fins and the melting front advances towards the center as time increases.

6.5.6 Section Conclusion

A detailed three-dimensional numerical investigation on the effect of transient and non-uniform heat flux on solar thermoelectric generator (solar TEG) performance was carried out in this study. A comparison between the performance of a solar thermoelectric generator with and without phase change material (PCM) was made. The main conclusions from this study are:

- 1) The placement of PCM on the top surface of a solar thermoelectric generator is effective in providing a stable electrical performance from the solar TEG under varying weather conditions.
- 2) The use of PCM on the top surface of a solar TEG has a great potential for protecting the solar thermoelectric generator when highly concentrated solar radiation is utilized.
- 3) The peak power output, temperature difference, and efficiency of the solar TEG decrease by 52.11%, 30.71% and 32.87% respectively, when the PCM height increased from 5mm to 20mm.
- 4) The use of PCM with a solar thermoelectric generator can ensure the solar TEG still provides power output during periods of zero or very low solar radiation.

6.6 Chapter Summary

This chapter presented the results obtained from the optimization studies, leading to the enhancement of the thermoelectric generator electrical and mechanical performance using innovative geometries such as annular, segmented and asymmetrical geometries. In addition, results obtained from the optimization of the thermoelectric generator with phase change material were presented. All the optimization studies were performed using COMSOL Multiphysics software. Furthermore, three-dimensional numerical studies were carried out and finite element method was used. The main findings from each study carried out were presented in the section conclusions while the general summary of the optimization results from the four studies carried out are respectively:

- 1) Results showed that the segmented annular thermoelectric generator had a greater electrical efficiency compared to the annular thermoelectric generator (ATEG) with Bismuth telluride material when the temperature difference was greater than 100 K. In addition, the electrical efficiency of the SATEG was found to be 21.7% and 82.9% greater than that of the Bismuth telluride ATEG and Skutterudite ATEG respectively at 200 K temperature difference. The results also showed that an increase in thermoelectric leg length can reduce the thermal stress and electrical performance of the segmented and non-segmented thermoelectric generators.
- 2) Results obtained showed that the optimized SASTEG provided a power output enhancement of 117.11% compared to that of the conventional TEG under rectangular pulsed heat condition. Also, the asymmetrical leg geometry used in the SASTEG n-type leg provided a reduced thermal stress of 39.21% in the

lower segment (cold side) compared to the symmetrical leg geometry used in the p-type leg lower segment.

- 3) Results showed that the power output of the segmented solar thermoelectric generators in Case 3 (75% Bi_2Te_3 material and 25% Skutterudite material), Case 4 (50% Bi_2Te_3 material and 50% Skutterudite material) and Case 5 (25% Bi_2Te_3 material and 75% Skutterudite material) increased by 44.07%, 59.12% and 37.9% respectively compared to that of Case 1 (100% bismuth telluride non-segmented solar TEG) at 13000 W/m^2 .
- 4) Results showed that the placement of PCM on the top surface of the solar thermoelectric generator is an effective approach to provide a stable electrical performance for the solar TEG under varying weather conditions. Furthermore, results revealed the effectiveness of the phase change material in protecting the solar thermoelectric generator under highly concentrated solar radiation.

CHAPTER 7 CONCLUSION AND FUTURE WORK

7.1 Conclusion

This research presented a detailed theoretical and experimental investigation of the performance of hybrid photovoltaic-thermoelectric system with flat plate microchannel heat pipe. Furthermore, the performance of the hybrid PV-TE system without heat pipe was investigated under steady state and transient conditions. In addition, electrical and mechanical performance enhancement of thermoelectric generators by geometry optimization was investigated. The thesis includes detailed literature review, conceptual design, mathematical analysis, computer simulation model development, experimental testing and model validation, optimization of the hybrid photovoltaic-thermoelectric systems with and without heat pipe, and thermoelectric generator optimization.

The main achievements from this research are: (1) development of a full range of three-dimensional simulation models, which were validated with experimental results and published data; (2) experimental setup and testing of a prototype PV-TE-MCHP system; (3) optimization of hybrid photovoltaic-thermoelectric systems with and without heat pipe; (4) thermoelectric generator optimization.

The main conclusions derived from this research are as follows:

7.1.1 PV-TE-MCHP Design

Effective thermal management of photovoltaic with thermoelectric generators typically requires the use of several thermoelectric generators to completely cover the back surface of the PV. However, the use of a flat plate microchannel heat pipe (MCHP) in this research resulted in a significant reduction in the quantity of thermoelectric generators needed thereby reducing the cost of the system. Furthermore, the flat plate structure of the MCHP enhanced its heat extraction

capability from the photovoltaic module due to the absence of geometry mismatch as in the case of cylindrical heat pipes therefore, thermal losses were reduced. In addition, the use of flat plate MCHP enabled uniform distribution of temperature across the photovoltaic surface thereby preventing the development of hotspots. Compared to the PV only system, the experimental average mean temperature deviation across the photovoltaic surface in the hybrid PV-TE-MCHP system after 1 h was 57.82% lower, thereby showing the temperature uniformity capability of the flat plate MCHP.

7.1.2 Computer Simulation Models

Based on the conceptual design of the hybrid PV-TE-MCHP system and components selected, a computer simulation model was developed to predict the performance of the hybrid system under steady state and transient conditions. Individual simulation models for the photovoltaic, thermoelectric generator and heat pipe were first developed before being integrated using COMSOL Multiphysics software. All the simulation models were validated with experimental results and published data. Furthermore, the three-dimensional nature of the simulation models allowed the better understanding of the heat transfer process in the systems and temperature distribution thereby enabling a more accurate prediction of the system performance.

Asides the three main simulation models including photovoltaic, thermoelectric generator and heat pipe, other optimization models including solar TEG, phase change material, contact resistance and thermal stress models were also developed and utilized for performance prediction and enhancement. Results from the simulation of the studied PV-TE-MCHP system based on the conceptual design showed that the overall efficiency of the PV-TE-MCHP was 4.04% and 10.75% greater than that of the PV only and PV-TE systems respectively at a wind speed of

0 m/s. Furthermore, at a high ambient temperature of 50 °C, the PV-TE-MCHP overall efficiency was found to be greater than that of the PV only and PV-TE systems by 9.76% and 14.46% respectively. Therefore, the hybrid PV-TE-MCHP is better for sunny regions with high ambient temperature.

7.1.3 Experimental Testing Under Laboratory Conditions

Several tests were carried out on the hybrid PV-TE-MCHP system with water cooling under a controlled laboratory environment. The feasibility of the hybrid system for electricity generation and hot water production was demonstrated. Solar radiation from a solar simulator was varied for different test scenarios and exergy analysis was performed. Furthermore, the effects of thermoelectric load resistance, insulation layer on the back surface of the flat plate microchannel heat pipe and solar radiation on the performance of the hybrid system was presented and a comparison with a photovoltaic only system was made. A crystalline silicon photovoltaic module with dimensions 675 mm x 85 mm x 2 mm was used in addition to a flat plate microchannel heat pipe with dimensions 750 mm x 60 mm x 3 mm. Furthermore, a commercial thermoelectric generator module (GM250-127-14-16) with dimensions 40 mm x 40 mm x 3.4 mm was attached to the condenser section of the heat pipe for waste heat recovery and electricity generation via Seebeck effect. The photovoltaic was attached to the evaporator section of the flat plate MCHP which extracts the accumulated heat at the back surface of the PV and transfers it to its condenser section. Consequently, one photovoltaic module, one flat plate MCHP and one thermoelectric generator were used to form the hybrid system.

Experimental results showed that the electrical conversion efficiencies of the photovoltaic-thermoelectric-microchannel heat pipe with and without insulation and that of the photovoltaic only after 1 h were 11.98%, 12.19% and 11.94% respectively.

Therefore, the hybrid system provided an enhanced performance. Furthermore, photovoltaic temperature in the hybrid system with and without insulation (62.2 °C and 61.9 °C respectively) was lower than that in the photovoltaic only system (67.9 °C) after 1 h. It was found that if water heating is the main requirement of the hybrid system, an insulation should be used to cover the back surface of the MCHP however, if enhanced electricity generation is desired, insulation should not be used. In addition, it was found that the average power output of the hybrid system increased from 1.86 W to 3.92 W when the solar radiation increased from 500 W/m² to 1000 W/m². Furthermore, the highest and lowest thermal efficiencies obtained were 69.53% and 56.57% respectively under certain conditions.

7.1.4 Thermoelectric Geometry Optimization

Thermoelectric geometry optimization was found to be an effective method to enhancement the performance of hybrid photovoltaic-thermoelectric systems and thermoelectric generators. Electrical and mechanical performance enhancement of thermoelectric generators using different innovative thermoelectric geometries including annular, segmented and asymmetrical geometries was presented. Consequently, optimization results from two different studies (steady state and transient) on thermoelectric geometry optimization in a hybrid photovoltaic-thermoelectric system were presented. In addition, optimization results from three different studies (segmented annular TEG, segmented asymmetrical TEG and segmented solar TEG) on thermoelectric geometry optimization in a thermoelectric generator were presented.

Results showed that thermoelectric geometry optimization could reduce significantly the negative impacts of the variable weather conditions on the hybrid system performance. In addition, it was found that the asymmetrical n-type and p-type

leg geometry provided enhanced thermoelectric generator only performance compared to the symmetrical n-type and p-type leg geometry although the reverse was the case for the hybrid concentrated photovoltaic-thermoelectric system. Furthermore, results showed that an increase in thermoelectric leg length could reduce the thermal stress and electrical performance of the segmented and non-segmented thermoelectric generators.

7.2 Limitations and Recommendations for Future Work

This section firstly addresses the research gaps and challenges faced. Secondly, follow-on works that can fill the gaps and tackle the challenges while also contributing an added value to the development of PV-TE systems are provided.

7.2.1 Limitations

Despite the satisfactory results obtained from the experimental and numerical investigation of the hybrid photovoltaic-thermoelectric-flat plate microchannel heat pipe (PV-TE-MCHP) system, the following limitations still exist which require further investigation.

- 1) A small-scale experiment was carried out in this research to test the feasibility of the hybrid PV-TE-MCHP for electricity generation and hot water production. Consequently, one photovoltaic module, one flat plate MCHP and one thermoelectric generator were used to form the hybrid system. The size of the photovoltaic module and flat plate microchannel heat pipe is small therefore, the power output obtainable from the hybrid system is limited.
- 2) The performance of the hybrid PV-TE-MCHP was experimentally tested under laboratory conditions using a solar simulator. However, this does not reflect the practical performance of the system. In addition, the difference in the

spectral responses of the artificial solar simulator and natural sunlight introduces measurement uncertainties.

- 3) Despite the performance enhancement obtainable by the use of the hybrid PV-TE-MCHP, the feasibility of the hybrid system for practical applications must be evaluated by performing economic and environmental analysis.
- 4) Although the hybrid PV-TE-MCHP still provides enhanced performance under normal solar radiation, the advantage of the hybrid system becomes more obvious under highly concentrated solar radiation which is not considered in this research.
- 5) Several numerical studies on thermoelectric geometry optimization in hybrid photovoltaic-thermoelectric systems and thermoelectric generators were presented in this research however, experiment on thermoelectric geometry optimization was not conducted and is therefore a limitation identified.

7.2.2 Recommendations for Future Work

Based on the limitations of the hybrid system investigated, recommendations are provided. In addition, thermoelectric geometry optimization in a hybrid system and thermoelectric generator is a growing area of interest to several researchers therefore, recommendations for future work are provided.

- 1) Large-scale experimental study is recommended to further test the performance of the hybrid PV-TE-MCHP system. A higher performance enhancement could be obtained by the use of a large photovoltaic module, several heat pipes and thermoelectric generators.
- 2) Experimental testing under natural sunlight is recommended as this will enable accurate testing of the system performance under actual varying weather conditions rather than under artificial solar radiation. Under laboratory

conditions, the effects of actual wind speed, solar radiation and ambient temperature variations cannot be tested accurately.

- 3) Economic and environmental analysis is recommended as it will accelerate the commercialization of the hybrid system. In addition, it will enable the evaluation of the hybrid system feasibility for practical applications in comparison to other systems.
- 4) Application of concentrated solar radiation is recommended because under such high solar radiation, the flat plate microchannel heat pipe can extract more heat thereby cooling the photovoltaic while providing a higher quantity of heat input to the thermoelectric generator for additional electricity generation.
- 5) Experimental investigation of performance enhancement obtainable via thermoelectric geometry optimization is recommended. In addition, thermoelectric geometry optimization using a combination of three-dimensional finite element method and multi-objective optimization is recommended for future research.
- 6) Although the computer simulation models used in this research could predict and optimize the performance of the hybrid systems and thermoelectric generator, it can be further improved to account for other parameters which affect the performance of the system including degradation of PV cells by environmental causes such as humidity and soiling.
- 7) Although water cooling which is used in this research provides enhanced performance compared to air cooling, the use of nanofluid cooling in the hybrid system could further reduce the temperature of the thermoelectric generator cold side and increase its temperature difference thereby increasing its power output.

REFERENCES

- Al-Merbati, A.S., Yilbas, B.S., Sahin, A.Z., 2013. Thermodynamics and thermal stress analysis of thermoelectric power generator: Influence of pin geometry on device performance. *Appl. Therm. Eng.* 50, 683–692.
- Amatya, R., Ram, R.J., 2010. Solar thermoelectric generator for micropower applications. *J. Electron. Mater.* 39, 1735–1740.
- Antonova, E.E., Looman, D.C., 2005. Finite elements for thermoelectric device analysis in ANSYS, in: 24th International Conference on Thermoelectrics. IEEE, pp. 200–203.
- Ariffin, M.R., Shafie, S., Hassan, W., Azis, N., Ya'acob, M.E., 2017. Conceptual Design of Hybrid Photovoltaic- Thermoelectric Generator (PV/TEG) for Automated Greenhouse System, in: 2017 IEEE 15th Student Conference on Research and Development (SCORED). pp. 309–314.
- Asaadi, S., Khalilarya, S., Jafarmadar, S., 2018. Numerical study on the thermal and electrical performance of an annular thermoelectric generator under pulsed heat power with different types of input functions. *Energy Convers. Manag.* 167, 102–112.
- Attivissimo, F., Di Nisio, A., Lanzolla, A.M.L., Paul, M., 2015. Feasibility of a photovoltaic-thermoelectric generator: Performance analysis and simulation results. *IEEE Trans. Instrum. Meas.* 64, 1158–1169.
- Babu, C., Ponnambalam, P., 2018. The theoretical performance evaluation of hybrid PV-TEG system. *Energy Convers. Manag.* 173, 450–460.
- Babu, C., Ponnambalam, P., 2017. The role of thermoelectric generators in the hybrid PV/T systems: A review. *Energy Convers. Manag.* 151, 368–385.
- Bathe, K.-J., 2014. *Finite Element Procedures*, 2nd ed. Englewood Cliffs New Jersey.

REFERENCES

- Bauknecht, A., Steinert, T., Spengler, C., Suck, G., 2013. Analysis of annular thermoelectric couples with nonuniform temperature distribution by means of 3-D multiphysics simulation. *J. Electron. Mater.* 42, 1641–1646.
- Beeri, O., Rotem, O., Hazan, E., Katz, E.A., Braun, A., Gelbstein, Y., 2015. Hybrid photovoltaic-thermoelectric system for concentrated solar energy conversion: Experimental realization and modeling. *J. Appl. Phys.* 118, 115104.
- Bjørk, R., Nielsen, K.K., 2018. The maximum theoretical performance of unconcentrated solar photovoltaic and thermoelectric generator systems. *Energy Convers. Manag.* 156, 264–268.
- Bjørk, R., Nielsen, K.K., 2015. The performance of a combined solar photovoltaic (PV) and thermoelectric generator (TEG) system. *Sol. Energy* 120, 187–194.
- BP, 2019. BP Energy Outlook: 2019 edition.
- Byon, C., 2016. Heat Pipe and Phase Change Heat Transfer Technologies for Electronics Cooling, in: Sohel Murshed, S.. (Ed.), *Electronics Cooling*. IntechOpen, Rijeka.
- Caillat, T., Borshchevsky, A., Fleurial, J.P., 1996. Properties of single crystalline semiconducting CoSb₃. *J. Appl. Phys.* 80, 4442–4449.
- Chapin, D.M., Fuller, C.S., Pearson, G.L., 1954. A new silicon p-n junction photocell for converting solar radiation into electrical power. *J. Appl. Phys.* 25, 676–677.
- Chaudhry, H.N., Richard, B., Ghani, 2012. A review of heat pipe systems for heat recovery and renewable energy applications. *Renew. Sustain. Energy Rev.* 16, 2249–2259.
- Chen, G., 2009. Introduction to Thermoelectricity [WWW Document]. Direct Solar/Thermal to Electr. Energy Convers. Technol. URL <http://web.mit.edu/nanoengineering> (accessed 3.28.20).

- Chen, G., Mu, Y., Zhai, P., Li, G., Zhang, Q., 2013. An investigation on the coupled thermal-mechanical-electrical response of automobile thermoelectric materials and devices. *J. Electron. Mater.* 42, 1762–1770.
- Chen, H., Wang, N., He, H., 2014. Equivalent circuit analysis of photovoltaic – thermoelectric hybrid device with different TE module structure. *Adv. Condens. Matter Phys.* 1–16.
- Chen, L., Lee, J., 2015. Effect of pulsed heat power on the thermal and electrical performances of a thermoelectric generator. *Appl. Energy* 150, 138–149.
- Chow, T.T., Pei, G., Fong, K.F., Lin, Z., Chan, A.L.S., Ji, J., 2009. Energy and exergy analysis of photovoltaic-thermal collector with and without glass cover. *Appl. Energy* 86, 310–316.
- Clin, T., Turenne, S., Vasilevskiy, D., Masut, R.A., 2009. Numerical simulation of the thermomechanical behavior of extruded bismuth telluride alloy module. *J. Electron. Mater.* 38, 994–1001.
- COMSOL Multiphysics, 2018a. Flat Heat Pipe [WWW Document]. Appl. Gall. URL <https://uk.comsol.com/model/flat-heat-pipe-43841> (accessed 2.13.19).
- COMSOL Multiphysics, 2018b. Heat Transfer Module User’s Guide. Version 5.4.
- Contento, G., Lorenzi, B., Rizzo, A., Narducci, D., 2017. Efficiency enhancement of a-Si and CZTS solar cells using different thermoelectric hybridization strategies. *Energy* 131, 230–238.
- Cotfas, D.T., Cotfas, P.A., Machidon, O.M., Ciobanu, D., 2016. Investigation of the photovoltaic cell/ thermoelectric element hybrid system performance. *IOP Conf. Ser. Mater. Sci. Eng.* 133, 0–10.
- Cui, T., Xuan, Y., Li, Q., 2016. Design of a novel concentrating photovoltaic-thermoelectric system incorporated with phase change materials. *Energy*

- Convers. Manag. 112, 49–60.
- Cui, T., Xuan, Y., Yin, E., Li, Q., Li, D., 2017. Experimental investigation on potential of a concentrated photovoltaic-thermoelectric system with phase change materials. *Energy* 122, 94–102.
- Cui, Y.J., Wang, B.L., Li, J.E., Wang, K.F., 2020. Performance evaluation and lifetime prediction of a segmented photovoltaic-thermoelectric hybrid system. *Energy Convers. Manag.* 211.
- Cui, Y.J., Wang, B.L., Wang, K.F., Zheng, L., 2019. Power output evaluation of a porous annular thermoelectric generator for waste heat harvesting. *Int. J. Heat Mass Transf.* 137, 979–989.
- Da, Y., Xuan, Y., Li, Q., 2016. From light trapping to solar energy utilization: A novel photovoltaic-thermoelectric hybrid system to fully utilize solar spectrum. *Energy* 95, 200–210.
- Dallan, B.S., Schumann, J., Lesage, F.J., 2015. Performance evaluation of a photoelectric-thermoelectric cogeneration hybrid system. *Sol. Energy* 118, 276–285.
- Daud, M.M.M., Nor, N.B.M., Ibrahim, T., 2012. Novel hybrid photovoltaic and thermoelectric panel. 2012 IEEE Int. Power Eng. Optim. Conf. PEOCO 2012 - Conf. Proc. 269–274.
- Dongxu, J., Zhongbao, W., Pou, J., Mazzoni, S., Rajoo, S., Romagnoli, A., 2019. Geometry optimization of thermoelectric modules: Simulation and experimental study. *Energy Convers. Manag.* 195, 236–243.
- Dou, Y., Wu, F., Fang, L., Liu, G., Mao, C., Wan, K., Zhou, M., 2016. Enhanced performance of dye-sensitized solar cell using Bi₂Te₃nanotube/ZnO nanoparticle composite photoanode by the synergistic effect of photovoltaic and

- thermoelectric conversion. *J. Power Sources* 307, 181–189.
- Dupré, O., Vaillon, R., Green, M.A., 2017. *Thermal Behavior of Photovoltaic Devices*. Springer International Publishing.
- El Chaar, L., Lamont, L.A., El Zein, N., 2011. Review of photovoltaic technologies. *Renew. Sustain. Energy Rev.* 15, 2165–2175.
- Elsarrag, E., Pernau, H., Heuer, J., Roshan, N., Alhorr, Y., Bartholomé, K., 2015. Spectrum splitting for efficient utilization of solar radiation: a novel photovoltaic–thermoelectric power generation system. *Renewables Wind. Water, Sol.* 2, 16.
- Elsheikh, M.H., Shnawah, D.A., Sabri, M.F.M., Said, S.B.M., Hassan, H.M., Bashir, A.M.B., Mohamad, M., 2014. A review on thermoelectric renewable energy: Principle parameters that affect their performance. *Renew. Sustain. Energy Rev.* 30, 337–355.
- Enescu, D., 2019. *Thermoelectric Energy Harvesting: Basic Principles and Applications*. Green Energy Adv.
- Erturun, U., Erermis, K., Mossi, K., 2015. Influence of leg sizing and spacing on power generation and thermal stresses of thermoelectric devices. *Appl. Energy* 159, 19–27.
- Erturun, U., Erermis, K., Mossi, K., 2014. Effect of various leg geometries on thermo-mechanical and power generation performance of thermoelectric devices. *Appl. Therm. Eng.* 73, 128–141.
- Erturun, U., Mossi, K., 2015. Thermoelectric devices with rotated and coaxial leg configurations: Numerical analysis of performance. *Appl. Therm. Eng.* 85, 304.
- European Commission, 2018. *A clean planet for all: A European strategic long-term vision for a prosperous, modern, competitive and climate neutral economy*.

Brussels.

European Thermodynamics Limited, 2014a. GM250-127-14-16 Thermoelectric generator module - Datasheet 44, 1–4.

European Thermodynamics Limited, 2014b. GM250-71-14-16 Thermoelectric generator module - Datasheet.

Evans, D.L., 1981. Simplified method for predicting photovoltaic array output. *Sol. Energy* 27, 555–560.

ExxonMobil, 2019. Outlook for Energy: A Perspective to 2040.

Ezzat, M.A., 2011. Theory of fractional order in generalized thermoelectric MHD. *Appl. Math. Model.* 35, 4965–4978.

Fabián-Mijangos, A., Min, G., Alvarez-Quintana, J., 2017. Enhanced performance thermoelectric module having asymmetrical legs. *Energy Convers. Manag.* 148, 1372–1381.

Faghri, A., 2014. Heat Pipes: Review, Opportunities and Challenges. *Front. Heat Pipes* 1.

Faghri, A., 2012. Review and Advances in Heat Pipe Science and Technology. *J. Heat Transfer* 134, 123001.

Faghri, A., 1995. *Heat Pipe Science And Technology*, 1st ed. Global Digital Press.

Fallah Kohan, H.R., Lotfipour, F., Eslami, M., 2018. Numerical simulation of a photovoltaic thermoelectric hybrid power generation system. *Sol. Energy* 174, 537–548.

Fan, L., Zhang, G., Wang, R., Jiao, K., 2016. A comprehensive and time-efficient model for determination of thermoelectric generator length and cross-section area. *Energy Convers. Manag.* 122, 85–94.

Fan, S., Gao, Y., 2019. Numerical analysis on the segmented annular thermoelectric

- generator for waste heat recovery. *Energy* 183, 35–47.
- Fan, S., Gao, Y., 2018. Numerical simulation on thermoelectric and mechanical performance of annular thermoelectric generator. *Energy* 150, 38–48.
- Ferreira-Teixeira, S., Pereira, A.M., 2018. Geometrical optimization of a thermoelectric device: Numerical simulations. *Energy Convers. Manag.* 169, 217–227.
- Fisac, M., Villasevil, F.X., López, A.M., 2014. High-efficiency photovoltaic technology including thermoelectric generation. *J. Power Sources* 252, 264–269.
- Francioso, L., De Pascali, C., Farella, I., Martucci, C., Cretì, P., Siciliano, P., Perrone, A., 2010. Flexible thermoelectric generator for wearable biometric sensors. *Proc. IEEE Sensors* 196, 747–750.
- Gang, P., Guiqiang, L., Xi, Z., Jie, J., Yuehong, S., 2012. Experimental study and exergetic analysis of a CPC-type solar water heater system using higher-temperature circulation in winter. *Sol. Energy* 86, 1280–1286.
- Gang, P., Huide, F., Tao, Z., Jie, J., 2011. A numerical and experimental study on a heat pipe PV/T system. *Sol. Energy* 85, 911–921.
- Gao, J.-L., Du, Q.-G., Zhang, X.-D., Jiang, X.-Q., 2011. Thermal Stress Analysis and Structure Parameter Selection for a Bi₂Te₃-Based Thermoelectric Module. *J. Electron. Mater.* 40, 884–888.
- Goldsmid, H.J., 2017. The Seebeck and Peltier effects, in: *The Physics of Thermoelectric Energy Conversion*. Morgan & Claypool.
- Green, M.A., Hishikawa, Y., Dunlop, E.D., Levi, D.H., Hohl-Ebinger, J., Ho-Baillie, A.W.Y., 2018. Solar cell efficiency tables (version 52). *Prog. Photovoltaics Res. Appl.* 26, 427–436.
- Grubisić-Čabo, F., Nizetić, S., Marco, T.G., 2016. Photovoltaic Panels: A Review of

- the Cooling Techniques. *Trans. FAMENA* 40, 63–74.
- Guo, X.Z., Zhang, Y.D., Qin, D., Luo, Y.H., Li, D.M., Pang, Y.T., Meng, Q.B., 2010. Hybrid tandem solar cell for concurrently converting light and heat energy with utilization of full solar spectrum. *J. Power Sources* 195, 7684–7690.
- Hadjistassou, C., Kyriakides, E., Georgiou, J., 2013. Designing high efficiency segmented thermoelectric generators. *Energy Convers. Manag.* 66, 165–172.
- Hajji, M., Labrim, H., Benaissa, M., Laazizi, A., Ez-Zahraouy, H., Ntsoenzok, E., Meot, J., Benyoussef, A., 2017. Photovoltaic and thermoelectric indirect coupling for maximum solar energy exploitation. *Energy Convers. Manag.* 136, 184–191.
- Hashim, H., Bompfrey, J.J., Min, G., 2016. Model for geometry optimisation of thermoelectric devices in a hybrid PV/TE system. *Renew. Energy* 87, 458–463.
- He, H., Liu, W., Wu, Y., Rong, M., Zhao, P., Tang, X., 2019a. An approximate and efficient characterization method for temperature-dependent parameters of thermoelectric modules. *Energy Convers. Manag.* 180, 584–597.
- He, H., Wu, Y., Liu, W., Rong, M., Fang, Z., Tang, X., 2019b. Comprehensive modeling for geometric optimization of a thermoelectric generator module. *Energy Convers. Manag.* 183, 645–659.
- He, W., Wang, S., Zhang, X., Li, Y., Lu, C., 2015a. Optimization design method of thermoelectric generator based on exhaust gas parameters for recovery of engine waste heat. *Energy* 91, 1–9.
- He, W., Zhang, G., Zhang, X., Ji, J., Li, G., Zhao, X., 2015b. Recent development and application of thermoelectric generator and cooler. *Appl. Energy* 143, 1–25.
- Hodes, M., 2010. Optimal pellet geometries for thermoelectric power generation. *IEEE Trans. Components Packag. Technol.* 33, 307–318.

- Höglblom, O., Andersson, R., 2014. Analysis of thermoelectric generator performance by use of simulations and experiments. *J. Electron. Mater.* 43, 2247–2254.
- Hsiao, Y.Y., Chang, W.C., Chen, S.L., 2010. A mathematic model of thermoelectric module with applications on waste heat recovery from automobile engine. *Energy* 35, 1447–1454.
- Huen, P., Daoud, W.A., 2017. Advances in hybrid solar photovoltaic and thermoelectric generators. *Renew. Sustain. Energy Rev.* 72, 1295–1302.
- Ibeagwu, O.I., 2019. Modelling and comprehensive analysis of TEGs with diverse variable leg geometry. *Energy* 180, 90–106.
- International Energy Agency, 2019a. *SDG7: Data and Projections*. Paris.
- International Energy Agency, 2019b. *Tracking Buildings*. Paris.
- International Energy Agency, 2019c. *Energy Policies of IEA Countries: United Kingdom*.
- International Energy Agency, 2019d. *Solar Energy: Mapping the Road Ahead*. Paris.
- Jäger-Waldau, A., 2019. *PV Status Report 2019*. EUR 29938 EN, Publ. Off. Eur. Union, Luxemb.
- Jeyashree, Y., Hepsiba, P.B., Indirani, S., Savio, A.D., Sukhi, Y., 2017. Solar Energy Harvesting using Hybrid Photovoltaic and Thermoelectric Generating System. *Glob. J. Pure Appl. Math.* 13, 5935–5944.
- Ji, J., He, H., Chow, T., Pei, G., He, W., Liu, K., 2009. Distributed dynamic modeling and experimental study of PV evaporator in a PV/T solar-assisted heat pump. *Int. J. Heat Mass Transf.* 52, 1365–1373.
- Jia, X., Gao, Y., 2014. Estimation of thermoelectric and mechanical performances of segmented thermoelectric generators under optimal operating conditions. *Appl. Therm. Eng.* 73, 333–340.

- Jia, X., Guo, Q., 2020. Design study of Bismuth-Telluride-based thermoelectric generators based on thermoelectric and mechanical performance. *Energy* 190, 116226.
- Ju, X., Wang, Z., Flamant, G., Li, P., Zhao, W., 2012. Numerical analysis and optimization of a spectrum splitting concentration photovoltaic-thermoelectric hybrid system. *Sol. Energy* 86, 1941–1954.
- Karana, D.R., Sahoo, R.R., 2019. Influence of geometric parameter on the performance of a new asymmetrical and segmented thermoelectric generator. *Energy* 179, 90–99.
- Kil, T.-H.H., Kim, S.S., Jeong, D.-H.H., Geum, D.-M.M., Lee, S., Jung, S.-J.J., Kim, S.S., Park, C., Kim, J.-S.S., Baik, J.M., Lee, K.-S.S., Kim, C.Z., Choi, W.J., Baek, S.-H.H., 2017. A highly-efficient, concentrating-photovoltaic/thermoelectric hybrid generator. *Nano Energy* 37, 242–247.
- Kim, S.J., We, J.H., Cho, B.J., 2014. A wearable thermoelectric generator fabricated on a glass fabric. *Energy Environ. Sci.* 7, 1959–1965.
- Kossyvakis, D.N., Voutsinas, G.D., Hristoforou, E. V., 2016. Experimental analysis and performance evaluation of a tandem photovoltaic-thermoelectric hybrid system. *Energy Convers. Manag.* 117, 490–500.
- Kraemer, D., Hu, L., Muto, A., Chen, X., Chen, G., Chiesa, M., 2008. Photovoltaic-thermoelectric hybrid systems: A general optimization methodology. *Appl. Phys. Lett.* 92, 243503.
- Kwan, T.H., Wu, X., 2016. Power and mass optimization of the hybrid solar panel and thermoelectric generators. *Appl. Energy* 165, 297–307.
- Kylili, A., Theodoridou, M., Ioannou, I., Fokaides, P.A., 2016. Numerical heat transfer analysis of Phase Change Material (PCM) -enhanced plasters. *COMSOL Conf.*

Munich 1–7.

- Lakeh, H.K., Kaatuzian, H., Hosseini, R., 2019. A Parametrical Study on Photo-Electro-Thermal Performance of an Integrated Thermoelectric-Photovoltaic Cell. *Renew. Energy* 138, 542–550.
- Lamba, R., Kaushik, S.C., 2018. Solar driven concentrated photovoltaic-thermoelectric hybrid system: Numerical analysis and optimization. *Energy Convers. Manag.* 170, 34–49.
- Lamba, R., Kaushik, S.C., 2017. Thermodynamic analysis of thermoelectric generator including influence of Thomson effect and leg geometry configuration. *Energy Convers. Manag.* 144, 388–398.
- Lamba, R., Kaushik, S.C., 2016. Modeling and performance analysis of a concentrated photovoltaic-thermoelectric hybrid power generation system. *Energy Convers. Manag.* 115, 288–298.
- Lavric, E.D., 2010. Sensitivity analysis of thermoelectric module performance with respect to geometry. *Chem. Eng. Trans.* 21, 133–138.
- Lekbir, A., Hassani, S., Ab Ghani, M.R., Gan, C.K., Mekhilef, S., Saidur, R., 2018. Improved energy conversion performance of a novel design of concentrated photovoltaic system combined with thermoelectric generator with advance cooling system. *Energy Convers. Manag.* 177, 19–29.
- Lekbir, A., Meddad, M., A., E., Benhadouga, S., Khenfer, R., 2019. Higher-efficiency for combined photovoltaic-thermoelectric solar power generation. *Int. J. Green Energy* 0, 1–7.
- Leonov, V., Torfs, T., Vullers, R.J.M., Van Hoof, C., 2010. Hybrid thermoelectric-photovoltaic generators in wireless electroencephalography diadem and electrocardiography shirt. *J. Electron. Mater.* 39, 1674–1680.

- Li, D., Xuan, Y., Li, Q., Hong, H., 2017. Exergy and energy analysis of photovoltaic-thermoelectric hybrid systems. *Energy* 126, 343–351.
- Li, D., Xuan, Y., Yin, E., Li, Q., 2018. Conversion efficiency gain for concentrated triple-junction solar cell system through thermal management. *Renew. Energy* 126, 960–968.
- Li, G., An, Q., Li, W., Goddard, W.A., Zhai, P., Zhang, Q., Snyder, G.J., 2015. Brittle Failure Mechanism in Thermoelectric Skutterudite CoSb₃. *Chem. Mater.* 27, 6329–6336.
- Li, G., Chen, X., Jin, Y., 2017a. Analysis of the primary constraint conditions of an efficient photovoltaic-thermoelectric hybrid system. *Energies* 10, 1–12.
- Li, G., Chen, X., Jin, Y., Ji, J., 2017b. Optimizing on thermoelectric elements footprint of the photovoltaic-thermoelectric for maximum power generation. *Energy Procedia* 142, 730–735.
- Li, G., Diallo, T.M.O., Akhlaghi, Y.G., Shittu, S., Zhao, X., Ma, X., Wang, Y., 2019a. Simulation and experiment on thermal performance of a micro-channel heat pipe under different evaporator temperatures and tilt angles. *Energy* 179, 549–557.
- Li, G., Ji, J., Zhang, G., He, W., Chen, X., Chen, H., 2016a. Performance analysis on a novel micro-channel heat pipe evacuated tube solar collector-incorporated thermoelectric generation. *Int. J. Energy Res.* 40, 2117–2127.
- Li, G., Pei, G., Ji, J., Su, Y., 2015a. Outdoor overall performance of a novel air-gap-lens-walled compound parabolic concentrator (ALCPC) incorporated with photovoltaic/thermal system. *Appl. Energy* 144, 214–223.
- Li, G., Pei, G., Ji, J., Yang, M., Su, Y., Xu, N., 2015b. Numerical and experimental study on a PV/T system with static miniature solar concentrator. *Sol. Energy* 120, 565–574.

- Li, G., Shittu, S., Ma, X., Zhao, X., 2019b. Comparative analysis of thermoelectric elements optimum geometry between Photovoltaic-thermoelectric and solar thermoelectric. *Energy* 171, 599–610.
- Li, G., Zhao, X., Ji, J., 2016b. Conceptual development of a novel photovoltaic-thermoelectric system and preliminary economic analysis. *Energy Convers. Manag.* 126, 935–943.
- Li, G., Zhao, X., Jin, Y.Y., Chen, X., Ji, J., Shittu, S., 2018a. Performance Analysis and Discussion on the Thermoelectric Element Footprint for PV–TE Maximum Power Generation. *J. Electron. Mater.* 47, 5344–5351.
- Li, G., Zhou, K., Song, Z., Zhao, X., Ji, J., 2018b. Inconsistent phenomenon of thermoelectric load resistance for photovoltaic–thermoelectric module. *Energy Convers. Manag.* 161, 155–161.
- Li, J.F., Liu, W.S., Zhao, L.D., Zhou, M., 2010. High-performance nanostructured thermoelectric materials. *NPG Asia Mater.* 2, 152–158.
- Li, P., Cai, L., Zhai, P., Tang, X., Zhang, Q., Niino, M., 2010. Design of a concentration solar thermoelectric generator. *J. Electron. Mater.* 39, 1522–1530.
- Li, Y., Witharana, S., Cao, H., Lasfargues, M., Huang, Y., Ding, Y., 2014. Wide spectrum solar energy harvesting through an integrated photovoltaic and thermoelectric system. *Particuology* 15, 39–44.
- Liang, D., Luo, Q., Li, P., Fu, Y., Cai, L., Zhai, P., 2018. Optimization and experimentation of concentrating photovoltaic/cascaded thermoelectric generators hybrid system using spectral beam splitting technology. *IOP Conf. Ser. Earth Environ. Sci.* 199, 52044.
- Liang, X., Sun, X., Tian, H., Shu, G., Wang, Y., Wang, X., 2014. Comparison and parameter optimization of a two-stage thermoelectric generator using high

- temperature exhaust of internal combustion engine. *Appl. Energy* 130, 190–199.
- Liao, M., He, Z., Jiang, C., Fan, X., Li, Y., Qi, F., 2018. A three-dimensional model for thermoelectric generator and the influence of Peltier effect on the performance and heat transfer. *Appl. Therm. Eng.* 133, 493–500.
- Liao, T., Lin, B., Yang, Z., 2014. Performance characteristics of a low concentrated photovoltaic- thermoelectric hybrid power generation device. *Int. J. Therm. Sci.* 77, 158–164.
- Lin, J., Liao, T., Lin, B., 2015. Performance analysis and load matching of a photovoltaic-thermoelectric hybrid system. *Energy Convers. Manag.* 105, 891–899.
- Lin, W., Shih, T.M., Zheng, J.C., Zhang, Y., Chen, J., 2014. Coupling of temperatures and power outputs in hybrid photovoltaic and thermoelectric modules. *Int. J. Heat Mass Transf.* 74, 121–127.
- Liu, H.-B., Meng, J.-H.H., Wang, X.-D.D., Chen, W.-H.H., 2018. A new design of solar thermoelectric generator with combination of segmented materials and asymmetrical legs. *Energy Convers. Manag.* 175, 11–20.
- Liu, Z., Sun, B., Zhong, Y., Liu, X., Han, J., Shi, T., Tang, Z., Liao, G., 2017. Novel integration of carbon counter electrode based perovskite solar cell with thermoelectric generator for efficient solar energy conversion. *Nano Energy* 38, 457–466.
- Lorenzi, B., Acciarri, M., Narducci, D., 2018. Suitability of Electrical Coupling in Solar Cell Thermoelectric Hybridization. *Designs* 2, 32.
- Lorenzi, B., Chen, G., 2018. Theoretical efficiency of hybrid solar thermoelectric-photovoltaic generators. *J. Appl. Phys.* 124.
- Lorenzi, B., Contento, G., Sabatelli, V., Rizzo, A., Narducci, D., 2017. Theoretical

- Analysis of Two Novel Hybrid Thermoelectric-Photovoltaic Systems Based on. *J. Nanosci. Nanotechnol.* 17, 1608–1615.
- Luo, B., Deng, Y., Wang, Y., Gao, M., Zhu, W., Hashim, H.T., Garcia-Canada, J., 2016. Synergistic photovoltaic-thermoelectric effect in a nanostructured CdTe/Bi₂Te₃ heterojunction for hybrid energy harvesting. *RSC Adv.* 6, 114046–114051.
- Luo, D., Wang, R., Yu, W., Zhou, W., 2020. Parametric study of a thermoelectric module used for both power generation and cooling. *Renew. Energy* 154, 542–552.
- Luo, D., Wang, R., Yu, W., Zhou, W., 2019. Performance evaluation of a novel thermoelectric module with BiSbTeSe-based material. *Appl. Energy* 238, 1299–1311.
- Ma, X., Shu, G., Tian, H., Xu, W., Chen, T., 2019. Performance assessment of engine exhaust-based segmented thermoelectric generators by length ratio optimization. *Appl. Energy* 248, 614–625.
- Machrafi, H., 2017. Enhancement of a photovoltaic cell performance by a coupled cooled nanocomposite thermoelectric hybrid system, using extended thermodynamics. *Curr. Appl. Phys.* 17, 890–911.
- Madan, D., Wang, Z., Wright, P.K., Evans, J.W., 2015. Printed flexible thermoelectric generators for use on low levels of waste heat. *Appl. Energy* 156, 587–592.
- Mahmoudinezhad, S., Atouei, S.A., Cofas, P.A., Cofas, D.T., Rosendahl, L.A., Rezania, A., 2019. Experimental and numerical study on the transient behavior of multi-junction solar cell-thermoelectric generator hybrid system. *Energy Convers. Manag.* 184, 448–455.
- Mahmoudinezhad, S., Rezania, A., Cofas, D.T., Cofas, P.A., Rosendahl, L.A.,

- 2018a. Experimental and numerical investigation of hybrid concentrated photovoltaic – Thermoelectric module under low solar concentration. *Energy* 159, 1123–1131.
- Mahmoudinezhad, S., Rezania, A., Rosendahl, L.A., 2018b. Behavior of hybrid concentrated photovoltaic-thermoelectric generator under variable solar radiation. *Energy Convers. Manag.* 164, 443–452.
- Makki, A., Omer, S., Sabir, H., 2015. Advancements in hybrid photovoltaic systems for enhanced solar cells performance. *Renew. Sustain. Energy Rev.* 41, 658–684.
- Makki, A., Omer, S., Su, Y., Sabir, H., 2016. Numerical investigation of heat pipe-based photovoltaic-thermoelectric generator (HP-PV/TEG) hybrid system. *Energy Convers. Manag.* 112, 274–287.
- Manikandan, S., Kaushik, S.C., 2016. Energy and exergy analysis of solar heat pipe based annular thermoelectric generator system. *Sol. Energy* 135, 569–577.
- Manikandan, S., Selvam, C., Pavan Sai Praful, P., Lamba, R., Kaushik, S.C., Zhao, D., Yang, R., 2019. A novel technique to enhance thermal performance of a thermoelectric cooler using phase-change materials. *J. Therm. Anal. Calorim.* 123456789.
- Mankel, C., Caggiano, A., Koenders, E., 2019. Thermal energy storage characterization of cementitious composites made with recycled brick aggregates containing PCM. *Energy Build.* 202, 109395.
- Marandi, O.F., Ameri, M., Adelshahian, B., 2018. The experimental investigation of a hybrid photovoltaic-thermoelectric power generator solar cavity-receiver. *Sol. Energy* 161, 38–46.
- Markets and Markets, 2019a. *Thermoelectric Generators Market by Application (Waste Heat Recovery, Energy Harvesting, Direct Power Generation, Co-*

REFERENCES

- generation), Wattage (<10 W, 10-1kW, >1kW), Temperature (<80°C, 80°-500°C, >500°C, Material, Vertical, Component, Region - Global Forecas.
- Markets and Markets, 2019b. Thermoelectric Modules Market by Model (Single-Stage, Multi-Stage), Type (Bulk Thermoelectric Modules, Micro Thermoelectric Modules, Thin-Film Thermoelectric Modules), Functionality, Offering, End-Use Application, and Region - Global Forecast to 2024.
- McKinsey & Company, 2019. Global Energy Perspective 2019: Reference Case, Energy Insights.
- Meng, X., Suzuki, R.O., 2016. Helical configuration for thermoelectric generation. *Appl. Therm. Eng.* 99, 352–357.
- Met Office, 2019a. MIDAS Open: UK hourly solar radiation data, v201901. *Cent. Environ. Data Anal.*
- Met Office, 2019b. MIDAS Open: UK hourly weather observation data, v201901. *Cent. Environ. Data Anal.*
- Miao, Z., Meng, X., Zhou, S., Zhu, M., 2020. Thermo-mechanical analysis on thermoelectric legs arrangement of thermoelectric modules. *Renew. Energy* 147, 2272–2278.
- Min, G., Rowe, D.M., 2007. Ring-structured thermoelectric module. *Semicond. Sci. Technol.* 22, 880–883.
- Min, G., Rowe, D.M., 1992. Optimisation of thermoelectric module geometry for “waste heat” electric power generation. *J. Power Sources* 38, 253–259.
- Ming, T., Wang, Q., Peng, K., Cai, Z., Yang, W., Wu, Y., Gong, T., 2015. The influence of non-uniform high heat flux on thermal stress of thermoelectric power generator. *Energies* 8, 12584–12602.
- Ming, T., Yang, W., Huang, X., Wu, Y., Li, X., Liu, J., 2017a. Analytical and

- numerical investigation on a new compact thermoelectric generator. *Energy Convers. Manag.* 132, 261–271.
- Ming, T., Yang, W., Wu, Y., Xiang, Y., Huang, X., Cheng, J., Li, X., Zhao, J., 2017b. Numerical analysis on the thermal behavior of a segmented thermoelectric generator. *Int. J. Hydrogen Energy* 42, 3521–3535.
- Minnich, A.J., Dresselhaus, M.S., Ren, Z.F., Chen, G., 2009. Bulk nanostructured thermoelectric materials: Current research and future prospects. *Energy Environ. Sci.* 2, 466–479.
- Mizoshiri, M., Mikami, M., Ozaki, K., 2012. Thermal-photovoltaic hybrid solar generator using thin-film thermoelectric modules. *Jpn. J. Appl. Phys.* 51, 1–5.
- Motiei, P., Yaghoubi, M., GoshtashbiRad, E., Vadiee, A., 2018. Two-dimensional unsteady state performance analysis of a hybrid photovoltaic-thermoelectric generator. *Renew. Energy* 119, 551–565.
- Mustofa, Djafar, Z., Syafaruddin, Piarah, W.H., 2018. A new hybrid of photovoltaic-thermoelectric generator with hot mirror as spectrum splitter. *J. Phys. Sci.* 29, 63–75.
- Nishijima, Y., Komatsu, R., Yamamura, T., Seniutinas, G., Saulius, J., 2017. Design concept of a hybrid photo-voltaic / thermal conversion cell for mid-infrared light energy harvester. *Opt. Mater. Express* 7, 3484–3493.
- Ouyang, Z., Li, D., 2018. Design of segmented high-performance thermoelectric generators with cost in consideration. *Appl. Energy* 221, 112–121.
- Ouyang, Z., Li, D., 2016. Modelling of segmented high-performance thermoelectric generators with effects of thermal radiation, electrical and thermal contact resistances. *Sci. Rep.* 6, 1–12.
- Pang, W., Liu, Y., Shao, S., Gao, X., 2015. Empirical study on thermal performance

- through separating impacts from a hybrid PV/TE system design integrating heat sink. *Int. Commun. Heat Mass Transf.* 60, 9–12.
- Pang, W., Yu, H., Zhang, Y., Yan, H., 2017. Electrical Characteristics of a Hybrid Photovoltaic/Thermoelectric Generator System. *Energy Technol.* 6, 1248–1254.
- Park, K.T., Shin, S.M., Tazebay, A.S., Um, H.D., Jung, J.Y., Jee, S.W., Oh, M.W., Park, S.D., Yoo, B., Yu, C., Lee, J.H., 2013. Lossless hybridization between photovoltaic and thermoelectric devices. *Sci. Rep.* 3, 1–6.
- Petela, R., 2003. Exergy of undiluted thermal radiation. *Sol. Energy* 74, 469–488.
- Pichanusakorn, P., Bandaru, P., 2010. Nanostructured thermoelectrics. *Mater. Sci. Eng. R Reports* 67, 19–63.
- Qing, S., Rezania, A., Rosendahl, L.A., Gou, X., 2018. Design of flexible thermoelectric generator as human body sensor. *Mater. Today Proc.* 5, 10338–10346.
- Ramirez, W.F., 1997. Solution of Partial Differential Equations, in: *Computational Methods in Process Simulation*. Butterworth-Heinemann, pp. 353–430.
- Rapp, B.E., 2017. Finite Element Method, in: *Microfluidics: Modeling, Mechanics and Mathematics*. Elsevier, pp. 655–678.
- Reay, D., Kew, P., McGlen, R., 2014. *Heat Pipes: Theory, Design and Applications*, 6th ed. Butterworth-Heinemann.
- Research and Markets, 2019. *Thermoelectric Generators Market by Application (Waste Heat Recovery, Energy Harvesting, Direct Power Generation, Co-generation), Wattage (1kW), Temperature (500°C), Material, Vertical, Component, Region - Global Forecast to 2025*.
- Rezania, A., Rosendahl, L.A., 2017. Feasibility and parametric evaluation of hybrid concentrated photovoltaic-thermoelectric system. *Appl. Energy* 187, 380–389.

REFERENCES

- Rezania, A., Rosendahl, L.A., Yin, H., 2014. Parametric optimization of thermoelectric elements footprint for maximum power generation. *J. Power Sources* 255, 151–156.
- Rodrigo, P.M., Valera, A., Fernández, E.F., Almonacid, F.M., 2019. Performance and economic limits of passively cooled hybrid thermoelectric generator-concentrator photovoltaic modules. *Appl. Energy* 238, 1150–1162.
- Rowe, D.M., 2006. *Thermoelectric Handbook: Macro to Nano*. CRC Press, Taylor & Francis Group.
- Rubitherm Technologies GmbH, 2020. RT25HC [WWW Document]. Tech. Data Sheet. URL https://www.rubitherm.eu/media/products/datasheets/Techdata_RT25HC_EN_15012020.PDF (accessed 1.28.20).
- Sahin, A.Z., Yilbas, B.S., 2013. The thermoelement as thermoelectric power generator: Effect of leg geometry on the efficiency and power generation. *Energy Convers. Manag.* 65, 26–32.
- Sallehin, N.Z.I.M., Yatim, N.M., Suhaimi, S., 2018. A review on fabrication methods for segmented thermoelectric structure. *AIP Conf. Proc.* 1972, 30003.
- Saqr, K.M., Mansour, M.K., Musa, M.N., 2008. Patient expectations for health supervision advice in continuity clinic: Experience from a teaching hospital in Thailand. *Int. J. Automot. Technol.* 9, 155–160.
- Shen, Z.-G.G., Liu, X., Chen, S., Wu, S.Y., Xiao, L., Chen, Z.-X.X., 2018. Theoretical analysis on a segmented annular thermoelectric generator. *Energy* 157, 297–313.
- Shen, Z.G., Wu, S.Y., Xiao, L., 2017. Assessment of the performance of annular thermoelectric couples under constant heat flux condition. *Energy Convers. Manag.* 150, 704–713.
- Shen, Z.G., Wu, S.Y., Xiao, L., 2015. Theoretical analysis on the performance of

- annular thermoelectric couple. *Energy Convers. Manag.* 89, 244–250.
- Shou, C., Luo, Z., Wang, T., Shen, W., Rosengarten, G., Wei, W., Wang, C., Ni, M., Cen, K., 2012. Investigation of a broadband TiO₂/SiO₂ optical thin-film filter for hybrid solar power systems. *Appl. Energy* 92, 298–306.
- Shu, G., Ma, X., Tian, H., Yang, H., Chen, T., Li, X., 2018. Configuration optimization of the segmented modules in an exhaust-based thermoelectric generator for engine waste heat recovery. *Energy* 160, 612–624.
- Sibin, K.P., Selvakumar, N., Kumar, A., Dey, A., Sridhara, N., Shashikala, H.D., Sharma, A.K., Barshilia, H.C., 2017. Design and development of ITO/Ag/ITO spectral beam splitter coating for photovoltaic-thermoelectric hybrid systems. *Sol. Energy* 141, 118–126.
- Singh, P., Singh, S.N., Lal, M., Husain, M., 2008. Temperature dependence of I-V characteristics and performance parameters of silicon solar cell. *Sol. Energy Mater. Sol. Cells* 92, 1611–1616.
- Skjølstrup, E.J.H., Søndergaard, T., 2016. Design and optimization of spectral beamsplitter for hybrid thermoelectric-photovoltaic concentrated solar energy devices. *Sol. Energy* 139, 149–156.
- Snyder, G.J., 2004. Application of the compatibility factor to the design of segmented and cascaded thermoelectric generators. *Appl. Phys. Lett.* 84, 2436–2438.
- Snyder, G.J., Ursell, T.S., 2003. Thermoelectric efficiency and compatibility. *Phys. Rev. Lett.* 91, 148301/1-148301/4.
- Soltani, S., Kasaeian, A., Sarrafha, H., Wen, D., 2017. An experimental investigation of a hybrid photovoltaic/thermoelectric system with nanofluid application. *Sol. Energy* 155, 1033–1043.
- Suarez, F., Parekh, D.P., Ladd, C., Vashaee, D., Dickey, M.D., Öztürk, M.C., 2017.

REFERENCES

- Flexible thermoelectric generator using bulk legs and liquid metal interconnects for wearable electronics. *Appl. Energy* 202, 736–745.
- Suzuki, R.O., Ito, K.O., Oki, S., 2016. Analysis of the Performance of Thermoelectric Modules Under Concentrated Radiation Heat Flux. *J. Electron. Mater.*
- Teffah, K., Zhang, Y., 2017. Modeling and experimental research of hybrid PV-thermoelectric system for high concentrated solar energy conversion. *Sol. Energy* 157, 10–19.
- Thirugnanasambandam, M., Iniyar, S., Goic, R., 2010. Review of Solar Thermal Technologies. *Renew. Sustain. Energy Rev.* 14, 312–322.
- Tian, H., Sun, X., Jia, Q., Liang, X., Shu, G., Wang, X., 2015. Comparison and parameter optimization of a segmented thermoelectric generator by using the high temperature exhaust of a diesel engine. *Energy* 84, 121–130.
- Tritt, T.M., Böttner, H., and, Chen, L., 2008. Thermoelectrics : Direct Solar Thermal Energy Conversion. *Harnessing Mater. Energy* 33, 366–368.
- Twaha, S., Zhu, J., Yan, Y., Li, B., 2016. A comprehensive review of thermoelectric technology: Materials, applications, modelling and performance improvement. *Renew. Sustain. Energy Rev.* 65, 698–726.
- U.S. Energy Information Administration, 2019. *International Energy Outlook 2019 with projections to 2050*. Washington, DC.
- United Nations, 2015a. *Transforming our world: the 2030 agenda for sustainable development*.
- United Nations, 2015b. *Paris agreement*.
- Ursell, T.S., Snyder, G.J., 2002. Compatibility of segmented thermoelectric generators. *Int. Conf. Thermoelectr. ICT, Proc.* 2002–Janua, 412–417.
- Van Sark, W.G.J.H.M., 2011. Feasibility of photovoltaic - Thermoelectric hybrid

- modules. *Appl. Energy* 88, 2785–2790.
- Vorobiev, Y., González-Hernández, J., Vorobiev, P., Bulat, L., 2006. Thermal-photovoltaic solar hybrid system for efficient solar energy conversion. *Sol. Energy* 80, 170–176.
- Wang, N., Han, L., He, H., Park, N.-H., Koumoto, K., 2011. A novel high-performance photovoltaic–thermoelectric hybrid device. *Energy Environ. Sci.* 4, 3676.
- Wang, X., Wang, H., Su, W., Mehmood, F., Zhai, J., Wang, T., Chen, T., Wang, C., 2019. Geometric structural design for lead tellurium thermoelectric power generation application. *Renew. Energy* 141, 88–95.
- Willars-Rodríguez, F., Chavez-Urbiola, E., Vorobiev, P., Vorobiev, Y. V, 2017. Investigation of solar hybrid system with concentrating Fresnel lens, photovoltaic and thermoelectric generators. *Int. J. Energy Res.* 41, 377–388.
- Wu, Y., Ming, T., Li, X., Pan, T., Peng, K., Luo, X., 2014. Numerical simulations on the temperature gradient and thermal stress of a thermoelectric power generator. *Energy Convers. Manag.* 88, 915–927.
- Wu, Y.Y., Wu, S.Y., Xiao, L., 2015. Performance analysis of photovoltaic-thermoelectric hybrid system with and without glass cover. *Energy Convers. Manag.* 93, 151–159.
- Xiao, J., Yang, T., Li, P., Zhai, P., Zhang, Q., 2012. Thermal design and management for performance optimization of solar thermoelectric generator. *Appl. Energy* 93, 33–38.
- Xu, Y., Xuan, Y., Yang, L., 2015. Full-spectrum photon management of solar cell structures for photovoltaic-thermoelectric hybrid systems. *Energy Convers. Manag.* 103, 533–541.

REFERENCES

- Xuan, Q., Li, G., Pei, G., Ji, J., Su, Y., Zhao, B., 2017. Optimization design and performance analysis of a novel asymmetric compound parabolic concentrator with rotation angle for building application. *Sol. Energy* 158, 808–818.
- Yang, J., 2005. Potential applications of thermoelectric waste heat recovery in the automotive industry. *Int. Conf. Thermoelectr. ICT, Proc. 2005*, 155–159.
- Yang, X., Zhai, P., Liu, L., Zhang, Q., 2011. Thermodynamic and mechanical properties of crystalline CoSb(3): A molecular dynamics simulation study. *J. Appl. Phys.* 109, 123517/1-123517/6.
- Yang, Z., Li, W., Chen, X., Su, S., Lin, G., Chen, J., 2018. Maximum efficiency and parametric optimum selection of a concentrated solar spectrum splitting photovoltaic cell-thermoelectric generator system. *Energy Convers. Manag.* 174, 65–71.
- Yilbas, B.S., Akhtar, S.S., Sahin, A.Z., 2016. Thermal and stress analyses in thermoelectric generator with tapered and rectangular pin configurations. *Energy* 114, 52–63.
- Yin, E., Li, Q., Li, D., Xuan, Y., 2019. Experimental investigation on effects of thermal resistances on a photovoltaic-thermoelectric system integrated with phase change materials. *Energy* 169, 172–185.
- Yin, E., Li, Q., Xuan, Y., 2018a. A novel optimal design method for concentration spectrum splitting photovoltaic-thermoelectric hybrid system. *Energy* 163, 519–532.
- Yin, E., Li, Q., Xuan, Y., 2018b. One-day performance evaluation of photovoltaic-thermoelectric hybrid system. *Energy* 143, 337–346.
- Yin, E., Li, Q., Xuan, Y., 2018c. Optimal design method for concentrating photovoltaic-thermoelectric hybrid system. *Appl. Energy* 226, 320–329.

- Yin, E., Li, Q., Xuan, Y., 2018d. Effect of non-uniform illumination on performance of solar thermoelectric generators. *Front. Energy* 12, 1–10.
- Yin, E., Li, Q., Xuan, Y., 2017. Thermal resistance analysis and optimization of photovoltaic-thermoelectric hybrid system. *Energy Convers. Manag.* 143, 188–202.
- Yu, H., Li, Y., Shang, Y., Su, B., 2008. Design and investigation of photovoltaic and thermoelectric hybrid power source for wireless sensor networks. 3rd IEEE Int. Conf. Nano/Micro Eng. Mol. Syst. NEMS 196–201.
- Zhang, A.B., Wang, B.L., Pang, D.D., Chen, J.B., Wang, J., Du, J.K., 2018a. Influence of leg geometry configuration and contact resistance on the performance of annular thermoelectric generators. *Energy Convers. Manag.* 166, 337–342.
- Zhang, A.B., Wang, B.L., Pang, D.D., He, L.W., Lou, J., Wang, J., Du, J.K., 2018b. Effects of interface layers on the performance of annular thermoelectric generators. *Energy* 147, 612–620.
- Zhang, G., Fan, L., Niu, Z., Jiao, K., Diao, H., Du, Q., Shu, G., 2015. A comprehensive design method for segmented thermoelectric generator. *Energy Convers. Manag.* 106, 510–519.
- Zhang, J., Xuan, Y., 2019. An integrated design of the photovoltaic-thermoelectric hybrid system. *Sol. Energy* 177, 293–298.
- Zhang, J., Xuan, Y., 2016. Investigation on the effect of thermal resistances on a highly concentrated photovoltaic-thermoelectric hybrid system. *Energy Convers. Manag.* 129, 1–10.
- Zhang, J., Xuan, Y., Yang, L., 2016. A novel choice for the photovoltaic-thermoelectric hybrid system: the perovskite solar cell. *Int. J. Energy Res.* 40, 1400–1409.

- Zhang, J., Xuan, Y., Yang, L., 2014. Performance estimation of photovoltaic-thermoelectric hybrid systems. *Energy* 78, 895–903.
- Zhang, X., Zhao, X., Smith, S., Xu, J., Yu, X., 2012. Review of R&D progress and practical application of the solar photovoltaic/ thermal (PV/T) technologies. *Renew. Sustain. Energy Rev.* 16, 599–617.
- Zhang, Y., Fang, J., He, C., Yan, H., Wei, Z., Li, Y., 2013. Integrated energy-harvesting system by combining the advantages of polymer solar cells and thermoelectric devices. *J. Phys. Chem. C* 117, 24685–24691.
- Zhang, Y., Xuan, Y., 2017. Preparation of structured surfaces for full-spectrum photon management in photovoltaic-thermoelectric systems. *Sol. Energy Mater. Sol. Cells* 169, 47–55.
- Zhou, J. cheng, Zhang, Z., Liu, H. jian, Yi, Q., 2017. Temperature distribution and back sheet role of polycrystalline silicon photovoltaic modules. *Appl. Therm. Eng.* 111, 1296–1303.
- Zhou, J., Yi, Q., Wang, Y., Ye, Z., 2015. Temperature distribution of photovoltaic module based on finite element simulation. *Sol. Energy* 111, 97–103.
- Zhou, Y.P., Li, M.J., Yang, W.W., He, Y.L., 2018. The effect of the full-spectrum characteristics of nanostructure on the PV-TE hybrid system performances within multi-physics coupling process. *Appl. Energy* 213, 169–178.
- Zhou, Z., Yang, J., Jiang, Q., Li, W., Luo, Y., Hou, Y., Zhou, S., Li, X., 2016. Large improvement of device performance by a synergistic effect of photovoltaics and thermoelectrics. *Nano Energy* 22, 120–128.
- Zhu, W., Deng, Y., Wang, Y., Shen, S., Gulfam, R., 2016. High-performance photovoltaic-thermoelectric hybrid power generation system with optimized thermal management. *Energy* 100, 91–101.

APPENDIX**Conceptual Design Simulation Parameters (Section 3.6)**

Geometric parameters used in simulation

Parameter	Value
Photovoltaic	
Area	675 mm x 85 mm
EVA height	0.625 mm
Polycrystalline silicon height	0.25 mm
TPT height	0.25 mm
Thermoelectric Generator	
Area	40 mm x 40 mm
Leg area	1.4 mm x 1.4 mm
Leg height	1 mm
Copper height	0.2 mm

APPENDIX

Ceramic height	1 mm
Flat plate heat pipe	
Evaporator	675 mm x 60 mm
Condenser	75 mm x 60 mm
Thickness	3 mm

Temperature dependent thermoelectric material properties (T is temperature in K) (European Thermodynamics Limited, 2014a)

	p-type	n-type
Electrical conductivity, σ [S/m]	$(0.015601732T^2 - 15.708052T + 4466.38095) \times 10^2$	$(0.01057143T^2 - 10.16048T + 3113.714229) \times 10^2$
Seebeck coefficient, S [V/K]	$(-0.003638095T^2 + 2.74380952T - 296.214286) \times 10^{-6}$	$(0.00153073T^2 - 1.08058874T - 28.338095) \times 10^{-6}$
Thermal conductivity, k [W/(m · K)]	$0.0000361558T^2 - 0.026351342T + 6.22162$	$0.0000334545T^2 - 0.023350303T + 5.606333$

APPENDIX

Optical properties of PV materials (Zhou et al., 2017)

Material	Reflectivity	Absorptivity	Transmissivity	Emissivity
EVA	2.00×10^{-2}	8.00×10^{-2}	9.00×10^{-1}	
Polycrystalline silicon	8.00×10^{-2}	9.00×10^{-1}	2.00×10^{-2}	
TPT	8.60×10^{-1}	1.28×10^{-1}	1.20×10^{-2}	9.20×10^{-1}

Remaining material properties used for simulation (COMSOL Multiphysics, 2018a; Zhou et al., 2017)

	Heat capacity, C_p [J/(kgK)]	Density, ρ [kg/m ³]	Seebeck coefficient, S [V/K]	Electrical conductivity, σ [S/m]	Thermal conductivity, k [W/(mK)]	Dynamic viscosity, μ [Pa·s]
EVA	2.09×10^3	9.60×10^2	-	-	3.11×10^{-1}	-
Silicon	6.77×10^2	2.33×10^3	-	-	1.30×10^2	-
TPT	1.25×10^3	1.20×10^3	-	-	1.50×10^{-1}	-

APPENDIX

Vapor	1874	<i>Ideal gas</i> ρ_v	-	-	0.0188	8.9 x 10 ⁻⁶
		$= \frac{p}{R_s T}$				
Water	4180	1000	-	-	0.61	-
Alumina	900	3900	-	-	27	-
Bi ₂ Te ₃ (p-n types)	154	7700	-	-	-	-
Copper	385	8960	-	59980000	238	-

Steady State PV-TE Simulation Parameters (Section 5.2)

Temperature dependent material properties (T is temperature in K) (Suzuki et al., 2016)

	p-type	n-type
Electrical conductivity, σ [S/m]	$(0.015601732T^2 - 15.708052T + 4466.38095) \times 10^2$	$(0.01057143T^2 - 10.16048T + 3113.714229) \times 10^2$
Seebeck coefficient, S [V/K]	$(-0.003638095T^2 + 2.74380952T - 296.214286) \times 10^{-6}$	$(0.00153073T^2 - 1.08058874T - 28.338095) \times 10^{-6}$
Thermal conductivity, k [W/(m · K)]	$0.0000361558T^2 - 0.026351342T + 6.22162$	$0.0000334545T^2 - 0.023350303T + 5.606333$

Material properties (Lamba and Kaushik, 2016; Teffah and Zhang, 2017; Wu et al., 2015)

Heat capacity, C_p [J/(kgK)]	Density, ρ [kg/m ³]	Seebeck coefficient, S [V/K]	Electrical conductivity, σ [S/m]	Thermal conductivity, k [W/(mK)]

APPENDIX

Alumina	900	3900	-	-	27
Bi ₂ Te ₃ (p-n types)	154	7700	$\pm S(T)$	$\sigma(T)$	$k(T)$
Copper	385	8960	-	58100000	401
Silicon (PV)	700	2329	-	-	148
Tedlar	1090	1780	-	-	0.2

Parameters used in hybrid PV-TE model

Parameters	Symbol	Value	References
Absorptivity of PV	α_{PV}	0.9	(Lamba and Kaushik, 2016)
Ambient temperature	T_{amb}	298 K	(Wu et al., 2015)
Area of PV	A_{PV}	0.0001 m ²	(G. Li et al., 2017a)
Area of TE element	A_{TE}	0.000014 m ²	(G. Li et al., 2017b)
Concentration ratio	c	5	(G. Li et al., 2017b)

APPENDIX

Emissivity of PV	ε_{PV}	0.8	(G. Li et al., 2017b)
Heat transfer coefficient	h_{amb}	5 Wm ⁻² K ⁻¹	(Ju et al., 2012)
Height of TE element	L	0.005 m	(G. Li et al., 2017b)
Solar irradiation	G	1000 W/m ²	(Wu et al., 2015)
Thickness of copper	H_{cu}	0.0001 m ²	(G. Li et al., 2017b)
Thickness of PV	H_{PV}	0.0003 m	(Lamba and Kaushik, 2016)
Thickness of tedlar	H_{ted}	0.000175 m	(Lamba and Kaushik, 2016)
Wind velocity	u_w	1 m/s	(G. Li et al., 2017b)
PV Cell A efficiency at standard test conditions (STC)	η_{PV}	10%	(Hashim et al., 2016)
Cell A temperature coefficient	φ_{PV}	0.001 K ⁻¹	(Hashim et al., 2016)

APPENDIX

PV Cell B efficiency at standard test conditions (STC)	η_{PV}	15%	(Guiqiang Li et al., 2015a)
Cell B temperature coefficient	φ_{PV}	0.004 K ⁻¹	(Guiqiang Li et al., 2015a)

Transient State PV-TE Simulation Parameters (Section 5.3)

Hybrid system geometric parameters

Parameter	Base value	Reference
Photovoltaic (PV)		
Area	$40\text{ mm} \times 40\text{ mm}$	
Glass thickness	3.2 mm	(Zhou et al., 2017)
EVA thickness	$4.6 \times 10^{-1}\text{ mm}$	(Zhou et al., 2017)
Polycrystalline silicon thickness	$1.8 \times 10^{-1}\text{ mm}$	(Zhou et al., 2017)
TPT thickness	$1.8 \times 10^{-1}\text{ mm}$	(Zhou et al., 2017)
Thermoelectric generator (TEG)		
Area	$40\text{ mm} \times 40\text{ mm}$	(He et al., 2019a)
Leg area	$1.5\text{ mm} \times 1.5\text{ mm}$	(He et al., 2019a)
Leg height	1.96 mm	(He et al., 2019a)
Top copper thickness	0.6 mm	(He et al., 2019a)

APPENDIX

Lower copper thickness	0.34 <i>mm</i>	(He et al., 2019a)
Ceramic thickness	0.86 <i>mm</i>	(He et al., 2019a)
Heat sink		
Area	40 <i>mm</i> × 40 <i>mm</i>	
Height	3.34 <i>mm</i>	
Number of fins	30	
Concentration ratio	30	(Zhang et al., 2014)
Heat sink heat transfer coefficient	500 <i>W/m²K</i>	(Zhang et al., 2014)

Thermoelectric material cubic polynomial functions (He et al., 2019a)

Property	p-type polynomial expression	n-type polynomial expression
----------	------------------------------	------------------------------

APPENDIX

Seebeck coefficient (V/K)	$-2.24407 \times 10^{-11}T^3 + 2.22834 \times 10^{-8}T^2 - 7.301$ $\times 10^{-6}T + 1.023698 \times 10^{-3}$	$1.68178 \times 10^{-11}T^3 - 1.77163 \times 10^{-8}T^2 + 6.203$ $\times 10^{-6}T - 9.54589 \times 10^{-4}$
Thermal conductivity (W/ m * K)	$-5.82609 \times 10^{-8}T^3 + 1.03491 \times 10^{-4}T^2 - 0.050117$ $+ 8.726$	$3.76869 \times 10^{-9}T^3 + 2.81722 \times 10^{-5}T^2 - 0.020577$ $+ 5.09531$
Electrical resistivity (Ωm^2)	$-7.75456 \times 10^{-13}T^3 + 7.77051 \times 10^{-10}T^2 - 0.01853$ $\times 10^{-5}T + 1.60117 \times 10^{-5}$	$-6.04782 \times 10^{-13}T^3 + 6.09155 \times 10^{-10}T^2 - 1.715$ $\times 10^{-7}T + 2.11951 \times 10^{-5}$

Mesh convergence test for hybrid system with different geometries

Element size	Hybrid power density (W/m ³)				Average PV cell temperature (K)			
	Case 1	Case 2	Case 3	Case 4	Case 1	Case 2	Case 3	Case 4
Coarser	6.76942E6	5.92968E6	5.95489E6	4.89517E6	433.92	447.7	446.92	467.34

APPENDIX

Coarse	6.76865E6	5.9276E6	5.95348E6	4.89271E6	433.93	447.73	446.94	467.38
Normal	6.76717E6	5.92517E6	5.95096E6	4.88711E6	433.95	447.77	446.98	467.49
Fine	6.76717E6	5.92517E6	5.95096E6	4.88711E6	433.95	447.77	446.98	467.49

PV-TE Contact Resistance Simulation Parameters (Section 5.4)

Hybrid system geometric parameters and properties

Parameter	Base value	Parametric value	Reference
Photovoltaic			
Area	$40\text{ mm} \times 40\text{ mm}$		
Glass thickness	3.2 mm		(Zhou et al., 2017)
EVA thickness	$4.6 \times 10^{-1}\text{ mm}$		(Zhou et al., 2017)
Polycrystalline silicon thickness	$1.8 \times 10^{-1}\text{ mm}$		(Zhou et al., 2017)
Tedlar polyester tedlar thickness	$1.8 \times 10^{-1}\text{ mm}$		(Zhou et al., 2017)
Thermoelectric generator			
Area	$40\text{ mm} \times 40\text{ mm}$		(He et al., 2019a)
Leg area	$1.5\text{ mm} \times 1.5\text{ mm}$		(He et al., 2019a)
Leg height	1 mm	$1\text{ mm} - 8\text{ mm}$	
Upper copper thickness	0.6 mm		(He et al., 2019a)

APPENDIX

Lower copper thickness	0.34 mm		(He et al., 2019a)
Ceramic thickness	0.86 mm		(He et al., 2019a)
Heat sink			
Area	40 mm × 40 mm		
Height	3.34 mm		
Number of fins	30	5 – 40	
Other design parameters			
Wind speed	1 m/s		(G. Li et al., 2018a)
Concentration ratio	30	10 – 80	(Zhang et al., 2014)
Heat sink heat transfer coefficient (h_{sink})	500 W/m ² · K	100 – 800 W/m ² · K	(Zhang et al., 2014)
R_{pv_te}	200 mm ² · K/W	0 – 1000 mm ² · K/W	(Yin et al., 2017)

APPENDIX

R_{teg_hsink}	$200 \text{ mm}^2 \cdot K/W$	$0 - 1000 \text{ mm}^2 \cdot K/W$	(Yin et al., 2017)
R_c	$1 \times 10^{-6} \text{ m}^2 \cdot K/W$	$1 \times 10^{-6} - 1 \times 10^{-3} \text{ m}^2 \cdot K/W$	(Ouyang and Li, 2016)
R_{cont}	$1 \times 10^{-9} \Omega \cdot \text{m}^2$	$1 \times 10^{-9} - 1 \times 10^{-6} \Omega \cdot \text{m}^2$	(Ouyang and Li, 2018)

Polynomial functions for thermoelectric material (He et al., 2019a)

Property	p-type polynomial expression	n-type polynomial expression
Seebeck coefficient (V/K)	$-2.24407 \times 10^{-11} T^3 + 2.22834 \times 10^{-8} T^2 - 7.301$ $\times 10^{-6} T + 1.023698 \times 10^{-3}$	$1.68178 \times 10^{-11} T^3 - 1.77163 \times 10^{-8} T^2 + 6.203$ $\times 10^{-6} T - 9.54589 \times 10^{-4}$

APPENDIX

Thermal conductivity ($W/m \cdot K$)	$-5.82609 \times 10^{-8}T^3 + 1.03491 \times 10^{-4}T^2 - 0.050117T + 8.726$	$3.76869 \times 10^{-9}T^3 + 2.81722 \times 10^{-5}T^2 - 0.020577T + 5.09531$
Electrical resistivity ($\Omega \cdot m^2$)	$-7.75456 \times 10^{-13}T^3 + 7.77051 \times 10^{-10}T^2 - 0.01853T + 1.60117 \times 10^{-5}$	$-6.04782 \times 10^{-13}T^3 + 6.09155 \times 10^{-10}T^2 - 1.715T + 2.11951 \times 10^{-5}$

Photovoltaic optical material properties (Zhou et al., 2017)

Material	Reflectivity	Absorptivity	Transmissivity
Glass	4.00×10^{-2}	4.00×10^{-2}	9.20×10^{-1}
EVA	2.00×10^{-2}	8.00×10^{-2}	9.00×10^{-1}
Polycrystalline silicon	8.00×10^{-2}	9.00×10^{-1}	2.00×10^{-2}
TPT	8.60×10^{-1}	1.28×10^{-1}	1.20×10^{-2}

APPENDIX

Other material properties considered (He et al., 2019a; Zhou et al., 2017)

	Heat capacity, C_p ($J/kg \cdot K$)	Density, ρ (k/m^3)	Seebeck coefficient, α (V/K)	Electrical conductivity, σ (S/m)	Thermal conductivity, κ ($W/m \cdot K$)	Emissivity
Glass	5×10^2	2.45×10^3	-	-	2.00	0.85
EVA	2.09×10^3	9.60×10^2	-	-	3.11×10^{-1}	
Silicon	6.77×10^2	2.33×10^3	-	-	1.30×10^2	
TPT	1.25×10^3	1.20×10^3	-	-	1.50×10^{-1}	0.92
Ceramic	900	3900	-	-	36	0.9
Bi_2Te_3	154	7700	$\alpha(T)$	$\sigma(T)$	$\kappa(T)$	
Copper	385	8960	-	58100000	238	0.07

APPENDIX

Mesh convergence test

Number of domain elements	Element size	Average PV cell temperature (K)	Hybrid output (W)	power
27,177	Extremely coarse	397.66	1.4181	
41,137	Extra coarse	397.71	1.4174	
70,093	Coarser	397.74	1.4171	
132,759	Coarse	397.76	1.4169	
310,815	Normal	397.8	1.4166	
766,093	Fine	397.8	1.4166	

PV-TE-Heat Pipe Simulation Parameters (Section 5.5)

Geometric parameters used in simulation (Yin et al., 2018d; Zhou et al., 2017)

Parameter	Value
PV	
Area	40 mm x 40 mm
Glass thickness	3.20 mm
EVA thickness	4.60×10^{-1} mm
Polycrystalline silicon thickness	1.80×10^{-1} mm
Tedlar/PET/Tedlar thickness	1.80×10^{-1} mm
TEG	
Area	40 mm x 40 mm
Leg area	1 mm x 1 mm
Leg thickness	1.5 mm
Copper thickness	0.3 mm

APPENDIX

Ceramic thickness	0.8 mm
Heat pipe	
Evaporator	40 mm x 40 mm
Condenser	40 mm x 40 mm
Thickness	5 mm

Temperature dependent thermoelectric material properties (T is temperature in K) (Suzuki et al., 2016)

	p-type	n-type
Electrical conductivity, σ [S/m]	$(0.015601732T^2 - 15.708052T + 4466.38095) \times 10^2$	$(0.01057143T^2 - 10.16048T + 3113.714229) \times 10^2$
Seebeck coefficient, S [V/K]	$(-0.003638095T^2 + 2.74380952T - 296.214286) \times 10^{-6}$	$(0.00153073T^2 - 1.08058874T - 28.338095) \times 10^{-6}$
Thermal conductivity, k [W/(m · K)]	$0.0000361558T^2 - 0.026351342T + 6.22162$	$0.0000334545T^2 - 0.023350303T + 5.606333$

APPENDIX

Optical properties of PV materials (Zhou et al., 2017)

Material	Reflectivity	Absorptivity	Transmissivity	Emissivity
Glass	4.00×10^{-2}	4.00×10^{-2}	9.20×10^{-1}	8.50×10^{-1}
EVA	2.00×10^{-2}	8.00×10^{-2}	9.00×10^{-1}	
Polycrystalline silicon	8.00×10^{-2}	9.00×10^{-1}	2.00×10^{-2}	
TPT	8.60×10^{-1}	1.28×10^{-1}	1.20×10^{-2}	9.20×10^{-1}

Remaining material properties used for simulation (COMSOL Multiphysics, 2018a; Zhou et al., 2017)

	Heat capacity, C_p [J/(kgK)]	Density, ρ [kg/m ³]	Seebeck coefficient, [V/K]	Electrical conductivity, S [S/m]	Thermal conductivity, σ [W/(mK)]	Dynamic viscosity, μ [Pa·s]
Glass	5×10^2	2.45×10^3	-	-	2.00	-

APPENDIX

EVA	2.09 x 10 ³	9.60 x 10 ²	-	-	3.11 x 10 ⁻¹	-
Silicon	6.77 x 10 ²	2.33 x 10 ³	-	-	1.30 x 10 ²	-
TPT	1.25 x 10 ³	1.20 x 10 ³	-	-	1.50 x 10 ⁻¹	-
Vapor	1874	<i>Ideal gas ρ_v</i>	-	-	0.0188	8.9 x 10 ⁻⁶
		$= \frac{p}{R_s T}$				
Water	4180	1000	-	-	0.61	-
Alumina	900	3900	-	-	27	-
Bi ₂ Te ₃ (p-n types)	154	7700	$\pm S(T)$	$\sigma(T)$	$k(T)$	-
Copper	385	8960	-	58100000	400	-

APPENDIX

Mesh convergence test

Number of domain elements	Element size	Average cell temperature (K)	Overall hybrid power output (W)
70,269	Coarse	310.72	0.798606514
148,342	Normal	310.72	0.798597914
328,627	Fine	310.72	0.798587814
1,205,452	Finer	310.71	0.798598067
3,547,403	Extra fine	310.71	0.798598067

Segmented Annular TEG Simulation Parameters (Section 6.2)

Geometric parameters of the segmented annular thermoelectric generator

	r ₁ (mm)	r ₂ (mm)	r ₃ (mm)	r ₄ (mm)	r ₅ (mm)	r ₆ (mm)	r ₇ (mm)	r ₈ (mm)	r ₉ (mm)	r ₁₀ (mm)	Length (mm)	Depth (mm)	Angle (degree)
Ceramic	Depends on study	-	-	-	-	-	-	-	29.2	30	0.8	2	-
Copper	-	Depends on study	-	-	-	-	-	28.8	-	-	0.4	1	-
Solder	-	-	Depends on study	-	-	-	28.6	-	-	-	0.2	1	-
Bi ₂ Te ₃	-	-	-	-	-	Depends on study	-	-	-	-	r ₇ -r ₆	1	-
CoSb ₃	-	-	-	Depends on study	Depends on study	-	-	-	-	-	r ₅ -r ₄	1	-

APPENDIX

θ_1	-	-	-	-	-	-	-	-	-	-	-	-	-	Depends on study
θ_2	-	-	-	-	-	-	-	-	-	-	-	-	-	Depends on study
θ_3	-	-	-	-	-	-	-	-	-	-	-	-	-	1

*“Depends on study” means the value changes based on the parametric study being considered. For example, if $L = 2$, then $r_6 = 26.6$, $r_5 = 26.4$, $r_4 = 24.4$, $r_3 = 24.2$, $r_2 = 23.8$ and $r_1 = 23$. However, if $L = 3, 4$ or 5 , the radius values change accordingly.

Properties of other materials used in numerical simulation (Al-Merbati et al., 2013; Caillat et al., 1996; Fan and Gao, 2018; Gao et al., 2011; Guodong Li et al., 2015; Yang et al., 2011)

Materials	Thermal conductivity, $\kappa \left(\frac{W}{m \cdot K} \right)$	Electrical conductivity, $\sigma \left(\frac{S}{m} \right)$	Specific heat capacity, $C_p \left(\frac{J}{kg \cdot K} \right)$	Density, $\rho_d \left(\frac{kg}{m^3} \right)$	Coefficient of thermal expansion, $\left(\frac{1}{K} \right)$	Young's Modulus, E (GPa)	Poisson's ratio
Ceramic	25	1e-12	800	3970	0.68e-5	340	0.22

APPENDIX

Copper	385	5.9e7	386	8930	1.7e-5	120	0.3
Solder	55	2e7	210	7240	2.7e-5	44.5	0.33
Bi ₂ Te ₃	-	-	154.4	7740	0.8e-5~ 1.32e-5	65-59	0.23
CoSb ₃	-	-	238.7	7582	6.36e-6	145.38	0.223

Segmented Asymmetrical TEG Simulation Parameters (Section 6.3)

Geometric dimensions of thermoelectric generator (Chen and Lee, 2015)

Parameter	Symbol	Value
Ceramic height	H_{ce}	0.75 mm
Solder height	H_{so}	0.175 mm
Copper height	H_{co}	0.3 mm
Leg height	H	1.15 mm
Ceramic depth	D	1.4 mm
Ceramic width	W_{ce}	3.92 mm
Leg width	W_{le}	1.4 mm
Copper width	W_{co}	1.68 mm

Temperature dependent thermoelectric material properties (Shen et al., 2018)

Material equations

Thermal conductivity

$$k_{nh}(T) = 6.943541 - 2.486028 \times 10^{-2}T + 9.749004 \times 10^5T^2 - 2.532973 \times 10^{-7}T^3 + 3.938164 \times 10^{-10}T^4$$

$$k_{ph}(T) = 1.003769 \times 10^1 + 1.569560 \times 10^{-1}T - 8.040513 \times 10^{-4}T^2 + 2.155576 \times 10^{-6}T^3 - 3.177501 \times 10^{-9}T^4 + 2.436340 \\ \times 10^{-12}T^5 - 7.572115 \times 10^{-16}T^6$$

$$k_{pc}(T) = 1.151451 \times 10^{-1} + 4.474949 \times 10^{-2}T - 2.597266 \times 10^{-4}T^2 + 5.558334 \times 10^{-7}T^3 - 3.676412 \times 10^{-10}T^4$$

$$k_{nc}(T) = 9.550516 - 5.393685 \times 10^{-2}T + 1.123143 \times 10^{-4}T^2 - 6.666667 \times 10^{-8}T^3$$

Electrical resistivity

$$\rho_{pc}(T) = 2.728214 \times 10^{-5} - 2.254395 \times 10^{-7}T + 7.275808 \times 10^{-10}T^2 - 6.25084 \times 10^{-13}T^3$$

$$\rho_{nc}(T) = 1.167186 \times 10^{-5} - 9.313746 \times 10^{-8}T + 3.786254 \times 10^{-10}T^2 - 3.582737 \times 10^{-13}T^3$$

$$\rho_{ph}(T) = 3.445724 \times 10^{-6} + 3.427092 \times 10^{-9}T + 4.683604 \times 10^{-12}T^2 - 3.534736 \times 10^{-15}T^3$$

$$\rho_{nh}(T) = 1.814895 \times 10^{-6} + 5.429077 \times 10^{-9}T + 1.743566 \times 10^{-12}T^2 - 2.665253 \times 10^{-15}T^3$$

Seebeck coefficient

$$\alpha_{pc}(T) = 1.4831 \times 10^{-3} - 1.3905 \times 10^{-5}T + 5.3964 \times 10^{-8}T^2 - 8.8088 \times 10^{-11}T^3 + 5.0618 \times 10^{-14}T^4$$

$$\alpha_{ph}(T) = 9.8267 \times 10^{-5} + 1.4455 \times 10^{-6}T - 4.8488 \times 10^{-9}T^2 + 9.2428 \times 10^{-12}T^3 - 8.6346 \times 10^{-15}T^4 + 3.0656 \times 10^{-18}T^5$$

APPENDIX

$$\alpha_{nh}(T) = 1.9164 \times 10^{-4} - 3.4758 \times 10^{-6}T + 1.7756 \times 10^{-8}T^2 - 4.9992 \times 10^{-11}T^3 + 7.7054 \times 10^{-14}T^4 - 6.1429 \times 10^{-17}T^5 + 1.9864 \times 10^{-20}T^6$$

$$\alpha_{nc}(T) = 1.5178 \times 10^{-2} + 1.7621 \times 10^{-4}T - 8.1434 \times 10^{-7}T^2 + 1.8488 \times 10^{-9}T^3 - 2.0649 \times 10^{-12}T^4 + 9.0988 \times 10^{-16}T^5$$

where k_{nh} and k_{ph} are the thermal conductivities of n-type and p-type CoSb₃ respectively. k_{pc} and k_{nc} are the thermal conductivities of p-type and n-type Bi₂Te₃ respectively. ρ_{pc} and ρ_{nc} are the electrical resistivities of p-type and n-type Bi₂Te₃ respectively. ρ_{ph} and ρ_{nh} are the electrical resistivities of p-type and n-type CoSb₃ respectively. α_{pc} and α_{nc} are the Seebeck coefficients of p-type and n-type Bi₂Te₃ respectively. α_{ph} and α_{nh} are the Seebeck coefficients of p-type and n-type CoSb₃ respectively.

Remaining material properties used in simulation (Al-Merbati et al., 2013; Caillat et al., 1996; Chen and Lee, 2015; Fan and Gao, 2018; Gao et al., 2011; Guodong Li et al., 2015; Yang et al., 2011)

Materials	Thermal conductivity, $\kappa \left(\frac{W}{m \cdot K}\right)$	Electrical conductivity, $\sigma \left(\frac{S}{m}\right)$	Specific heat capacity, $C_p \left(\frac{J}{kg \cdot K}\right)$	Density, $\rho_d \left(\frac{kg}{m^3}\right)$	Coefficient of thermal expansion, $\left(\frac{1}{K}\right)$	Young's Modulus, E (GPa)	Poisson's ratio	Seebeck coefficient, α (V/K)
Ceramic	25	1e-12	800	3970	0.68e-5	340	0.22	0

APPENDIX

Copper	385	5.9e7	386	8930	1.7e-5	120	0.3	6.5e-6
Solder	55	2e7	210	7240	2.7e-5	44.5	0.33	0
Bi ₂ Te ₃	-	-	154.4	7740	0.8e-5 ~ 1.32e-5	65-59	0.23	-
CoSb ₃	-	-	238.7	7582	6.36e-6	145.38	0.223	-

Segmented Solar TEG Simulation Parameters (Section 6.4)

Geometric parameters (European Thermodynamics Limited, 2014b; Yin et al., 2018d)

Parameter	Value
Ceramic height	0.8 mm
Copper height	0.3 mm
Leg height	1 mm
Solder height	0.175 mm
Ceramic depth	30 mm
Ceramic width	30 mm
Leg width	1 mm
Leg depth	1 mm

APPENDIX

Remaining material properties used in simulation (Fan and Gao, 2019; Gao et al., 2011)

	Coefficient of thermal expansion, $\left(\frac{1}{K}\right)$	Density, $\rho_d \left(\frac{kg}{m^3}\right)$	Specific heat capacity, $C_p \left(\frac{J}{kg \cdot K}\right)$	Young's Modulus, (GPa)	Poisson's ratio	Thermal conductivity, $\kappa \left(\frac{W}{m \cdot K}\right)$	Electrical conductivity, $\sigma \left(\Omega^{-1} \cdot m^{-1}\right)$
Ceramic	0.68e-5	3970	800	340	0.22	25	1e-12
Solder	2.7e-5	7240	210	44.5	0.33	55	2e7
Copper	1.7e-5	8930	386	120	0.3	385	5.9e7
Bi ₂ Te ₃	0.8e-5-1.32e-5	7740	154.4	65-59	0.23	-	-
Skutterudite	0.8e-5	6800	225	110	0.21	-	-

Solar TEG with PCM Simulation Parameters (Section 6.5)

Geometric parameters (European Thermodynamics Limited, 2014b; Yin et al., 2018d)

Parameter	Value
Ceramic height	0.8 mm
Copper height	0.3 mm
Leg height	1 mm
Ceramic depth	30 mm
Ceramic width	30 mm
Leg width	1 mm
Leg depth	1 mm
PCM container height	6 mm
PCM height	5 mm
PCM fin width	0.5 mm

APPENDIX

Other material properties used in simulation (Yin et al., 2018d)

	Heat capacity, C_p [J/(kgK)]	Density, ρ [kg/m ³]	Seebeck coefficient, [V/K]	Electrical conductivity, α [S/m]	Thermal conductivity, σ [W/(mK)]	Emissivity k
Ceramic	850	3960	-	-	18	0.9
Bi ₂ Te ₃	154	7700	$\pm \alpha(T)$	$\sigma(T)$	$k(T)$	-
Copper	385	8960	-	5.998×10^7	400	-
SSA	-	-	-	-	-	0.05

Properties of RT25HC phase change material (Rubitherm Technologies GmbH, 2020)

Properties	RT25HC
Melting area (°C)	22-26
Peak melting point (°C)	25
Congealing area (°C)	26-22

APPENDIX

Heat storage capacity(kJ/kg) 230

Specific heat capacity ($kJ/kg/K$) 2

	Liquid	Solid
Thermal conductivity ($W/m/K$)	0.2	0.2
Density (kg/m^3)	770	880

Mesh convergence test

Number of domain elements	Element size	Maximum power output (mW)	Maximum temperature (°C)
8,652	Extremely coarse	5.44	27.13
17,285	Extra coarse	5.75	27.40
34,823	Coarser	5.61	27.21

APPENDIX

104,522	Normal	5.25	27.13
156,960	Fine	5.25	27.13
